January 2013

Design, Manufacturing, and Assembly of a Flexible Thermoelectric Device

Christopher Anthony Martinez
University of South Florida, camarti9@mail.usf.edu

Design, Manufacturing, and Assembly of a Flexible Thermoelectric Device

by

Christopher Martinez

A thesis submitted in partial fulfillment
of the requirements for the degree of
Master of Science in Mechanical Engineering
Department of Mechanical Engineering
College of Engineering
University of South Florida

Major Professor: Nathan Crane, Ph.D.
Kyle Reed, Ph.D.
Frank Pyrtle, Ph.D.

Date of Approval:
June 29, 2013

Keywords: thermoelement, circuit board, heat transfer,
scalable, design for assembly

DEDICATION

I dedicate this thesis to the self-made individual, the personal pioneer who elevates their standings to a position far removed from where they originated.

ACKNOWLEDGMENTS

I would like to thank Dr. Nathan Crane for extending his guidance, ingenuity, and patience with me on this project. It was through Dr. Crane that I began research as an undergraduate here at USF and it is under his mentorship that I conclude it as a graduate student.

I would also like to thank Dr. Kyle Reed for his support. Dr. Reed's troubleshooting assistance during the control system portion of the research was time spent that this thesis cannot lay testament to.

The University of South Florida and their Mechanical Engineering department have been tremendously helpful to me during my academic career. Without the college's resources, professors, faculty, and staff this thesis would not be possible.

Lastly, I would like to thank those who have made the longest and largest contributions toward my success, my family and friends. I owe thanks to my mother Frances Martinez for her endless encouragement and faith in my abilities, my brother Joseph Martinez, my sister-in-law Ellen Martinez, my cousin Jeffery Sawick, my aunt Elizabeth Reiff, and my soon to be mother-in-law Sandi Kahn all of whom expressed interest which reinvigorated my own, and my fiancé Julie Kahn for her tireless support. Thank you also to my friend Yohannes Samuel, my lab mates Jose Carballo, Benjamin Hahne, and Qi Ni for providing help in their areas of expertise, and Brian Bertram for his help while I was an undergraduate.

This work was funded in part by support from the National Science Foundation through grant CMMI-0927637.

TABLE OF CONTENTS

LIST OF TABLES

LIST OF FIGURES

ABSTRACT

This thesis documents the design, manufacturing, and assembly of a flexible thermoelectric device. Such a device has immediate use in haptics, medical, and athletic applications. The governing theory behind the device is explained and a one dimensional heat transfer model is developed to estimate performance. This model and consideration for the manufacturing and assembly possibilities are the drivers behind the decisions made in design choices. Once the design was finalized, manufacturing methods for the various components were explored. The system was created by etching copper patterns on a copper/polyimide laminate and screen printing solder paste onto the circuits. Thermoelectric elements were manually assembled. Several proof of concept prototypes were made to validate the approach. Development of the assembly process also involved proof of concept prototyping and partial assembly analysis. A full scale device was produced and tested to assess its thermoelectric behavior. The resulting performance was an interface temperature drop of 3 °C in 10 seconds with 1.5 *A* supplied, and a maximum temperature drop of 9.9 °C after 2 minutes with 2.5 *A* supplied. While the measured behavior fell short of predictions, it appears to be adequate for the intended purpose. The differences appear to be due to larger than expected thermal resistances between the device and the heat sinks and some possible degradation of the thermoelectric elements due to excess solder coating the edges.

CHAPTER ONE: INTRODUCTION

Motivation

The purpose of this research is to design a flexible (bending diameter of 2 inches about a single axis) and wearable (currently as a scientific instrument but with future alternatives as an accessory or integrated into apparel) thermoelectric device (TED) that can achieve a 15 °F temperature change within 10 seconds at different longitudinal sections of the human to device interface. Since the device will be worn, the current carrying surfaces must be isolated, and it must present no potential danger to the user. This design must also allow for iteration based scalability (can increase or decrease the device's blanketing area) and adaptability (modifications can be made to accommodate different power sources, heat sources, heat sinks, and performance metrics).

The immediate application of this device (at the time of writing) is to study the human perception of multiple dynamic temperature inputs over small and large areas of the body. Part of our study will involve safe investigation of the 'thermal grill illusion'. Discovered in 1896 by Torsten Thunberg, the 'thermal grill illusion' involves the production of a burning sensation when warm ($T \geq 104$ °F) and cold ($T \leq 68$ °F) temperature sources are paired within close proximity and applied to the human body. [1] A better comprehension of the underlying physiological causes for this response would improve the scientific community's understanding on the operation of the ventrolateral spinothalamic tract; which "mediates the perception of pain and temperature." [2]

However, this device has the potential to be used for more than misdirecting an individual's sensory perception. It could be used in athletics or other activities that involve extensive physical exertion. In these scenarios, the device would provide cooling for the individual, attenuating the onset of thermal fatigue. Stanford University is currently developing a "cooling glove" for this purpose. For their design, participants wear a multilayered glove which has cooled water circulated through its envelope. [3]

A derivative of this device could also be used in the examination of people suffering from nerve damage, like that of painful diabetic neuropathy (PDN). Currently electrophysiological procedures are capable of exploring the condition of large neural fibers, those which perceive touch and proprioception. However, these procedures do not analyze the smaller neural fibers, those which are sensitive to cold and hot stimulation, and pain. These smaller fibers are first affected by the disease which then progresses to the larger ones. [4] The temperature resolution this device is capable of producing is proportional to the incremental change of electric current supplied. Therefore it is plausible to use this device in an examination process where the physician records the patient's responses to various temperatures achieved with a high level of precision.

Previous Work

This research is directly inspired by Patrick McKnight's work in his thesis "Finite element analysis of thermoelectric systems with applications in self assembly and haptics." In Chapter 4 – Thermal Haptic Display, Mr. McKnight discusses the creation of a thermoelectric device that can create multiple temperatures along a series of independent pathways where each of these pathways share a common control surface that is in contact with human skin. He outlined a control system for the device and

developed a thermoelectric prototype that was able to successfully heat one side of the device to 42 °C (108 °F). [5]

At the time of this publication there are few research articles relating to the keywords “flexible thermoelectric cooler”. This may be due in part to the 2001 U.S. patent on such devices. [6] This patent covers flexible column based single and multi-layer TE devices where the flexibility is often suggested to be achieved by cutting the circuit board and weakening it. The author does say frequently however that at least one of the circuit boards must be rigid.

In 2008 researchers in Taiwan investigated the development of low cost rigid micro scale thermoelectric coolers. Fabrication was completed using microelectromechanical systems (MEMS) and two different methods for structuring the thermoelements were applied. The first was a column based arrangement that used bismuth telluride and bismuth antimonide elements. The alternative arrangement was a “bridge type” structure; where polysilicon thermoelements and conductive metal were interwoven in a crosshatched pattern. The authors concluded that their bridge type assembly, with 62,500 elements covering a 100 mm^2 chip yielded the best results; with a 2 °F temperature difference achieved by a 200 *mA* driving current. However, both of their configurations required multiple photomasks (4 for the column type, 5 for the bridge type), and the bridge type arrangement required being raised above 1800 °F twice during the manufacturing process. [7] These occurrences increase development duration and energy expenditure, both of which have cost correlations.

Thermoelectric devices possess utility beyond their use as mechanically static heat pumps. Inherent to the thermoelectric property is the ability to generate voltage when supplied a temperature gradient (refer to Seebeck effect within the Conceptual Background section). [8] Research is being done to exploit this phenomenon for energy

generation and or recapturing since thermodynamics proves that anything which does work produces heat. [9]

For example, at the University of Salento in Italy, L. Francioso and colleagues prototyped a wearable flexible thermoelectric device designed to use an individual's body heat as a means for energy generation. Their intention is to develop a product that could be used by the elderly to power biometric devices. Francioso developed their thermoelectric device using thin film deposition to place 500 nm thick antimony telluride and bismuth telluride thermocouples on a 50 μm thin substrate. The device measured 70 x 30 mm (approx. 2.76 x 1.18 inches), featured 100 thermoelements, and provided a 0.05 open circuit voltage when a 9 °F temperature difference was applied across the device. From their data they concluded that it would take 734 thermocouples to achieve 3 volts. [9]

Conceptual Background

In the early 1820's Thomas J. Seebeck observed the production of a magnetic field when heat was applied to one end of a metallic loop. This loop was created by joining two electrically conductive but different metals end to end (not braided, see Figure 1).

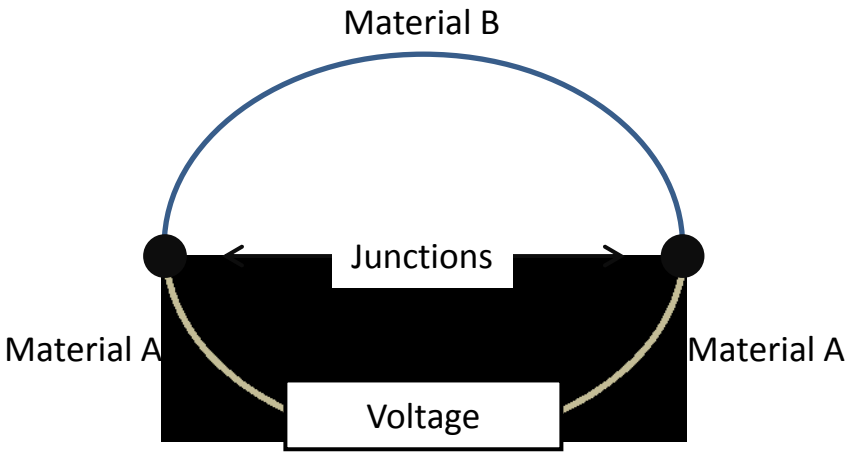

Figure 1: Simple thermoelectric circuit

In order to explain this response the Seebeck effect was created. The Seebeck coefficient (Equation 1) is a material property that represents the amount of voltage that can be achieved per degree temperature change across the material. [8]

$$V = \alpha(T_2 - T_1) \quad \text{Equation 1}$$

where V is voltage, α is the Seebeck coefficient in *V/K*, and both T_2 and T_1 represent the temperatures measured in Kelvin at different locations of the material.

As the different periodic elements have distinct relationships with the way in which electrons orbit them, then a compliant change in this relationship must occur between adjoining dissimilar materials which are passing current between them. This transmission of electrons and its subsequent effects brings with it an inflow or outflow of heat in order to balance the energy within the system. [8]

Later in the early 19th century Jean-Charles Peltier discovered that heat transfer also occurs at the connections between the different conductive elements when both elements are exposed to different temperatures. This occurrence has been accounted for mathematically (Equation 2).[8]

$$\dot{Q} = \pi I \quad \text{Equation 2}$$

where $\dot{Q}$ is the heat transfer in *W*, π is the Peltier coefficient in *W/A*, and I is the current flowing through the circuit in *A*. This heat transfer has been facilitated by doping the thermoelements to have either a higher (n-type) or lower (p-type) than normal quantity of free electrons (Figure 2). [10][11]

The final fundamental discoveries were made in the middle of the 19th century by William Thomson. He established the relationships between the Peltier and Seebeck Effects (Equation 3) and is credited with the discovery of yet another effect. The Thomson effect accounts for the heat production that occurs in a lone conductive material, independent of the Joule effect, when current flows thru the material while its

ends are also exposed to different temperatures (Equation 4), where β represents the Thomson coefficient in *V/K*. [8][10]

$$\alpha T = \pi$$ Equation 3

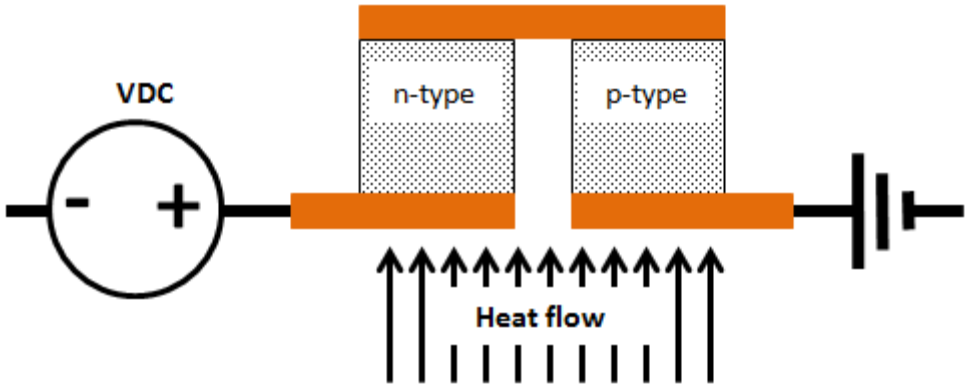

Figure 2: Heat flow through a column based thermoelectric circuit

$$Q = \beta I(T_2 - T_1)$$ Equation 4

The Joule effect, commonly known as resistive heating, is the production of heat when electrical current is passed through an electrically resistive object where R is the object's resistance in ohms (Equation 5). The knowledge of this occurrence has been accounted for and manipulated in multiple ways, whether it is for the creation of heat inside a toaster or the necessity of cooling fans inside of a laptop. [12]

$$Q = I^2 R$$ Equation 5

Thermoelectric Materials

Since the establishment of a temperature gradient is the desired result, the thermoelement will ideally have low thermal conductivity. Moreover, to avert the production of resistive heating resulting from the current flow it would also have low electrical resistivity. However, kinetic theory expresses thermal conductivity, k in *W/(m K)*, as:

$$k = k_e + k_{ph}$$ Equation 6

where k_e represents electron related thermal conductivity, which is proportional to electrical conductivity, and k_{ph} is the phonon related thermal conductivity. [12] This relationship illustrates the difficulty with producing a thermally resistive material with high electrical conducitivty, and why conductors and semiconductors are considered in thermoelectric sciences.

Recognition of these desired characteristics lead to the development of the power factor, pf in *W/K* (Equation 7)

$$pf = \alpha^2 \sigma$$ Equation 7

where σ is the electrical conductivity of the thermoelement in siemens (S). [8] This value helps researchers quickly identify if a material has desirable properties. Another valuable method for evaluating a thermoelectric circuit is in the calculation of its figure of merit, z in K^{-1} (Equation 8). [11]

$$z = \frac{(\alpha_1 + \alpha_2)^2}{\left(\sqrt{k_1\rho_1} + \sqrt{k_2\rho_2}\right)^2}$$ Equation 8

where ρ is the electrical resistivity in Ω*m,* and the subscripts indicate the branch of the thermoelectric circuit being referenced. Multiplying the figure of merit by the ambient temperature and using the material's thermoelectric properties at that temperature allows for quantifying the system's performance within a given environment. The performance of different thermoelement compounds varies with temperature and can be seen in (Table 1). Since the focus of the research is to recreate temperatures people could naturally be exposed to, bismuth will be the thermoelement employed.

Table 1: Thermoelements and their temperature specific performance

Compound	**Temperature Range (K)**	**Z value (K^{-1})**
Bismuth antimonide [8]	120 T 280	0.003
Bismuth telluride [10]	273 T 473	0.002
Silver antimony telluride [8]	T 500	0.002

Outline

As the title implies, this thesis covers the design, assembly, and manufacturing methods for a flexible thermoelectric device. These three areas of product development are heavily dependent upon one another. Any time a decision was made it was reached with design goals in mind. These decisions often occurred at different stages of the process, resulting in a tendency for sections to overlap. Information pertaining to the product's development was categorized by its relevance. This approach was either cause driven (methods and approach) or effect driven (results and dimensional).

Chapter Two: Thermoelectric Device Design starts with the Device Modeling section, where a 1-D heat transfer model is used to estimate the thermoelectric behavior for different device configurations. The Device Requirements section details the demands and desired attributes of the device, beyond what was explained in the first paragraph of the Introduction. Then it progresses onto the Materials section where explanation is provided on material choice (thermoelement, circuit board, and solder paste) and their properties. Then the chapter concludes with the Circuit Boards and Staging Area sections. There the circuit board’s final dimensions, number of thermoelements, and relevant calculations provide foresight for the manufacturing and assembly objectives.

Chapter Three: Manufacturing begins with explaining the two manufacturing processes utilized, etching and milling. That leads in to sections explaining preliminary tests using those processes to create circuit boards, solder stencils, and alignment components. The chapter concludes with the production of the final components; the circuit boards, thermoelement templates, and solder stencil.

Chapter Four: Assembly details the procedure followed to assemble the TE device. In the Final Assembly Results and Discussion section the problems encountered

(post assembly processing, adequate solder reflow duration) during the assembly processes and how they were overcome are explained.

The testing methods for evaluating performance are explained in the first section of Chapter Five: Device Performance. The results obtained from these testing methods are analyzed in the Performance Data section. In this section an approach toward analyzing the 12,000 data points is explained and an interpretation of the results can be applied to predicting functionality.

In Chapter Six: Conclusions and Future Work the conclusions, sources of error, and future work considerations are explained for each of the topics covered by this research (Design, Manufacturing, Assembly, and Performance).

CHAPTER TWO: THERMOELECTRIC DEVICE DESIGN

This chapter details the progression of the circuit board's development. These details extend from estimating device performance and interface conditions through to the final design choice.

Environmental Parameters

The approximated environmental conditions for the TE device are:

- Ambient air temperature of 21 °C (70 °F) with 60% relative humidity.
- Skin surface temperature of 29 °C (85 °F).
- Inactive interface temperature of 27 °C (80 °F).

Device Requirements

The device must be:

- Multichannel: Device must be able to independently vary the temperature at five locations.
- Flexible: Capable of 2 inch (50.8 mm) bending diameter without permanent damage.
- Wearable: The user must be protected from hazards.. Dangers to be avoided include but are not limited to: hazardous chemical exposure, moving parts, and electrical exposure.
- Fast thermal response: 15 °F interface temperature change within 10 seconds.
- Compact: Device overlay dimensions of approximately 2 x 3 inches (50.8 x 76.2 mm).

- Supply sufficient heat flux: Capable of producing a thermal flux greater than 8.2 mW/cm^2 (see Forearm Modeling for calculation details) at each of the device's 5 independent sections.
- Adequate temperature range: Capable of generating an interface temperature range between 16 °C and 32 °C (60 and 90 °F).
- Allow temperature measurement: Able to accommodate at least one temperature sensor per independent section.
- Standardized manufacturing: Constructed by standard manufacturing practices or directly adaptable for mass production.
- Minimal allowable temperature: Kept from reaching the environment's dew point of 13 °C (56 °F).
- Repairable: not all causes of device failure (i.e. poor solder connection) should be terminal.
- Built by a deadline: Completed by the summer of 2013.

Device Modeling

This section discusses the manner in which the thermoelectric effect was estimated. The chosen thermoelement's size, cooling flux, surface temperatures, current required, number of elements, and device overlay area are relayed in the Modeling Conclusions subsection.

One dimensional steady state analysis was used in the estimation of the device's performance. The model used was one developed by Andrew Miner [13]. He creates two equations that are energy balances for the hot and cold sides of the thermoelectric device, where each term represents a flux in W/m^2.

The energy balance for the hot side is:

$$(T_a - T_h)K_h + IST_h + (T_c - T_h)K_e + I^2\left(\frac{R}{2} + R_i\right) = 0 \qquad \text{Equation 9}$$

where subscripts c and h signify the cold and hot side of the circuit, respectively. T_a is the ambient temperature (all temperatures in Equation 9 through Equation 19 are in Kelvin), T_s is the skin's surface temperature, K is the thermal conductance in *W/(m^2 K)*, I is the sum of the current densities through each of the thermoelements *A/m^2*, S is the Seebeck coefficient (previously referenced as α), K_e is the thermoelement's thermal conductance, R is the equivalent contact resistance from all of the thermoelements *Ωm^2*, and R_i is the electrical contact resistance between components. For this research it was assumed that T_a was 16 °C (289 K) and T_s was 26 °C (299 K).

The energy balance for the cold side is:

$$(T_h - T_c)K_e + I^2\left(\frac{R}{2} + R_i\right) - IST_c + (T_s - T_c)K_c = 0 \qquad \text{Equation 10}$$

Solving for T_c from the hot side energy balance yields:

$$T_c = T_h + \frac{\left(-(T_a - T_h)K_h - IST_h - I^2\left(\frac{R}{2} + R_i\right)\right)}{K_e} \qquad \text{Equation 11}$$

Conversely, solving for T_h from the cold side energy balance yields:

$$T_h = Tc + \frac{\left(-I^2\left(\frac{R}{2} + R_i\right) + IST_c - (T_s - T_c)K_c\right)}{K_e} \qquad \text{Equation 12}$$

Manipulation of Equation 9 and Equation 10 allows for T_c and T_h to be solved explicitly:

$$T_c = \frac{A + B}{C} \qquad \text{Equation 13}$$

where

$$A = 2K_eK_hT_a + 2K_eK_cT_s + 2K_cK_hT_s + 2I^2K_eR \qquad \text{Equation 14}$$

$$B = I^2K_hR + 4I^2K_eR_i + 2I^2K_hR_i - I^3RS - 2I^3R_iS - 2IK_cST_s \quad \text{Equation 15}$$

$$C = 2K_eK_c - 2I^2S^2 + 2K_eK_h + 2K_cK_h - 2IK_cS + 2IK_hS \quad \text{Equation 16}$$

and

$$T_h = \frac{D + E}{C} \quad \text{Equation 17}$$

where

$$D = 2K_eK_hT_a + 2K_eK_cT_s + 2K_cK_hT_a + 2I^2K_eR \quad \text{Equation 18}$$

$$E = I^2K_cR + 4I^2K_eR_r + 2I^2K_cR_r + I^3RS + 2I^3R_iS + 2IK_hST_a \quad \text{Equation 19}$$

Specifying all of the values for the terms in Equation 13 and Equation 17 allowed for calculation of the device's output temperatures. Calculations were completed using MATLAB (Appendix A: 1D Model MATLAB Code).

Our application of this model assumes that the skin and ambient temperatures are held constant, heat only travels by conduction in one dimension, all materials are homogenous, material properties of the p and n type thermoelements are the same, and that temperature effects on material properties are negligible.

The one dimensional model describes heat as flowing through the succession of materials in their layered sequence and the current flows through the electrical circuit in series. However, layering materials does not increase the equivalent conductivity, like what a series model would provide. Instead the equivalent conductivity should be less than any of the constituent values. Due to the model's use of heat fluxes, each conductivity must be converted to its relative conductance. This is achieved by dividing each material's conductivity by their 1-D heat transfer length. Once that is complete the

equivalent thermal conductance involves representing their values in parallel (Equation 20). An important relationship to note is that thermal contact resistance is already represented as the inverse of conductance.

$$K_{eq} = \left(\frac{1}{K_1} + \frac{1}{K_2} + \cdots + \frac{1}{K_n}\right)^{-1} \quad \text{Equation 20}$$

Included within the K_c value are the thermal contact resistances between the device and forearm, from each solder connection, and from the epoxy that bonds the copper to the substrate. However, not all of the dimensions and materials to be used were known during the preliminary estimates of the device's performance (Appendix A: 1D Model MATLAB Code). Table 2 explains the approximated values for the modeling parameters. The most significant of these was assumed the hot side thermal conductance value (K_h) because of its influence on the amperage for the peak cooling flux. Increasing K_h resulted in an increased cooling flux but also increased its current requirement. Since the top side's heat removal method and subsequent interface interaction was unknown it was decided that the outbound conductance would be represented as an additional layer of solder and copper. K_h was assumed to be higher than K_c because the surface could be optimized. It was not until after a supplier for desirable circuit board material was found that this layer was defined as layers of adhesive and polyimide (Figure 3). Applying the assumed values the performances of 4 different thermoelement dimensions were calculated and compared (Table 3).The thermal fluxes were converted to *W/cm²* from *W/m²* to present their values on a scale relative to the device's size.

Table 2: Values of assumed modeling parameters

Parameter	Value
K_c	934 $\frac{W}{m^2 K}$
K_h	8990 $\frac{W}{m^2 K}$

Table 2 (Continued)

K_e	1193 $\frac{W}{m^2 K}$
T_a	16 °C
T_s	26 °C
R	16.8 $n\Omega m$
R_i	0
I	0 to 6.15 $\frac{A}{m^2}$ (results in 0 to 12 A)

Table 3: Preliminary estimates for thermoelement performance

Base Area (mm, in)^2	Height (mm, in)	Cooling (W/cm^2)	Max cooling amperage
1.397, 0.055	1.676, 0.066	4.0352	5.4
1.397, 0.055	1.702, 0.067	4.0335	5.3
0.5588. 0.022	1.016, 0.04	4.1284	1.2
0.635. 0.025	1.016, 0.04	4.1262	1.5

.

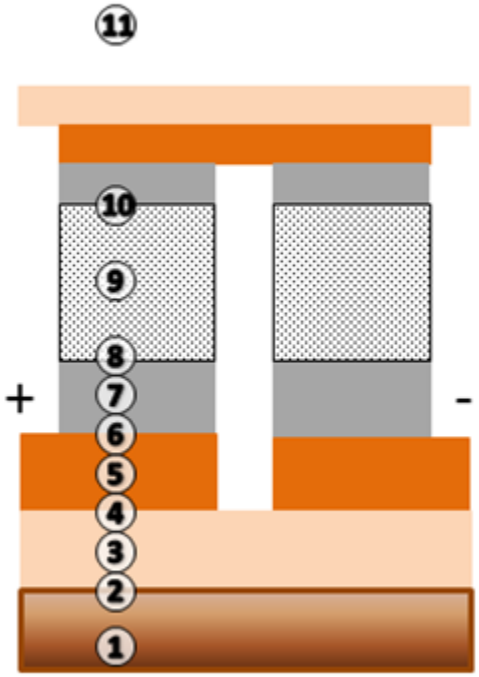

1. Skin temperature, T_s
2. Device to interface thermal contact resistance, $R_{th,skin}$
3. Substrate conductance, K_{subs}
4. Adhesive thermal contact resistance, $R_{th,adh}$
5. Adhesive conductance, K_{adh}
6. Solder thermal contact Resistance, $R_{th,sold}$
7. Solder conductance, K_{sold}
8. Cold side temperature location, T_c , and solder thermal contact resistance, $R_{th,sold}$
9. Thermoelement conductance, K_{BiTe}
10. Hot side temperature location, T_h , and solder thermal contact resistance, $R_{th,sold}$
11. Ambient temperature, T_a

Figure 3: 1-D locations of thermal resistance and their contribution to the model

Thermoelements with a base less than one square millimeter were dismissed from consideration for this project due to the difficulty anticipated in accurately manipulating their placement by hand (with the tools allotted). Due to their higher cooling performance and satisfaction of the dimensional requirement the 1.397 mm^2 x 1.676 mm elements were selected to be used on the device. Figure 4 and Figure 5 illustrate the selected thermoelement's estimated performance profile (without accounting for the element fill factor). The cold and hot side temperatures at 5.4 amps are -17 and 38 °C respectively (2 and 101 °F).

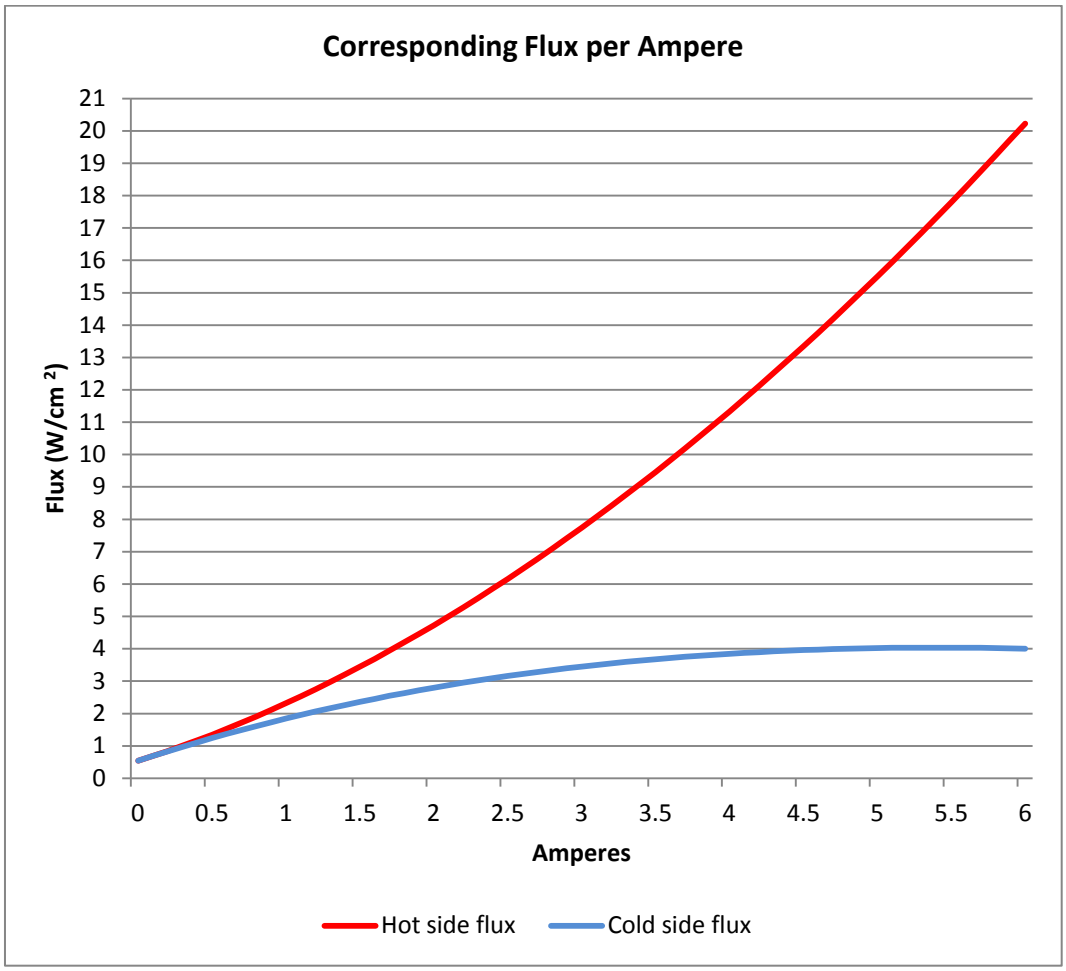

Figure 4: 1-D heat transfer model's estimated thermal fluxes for each surface

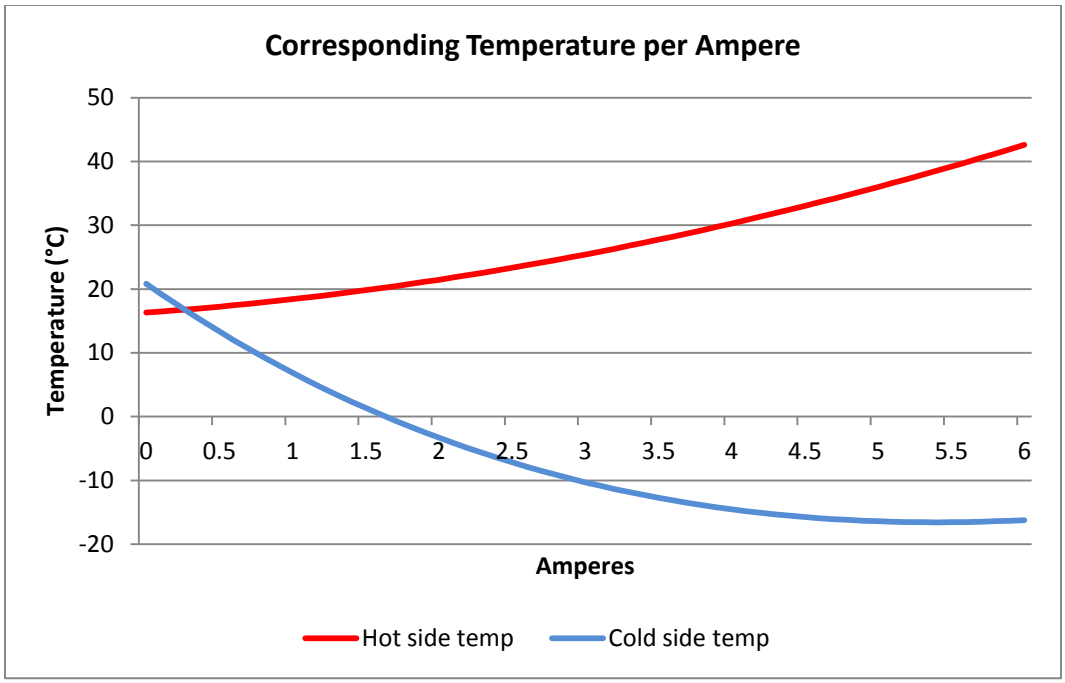

Figure 5: 1-D heat transfer model's estimated temperatures for each surface

Modeling Conclusions

Of the thermoelements accessible to the lab, the 1.397 x 1.397 x 1.676 mm thermoelement size was chosen for this design because of its peak cooling performance at 5.4 *A*; 4.0352 W/cm^2 cooling flux, and cold and hot side temperatures of -17 and 38 °C. These thermoelements would have a column oriented arrangement and alternate between p and n-type composition (Figure 6). To simplify the design process the base dimensions of the thermoelement are rounded up to 2 mm, allowing the approach of referencing the device's dimensions in terms of equivalent thermoelements. The Circuit Boards section explains how this was implemented. The results were overlay dimensions of 2.44 x 3.23 inches (62 x 82 mm). This is just beyond the 2 x 3 inch (50.8 x 76.2 mm) approximated requirement but is worth the compromise (see Adjusted Performance Estimates) with 180 thermoelements. It was also concluded that the best way to safely handle the peak 5.4 *A* value was if the bottom substrate remained an uncompromised electrically insulating surface with no holes or separations.

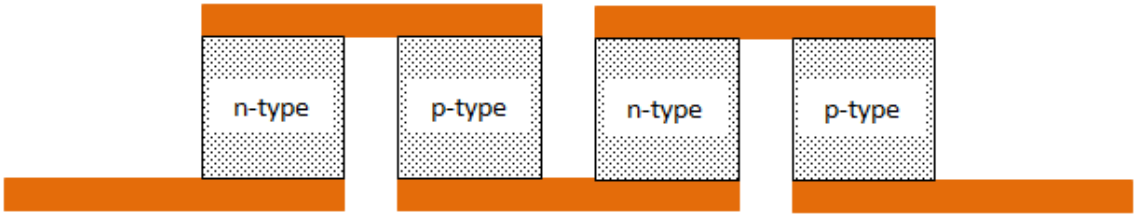

Figure 6: Example of a side view of a column based arrangement of thermoelements mounted perpendicularly to electrically conductive material

Forearm Modeling

It is necessary to quantify the body's combating heat flux. In this chapter a lower bound estimate of the forearm's heat flux was calculated as the sum of convection, radiation, irradiation, and evaporation fluxes from the skin's surface. Furthermore, the assumption was made that the temperatures experienced by the wearer would not provoke bodily temperature compensation, including additional perspiration or shivering. This value was later incorporated in the Adjusted Performance Estimates section to establish the relativity of the device's estimated performance.

Lower bound estimates of the forearm heat flux were made using equations from the model developed by Fiala et al. Their data is based on a humanoid with 73.5 kg of mass and 14% body fat, in an environment with an effective air velocity of 0.05 *m/s* ($v_{air,eff}$), and 30 °C (86 °F) ambient air (T_{air}) and surrounding surface temperatures (T_{sf}), where use of a_{nat} in $W^2/(K^{5/2}\ m^4)$, a_{frc} in $W^2 s/(m^5\ K^2)$, and a_{mix} in $W^2/(m^4\ K^2)$ in Equation 23 are regressed coefficients provided by Fiala et al. [14]

For this research the ambient air and interface temperature were replaced with 21 °C and 29 °C respectively (Environmental Parameters section), and the effective air velocity was 0.01 m/s. All temperatures used in this section were converted to Kelvin.

The skin's heat flux, q_{sk}, is the sum of the heat fluxes that interact with the skin's surface.

$$q_{sk} = q_c + q_R - q_{sR} + q_e \quad \text{Equation 21}$$

where q_c, q_R, q_{sR}, and q_e are the heat fluxes due to convection, radiation, irradiation, and evaporation, respectively. The irradiation heat flux value was assumed to be zero. The convection equation is:

$$q_c = h_{c,mix} \cdot (T_{sf} - T_{air}) \quad \text{Equation 22}$$

where T_{sf} is the temperature of the skin's surface at the area of interest and T_{air} is the temperature of the air. The convection coefficient, $h_{c,mix}$ in *W/(m² K)*, is:

$$h_{c,mix} = \sqrt{a_{nat}\sqrt{T_{sf} - T_{air}} + a_{frc} v_{air,eff} + a_{mix}} \quad \text{Equation 23}$$

The heat flux due to convection was calculated to be 33 *W/m²*.

The radiation contribution is:

$$q_R = h_R \cdot (T_{sf} - T_{sr,m}) \quad \text{Equation 24}$$

where $T_{sr,m}$ is the mean temperature of the surrounding surfaces and h_R is the local radiation heat-exchange coefficient in *W/(m² K)*, calculated using:

$$h_R = \sigma \epsilon_{sl} \epsilon_{sr} \psi_{sf-sr} (T_{sf}^2 + T_{sr,m}^2)(T_{sf} + T_{sr,m}) \quad \text{Equation 25}$$

where σ is the Stefan-Bolzmann constant in *W/m² K⁴*, ϵ_{sl} and ϵ_{sr} are the emissivities (dimensionless) of the body and surrounding surfaces respectively, and ψ_{sf-sr} is the view factor (dimensionless). These values were also provided in Fiala's paper. [14] The heat flux due to radiation was calculated to be 37 *W/m²*.

Assuming steady state and that no water vapor pressure existed on the skin's surface the evaporation heat flux calculation is:

$$q_e = \frac{P_{osk,sat}}{R_{e,sk}} \quad \text{Equation 26}$$

where $P_{osk,sat}$ is the saturated vapor pressure within the considered area of skin in *Pa*, and $R_{e,sk}^{-1}$ is the skin moisture permeability *W/(m² Pa)*. [14] The resulting evaporation flux is 12 *W/m²*.

This results in a total forearm heat flux of 82 *mW/cm²*. When incorporating the fill factor this results in the TE channel outputting a flux that is more than 80 times greater than that of the forearm (please see Adjusted Performance Estimates section).

Component Attachment

Even though components attachment is an assembly process it has a great effect on the circuit's design. It dictates whether current will be present on two sides of the board and the properties of solder that should be used. Therefore, these options are discussed briefly in this section. There are two primary methods for mounting an electrically conductive circuit board component, either with through hole or surface mounting techniques. [15]

Through hole mounting requires the circuit board itself to have a hole, or series of holes, and the attaching component must have an equivalent number of pins. These holes are located somewhere along the board's conductive tracing (Figure 7). The pins of the attaching components pass through the circuit board's holes and are soldered to the side opposite where the part took entry (Figure 8). This provides excellent part attachment because the pins physically anchor the component to the board.

Surface mounting allows for part attachment to a single side of the circuit board by use of a solder pad. The electrically conductive parts of the component are placed on top of the solder pad(s) and after reflowing the solder the junction becomes a hardened joint (Figure 9 and Figure 10). For the reason that surface mounting does not produce current carrying protrusions on the opposite side of the board and therefore removes a

potential source of electric shock to the user, it was chosen as the method of attachment.

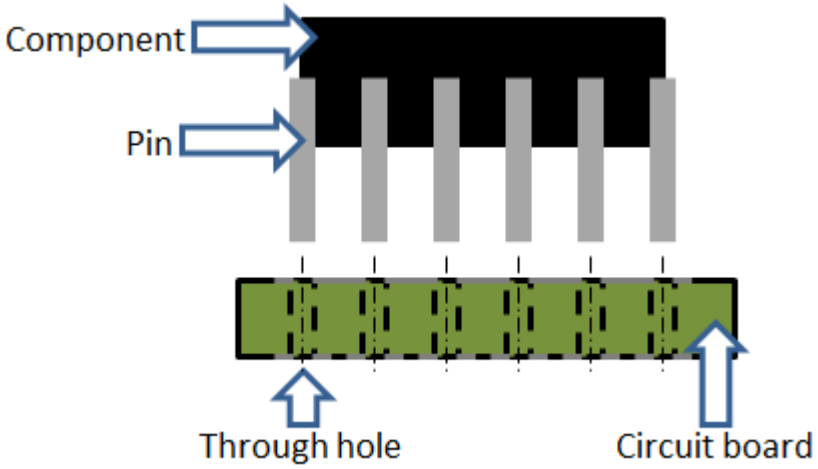

Figure 7: Diagram of intended through hole pin placement to circuit board placement and mating surfaces

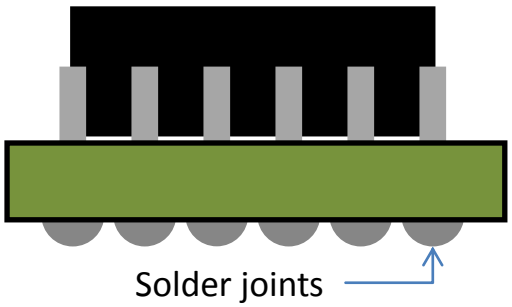

Figure 8: Example of a through hole mounted electrical component soldered to a circuit board on the side opposite its insertion

In order to reach the device's full estimated potential, the circuit board's traces must safely operate with current magnitudes up to 5.4 *A* (see Modeling Conclusions for details). The thermoelement's dimensions (1.397 mm^2 x 1.676 mm) play a governing role in determining the solder pad thickness. If the solder pad is too thick then solder runoff during the reflow process could create thermal and electrical shorts, or bypass the thermoelement altogether. Furthermore, coating the sides of the thermoelement with excess solder could cause it to diffuse into the thermoelement during the reflow process,

lessening its thermoelectric properties. Alternatively, an inadequate amount of solder paste will give rise to high thermal and electrical contact resistances. In addition to the solder paste's thickness, the height uniformity of the solder pads is also very important. Discontinuities in solder pad thickness could produce circuit board deflection anomalies with subsequent residual stresses, an open circuit, or could embed the thermoelement below the surface of the solder paste (Figure 11).

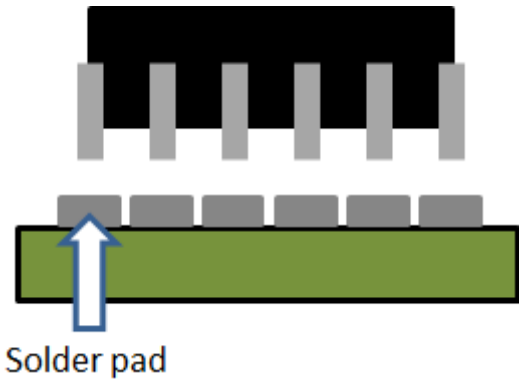

Figure 9: Example of a solder pad mounting arrangement: component, solder pads, and circuit board surface

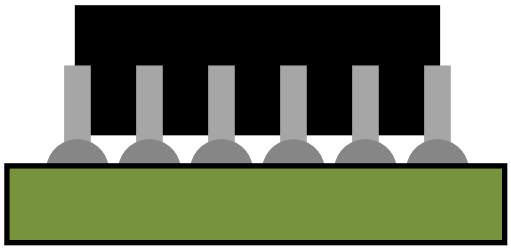

Figure 10: Example of solder joints created by reflowing the solder of the assemble post part placement

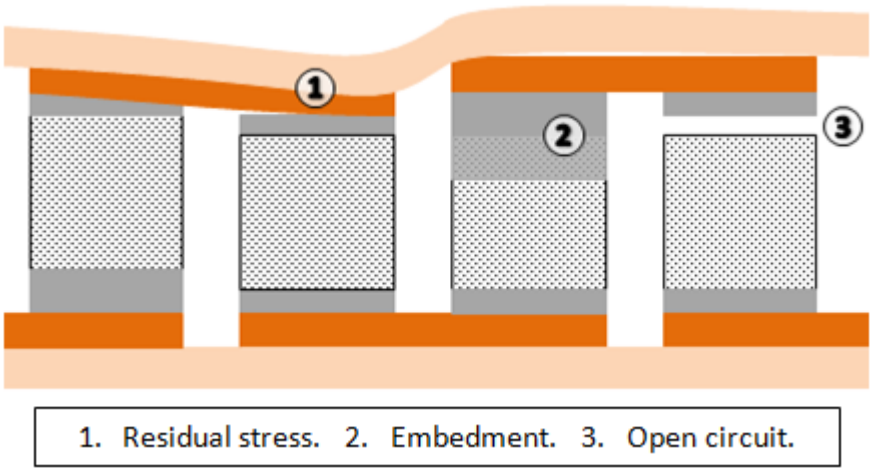

Figure 11: Problems resulting from uneven solder pads

Temperature Sensors

A minimum of 6 mm of spacing between circuit channels was selected for two reasons. This would provide space to accommodate the attachment of one temperature sensor (measuring approximately 2 mm wide by 8 mm long) within close proximity of each electrical channel, and still permit adequate flexibility. According to All Flex's design guide, "[the] bend radius of a flex should be approximately 10 times the material thickness." [16] With 5 channels (n_{ch}) there will be 4 locations between them for temperature sensors (n_{ch}-1). If those spaces have 4 mm of flexible surface (channel width, w_{ch}, less sensor width, w_{temp}) then this contributes to an achievable bending radius of 16 mm (0.63 in), or a 32 mm (1.26 in) diameter (Equation 27). This is smaller than the 50.8 mm (2 inch) requirements and according to the All Flex suggestion it necessitates a substrate thickness of 1.6 mm which is a significantly greater thickness than what would be utilized for this project. Preferable sensor placement would be at the center, against the edge of the channel where the cumulative effects of the system's heat transfer would be most noticeable.

$$r_{bend} = (n_{ch} - 1) \cdot (w_{ch} - w_{temp})$$ Equation 27

The materials that comprise the circuit board (polymer, adhesive, conducting element, etc.) must remain functionally stable when exposed to 200 °C (392 °F) for durations lasting up to an hour. This constraint arises from the conditions of the solder reflow process.

The device has to be able to accommodate a variety of methods for regulating the temperature on its outward facing side. Therefore, the surfaces that comprise the outward face of the device must have independent neutral axes (to allow flexibility), smooth surfaces (minimize contact resistance), non-permeable (allow for thermal grease), and rigid (to prevent an additional degree of freedom).

Lastly, the device must allow for the attachment or accommodation of a method for fastening it to the wearer's arm. However, a confirmed fastening method was not configured or established in this research.

Materials

In this section details are provided about the material properties of the circuit components; thermoelements, substrate material, and solder paste. It also explains the reason behind their choice.

Thermoelectric Elements

As mentioned previously (Chapter One: Introduction) bismuth telluride performs well within the temperature range that humans are acclimated to. [10] Table 3 details the performance of p-type bismuth telluride. These values depend not only on environmental conditions (temperature, atmosphere, etc.) but on the element's height (distance between current carrying surfaces) due to unique interactions with the element's minority carriers. [8] Table 4 explains the inputs used in the preliminary 1-D model. Marlow Industries donated the thermoelements used in this research.

Table 4: P-type bismuth telluride properties

Property	Value
Seebeck coefficient [8][10]	$120 \leq \alpha \leq 240 \frac{\mu V}{K}$
Thermal conductivity [8]	$k \geq 1.8 \frac{W}{m K}$
Electrical resistivity [10]	$\rho \geq 9.27 \mu \Omega m$

Table 5: Bismuth telluride properties used in the preliminary 1-D model

Property	Value
Seebeck coefficient	$240 \frac{\mu V}{k}$
Thermal conductivity	$2 \frac{W}{m K}$
Electrical resistivity	$10 \mu \Omega m$

Substrate Material

The original intent of this research was to deliver the circuit board's design to an outside manufacturer, and upon receipt of the completed circuit board assemble the device in the lab. However, the feedback received after contacting multiple manufacturers led to the consensus that this project would have to encompass manufacturing as well. A possible reason the manufacturers avoided this project is due to the pre-existing patent on such a device (which was not known at the time). [6]

A search began for flexible circuit board material. The idea of connecting multiple rigid circuit boards by some flexible means was considered. That approach however would violate the low level complexity requirement of this project (see Modeling Conclusions section for details) and was consequently abandoned.

The thickest layer of copper available was sought to safely operate the 5.4 *A* current flow, and limit the design's dependence on trace width compensation for satisfying the electric load. DuPont's Pyralux flexible circuit board material, product FR9610 was selected. This is composed of a 6 ounce (0.0084 inch thick) copper foil bonded to a 0.001 inch thick polyimide substrate (Kapton) with a flame retardant acrylic

adhesive. [16][17] It satisfies the material property requirements; rated for temperatures beyond 200 °C , and the Kapton provides a volume resistivity of 10^9 *MΩcm*. [16][18] Table 6 details the material properties of the flexible circuit board with adhesive values taken from a competitor's product for reference purposes.

Table 6: Material properties of the flexible circuit board

Property	Value
Copper – Thermal conductance [12]	$1.88 \frac{MW}{m\,K}$
Copper – Electrical resistivity [19]	$1.75 \cdot 10^{-8}\ \Omega m$
Kapton – Thermal conductance[18]	$4724 \frac{W}{m^2\,K}$
Kapton – Electrical resistivity [16]	$10^9\ M\,\Omega\,cm$
*Adhesive – Thermal conductance [20]	$5784 \frac{W}{m^2\,°C}$
*Adhesive – Electrical resistivity [20]	$15\ M\,\Omega\,cm$

According to All Flex's Design Guide the required trace width necessary to accommodate 6 amps on 6 ounce copper is 1.88 mm (0.074 in). [17] This led to the decision of designing the trace width to be 2 mm (0.079 in). To provide the 5.4 amps 14 gauge (AWG) wire was to be used. [21] Calculating wire gauge with Equation 28 yields an anticipated exposed wire diameter of 1.69 mm (0.064 inches).

$$D_{wire} = 0.127\left(92^{\left(\frac{(36-n)}{39}\right)}\right) \qquad \text{Equation 28}$$

Solder Paste

The choice of solder paste is largely dependent on the methods it will be applied. [15,22] For this reason the solder paste's method of delivery will be selected first. Of the five methods Coombs (author of the Printed Circuits Handbook) explains for dispensing solder paste (pin transfer, stencil printing, time pressure-pump, Archimedes screw pump, positive displacement pump) the stencil printing method was selected because it does not require the use of a specialized pump or automated equipment. [15] It is something

that can be fabricated with the lab's resources and this process is explained in further detail in several sections of Chapter Three: Manufacturing.

Coombs recommends that for stencil printing applications a solder paste with a viscosity of 400 – 800 *kcps* be used. [15] A 25 gram cartridge of Multicore brand solder paste, product number SN62RA10BAS86, was purchased online from Newark.com. This is a 63% tin, 36% lead, and 2% silver paste composition by weight with a viscosity of 500 *kcps*, melting point of 179 °C (354 °F), and can be used as a no clean solder. [23][22]

Circuit Boards

Two circuit boards are used to make the column based (Figure 6) thermoelement arrangement. For simplicity, the thermoelement's perceived base dimensions were rounded up to 2 mm during the design of the circuit board's traces. This allowed for the trace dimensions to be thought of in terms of equivalent thermoelement count. Therefore, a single thermoelement was the smallest spacing increment from this perspective and was chosen as the unit of unoccupied space between thermoelements of the same channel (Figure 12 and Figure 13).

The intended dimension of each trace segment is 2 mm wide and all of them are 6 mm long, with the exception of the 10 mm long segments that connect to the power supply on the bottom circuit board. For each channel a 2 mm space is provided between the trace segments, and a 6 mm space is placed between channels (Figure 13). A total of five temperature sensors (2 x 8 mm) are to be placed in a 3 x 10 mm space next to the center point of each channel. With the exception of one outer channel each sensor occupies the space between the channels (Figure 12).This design allowed for the placement of 180 thermoelements on a 62 x 82 mm area (2.44 x 3.23 inches). Figure 14 shows the location of the thermoelements on the bottom circuit board. The top circuit

board will be cut along the longitudinal centerline between channels to allow for device flexibility (Figure 15).

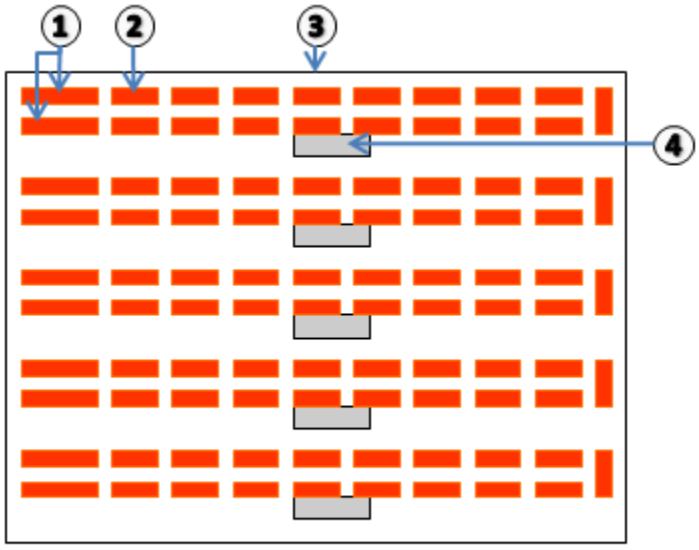

1.) Power connection trace segments. 2.) Trace segment.
3.) Device perimeter. 4.) Temperature sensor location.

Figure 12: Bottom TE circuit traces with designated areas for temp sensor placement

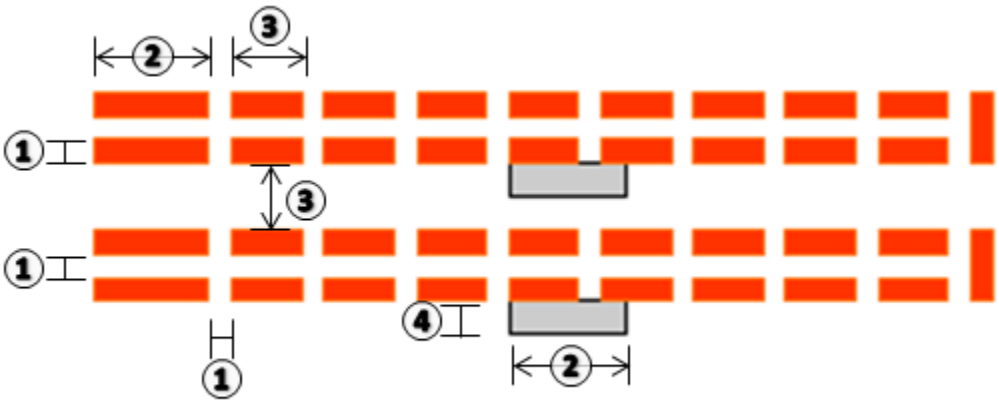

Figure 13: Gap, trace segment, and temperature sensor dimensions for the bottom circuit board

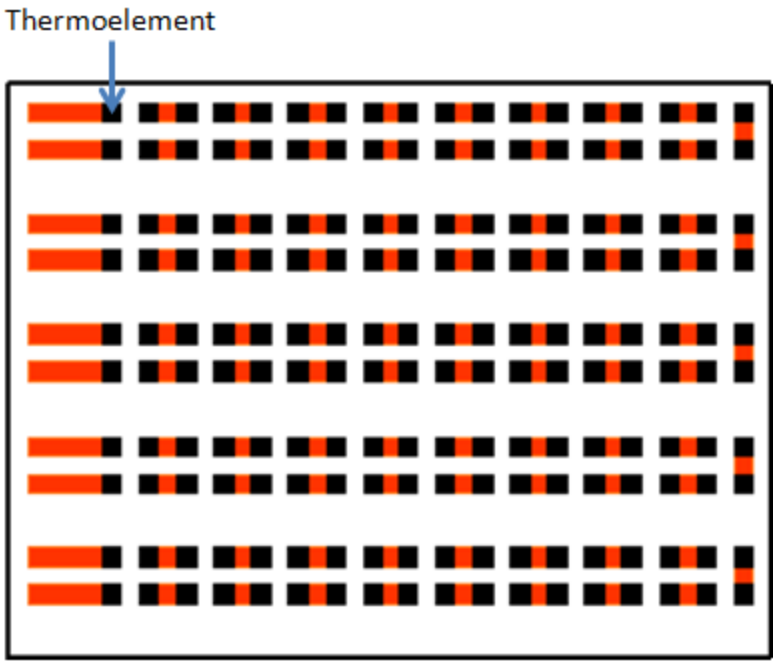

Figure 14: Dark squares represent the locations of the 180 thermoelement blocks on the 5 channels of the bottom circuit board

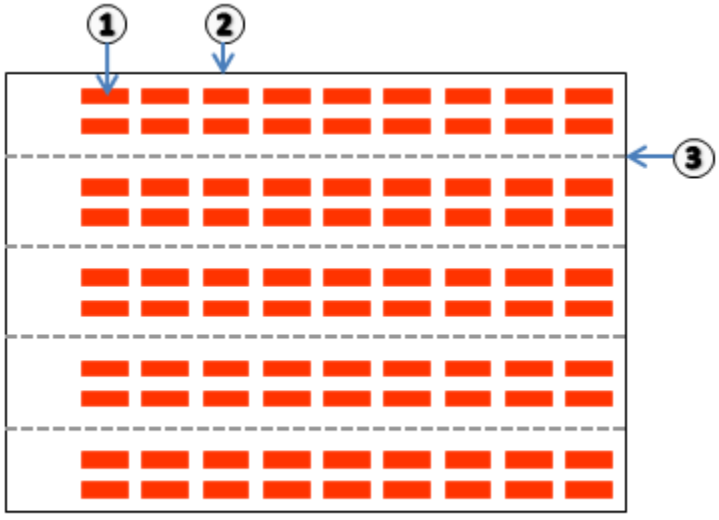

1.) Trace segment. 2.) Preprocessing top circuit board perimeter.
3.) Post processing cut lines.

Figure 15: Upper TE circuit traces

Adjusted Performance Estimates

In the Device Modeling section it was explained that the area opposite the thermoelement output cold and hot side temperatures of -17 and 38 °C, respectively, at 5.4 *A*. Moreover, this produced cold and hot side fluxes of 4 and 17 W/m^2 respectively. These fluxes are based on the area of the elements themselves. However, due to the spacing between thermoelements, the average cooling and heating capabilities per unit area are lower. A simple conservative model that takes into account the spacing between elements of the same channel, but not the spacing between channels or surrounding substrates was created by assuming that the heat is spread uniformly over the surface. The fill factor, f, is the scalar value used to correct the performance values, and it's found by dividing the total area occupied by thermoelements on a given channel ($A_{tot,elem}$) by the area of that channel ($A_{total,channel}$) (Equation 29). Figure 16 illustrates how this value is derived from the present circuit board design.

$$f = \frac{A_{tot,elem}}{A_{total,channel}} \qquad \text{Equation 29}$$

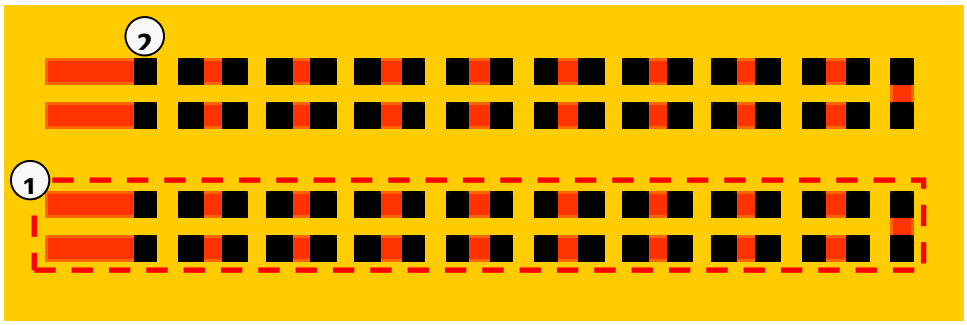

1. Channel area = (6 x 78) mm
2. Single thermoelement area = (1.397 x 1.397) mm

Figure 16: Dimensions used when calculating the fill factor

A thermoelement occupies 1.952 mm^2 of space and there are 36 in one channel. Therefore $A_{tot,elem}$ is equal to 70.26 mm^2. $A_{total,channel}$ is 468 mm^2 and applying these

values to Equation 29 yields a fill factor of 0.15 or 15%. The corrected flux values are the fill factor multiplied by the previous maximum flux value:

$$Q_{C,corrected} = f \cdot Q_C \quad \text{Equation 30}$$

$$Q_{H,corrected} = f \cdot Q_H \quad \text{Equation 31}$$

where subscripts C and H indicate hot and cold respectively, and Q indicates flux. For the bottom circuit board the corrected cold side flux is 0.61 *W/cm*^{2} and hot side flux is 2.6 *W/cm*^{2}. The device's surplus power per unit area is calculated by dividing the corrected cold side flux by the previously calculated forearm heat flux (82 *mW/cm*^{2}). This calculation estimates the device's cooling flux to be 74 times greater than the heat flux provided by the human forearm. This result supports the notion that the device will cool the wearer. Heating the bottom circuit board is not a concern because the thermoelectric effect supplements the Joule heating effect which can be manipulated by simply increasing the current (Equation 5).

Design for Assembly

A principle that has been successfully applied to many disciplines is the concept of beginning with the end in mind. [24] Even though assembly is the last step before having a finished product it should be taken into account through all stages of the design process. [25] Consideration during the design stage has been made in an effort to ensure uniform assembly independent of the laborer, make handling the device during its development stages easier, and prevent costly adjustments from having to be made near the anticipated end of the project.

For this project three guidelines were applied from the *Manufacturing Process Selection Handbook*: [26]

- Modularize the design.

- Provide a base for assembly to act as a fixture or work carrier.
- Design the assembly process in a layered fashion (from above).

The interactions between the circuit boards and their work carrier, and the method for compromising between alignment accuracy and cost are described in this section.

The top and bottom circuit boards have features to minimize alignment error during assembly. These features are tabs that extend outward from the center of the circuit board, have holes that coincide with an assembly chassis (see Staging Area section for details), and are cut off after assembly is complete (Figure 17).

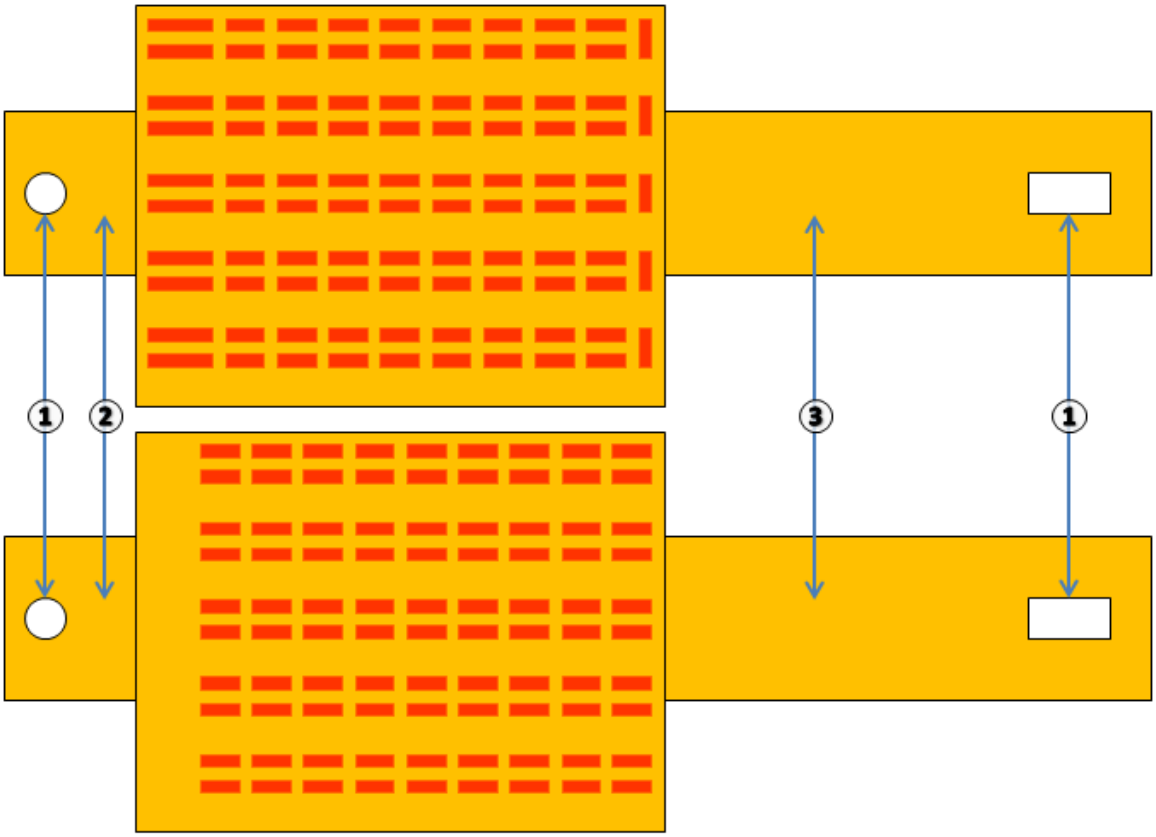

Figure 17: Top and bottom circuit boards with alignment tabs

The distances from the circuit board to the left and right alignment holes were computed using the following approach. It was assumed that the alignment holes would be oversized by a value of δ:

$$\delta = r_{eq} - r_{post} \qquad \text{Equation 32}$$

where r_{eq} is the alignment hole's equivalent radius and r_{post} is the radius of the alignment post, both are in units of meters (Figure 18). The goal was to keep δ as small as possible, however, its existence is inevitable in this design scenario. Therefore, the effects of δ had to be managed.

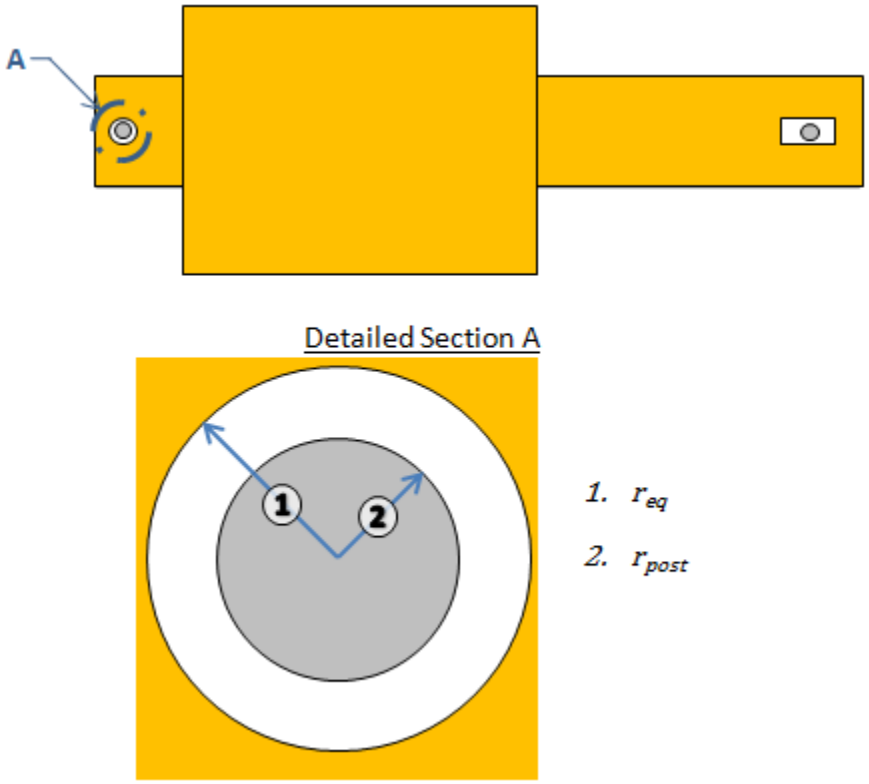

Figure 18: Visual representation of Equation 32

Since both circuit boards were aligned to the same posts they would each create their own angle of misalignment θ_{err} in *Rad*. This angle gives rise to a misalignment distance, s_{err}, expressed by:

$$s_{err} = r_{align}\theta_{err}$$ Equation 33

where r_{align} is the distance between the staging area's posts in millimeters and is calculated as:

$$r_{align} = r_{left} + w_{cb} + r_{right}$$ Equation 34

where r_{left} is distance from the left side edge of the circuit board to the center of the left side alignment hole, w_{cb} is the width of the circuit board, and r_{right} is the distance from the right side edge of the circuit board to the center of the right side alignment hole (Figure 19).

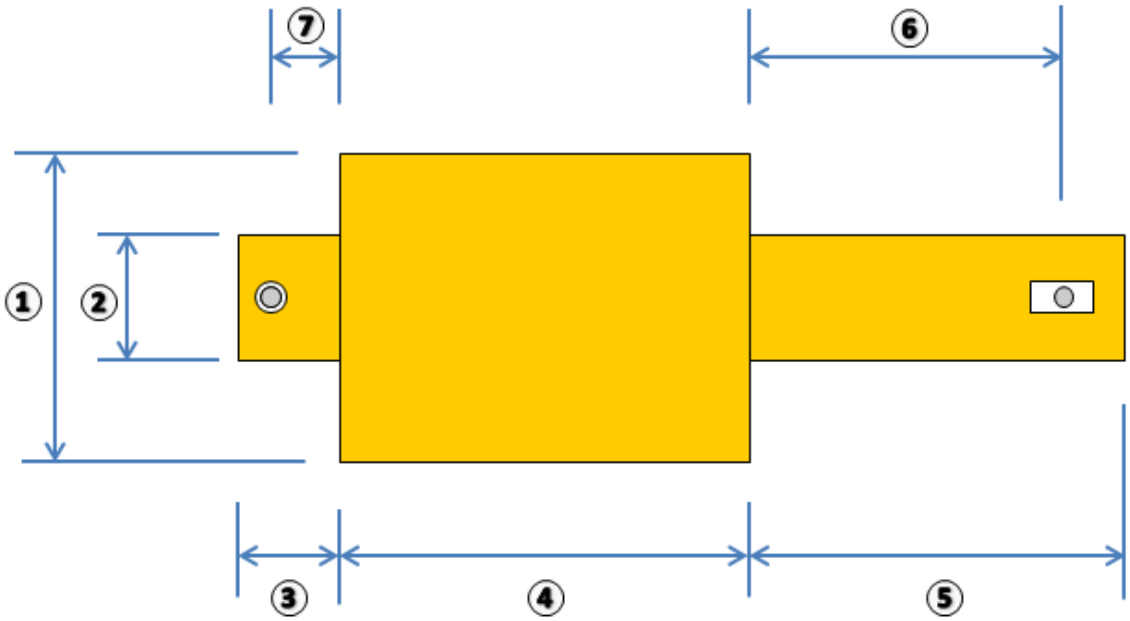

1. h_{cb}
2. h_{tab}
3. $w_{L,tab}$
4. w_{cb}
5. $w_{R,tab}$
6. r_{right}
7. r_{left}

Figure 19: Dimension notation for the preprocessed circuit board

Assuming the center points of the alignment holes for both circuit boards are the same, then the maximum value of s_{err} can be expressed as:

$$s_{err} = 2\delta$$ Equation 35

Combining Equation 33 and Equation 35 offers an approach toward minimizing alignment error:

$$\theta_{err} = \frac{2\delta}{r_{align}}$$ Equation 36

Treating 2δ as a constant, r_{align} can be manipulated to achieve a desired θ_{err}; where a small or large r_{align} value produces a large or small θ_{err}, respectively. The sum of r_{left} and w_{cb} needed to be as small as possible because the maximum error could be approximated by the block misalignment at the center point of the circuit board's right side edge. This led to an asymmetric design for the circuit board tabs (Figure 20).

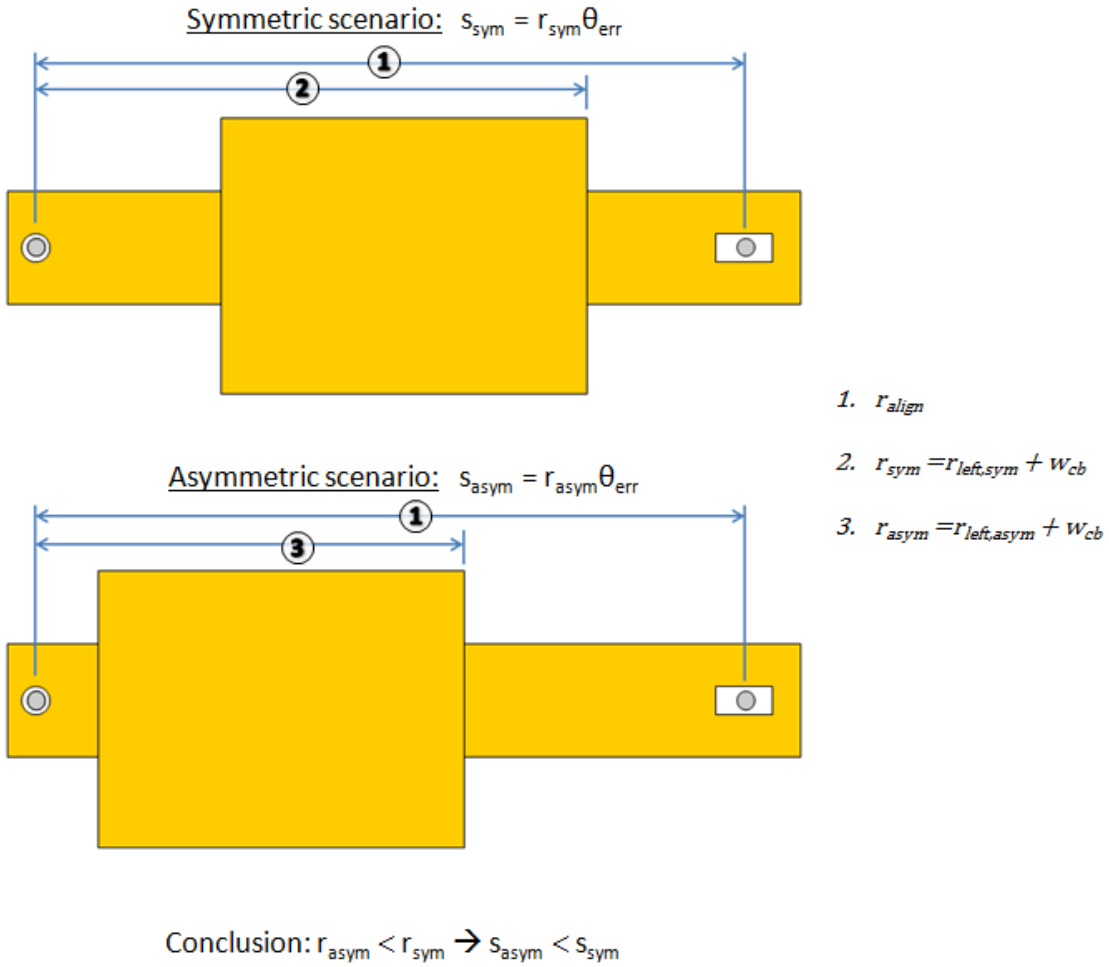

Figure 20: Demonstrated benefit of asymmetric preprocessing circuit board design

Optimizing Preprocessing Design

Taken as a reference it was assumed that δ was equal to half the difference between the major and minor diameter of a 1/4 x 20 stud, 0.79 mm (0.0312 inches). [27] Table 7 details the values assigned to $w_{L,tab}$ (left side alignment tab width), r_{left}, w_{cb}, h_{cb} (circuit board height), and h_{tab} (alignment tab height).

Table 7: Preliminary board dimensions used for alignment and cost optimization

Dimension	Value (mm)
$w_{L,tab}$	25.4
r_{left}	12.7
w_{cb}	82
h_{tab}	62

An undefined cost value was associated with a unit area of circuit board material. This allowed for assessing cost increases associated with increasing r_{align}. Equation 37 calculates the percent alignment improvement (PI) from each incremental increase of r_{align}, where $(s_{err})_i$ is the corresponding displacement error at the edge of the circuit board. This could be compared to the cost resulting from increasing sacrificial alignment material. To do this the total alignment material from each increase is normalized to the fixed area of the circuit board (RAM, Equation 38). The desired r_{align} value is the one that produces the minimum difference between RAM and PI; r_{align} values were increased by 12.7 mm (0.5 inch) increments, RAM is assumed to be greater than PI, the products associated with r_{right} equal to zero are neglected, and so are the areas of the alignment holes.

$$PI = 1 - \frac{(s_{err})_i}{2\delta} \qquad \text{Equation 37}$$

$$RAM = \frac{w_{L,tab} \cdot h_{tab} + \left(r_{right} + 12.7\right) \cdot h_{tab}}{w_{cb} \cdot h_{cb}} \qquad \text{Equation 38}$$

The 12.7 mm in Equation 38 is the chosen width beyond the alignment hole that comprises the right side alignment tab, $w_{R,tab}$ (Figure 19). This method resulted in a r_{align} value of 158.75 mm (rounded to 6.25 from 6.229 inches). However, a calculation error was observed after the circuit board had been assembled. Correct manipulation of this approach would have suggested a r_{align} value of 145.5 mm (5.73 inches)(Figure 21). The alignment holes in the left and right alignment tabs are 6.4 and 6.4 x 12.7 mm respectively (0.25 and 0.25 x .5 inches).

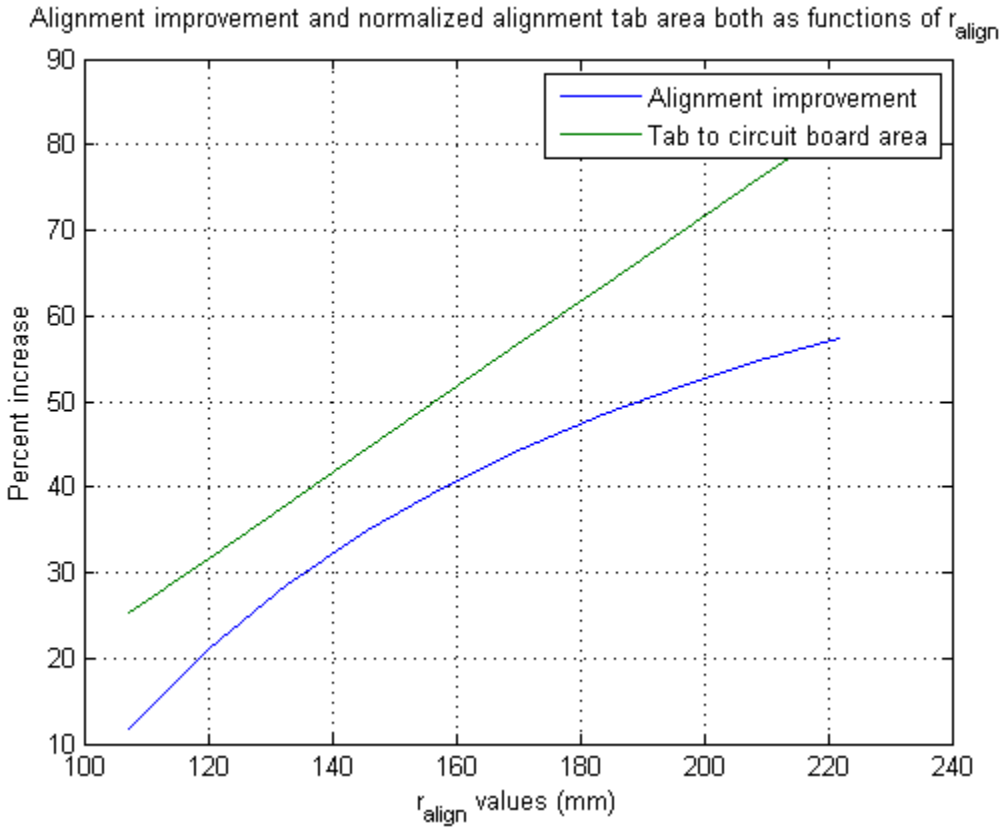

Figure 21: Alignment improvement and normalized tab area both as functions of r_{align}

Staging Area

The staging area had to meet the following requirements (required material properties based off of values catalogued at room temperature):

- Provide a base for assembly to act as a fixture or work carrier. [25]
- Design the assembly process in a layered fashion (from above). [25]
- Be able to withstand repeated exposure to temperatures reaching 300 °C (572 °F) for lengths up to one hour.
- Not adhere to polyimide when exposed to high temperatures.
- Be able to have solder flux cleaned from it.
- Have a thermal conductivity greater than 15 *W/(m K)*.
- Possess a thermal expansion coefficient less than 100 m^2/s.
- Be made from cost effective material.
- Ideally weigh less than 5 *lbs.*

The Circuit Boards section provided details about the preprocessing board's dimensions, most notably the 158.8 mm (6.25 inch) space between the center points of 6.4 mm (0.25 inch) diameter posts. The material chosen was aluminum and its material properties are listed in Table 8. Soldering aluminum requires a different flux and solder material than what is being used in this research. [28] Also there have been no instances in the lab where the polyimide has adhered to the aluminum during their mated exposure to temperatures greater than 200 °C. Lastly, while aluminum's relative cost is about 8 times higher than steel's, it's lower density is more favorable (steel: 8000 kg/m^3), and it's not as costly as magnesium (15 times greater than steel). [19]

Table 8: Material properties of 2046-T6 aluminum alloy

Property	Value
Melting temperature [12]	502 °C
Thermal conductivity [12]	177 $\frac{W}{m\,k}$

Table 8 (Continued)

Coefficient of thermal expansion [19]	$23.6 \cdot 10^{-6}\ ^{\circ}C^{-1}$
Density [12]	2770 $\frac{kg}{m^3}$

The base plate for the staging area was made rectangular, 101.6 x 203.2 mm (4 x 8 inches) and 6.4 mm (0.25 inches) thick, to facilitate easy manufacturing with accessible stock. The alignment posts have a 6.4 mm diameter and are 31.8 mm (1.25 inches) long. They were pressed into holes 22.2 mm away from the 101.6 mm edges along the centerline between the 203.2 mm edges (Figure 22). The machine shop at the University of South Florida donated the aluminum necessary for the staging area and assembled it as well (Figure 23).

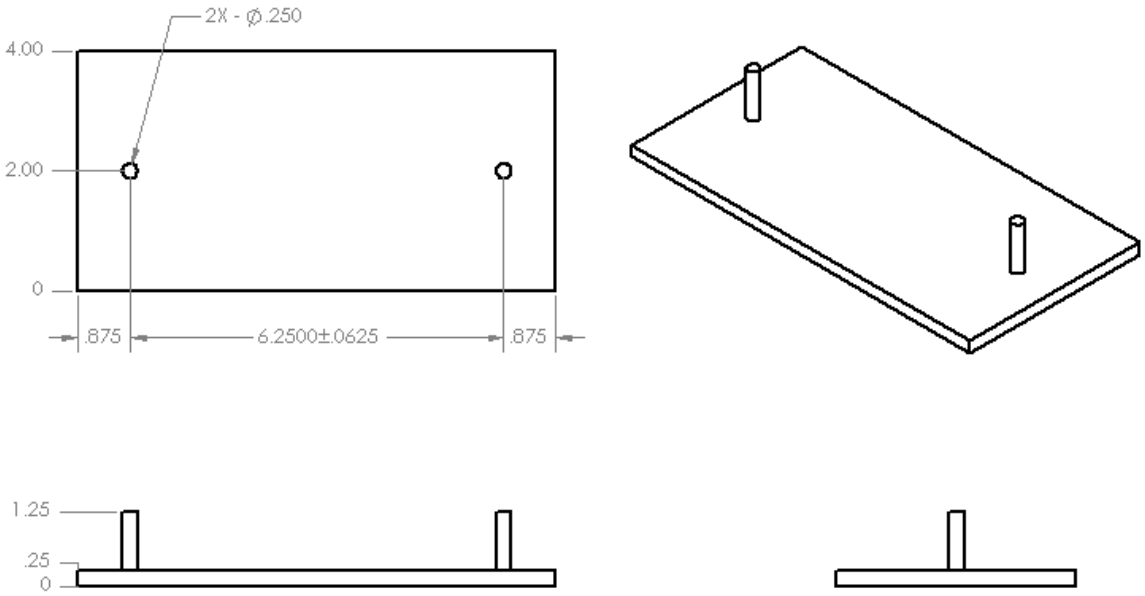

Figure 22: Staging area assembly view from multiple perspectives and dimensioned

Figure 23: Full scale staging area manufactured by the University of South Florida machine shop

CHAPTER THREE: MANUFACTURING

Device and assembly components not available by a third party supplier are to be made using standard manufacturing practices. Due to tooling costs this project utilized less automation than what could be seen in industry. However, all of the methods applied can be adapted for mass production. The manufacturing processes applied were milling operations and chemical etching. Their respective procedures and results are cataloged in this chapter.

Manufacturing Process Overview

There are three unique types of items that have to be made for this project; the circuit boards, solder stencil, and thermoelement templates. The key steps in each are briefly summarized below and then described in more detail.

Each of the circuit boards are cut from stock material, given a rough polish on the copper side, covered with a patterned etchant mask, submerged in an etchant, removed from the etchant and chemically neutralized after the unwanted copper has dissolved, removed of their etchant mask, and given a final rough polish prior to assembly.

The goal of the solder stencil is to apply a uniform layer of solder on each circuit board that is close to 10% of the thermoelement's height (a value of 0.168 mm). It is made by cutting the stencil using a 3-axis mill, cleaning out debris, and deburring by hand.

The thermoelement templates are used to aid in correct placement of the 180 thermoelements, and to prevent placing a p and n-type element in the wrong location.

Each template is cut using a CNC mill (Techno Inc., Model: Davinci Series 1012) to create the desired apertures and cleaned before use.

Procedures

Etching Procedure

The following step by step description of the finalized etching process used for creating the circuit boards was developed from multiple sources and personal experience. [29–32] The etching trials followed a very similar procedure with minor variations such as different ironing techniques and corresponding work area arrangements, and post abrading cleaning methods.

The etching process involves the use of an etchant (corrodes the surface of the work piece) and an etchant mask (a layer that is chemically neutral to the etchant). Once the work piece materials are identified, in this instance copper and brass, an etchant specific to the material must be selected. Ferric chloride was the etchant used in this research and while it reacts with all metals it is typically used to etch copper. The etchant mask utilized was primarily laser printer toner and acrylic paint was used for touching up areas of poor transfer.

A drawing of the desired pattern is printed in black ink on common overhead projector transparency using a laser printer. The surface of the work piece receiving the etchant mask was first abraded longitudinally and laterally with Grade 3 (coarse) Rhodes American steel wool. That process was then repeated with Grade 0000 (fine) Rhodes American steel wool. After that a paper towel was used to remove the surface debris. In preliminary tests, the surface was rinsed with acetone and then wiped with a paper towel but that step was removed because its contribution toward developing an oxide layer on the work piece's surface had not been quantified.

The work piece was placed on top of a folded cotton shirt. This would aid in uniformly distributing pressure and restrain work piece movement with frictional resistance during the ink transfer process. Next, the patterned transparency was aligned with the work piece and fixed to the work table at one end by two clamps.

A household Shark GI468 iron was set to its polyester setting and swept along the full length of the transparency, from the clamped side downward, with the pressure you might apply when sealing an envelope. A transparency with 7 inches of swept length was covered in approximately 4 seconds with each pass. This was done for 2 minutes and then the iron was rested (hot side down) on top of the transparency for 30 seconds. The process concluded with sweeping the iron across the transparency for 1 minute. For cool down the work piece was left in place for 2 minutes, and then the transparency and work piece with bond intact were transferred to a room temperature surface. After a minimum of 6 minutes have passed the transparency was peeled from the work piece.

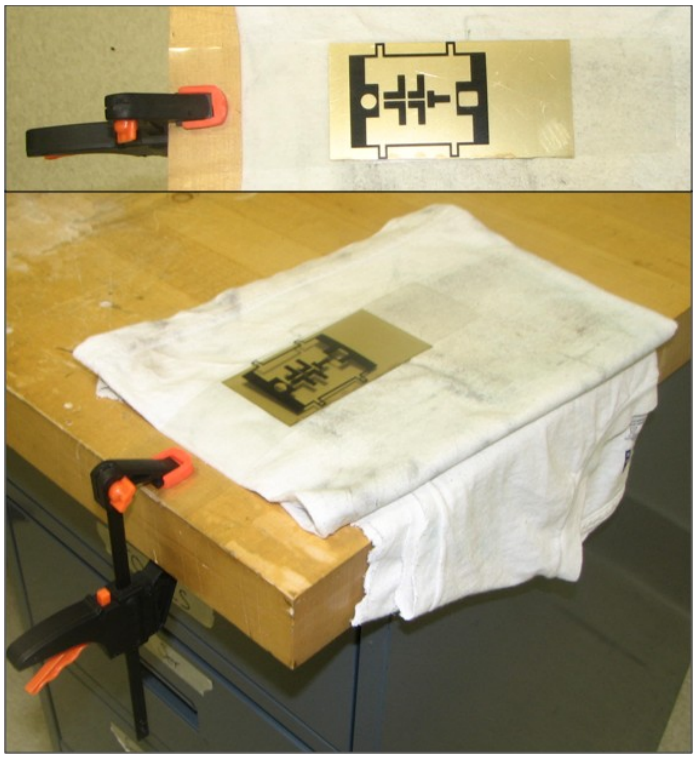

Figure 24: Mock example of ironing arrangement for ink transference to brass or copper. Above, Top view. Bottom, Isometric view

This process was derived through multiple trial and error attempts where heat setting, ironing method, and duration were varied. It was also found that; the iron is hottest at the frontal tip, the printer ink can be moved under shearing forces along the surface of the transparency at temperatures of 85 °C or higher, and that the ink does not coalesce as a droplet at 130 °C (testing was not conducted beyond that temperature). The middle observation enforces the need for a sweeping motion to take place for successful transfer of the toner from the transparency to the metal. Areas of poor transfer are touched up by hand with acrylic paint and allowed to dry overnight.

The part is then submerged in etchant until only the desired material remains. The etching duration is dependent on the size of the etched surface area, the material's desired etched depth, the temperature of the solution, if the etchant is circulated in some fashion, and the condition of the etchant prior to etching.

In the finalized etching process the etchant bath was contained in a 2 L plastic container, heated to 50 °C, and agitated with air blown beneath the surface of the solution. A magnetic stirrer was previously used but in between etching inspections it proved to be difficult to reposition the stirrer underneath a protective cage that kept it from colliding with the material.

After etching was completed the part was removed from the solution and chemically neutralized with baking soda. The resulting solids were wiped from the part and it was washed with soap and water. The remaining etchant mask was cleaned off by spraying the component with acetone and wiping it clean.

Milling Procedure

The object to be milled attached to an intermediary plastic board with masking tape. This board serves as a sacrificial surface during the milling process in order to prevent the mill bit from damaging the mill table. This board has also been sanded down on all surfaces between uses to prevent significant surface burrs (due to previous milling

operations) from disturbing the mating of the material to the board, and the board to the mill table.

The board is then placed up against a 90° frame on the mill table. The board is fully restrained by 3 tapered work piece restraints. Depending on the work piece, WD-40 may be sprayed on the surface as a cooling film during metal to metal contact (the toughest material milled are 0.014 inch thick brass sheets).

The motor and desired bit are attached to the mill head. An engraving bit was used with an offset center where the edge angles were 15° and 30°. The plunge and movement speeds were set to 5 inches per minute, and the motor operated at 25,000 rpm. When lubricant is used the partitioning mill head brush is also attached to contain the spatter.

After the safety shield is lowered the mill is turned on and controlled from the computer with the Techno GCODE Interface Program (Appendix D: Stencil and Middle Template Gcode). From here inputs can be entered manually through the Jog graphical user interface or by uploading a predesigned program (written in Gcode). The finished product is removed from the mill table and cleaned of debris and liquid. Next the work piece is removed from the intermediary board and further cleaned.

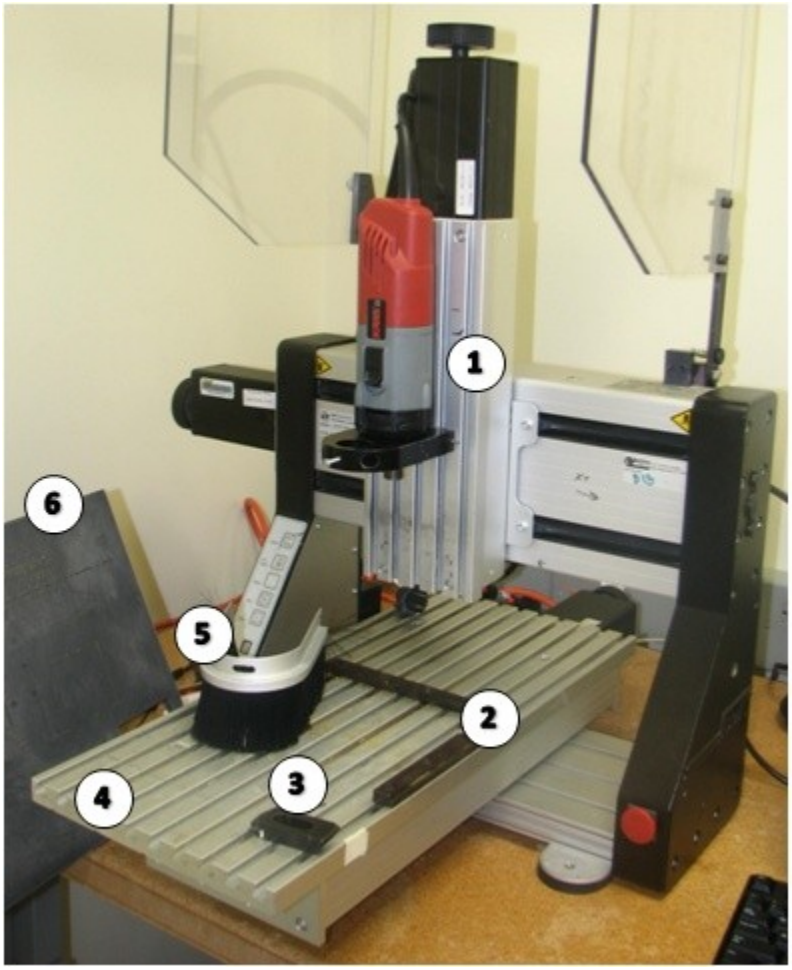

1. Mill head.
2. 90° frame.
3. Work piece restraint.
4. Mill table.
5. Partitioning mill head brush.
6. Sacrificial work piece board.

Figure 25: Picture and labels of the mill assembly

Preliminary Etching Tests

These are the etching tests that were conducted prior to the final assembly. These include solder stencil and circuit board etching trials. Their results are reported in their respective sections.

Solder Stencil Etching

The original intent was to etch the desired features on the circuit board and the solder stencil. The first object tested was a 0.25 mm (0.010 inch) thick brass sheet with four 2.45 mm square apertures (Figure 26). The etching duration was 18.5 minutes. This

value is fast comparatively speaking but it's because the part was simultaneously etched on both sides.

The result was a mean aperture square side length of 2.37 mm with a standard deviation of 0.074 mm, and a deposited solder paste thickness of approximately 0.41 mm (Figure 27). Exact reasons for the deposited solder paste being thicker than the stencil are unknown; it is believed to be a function of the smearing method, and parallelism between the entirety of the circuit board and solder stencil surfaces.

Figure 26: First etched sample – Brass trial solder stencil

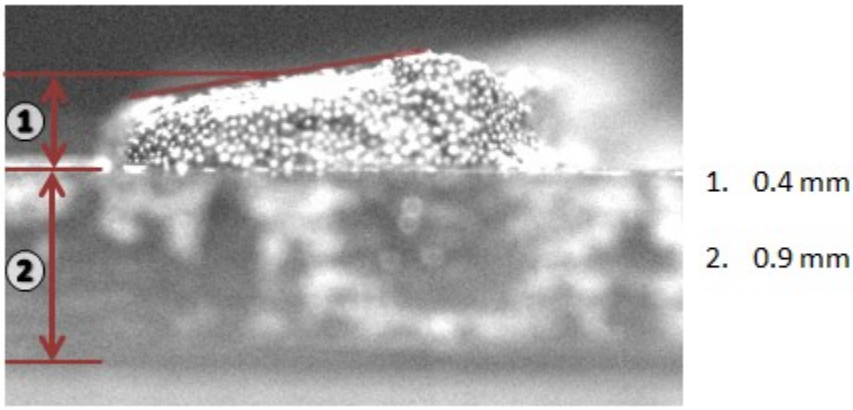

Figure 27: Deposited solder using the first brass stencil

A solder stencil was made for the first trial assembly (Figure 28 and Figure 29). The apertures were designed to be 2 mm squares. However, the mean length of the

square aperture was 2.27 mm (0.0894 inches) with a standard deviation of 0.198 mm (0.0078 inches).

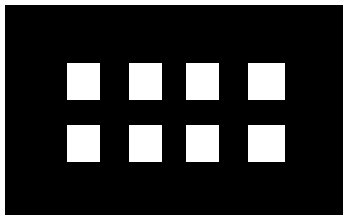

Figure 28: Negative image for the transparency of the second etched solder stencil

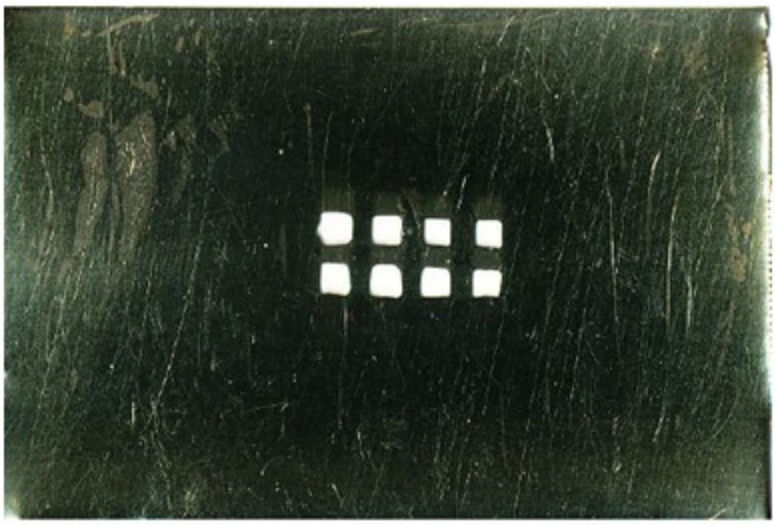

Figure 29: Second etched brass solder stencil

Circuit Board Etching

The negatives of the first trial circuit board were created (Figure 30). Following the successful completion of all the steps leading to post etching cleanup it was observed that circuit board's traces were smaller than designed. This was the result of the etchant corroding the copper at the perimeter of the mask as the surrounding surfaces deteriorated. This unanticipated corrosion removed approximately 1 mm from the width and height of each trace (Figure 31). The pitting and rough surfaces that developed from this process might have been a consequence of either inadequate touch up work or from leaving the part in the etchant for too long. In the first several etching

attempts permanent marker was used to touch up the work pieces. However, by the third trial assembly this was abandoned entirely and only acrylic paint was used. Subsequent masks oversized the traces by 1 mm in each direction to compensate.

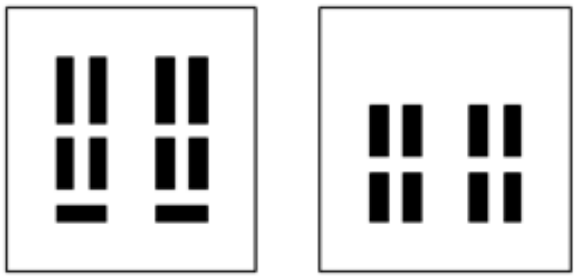

Figure 30: Negative image for the transparency of the first trial assembly

Figure 31: Etched results for the first trial assembly

The negatives for the second trial circuit board were oversized from the first attempt (Figure 32). However the top circuit board was patterned twice. To correct this the extended trace width for the power connections were painted on. The etching duration was approximately 1 hour and 20 minutes. The circuit boards resulting from the post etching clean up can be seen in Figure 33. The reduction in surface pitting (compared to Figure 31) is the result of an improved etching mask transference and touch up procedure. Although it was not realized until after the two boards were

assembled, they did not create two electrical circuits. This resulted from the lack of a bridging trace on the bottom circuit board (as compared to Figure 31), and the trace segments of both circuit boards were positioned on top of one another instead of overlapping.

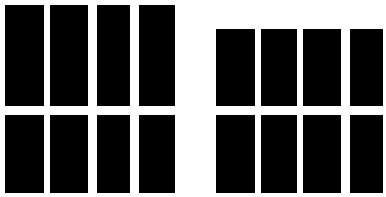

Figure 32: Negative image for the transparency of the second trial assembly

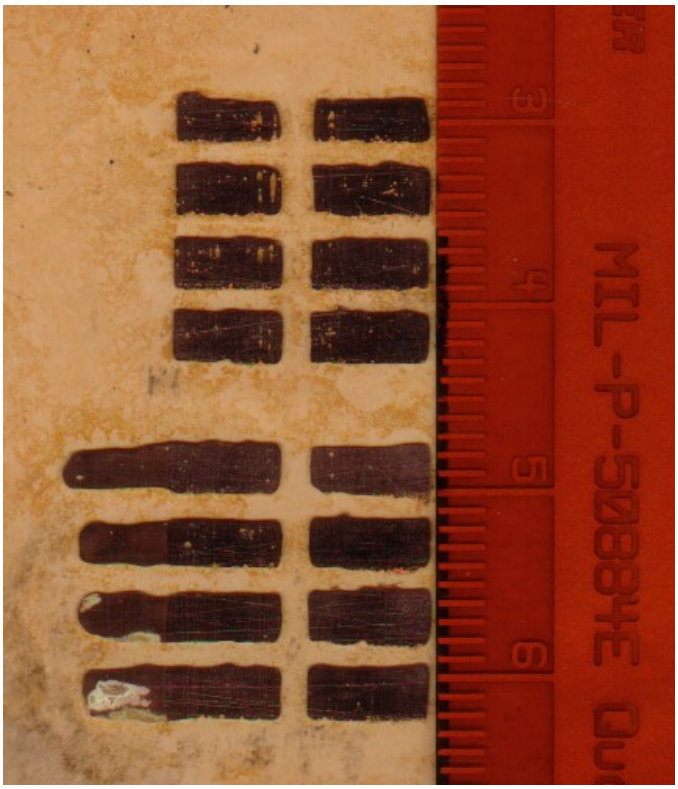

Figure 33: Etched results for the second trial assembly

The negatives for the third attempt included the bottom circuit board's bridging trace and it also had features extending outward from each trace. The purpose of these extensions was to allow for electrical measurements to be taken more easily since the

traces were shrouded by the substrates (Figure 34). At this time a trial staging area assembled to test the proposed assembly process. That's why there are alignment holes on either end of the circuit board. However, the white spaces between the alignment holes and the preprocessing circuit board frame had to be painted. If not then the integrity of the alignment holes would be severely compromised. Figure 35 shows the circuit boards prior to their assembly. The total etching duration was 1 hour and 50 minutes. Modifications were proposed after two failed attempts to remove the excess material without breaking the device (detailed in the Post Processing Difficulty section of the Assembly chapter).

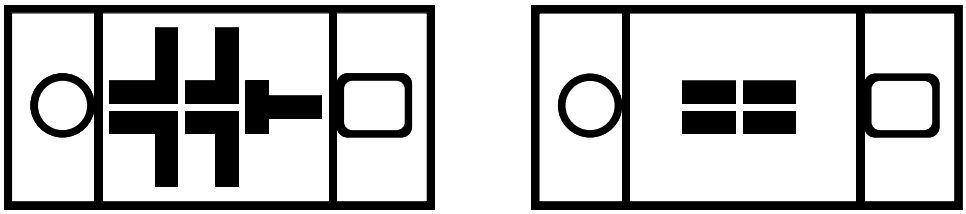

Figure 34: Negative image for the transparency of the third trial assembly

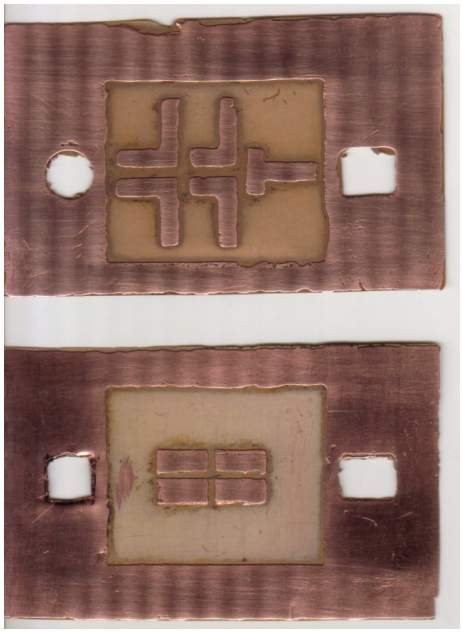

Figure 35: Etched results for the third trial assembly

Inspired by manufacturing challenges, three changes were made to the preprocessing circuit board's design in the fourth and final trial assembly (Figure 36). First, the distances between the bottom circuit board's trace and the preprocessing frame were increased. Second, the perimeters of the top and bottom circuit board were made unequal. This asymmetry would allow for easier isolation of the alignment material during post-processing removal. Lastly, tabs that extended the frame's perimeter were added to allow for a cutting wheel to be passed over the substrate and intersect another cutting wheel pathway that would run the width of the device (Figure 36). The etching duration for these circuit boards was approximately 2 hours.

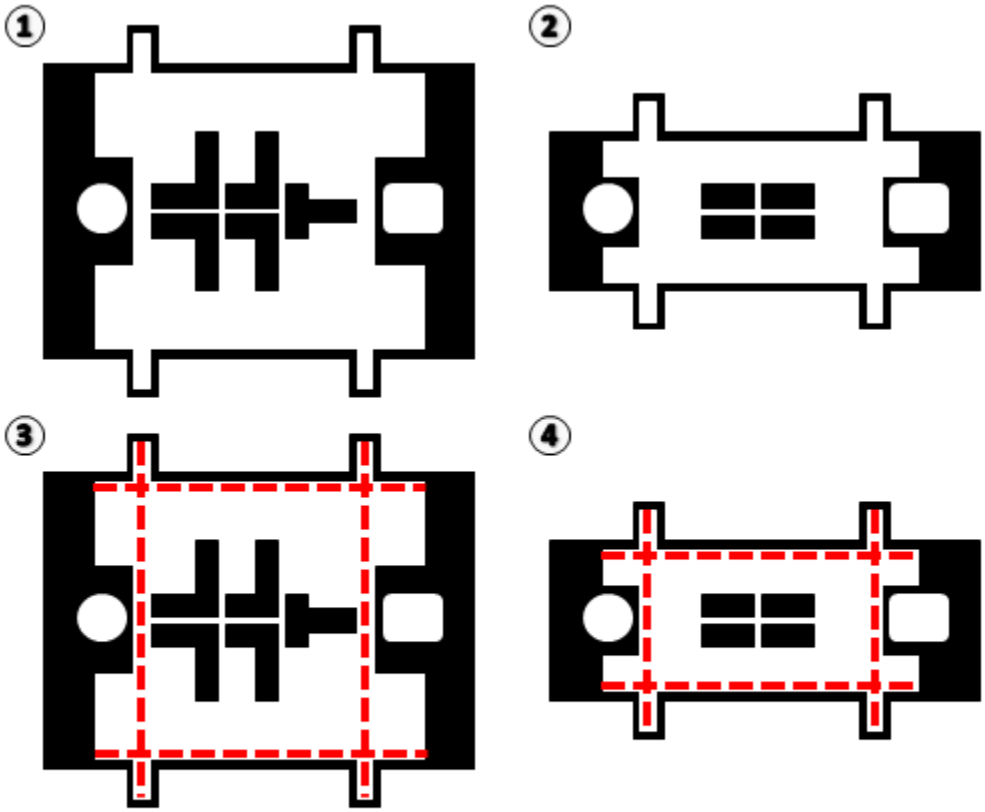

1. *Bottom circuit board.*
2. *Top circuit board.*
3. *Cutting wheel pathways for the bottom circuit board.*
4. *Cutting wheel pathways for the top circuit board*

Figure 36: Negative image for the transparency of the fourth trial assembly and the intended cutting wheel path

Preliminary Milling Tests

These are the milling tests that were conducted prior to the final assembly. These include solder stencil and thermoelement template milling trials, where 1 mm and 2 mm aperture sizes were analyzed as well. Their results are reported in their respective sections.

Solder Stencil Milling

The possibility of milling the solder stencil was explored after seeing the results obtained from etching 0.25 mm (0.010 inch) thick brass sheets. A thinner material was also chosen; copper foil with a thickness of 0.10 mm (0.004 inch) replaced the brass. With this foil a comparison was made between the solder deposited from 2 mm and 1mm aperture sizes (Figure 37). Also included in this comparison were the results from reflowing the solder at different temperatures.

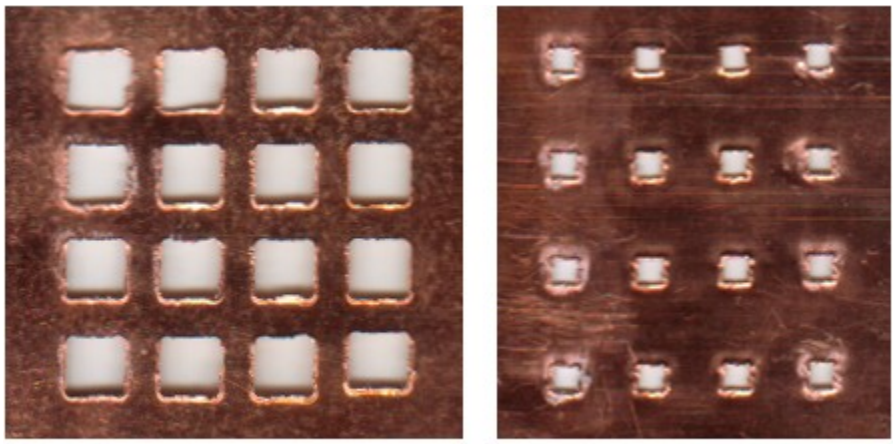

Figure 37: 2mm and 1mm aperture milled solder stencils

It was observed that heating the solder paste until the oven air temperature reached 180 °C produced inadequate solder joints. As illustrated in Figure 38, the solder

grains barely melted if at all. From this figure it is also interesting to note that the solder paste thickness deposited by the copper foil is four grains or less.

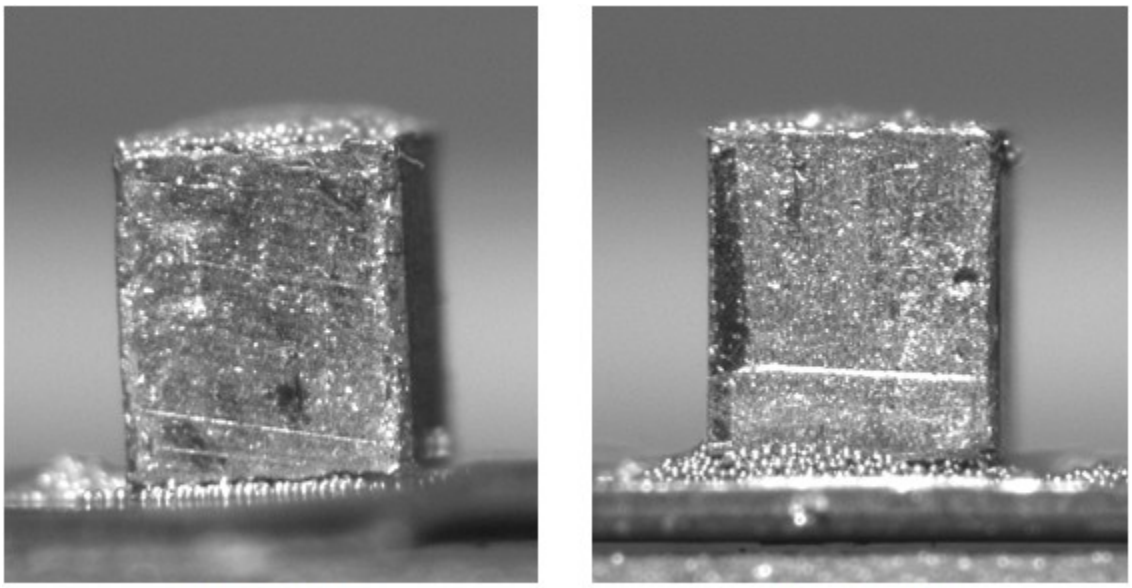

Figure 38: 1mm and 2 mm apertures, solder reflow at 180 °C

It was not until the oven air temperature reached 190 °C that a satisfactory solder joint was produced. However, two short comings are observable for each aperture size. Figure 39 illustrates the potential for developing significant air gaps if thermoelement alignment is not controlled with exacting precision. Air gaps like these create poor thermal conductivity at the thermoelement to circuit board interface, and limit the amount of electrical current that can safely pass through that junction. Ultimately the factors result in poor thermoelectric performance.

The glossy translucent film on the left image of Figure 40 might represent the solidification of solder flux byproduct around the base of the thermoelement. This creates an alternative thermal pathway around the thermoelement and diminishes

device performance. Be that as it may this problem can be addressed by cleaning the solder joints with the appropriate solution and agitation method.

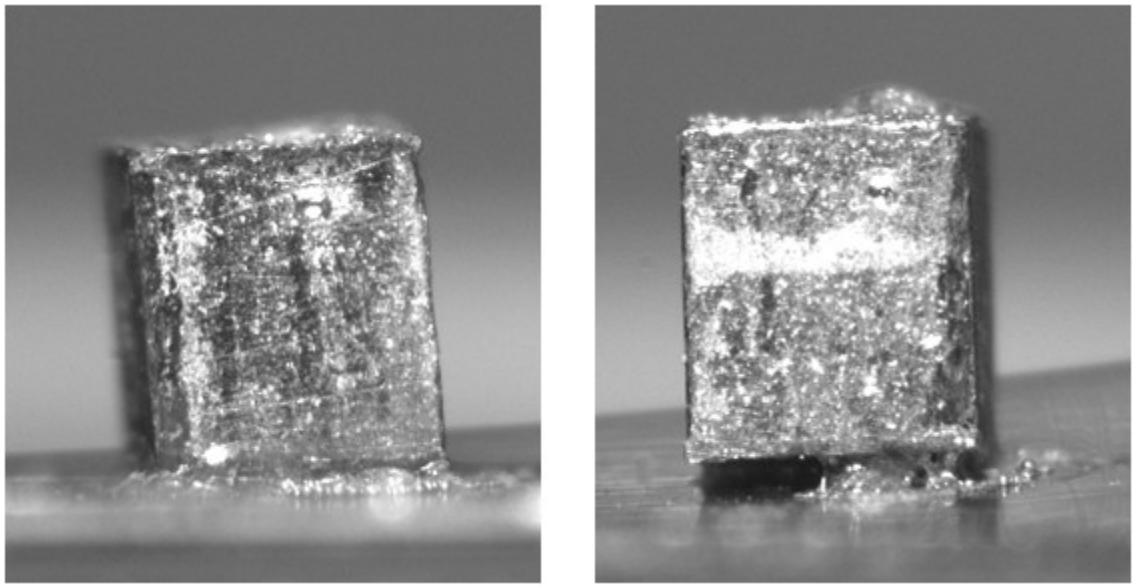

Figure 39: Two samples of the 1 mm aperture, solder reflow at 190 °C

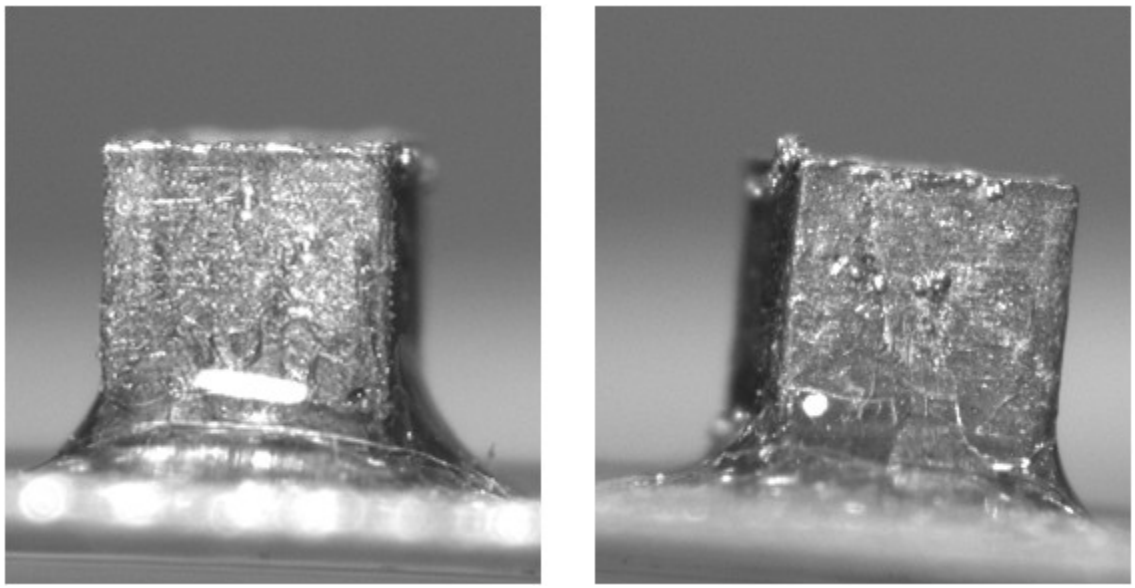

Figure 40: Two samples of the 2 mm aperture solder reflow at 190 °C

The results from using the 1 mm aperture and 200 °C oven air temperature illustrate the ideal mating between the thermoelement and the circuit board (Figure 41).

Conversely, use of the 2 mm aperture at the same temperature shows signs that the solder paste is gathering where the excess flux was previously (judging by the dull tapering surface at the base, Figure 42).

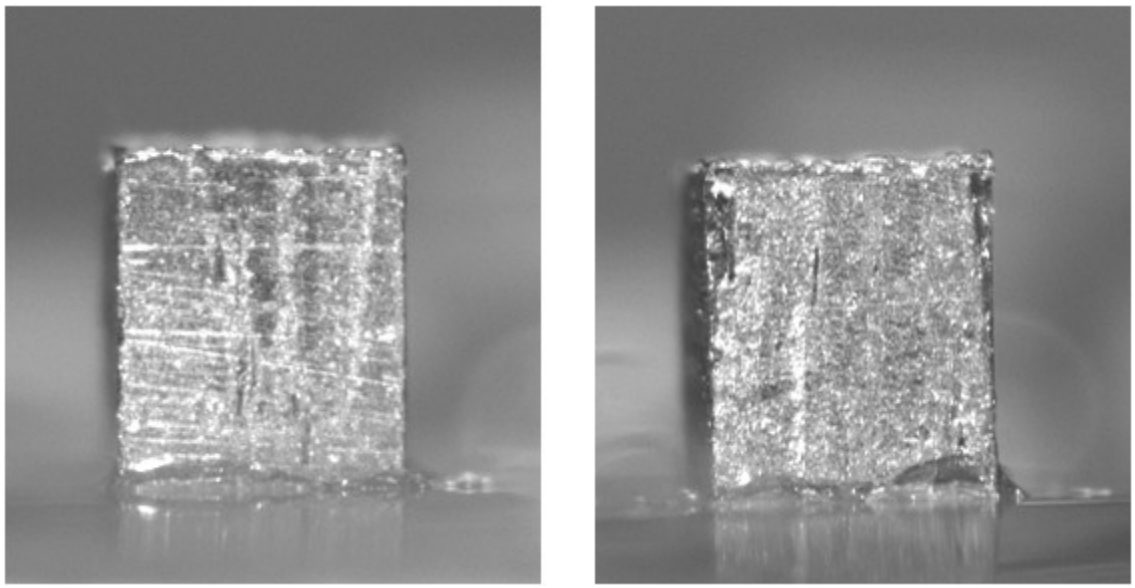

Figure 41: Two samples of the 1 mm aperture solder reflow at 200 °C

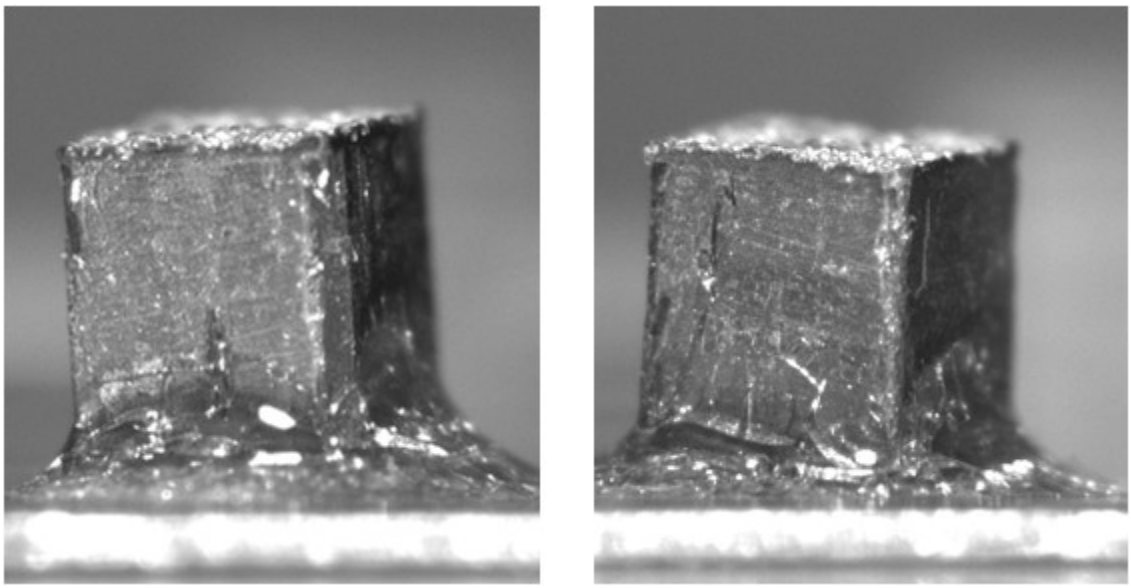

Figure 42: Two samples of the 2 mm aperture solder reflow at 200 °C

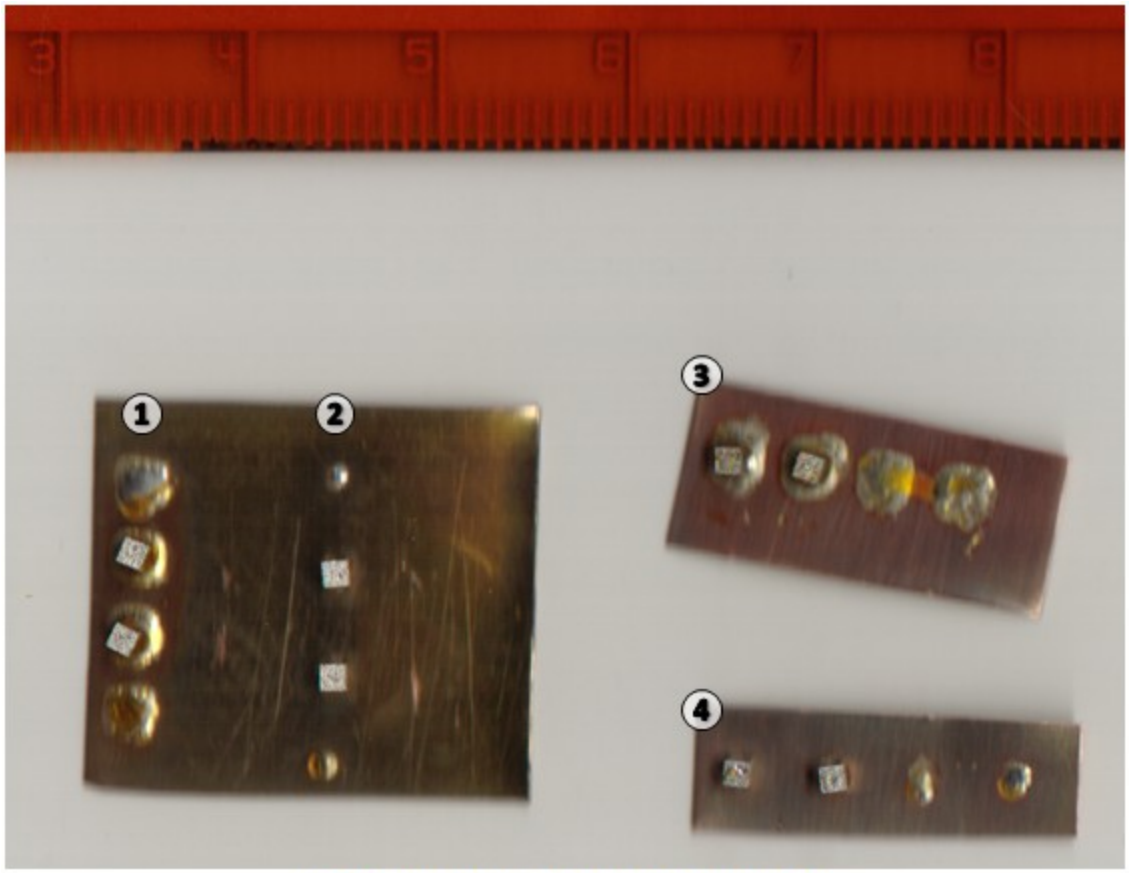

1. 2 mm aperture, solder reflow at 200 °C.
2. 1 mm aperture, solder reflow at 200 °C.
3. 2 mm aperture, solder reflow at 190 °C.
4. 1 mm aperture, solder reflow at 190 °C.

Figure 43: Top view of solder reflow results from different temperature exposures and stencil (1mm and 2mm) uses

Figure 44 demonstrates the solder joint quality of the first trial assembly. The 2 mm square dimension aperture was made in the 0.10 mm (0.001 inch) thick copper foil. The thermoelement on the left hand side of the figure has solder paste ascending the thermoelement's faces. While the right hand side thermoelement has only minor soldering imperfections on the thermoelement. Due to the alignment forgiveness inherent to using a larger solder pad and to continue working with the 2 mm thermoelement convention the 2 mm apertures were selected for continued use.

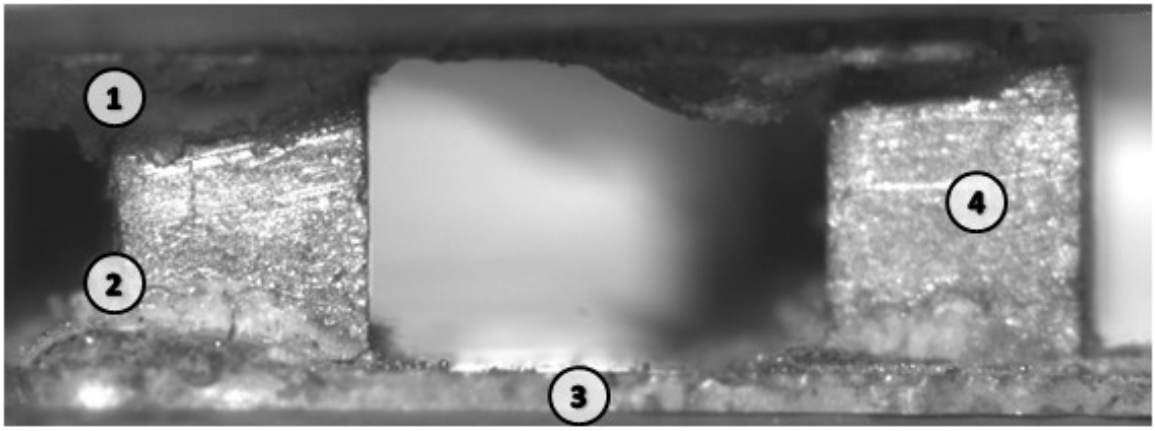

1. Descended solder paste.
2. Ascended solder paste.
3. Copper trace segment.
4. Thermoelement.

Figure 44: Profile picture taken of the first trial assembly to analyze solder joint quality

However, it was found that the brass foil underwent plastic deformation too easily during its own manufacturing and when used as a stencil. In an attempt to overcome this problem the stencil was mounted to a wooden rectangular frame in much the same way a painter's canvas would be (Figure 45); the frame was built first, the copper foil was wrapped around it, and the apertures were made last. However, there was about 6.35 mm (0.25 inches) of deflection at its center. Moreover, the need to ensure the frame's planar uniformity added another potential source of assembly error. Inconsistencies in this planar face would contribute to a non-uniformity of solder paste thickness.

Multiple aperture sets were made in the framed solder stencil at different locations to allow for analysis of the hole's dimensional dependence on its proximity to the wooden frame. This was not completed however because an alternative solder stencil material was being investigated; due to the fragile nature of the copper foil and the added complexity of incorporating a frame.

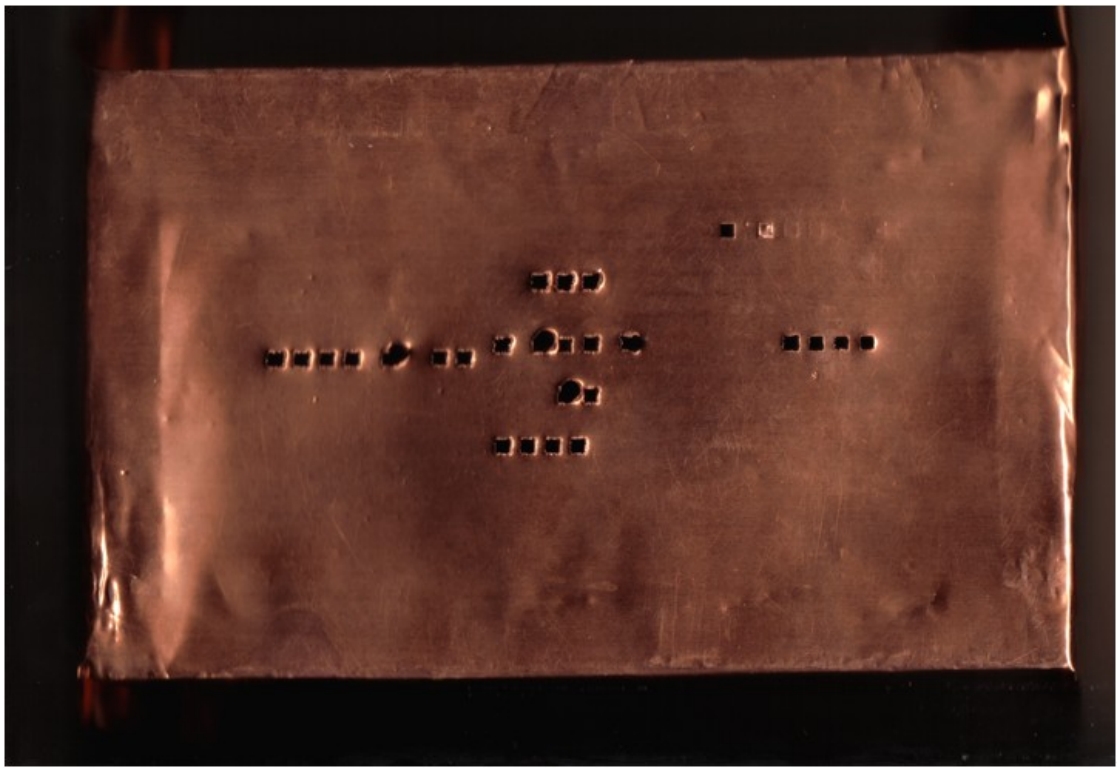

Figure 45: Framed 2 mm solder stencil

The transparency film was tried as a solder stencil material (Figure 46). It was also 0.10 mm (0.004 inch) thick and all deformations that took place while being manipulated were within the material's elastic region. Additional benefits were realized when comparing this to copper; less aggressive on the mill's bit, no need for liquid cooling, and no perforation crown on the side opposite where the mill bit takes entry. There is however the risk of developing micro frays along the aperture's perimeter if not milled properly.

Figure 46: Transparency based solder stencil used on third and fourth trial assemblies

Thermoelement Template Milling

The thermoelement templates were made from 0.36 x 101.6 x 254 mm (0.014 x 4 x 10 inch) brass sheet stock, where three 38.1 x 101.6 mm (1.5 x 4 inch) sections were cut off for the templates. Since they were cut with shears there was curling that occurred across the width of the segment. This required them to be hammered flat, however the surface's unevenness was still apparent.

They were milled (with inputs provided manually) independently (Figure 47). The top template provides a fixed alignment space for placing p-type thermoelements. The middle template is similarly used to provide a fixed alignment space for placing the n-type thermoelements on the remaining solder pad vacancies. The bottom template acts as a shim that prevents the middle template from disturbing the circuit board's solder paste.

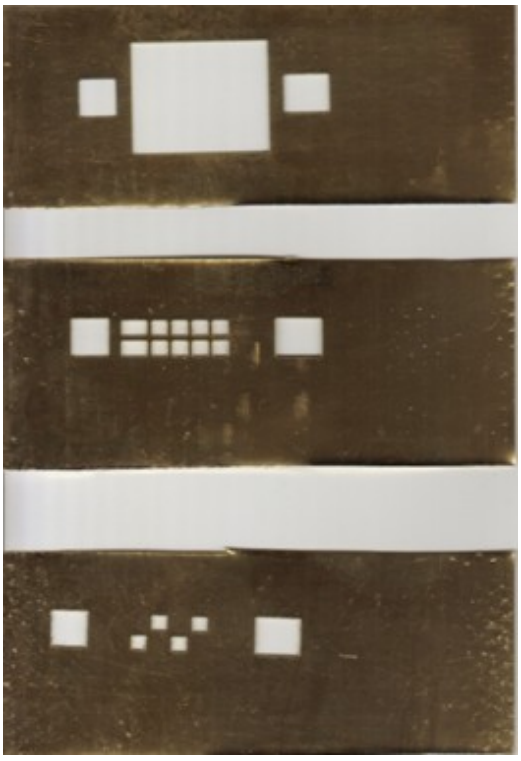

Figure 47: Brass thermoelement alignment templates for the third and fourth trial assemblies. (top) Elevates the middle template above the solder's height. (middle) Used for the remaining vacancies (n-type thermoelements) (bottom). Used for p-type thermoelement placement.

Staging Area

The trial assembly staging area (Figure 48) is made from a plate of what is believed to be plain carbon steel. The hole at the top serves no purpose for this project, this steel was previously kept in the lab for miscellaneous use. The intended distance between the center points of the alignment posts was 41.27 mm (1.625 inches). Threaded studs (1/4 x 20 x 3) were used in place of pressed in posts. The holes for these studs were drilled with a 0.125 inch pilot hole and again with a #7 drill bit. Then they were tapped for 1/4 x 20 thread.

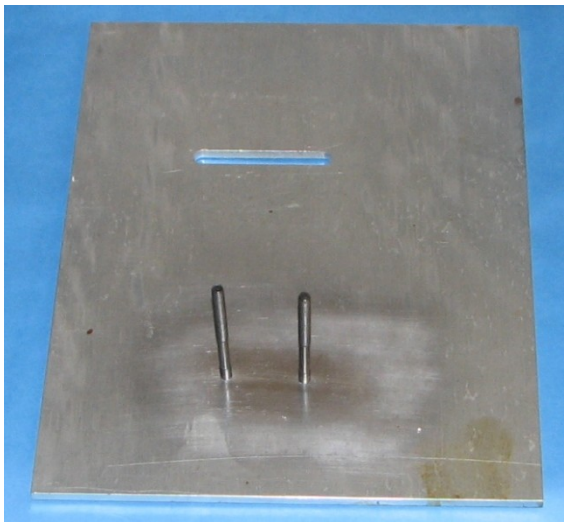

Figure 48: Trial assembly stage with a stainless steel base and two 1/4 x 20 x 3 studs.

Final Component Results

This section explains the manufacturing results obtained producing the circuit boards, solder stencil, and thermoelements templates. It also explains the unique developments that influenced their final manufacturing method.

Circuit Boards

Due to the unanticipated erosion on the periphery of each trace segment the mask's trace segment dimensions were: 3 x 7 mm, 3 x 11 mm on the power connection segments, a 1 mm space between segments of the same channel, and 5 mm of space

between the channels (Figure 49 and Figure 50). No mask is provided for the temperature sensor location; the copper would create an electrical and thermal short for the circuit, provide an additional layer of thermal resistance for the temperature sensor, and be a potential source of electrical interference to the temperature sensor.

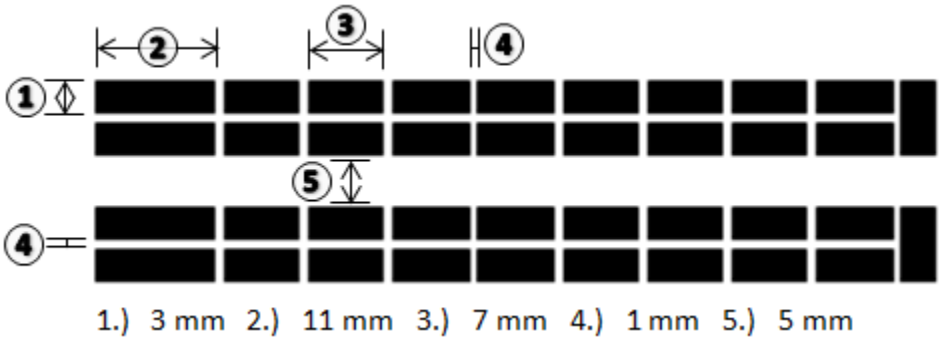

Figure 49: Gap and trace dimensions for the bottom circuit board etch mask

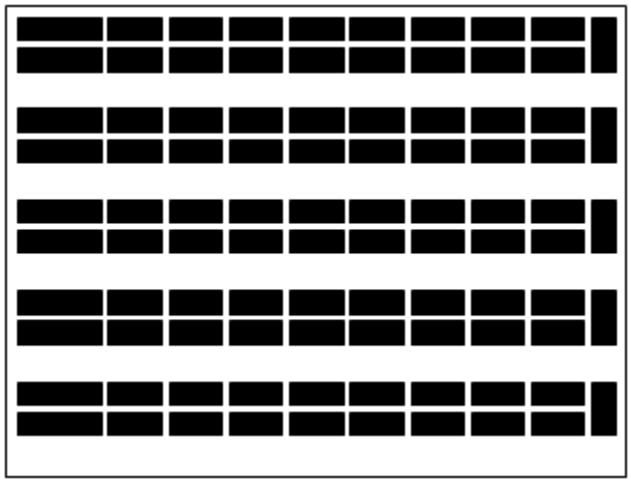

Figure 50: Bottom circuit board etching mask

The bottom and top preprocessing circuit boards used are shown in Figure 51. The etching durations for the final top and bottom circuit were 7 and 10 hours respectively. Etch times were long because of two reasons. First, the etchant used was saturated with reacted copper. Second, the relatively large surface area and volume of copper to be etched compounded the saturation problem. A successful post etching

bottom circuit board was not achieved until the third attempt. The first attempt's possible causes for failure were from collision with the magnetic stirrer and an inadequate duration for allowing the touch up paint to dry (2 hours). The second attempt failed because the preliminary circuit board frame did not surround the board's entire perimeter, and a small incision compromised this area. Subsequently this led to the polyimide tearing under its own weight during routine etching inspection.

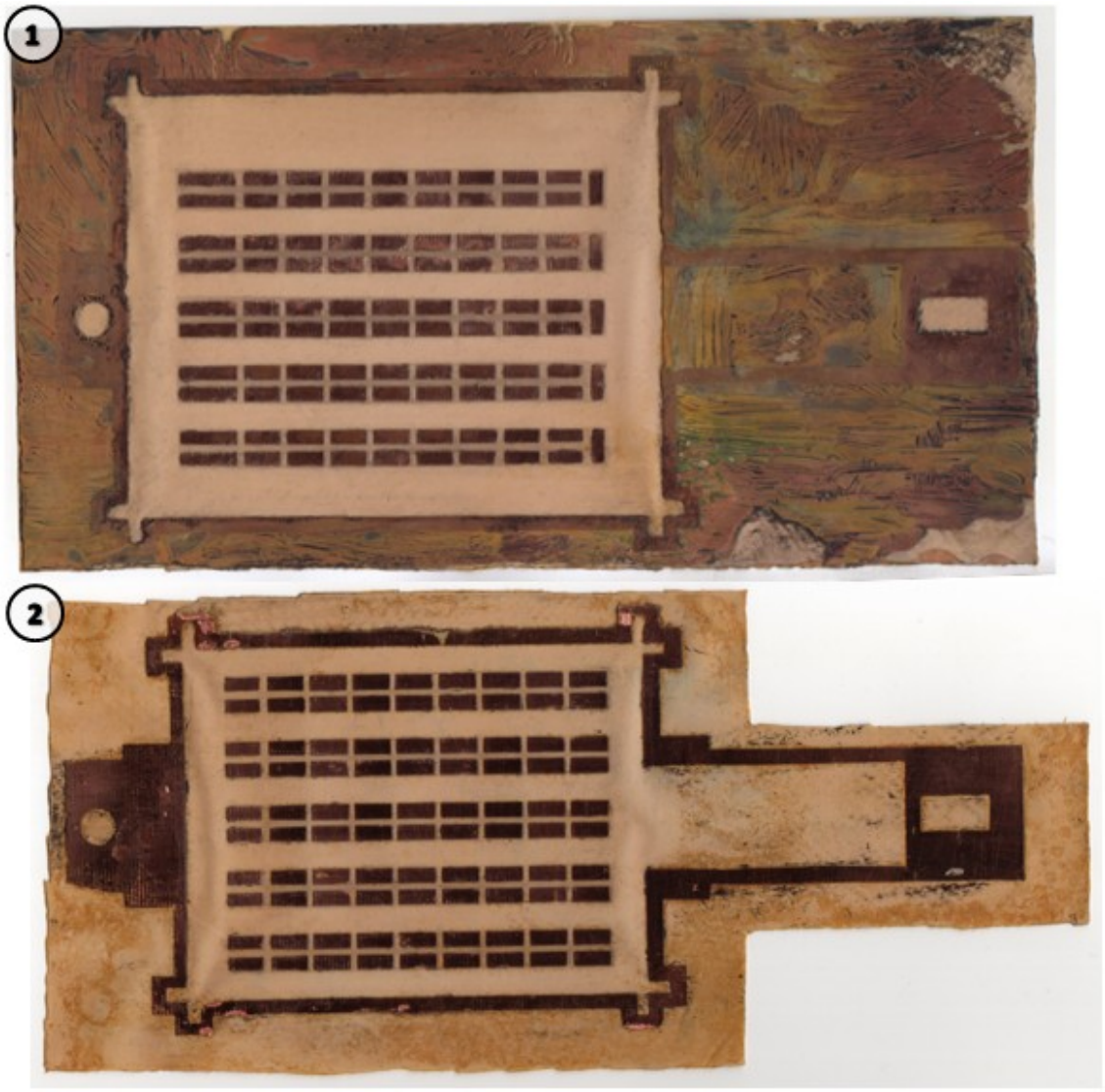

Figure 51: Post etching bottom (1) and top (2) circuit boards for the full scale assembly

Solder Stencil

The idea of creating the solder stencil apertures by etching was abandoned in favor of the CNC mill. Even though etching offered the ability to create multiple parts in a single batch of solution there was also a longer preparation time required (transferring the mask) and a time dependency on etching performance (etching process slows as it becomes saturated with dissolved material).

To avoid the possibility of ruining a work piece by human error the mill was operated by a pre-written program rather than manual individual inputs at the time of manufacturing. A MATLAB program was written to create the g-code for the stencil design (see Appendix C: MATLAB Gcode Generator for code details). Figure 52 illustrates the programmed pathway for the cutting tool.

Figure 52: Automated pathway preview of the mill's cutting tool for the full scale transparency based solder stencil

The four standalone holes in the final solder stencil (Figure 53) were from the first automated attempt of the solder stencil. Due to the plunge depth set at that time the apertures were made too wide, shortening the space between them. This was corrected by milling under sized apertures and boring them out afterward with a separate milling operation (work piece was not removed and reference positions remained the same).

The choice to bore the holes out instead of increasing the plunge depth during the initial pass is because the increased plunge depth will result in shortening the spaces between the apertures, a vital distance to maintain for the solder stencil.

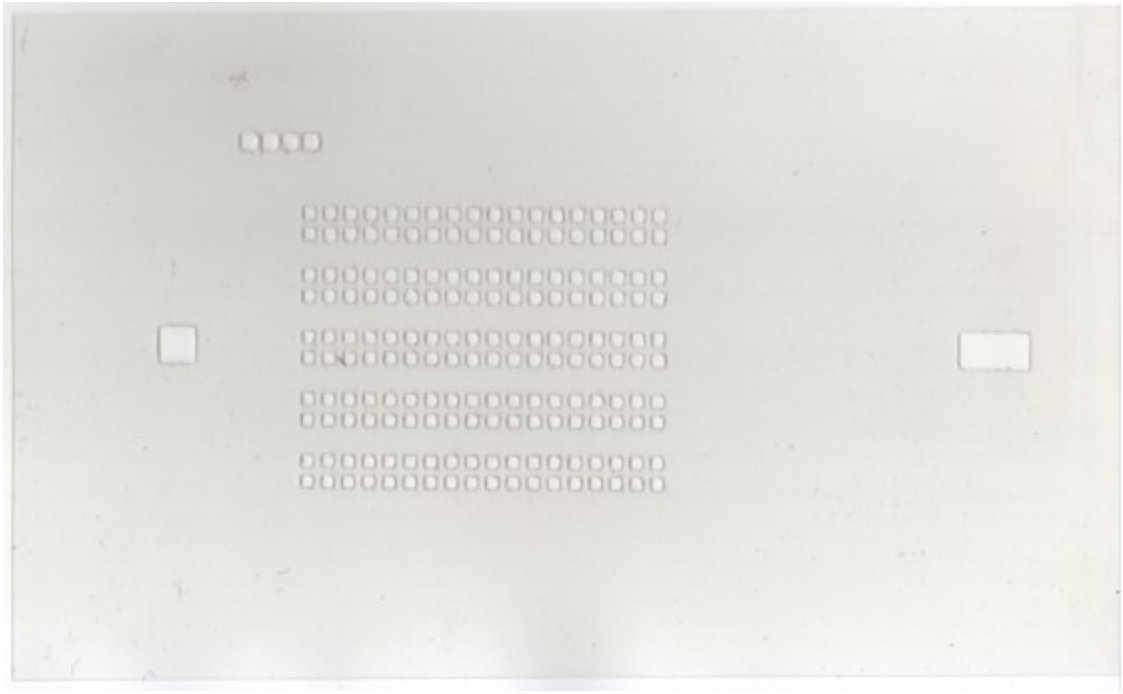

Figure 53: Transparency based solder stencil for the full scale assembly

Thermoelement Templates

Like the full scale transparency solder stencil the thermoelement templates were created using the milling process, where the inputs were automated by programs written for each template (see Appendix D: Stencil and Middle Template Gcode for sample code). Figure 54, Figure 55, and Figure 56 illustrate the programmed pathways the cutting tool would take for the bottom, middle, and top templates respectively. The same 0.36 x 101.6 x 254 mm (0.014 x 4 x 10 inch) brass sheets that were used for the trial templates were used for the full scale templates. Since the sheets were longer than desired their lengths were cut down to 203 mm (8 inches) with a Dremel cutting disk. This tool was used to remove the excess material without bending the sheet. These

ends of the sheets were deburred to ensure a flush continuous mating surface with the work board. The finished templates can be seen in Figure 57.

Figure 54: Automated pathway preview of the mill's cutting tool for the full scale bottom thermoelement template

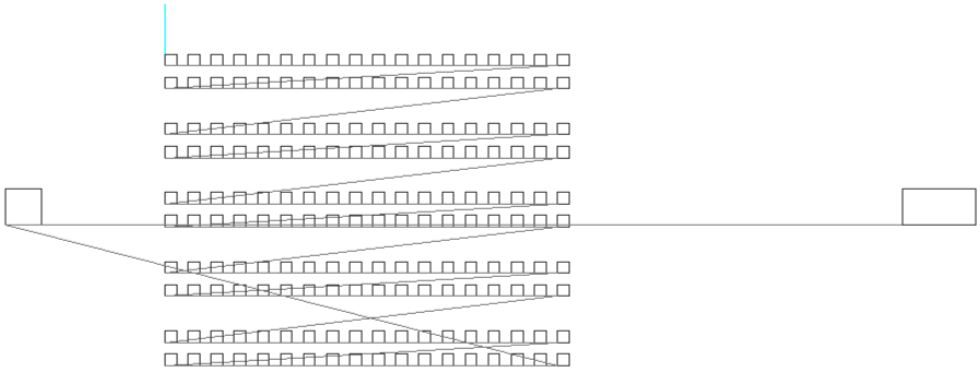

Figure 55: Automated pathway preview of the mill's cutting tool for the full scale middle thermoelement template

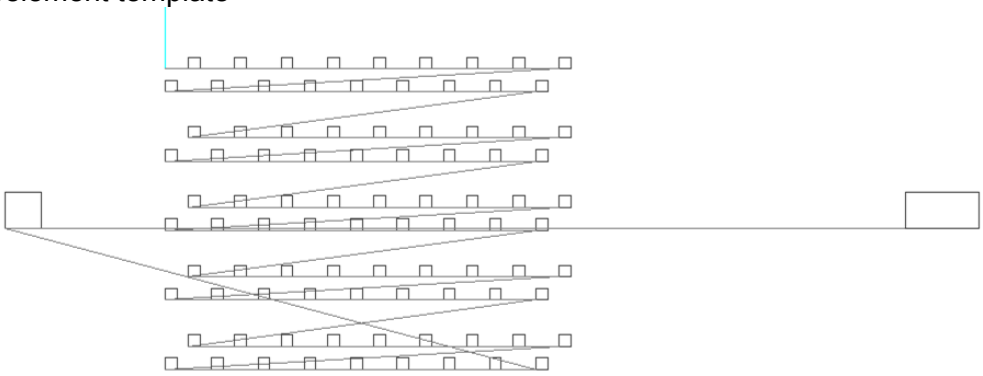

Figure 56: Automated pathway preview of the mill's cutting tool for the full scale top thermoelement template

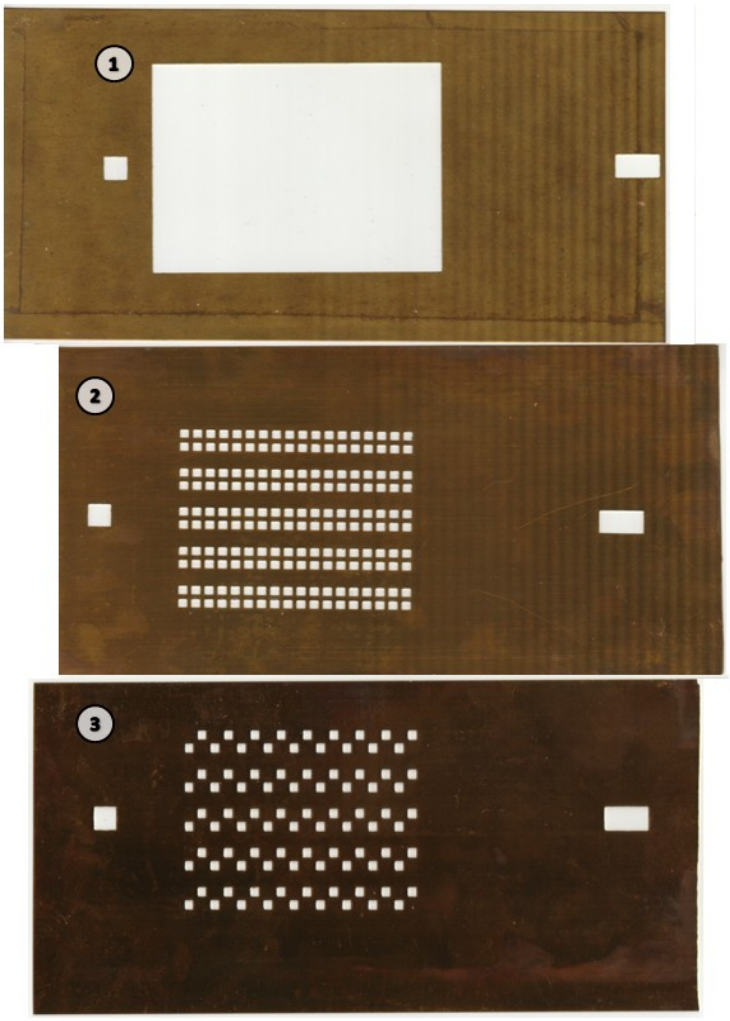

Figure 57: Finished full scale thermoelement templates. 1.) Bottom full scale thermoelement template. 2.) Middle full scale thermoelement template. 3.) Top full scale thermoelement template

CHAPTER FOUR: ASSEMBLY

The following chapter explains how all of the components come together in a step by step process. The development of this final procedure was not arrived upon immediately. Some of the problems encountered had their origins in manufacturing or even design, and had to be addressed accordingly.

Steps

The steps taken to assemble the trial devices are the same as those used for the full scale device. For this reason there will often be pairs of figures representing each step. One picture will be a schematic of the process and the other will be the result of carrying out that process on the final device.

First the top circuit board is placed on the staging area and the solder stencil is placed on top of the circuit board (Figure 58 and Figure 59). Solder paste is then deposited by hand with the syringe the paste came in. The syringe is held a quarter inch above the circuit board and an excess amount is deposited in each of the stencil's apertures (about two to three times the aperture's volume). From previous trials it was found that it's better to have an excess amount of solder in the aperture ready for wiping than just what appears to fill the space. Once all of the apertures are adequately filled a brass sheet is used to wipe the solder paste across the stencil (Figure 58). The deposited solder paste was then examined to see how well it filled the aperture. If there were any gaps a small amount of paste was deposited at the specific aperture and the stencil was wiped over again at that location.

The solder stencil and top circuit board are then removed. The bottom circuit board is then placed on the staging area and this process is repeated, with the exception that the circuit board is not removed at the end. This creates discrete solder pads on each circuit board (Figure 60, Figure 61, and Figure 62).

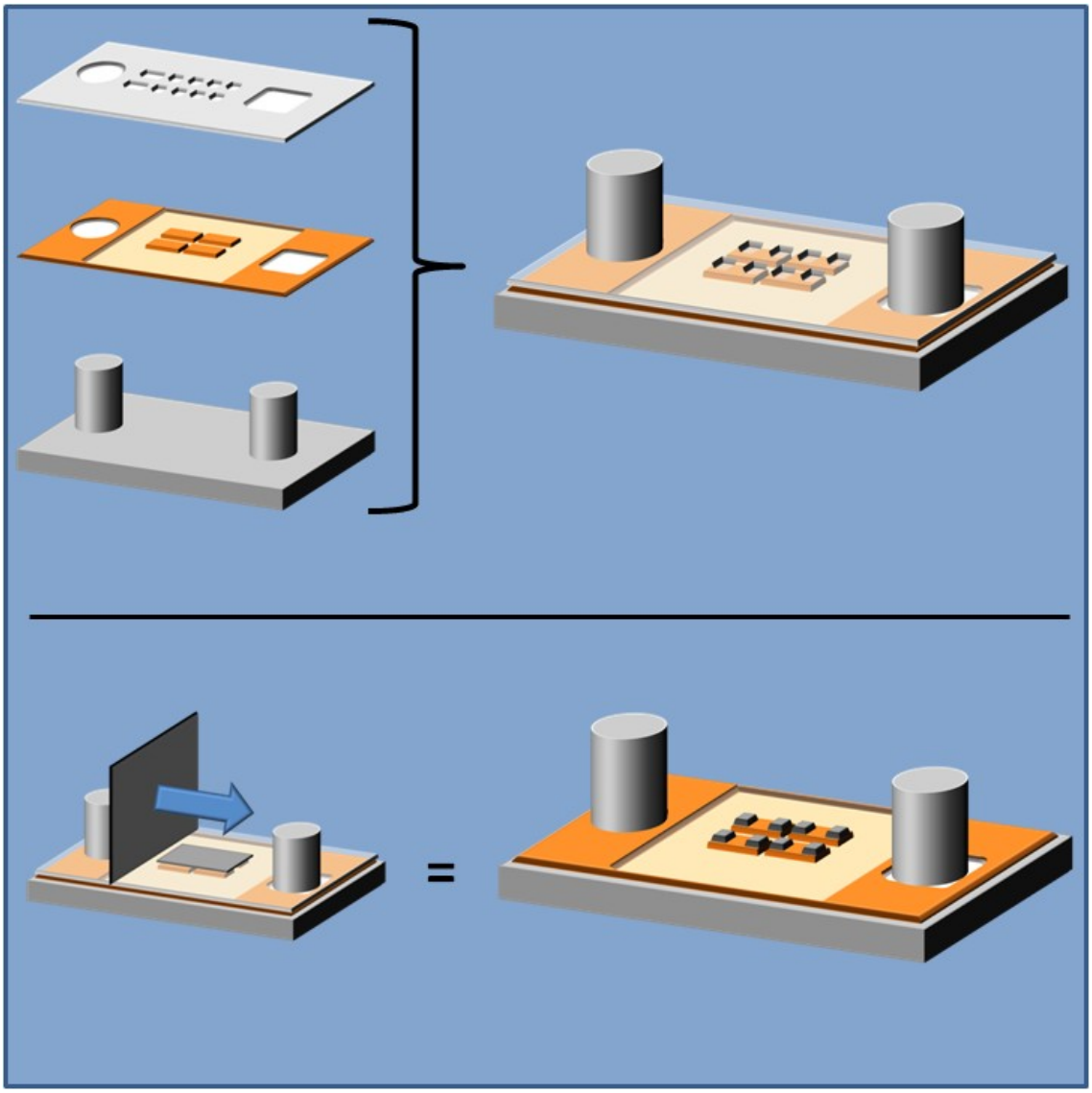

Figure 58: Schematic of solder paste application process

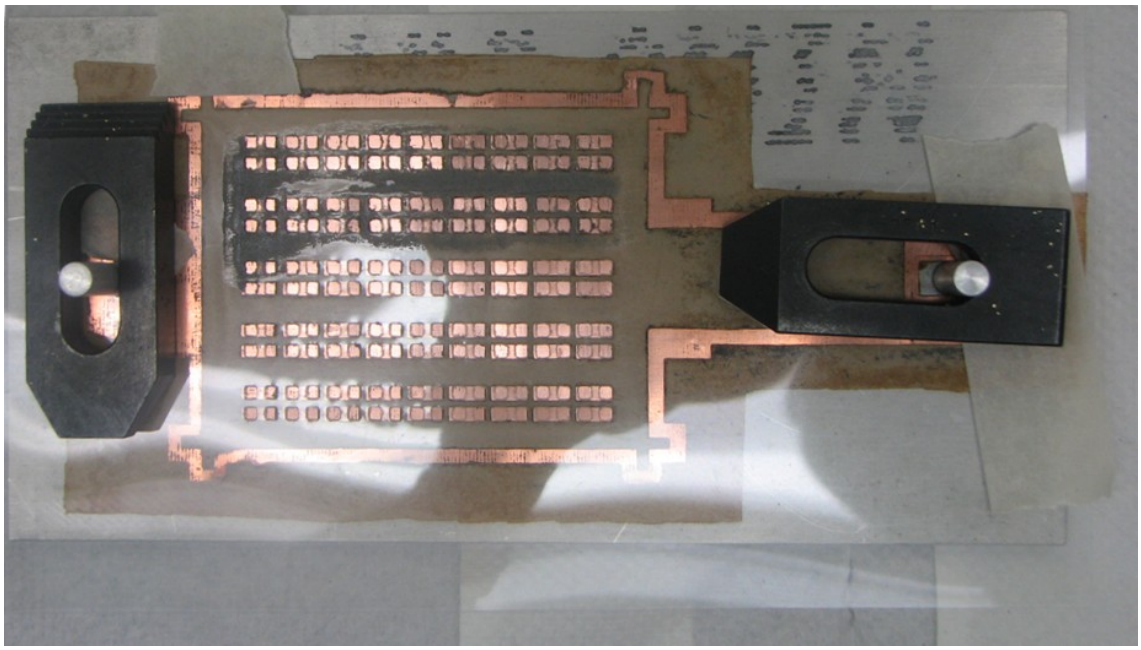

Figure 59: Solder stencil on top of the top circuit board prior to solder paste application

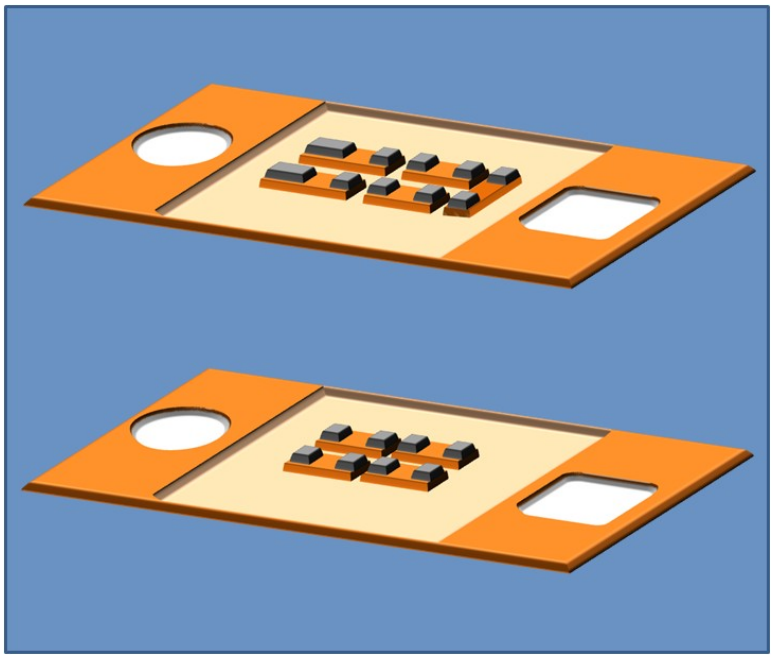

Figure 60: Schematic of the post solder paste application results

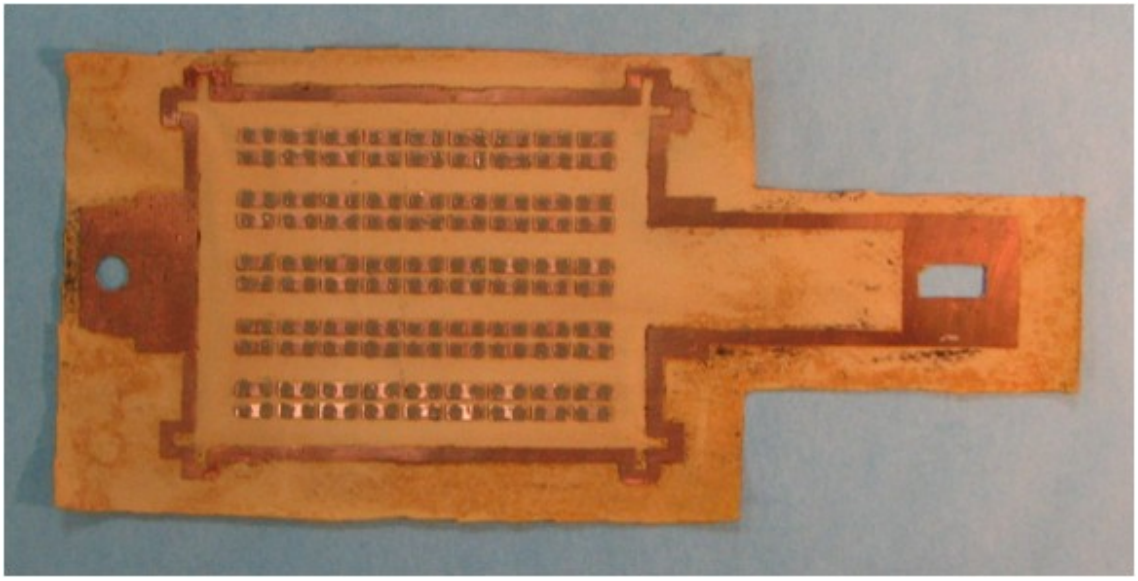

Figure 61: Top circuit board after successful solder paste application

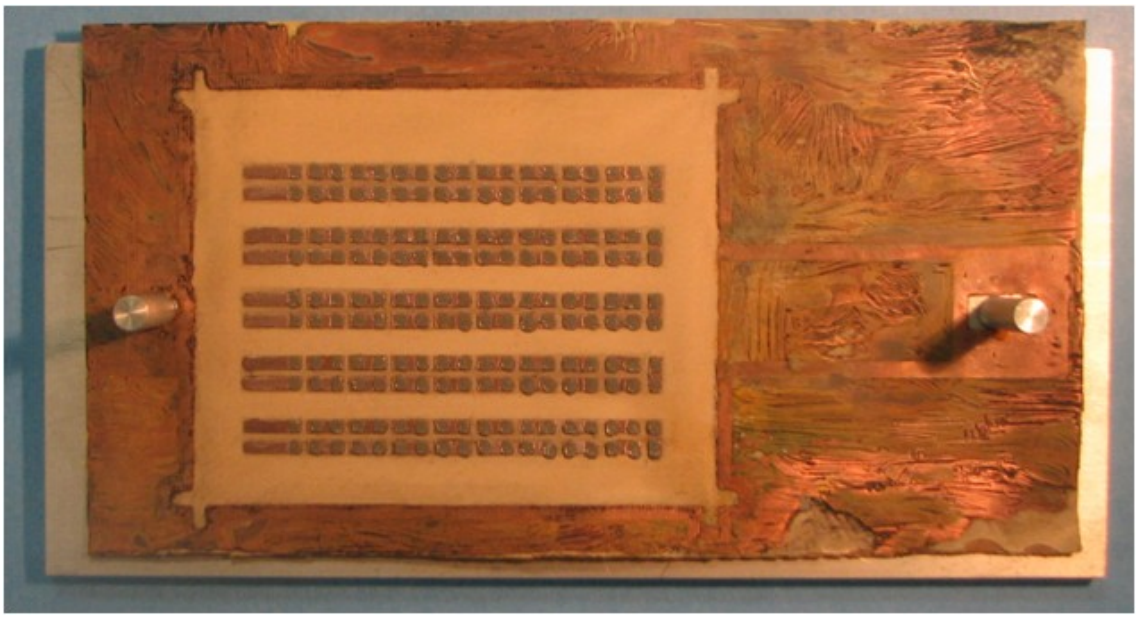

Figure 62: Bottom circuit board after successful solder paste application

The bottom, middle, and top thermoelement templates are then placed on top of the circuit board in that order (Figure 63, and Figure 64). The p-type thermoelements are placed by hand within the first set of holes on top of the solder pads with a pair of tweezers. The top thermoelement template is then removed and the n-type

thermoelements are placed in the remaining middle template vacancies in the same manner (directly corresponds to vacant solder pads)(Figure 65). The middle and bottom thermoelement templates are removed, leaving the bottom circuit board populated with thermoelements (Figure 63, Figure 66, and Figure 67).

The top circuit board is then placed on top of the staging area's arrangement (Figure 68). A mass is added to apply pressure and the assembly is then placed in the oven (Figure 69). For the trial assembly this mass was 92 g and for the full scale assembly it was 292 g. Both had the bulk of this mass focused at the center but for the full scale assembly the resulting pressure was almost evenly distributed across the assembly by the thermoelement templates (Figure 69). This assembly was then placed in the oven (Thelco, Model 27). The time and temperature profile for reflowing the solder is dependent on the size of the circuit board assembly (for further detail refer to the Final Assembly Results and Discussion section of this chapter).

The arrangement is removed from the oven once the appropriate time has passed and it has cooled down to room temperature. The assembly is then removed from the staging area. In the finishing process, the thermoelectric device is cut from the surrounding alignment material. This is done by stacking three 0.36 mm (0.014 inch) brass sheets and placing them in between the surfaces of the circuit board. A cutting wheel is rolled along the inside rigid edge of the top circuit board (refer to Figure 36 in the Circuit Board Etching section of the Manufacturing chapter) and the brass sheets act as a table keeping the circuit board level during this process. This is repeated along the perimeters of each circuit board. The end result is the extracted thermoelectric device (Figure 70 and Figure 71).

In the full scale and final trial scale assembly wires were soldered to the device after verifying electrical continuity. Acetone was applied to the power supply connections on the device and were brushed clean. Any remaining residue was wiped off prior to

soldering. Next 26 AWG wire was soldered to each power supply connection from the device with thin gauge solder (brand unknown), rosin soldering flux (RadioShack part number 64-022), and a 45 watt pencil iron (Craftsman model number 954042) (Figure 71).

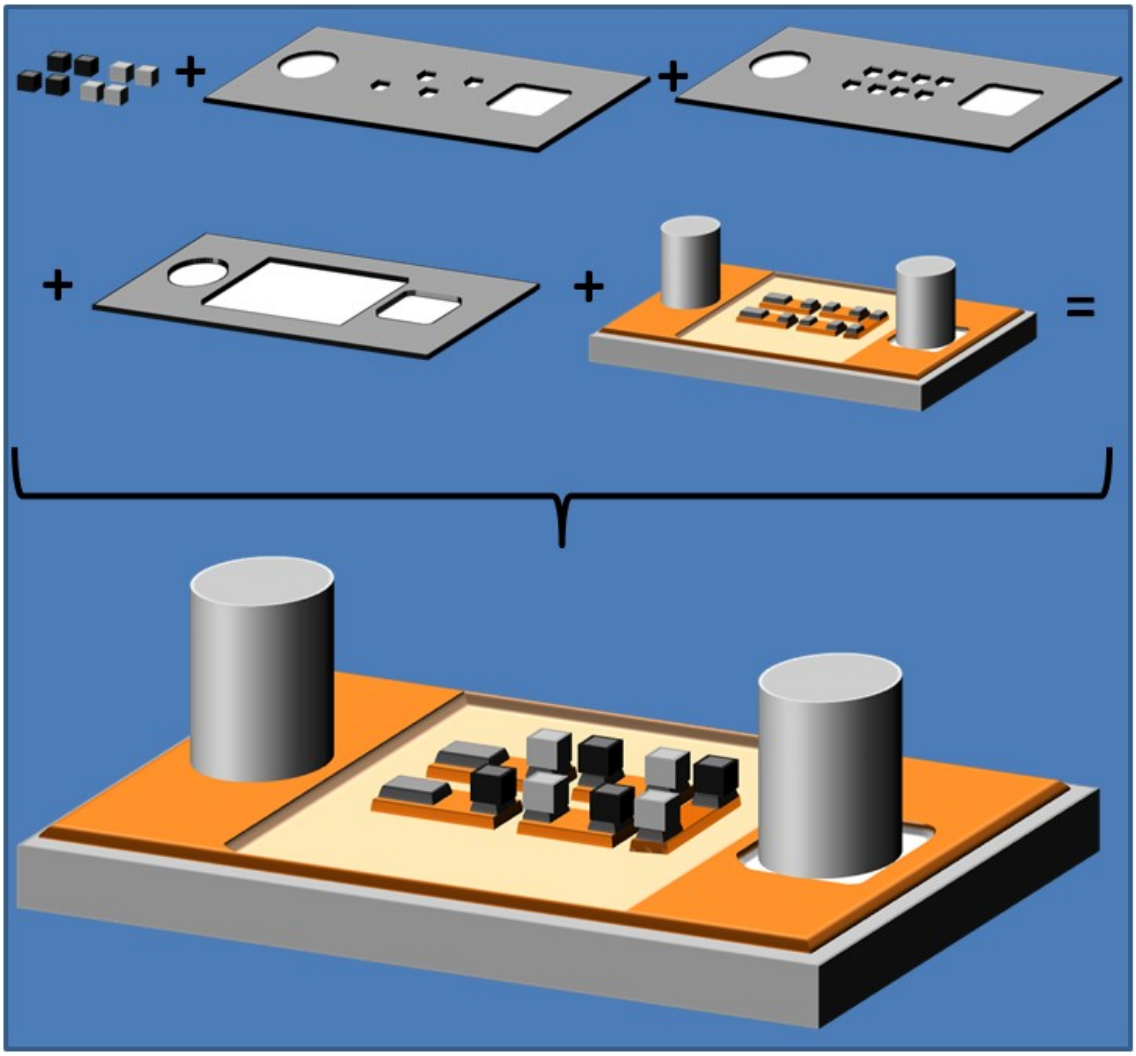

Figure 63: Schematic of the thermoelement and thermoelement template application process

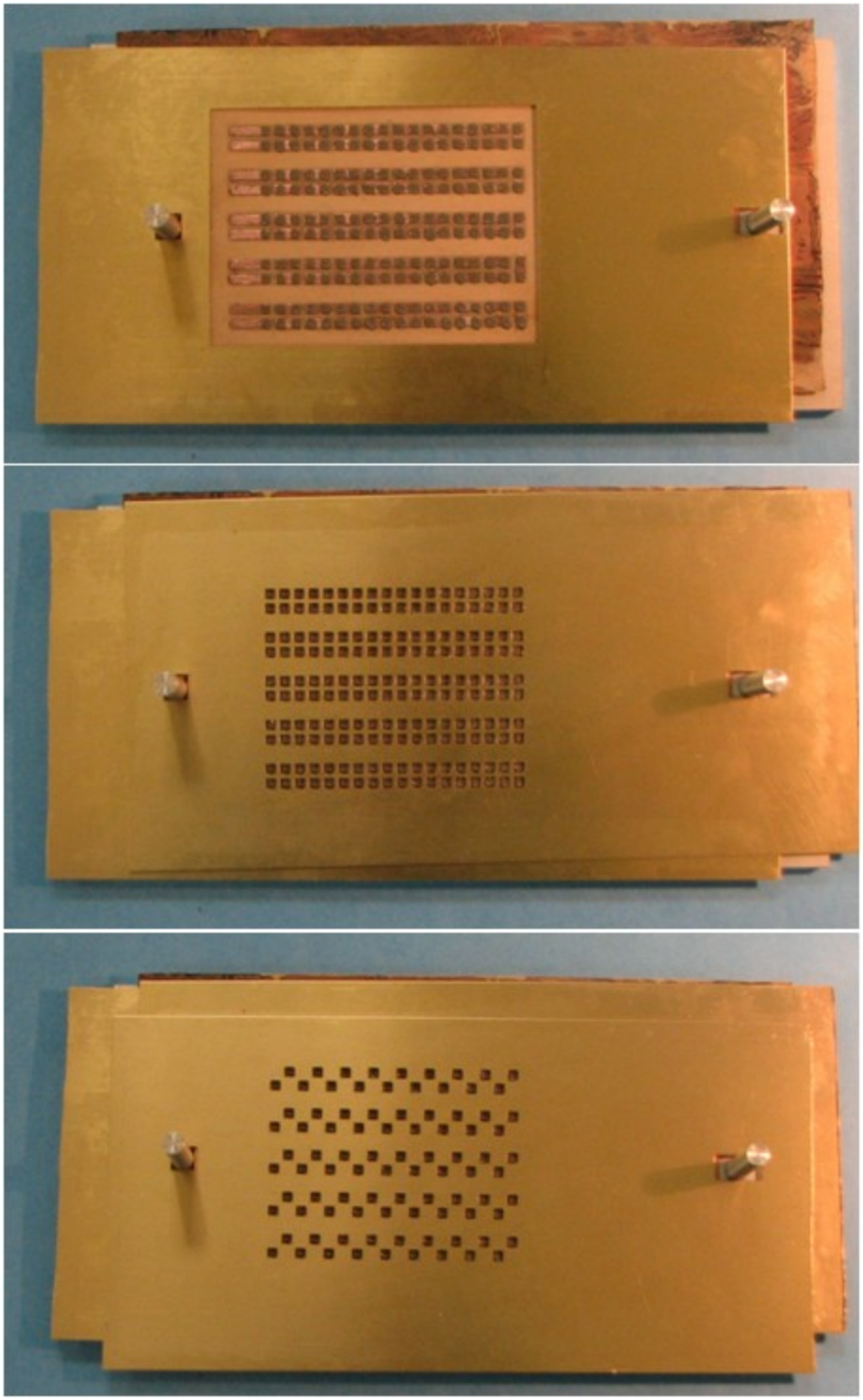

Figure 64: Bottom, middle, and top thermoelement templates applied to the bottom circuit board

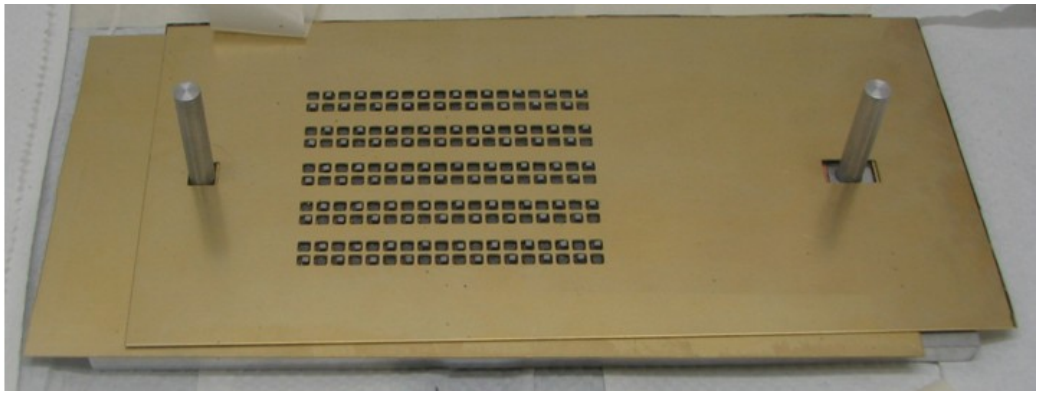

Figure 65: Top thermoelement template removed after p-type thermoelements are positioned

Figure 66: Remaining thermoelement templates removed after n-type thermoelements are positioned

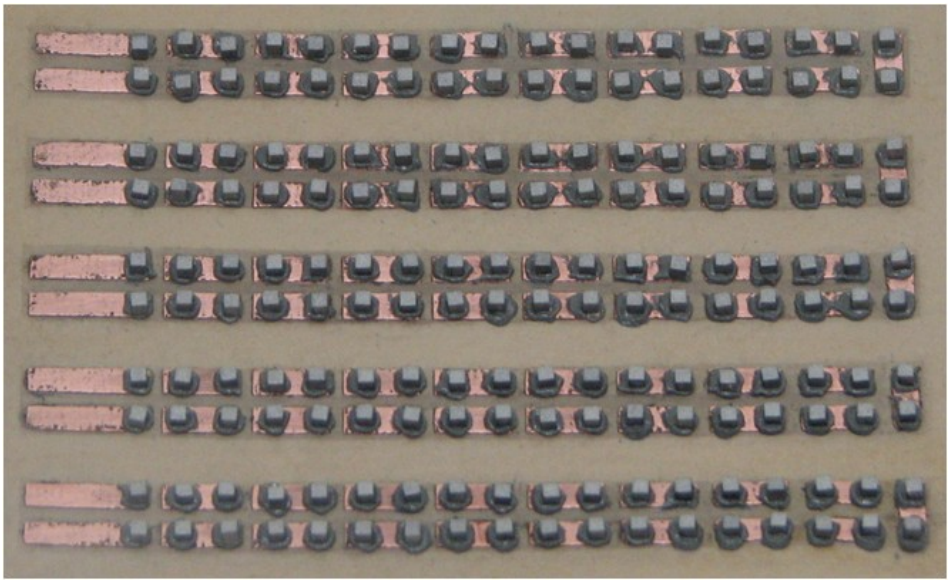

Figure 67: Close up of the thermoelements positioned on the bottom circuit board

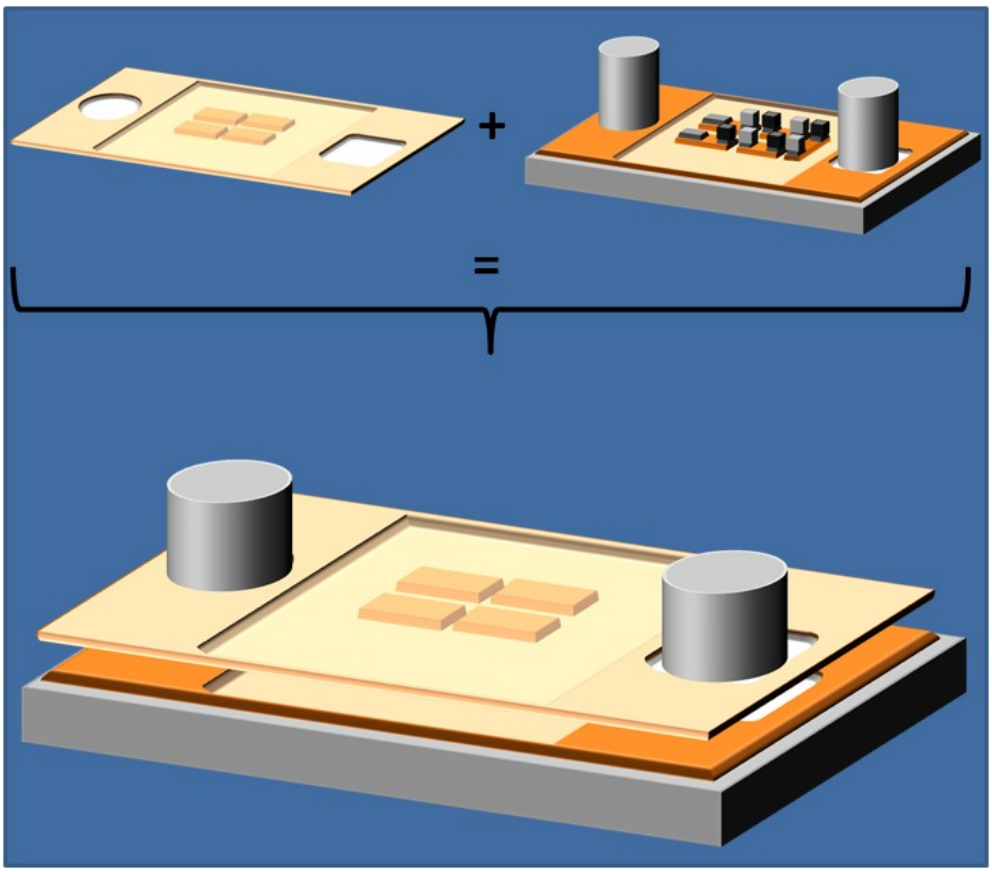

Figure 68: Schematic of the top circuit board placed on top of the thermoelements

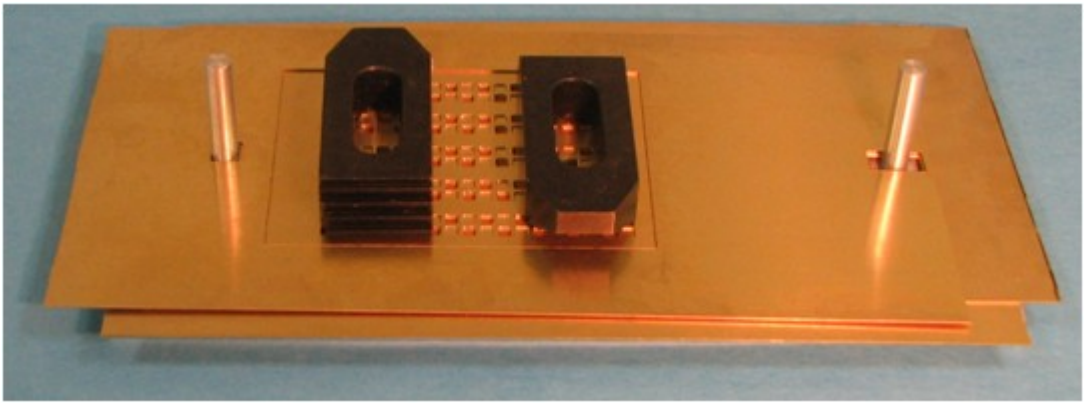

Figure 69: Assembled circuit boards with thermoelement templates and mill restraints used as weights for the reflow process

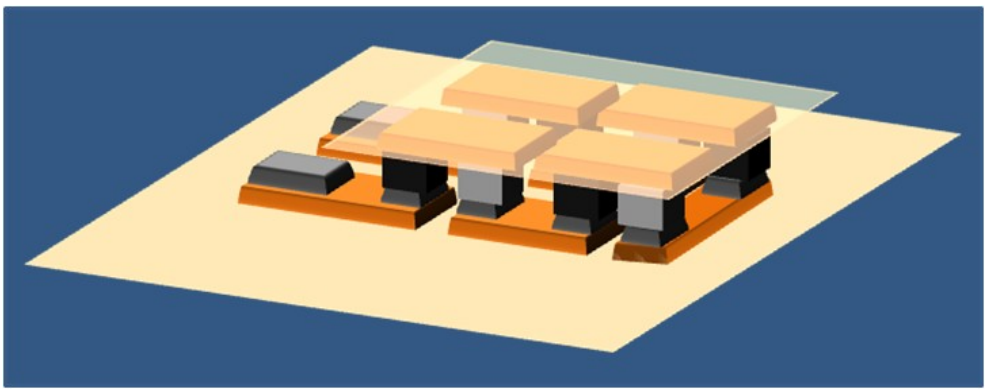

Figure 70: Schematic of the post processing circuit board

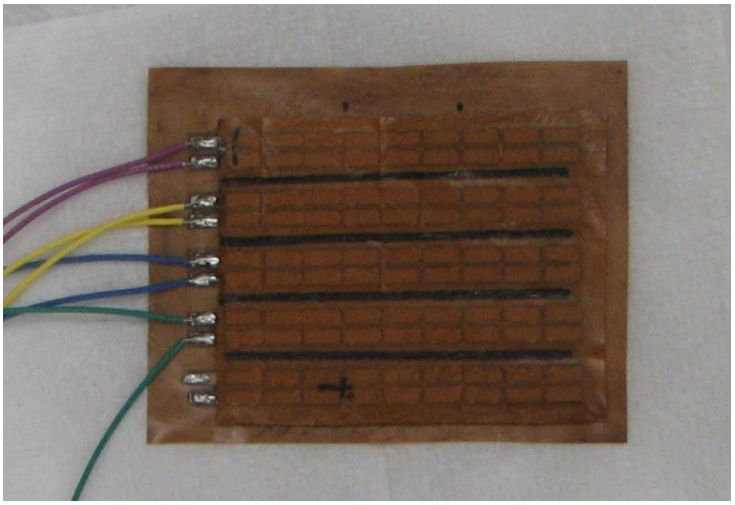

Figure 71: Actual post processing circuit board with wires attached

Trial Assembly Results and Discussion

This section provides explanation of the motivation for creating trial assemblies and the problems encountered during post processing.

Trial Assembly Motivation

Prior to investing time and material resource on creating the final design concept it was believed that an adequate number of proof of concept prototypes should be completed. Kevin Otto and Kristin Wood, authors of *Product Design* define this prototyping approach as a means of answering specific feasibility questions regarding a product. [33] There were no explicit conditions that defined the number of trials this

project would create, only that there were enough to justify the validity of the manufacturing and assembly approaches.

The first two prototypes (Figure 72 and Figure 73) were made with the purpose of evaluating the manufacturing approaches for the circuit board and solder stencil. They were assembled without the aid of alignment tools or the staging area. Questions were asked like “can this produce the desired geometry,” and “does this result appear to be repeatable?” The discussion on those matters is in the Manufacturing section of the Conclusions chapter, but the short answer is yes.

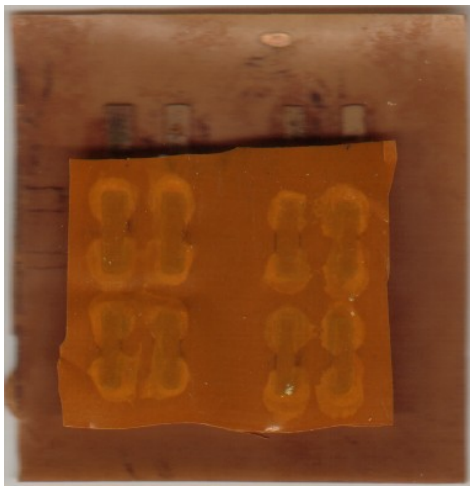

Figure 72: Top view of the first trial assembly

Figure 73: Top view of the second trial assembly

The first trial assembly (Figure 72) showed the need for increasing the individual trace segment dimensions of the etching mask to compensate for the erosion that occurred around the trace segment periphery during etching. This approach was applied in subsequent etching procedures because it improved the accuracy of the trace segment dimensions produced. The second trial assembly (Figure 73) is the result of an improved etching mask transference, touch up procedure, and the first application of the etching mask's dimensional compensation for the etching process. The incision which separated the top substrate between the two intended channels also allowed for demonstration of the design's flexibility.

The next two prototypes (Figure 74 and Figure 75) were made to demonstrate the soundness of the assembly process and utilized the manufacturing lessons learned from the previous two prototypes. These assemblies incorporated the trial staging area, methods for aligning the components, and use of thermoelement templates. Again, the questions that dictated the project's direction were with regards to accuracy and repeatability of the process (see Manufacturing Conclusions).

Figure 74: Top view of the third trial assembly

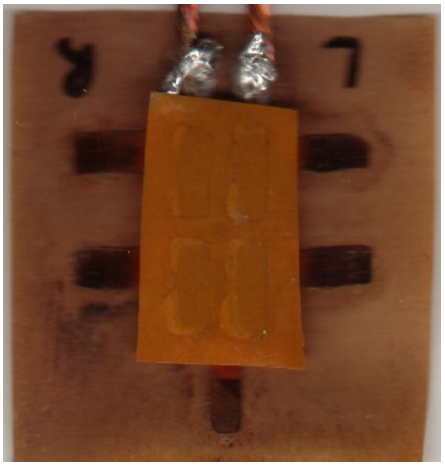

Figure 75: Top view of the fourth (final) trial assembly

The third trial assembly (Figure 74) proved the repeatability of this assembly approach by the ease in which the multiple repairs were made to the device. The final trial assembly demonstrated the achievement of a working thermoelectric device by this assembly method. From this it was concluded that adequate manufacturing and assembly methods had been developed in order to begin production of the full scale device. A transparent superposition of the fourth assembly on top of the third assembly reveals the manufacturing and assembly processes repeatability (Figure 76).

Figure 76: Transparent superposition of the fourth trial assembly on top of the third trial assembly

Post Processing Difficulty

The first attempt at removing the excess material was during the third trial assembly. The alignment tabs of both circuit boards were cut simultaneously with scissors. This resulted in the planar rotation of the top circuit board relative to the bottom one, shearing the solder joints. After being repaired another attempt was made. In an effort to change the plane of motion, and remove the moment arm that previously contributed to failure, one of the alignment tabs were bent upwards at 90° prior to being cut with industrial shears. However, this again resulted in failure. A Dremel cutting disk ultimately separated the device from the alignment material. Despite the success of this approach an alternative method that did not involve the use of a power tool was preferred. This motivated the design changes for the fourth trial assembly iteration and the use of a cutting wheel. This worked successfully on the full scale and final trial assemblies.

Final Assembly Results and Discussion

Difficulty was encountered in properly reflowing the solder on the full scale assembly. The oven's air temperature was measured by a thermal probe inserted at its exhaust vent at the top of the oven. This sensor penetrated several inches into the oven's atmosphere but never touched the device. During the first reflow attempt the oven air heated to 200 °C with the oven turned off at that point, as was done during the trial assemblies (Table 9). However the door remained closed for 11 minutes 21 seconds (instead of the 1 minute used during trial assemblies), at which time the air temperature reached 170 °C. This was done as a cautious attempt to provide additional heat exposure to the larger assembly. After visual inspection of the solder joints it was concluded that the solder was not adequately reflowed. The joints looked like those in Figure 38 from the Solder Stencil Milling section of the Manufacturing chapter.

Table 9: Time and temperature profile for the first full scale solder reflow attempt

Time and temperature profile for the first full scale solder reflow attempt			
Time (minutes)	**Temperature (°C)**	**Time (minutes)**	**Temperature (°C)**
0	23.2	31	189
23	185.8	32	186.4
24	189.8	33	183.7
25	193.7	34	181
26	197.6	35	178.4
26:39*	200	36	175.8
27	199.9	37	173.3
28	196.4	38**	170.7
29	193.7	39	126.2
30	191.4	40	102.6

* Oven turned off
** Oven door opened

A 10% increase in the temperature set point for turning off the oven (220 °C), and keeping the oven door closed until the inside air reached the solder paste's melting point (179 °C) was decided. Table 10 shows the temperature profile of the second reflow attempt. The resulting joint quality is comparable to that seen in Figure 44.

Table 10: Time and temperature profile for the second full scale solder reflow attempt

Time and temperature profile for the second full scale solder reflow attempt			
Time (minutes)	**Temperature (°C)**	**Time (minutes)**	**Temperature (°C)**
0	23.2	36	209.4
27	203.8	37	206
28	206.8	38	203.3
29	210.1	39	200.5
30	213.2	40	197.6
31	216.2	41	194.6
32	219.1	42	191.7
32:19*	220	43	188.9
33	219.2	46:33**	179
34	215.4	47	157.7
35	212.4	48	115

* Oven turned off
** Oven door opened

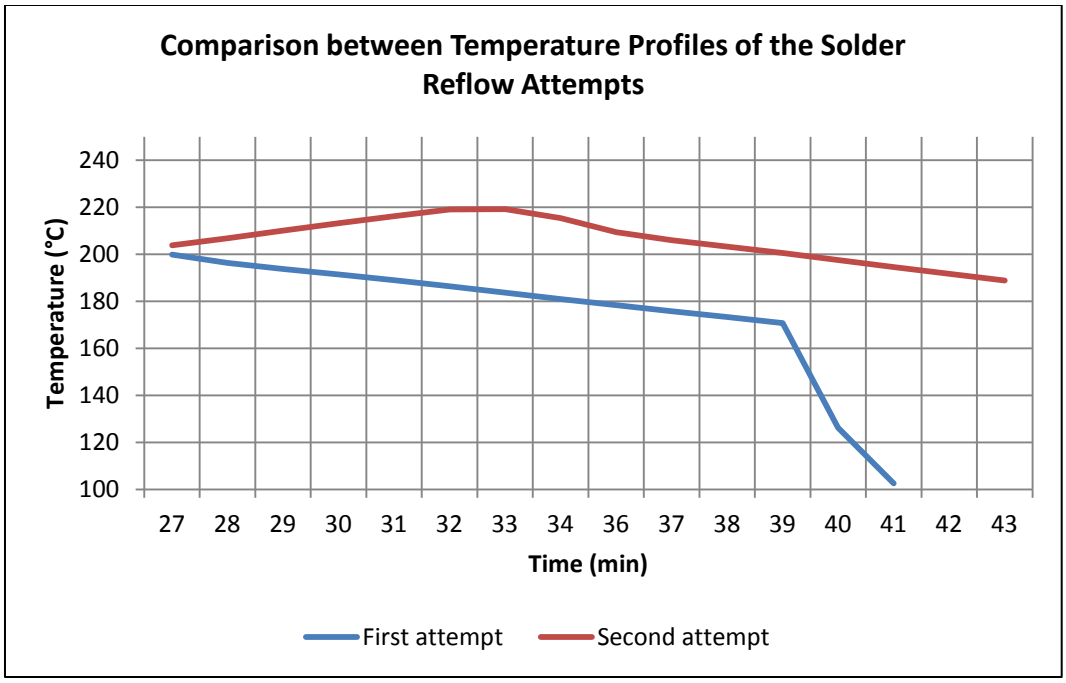

Figure 77: Comparison between temperature profiles of the solder reflow attempts

Closing Remarks

There was measured continuity in all of the circuit's channels following the completion of the device. In the days following, the bottom channel of the device developed an intermediate open circuit. The source of the circuit's problem was isolated to the connection of a single thermoelement. An unsuccessful attempt was made to repair this connection. On the other hand, there may have been electrical shorts between elements as well as those observed in Figure 67. This could substantially degrade the device performance. This could be reduced by using smaller apertures, or thinner stencils to reduce the amount of solder deposited. More pressure during the stencil operation may also reduce leakage of the paste beyond the stencil holes, and smoother aperture walls would reduce disturbing the solder when the stencil is lifted.

The troubles experienced reflowing the solder is an indication of an area which needs to be addressed in greater detail. In order for this process to be repeatable and

reliable the connections at the solder joints must be adequate but not excessive, where the thermoelement is embedded in the solder paste. Future testing could involve measuring the circuit board or a component's temperature with a probe directly instead of measuring the oven's air temperature.

In addition to the reflow duration the amount of solder paste deposited also needs to be addressed. I believe a significant contributor toward the paste's poor dimensional tolerance is from boring the apertures. Had they been cut as well as the trial stencil's I don't believe problems related to excessive solder paste would be so prevalent.

CHAPTER FIVE: DEVICE PERFORMANCE

The goal of the following chapter is to provide an explanation on how the interpreted pilot performance data was achieved. This will involve explaining the device's testing and data collection methods, the results of this data, and how it compares with the 1-D model.

Testing Methods

The following section details the data acquisition system, and testing arrangement for the thermoelectric device. The average time it took to test each channel was 15 minutes. The average change in surface temperature for the hot and cold side reservoirs over the course of each test were 2 and 6 °C, respectively. The elevated hot side temperatures were a significant reason for the relatively large change in the cooling reservoir's temperature

Data Acquisition

The data was obtained by using 5 resistance temperature detectors (RTDs). Each RTD was attached to a Wheatstone bridge, which housed 3 other resistors (values ranging from 100 to 200 Ω), a variable resistor (used to adjust the RTD's resistance), and a 0.1 μF capacitor on the output voltage signal for conditioning. From there the data was relayed to an analog to digital converter (ADC) (Phidgets, part number 1018-2). This digital information was then relayed to a computer by USB. A MATLAB program was written to interface with the ADC (Appendix G: MATLAB Temperature Sensor Measurement Code). MATLAB then took the information and applied a conversion formula that was made during sensor calibration. The result was an on screen display of

continuously captured temperature data (in Fahrenheit) whenever the program was running. Once the program completed its cycle it exported the data into a spreadsheet for analysis and closed communication with the Phidgets device.

Temperature Sensor Calibration

Each temperature sensor was submerged along with a Type K thermocouple (provided the measured reference temperature) in water at two different temperatures. Table 11and Table 12 illustrate the resistance values gathered during sensor calibration.

Table 11: Hot temperature exposure for sensor calibration

RTD	Display Value	Temperature (°F)
Sensor 0	328	111
Sensor 1	335	109.9
Sensor 2	240	107.1
Sensor 4	300	106.4
Sensor 5	240	105.9

Table 12: Cold temperature exposure for sensor calibration

RTD	Display Value	Temperature (°F)
Sensor 0	97	55.2
Sensor 1	106	55
Sensor 2	31	54.8
Sensor 4	91	55.2
Sensor 5	40	55.9

These values were used to approximate the equation of a line (Equation 39) which would allow for converting the resistances into temperatures within MATLAB.

$$y = ax + b$$ Equation 39

where y is the temperature value converted from the sensor's resistance, x is the sensor's resistance, a is the slope in degrees of temperature per resistance, and b is the y intercept in degrees of temperature. Table 13 details the values of these constants for each sensor.

Table 13: Temperature sensor constants for resistance to temperature conversion

RTD	a value	b value
0	0.2416	31.77
1	0.2397	29.59
2	0.2502	47.04
4	0.2450	32.91
5	0.2500	45.90

System Arrangement

A Walgreens brand 1.75 L (59.15 oz) flexible bottle was filled to two thirds capacity with water. The bottle's initial surface temperature at the time of testing ranged from 27 to 29 °C (81 to 84 °F). This water was used for a series of tests on a channel and then changed for fresh water when switching to the next channel. The water filled bag was used to simulate the thermal characteristics of the adult forearm. Three temperature sensor alignment marks were made on the bottle, each 25 mm (0.098 inches) away from one another. These distances were chosen because it's the spacing between the front, center, and rear of the device.

Three sensors were aligned to these marks (from left to right: sensors 0,1, and 2) with their measuring elements facing the bottom of the TE device and held in place by duct tape (Figure 78). Petroleum jelly was used as a thermal paste and was applied on the surface of the flexible bottle, on the measurement faces of the sensors, and on the bottom of the TE device.

The TE device was then aligned and placed on top of the three temperature sensors. Two temperature sensors were then aligned to the top of the device (from left to right: sensors 4 and 5), 21 mm away from the edge of the last copper trace on either side. The sensor's measuring elements were oriented to face the top of the TE device. Petroleum jelly was applied to the top of the TE device and the back of the temperature sensor (Figure 79).

Figure 78: Water bottle with bottom sensors attached

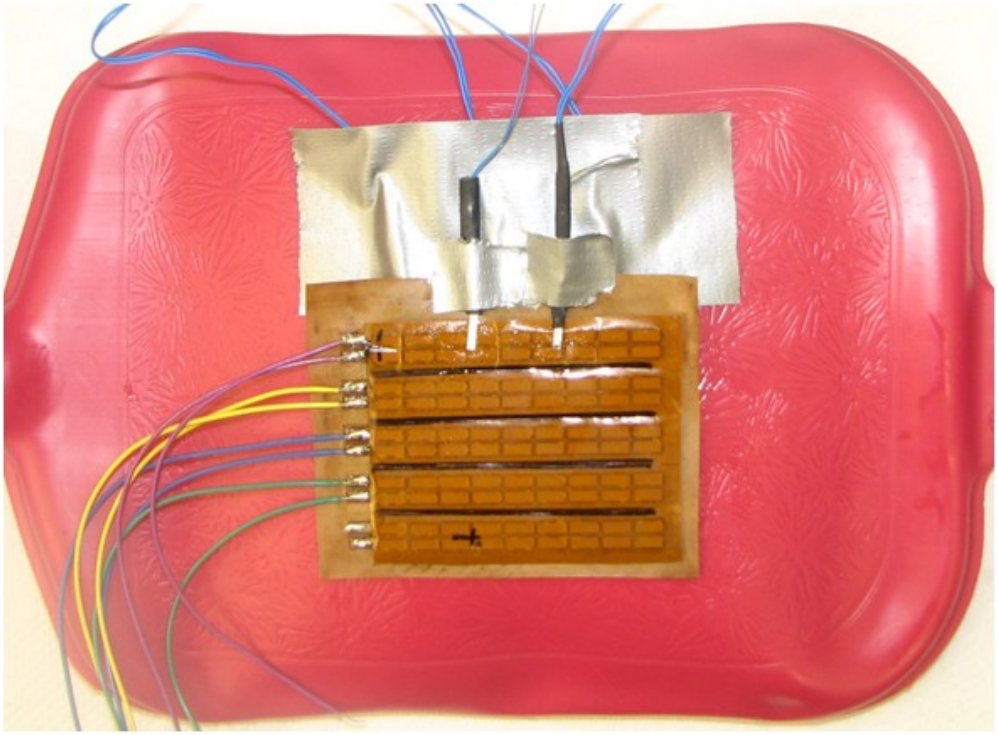

Figure 79: TE device with sensors on both its underside and topside

The cooling for the top side of the TE device was provided by a 0.562 L (19 oz) Bard disposable urine bag. This product was used because in future testing it will act as a flexible fluid reservoir that will allow cooling fluid to flow through it. The initial temperature of the bag ranged from 21 to 19 °C (70 to 67 °F). Water in the cooling bag was also replaced when switching to test a new TEC channel.

The cooling bag was positioned, with its center line as close to the center line of the channel being tested, on top of this assembly while holding the top side temperatures in place by their wire ends (Figure 80).

Figure 80: Complete TE device testing arrangement

A power source (Electro Industries Model DIGI 185) was used to supply the TE device with the desired current. Prior to connecting the power source to the device the amperage value was adjusted while connected to a 1Ω resistor which could handle 50 *W*

of power. The positive and negative leads from the power supply were connected to the p-type and n-type thermoelement trace segments respectively, and a paper towel was placed over the TE device's exposed solder joints. Temperature data for each of the four operational TE device channels were collected with amperage inputs ranging from 0.5 to 2.5 *A* in 0.5 *A* increments, with the duration of each data set being 2 minutes. During testing slight hand pressure was applied on top of the assembly to maintain good thermal contact between the system components.

Performance Data

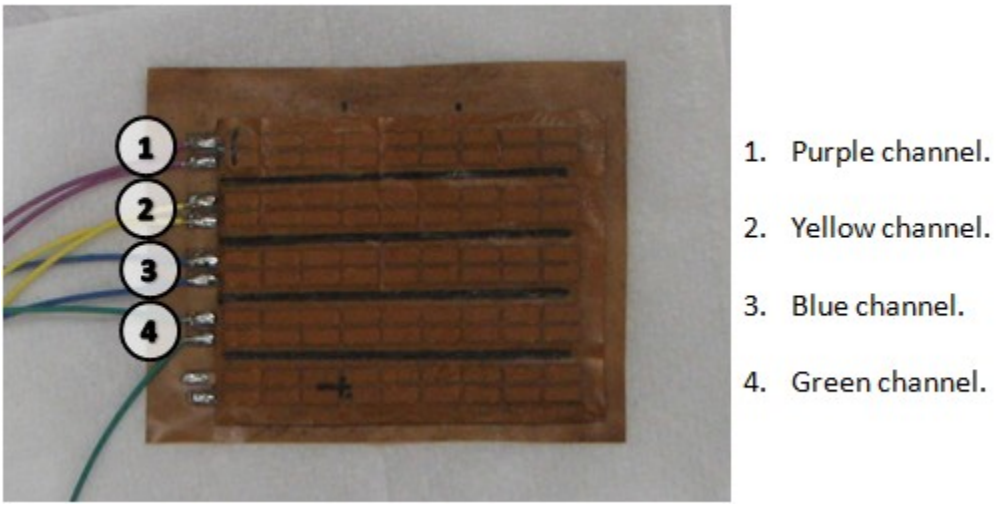

Figure 81: Description of channel notation on the TE device

Analysis of a Single Sensor across a Range of Amperages

The analysis of a single sensor across a range of amperages provides an idea of the trend in the device's performance. Figure 82 shows that the fastest rate of temperature change achieved within the tested parameters occurred at 2.5 *A*. Due to the decreases in the magnitude of temperature change as 2.5 *A* is approached I believe this amperage is very near this channel's peak performance. From previous experience with TE devices this temperature profile and associated trends are to be expected. It is also

expected that the center location would have the largest magnitude of temperature change due to the cumulative cooling from the other thermoelements.

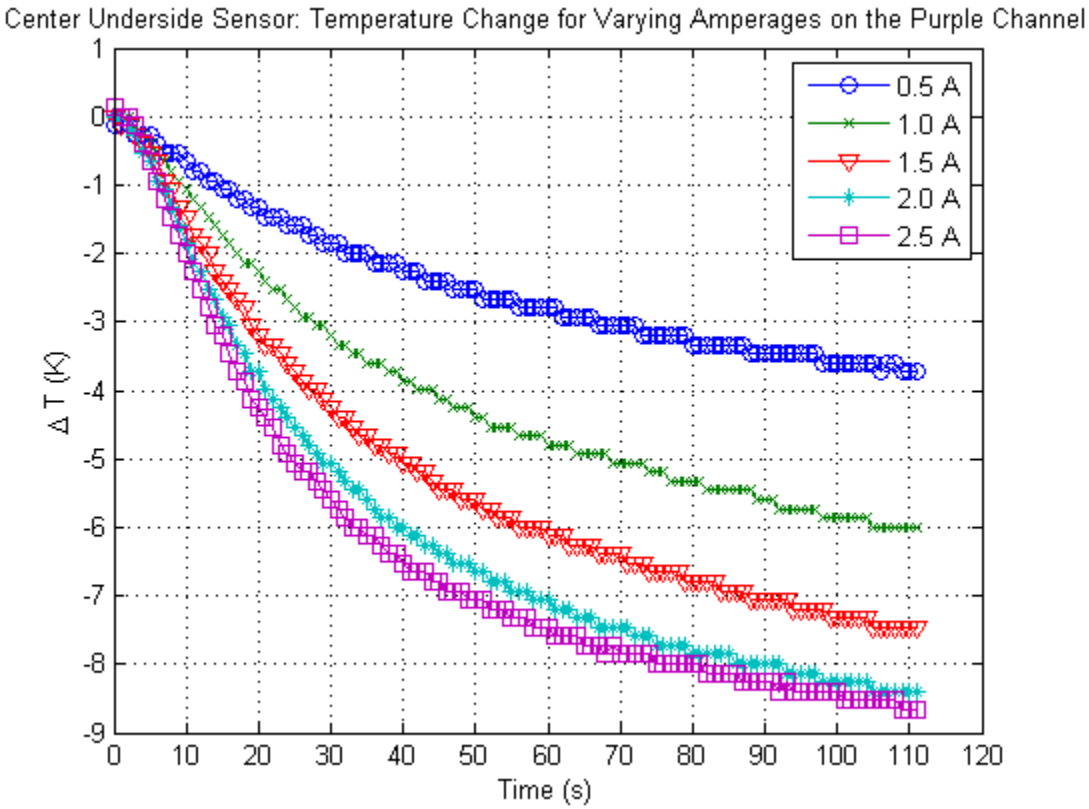

Figure 82: Center underside sensor's measurement of temperature change when varying amperage on the purple channel

Analysis of a Single Sensor across a Range of Channels

Comparing the temperature change between the device's channels at a common location provides an indication of the system's mean performance in that area. This mean is representative of device and environment conditions. Figure 83 shows a large disparity between the blue and green channel's capabilities. Moreover, the blue channel almost begins to increase in temperature and it has reached its maximum change in temperature faster than any of the other channels. Similarly the yellow channel has the fastest average cold side time constant, however, it has the smallest temperature change of all four channels.

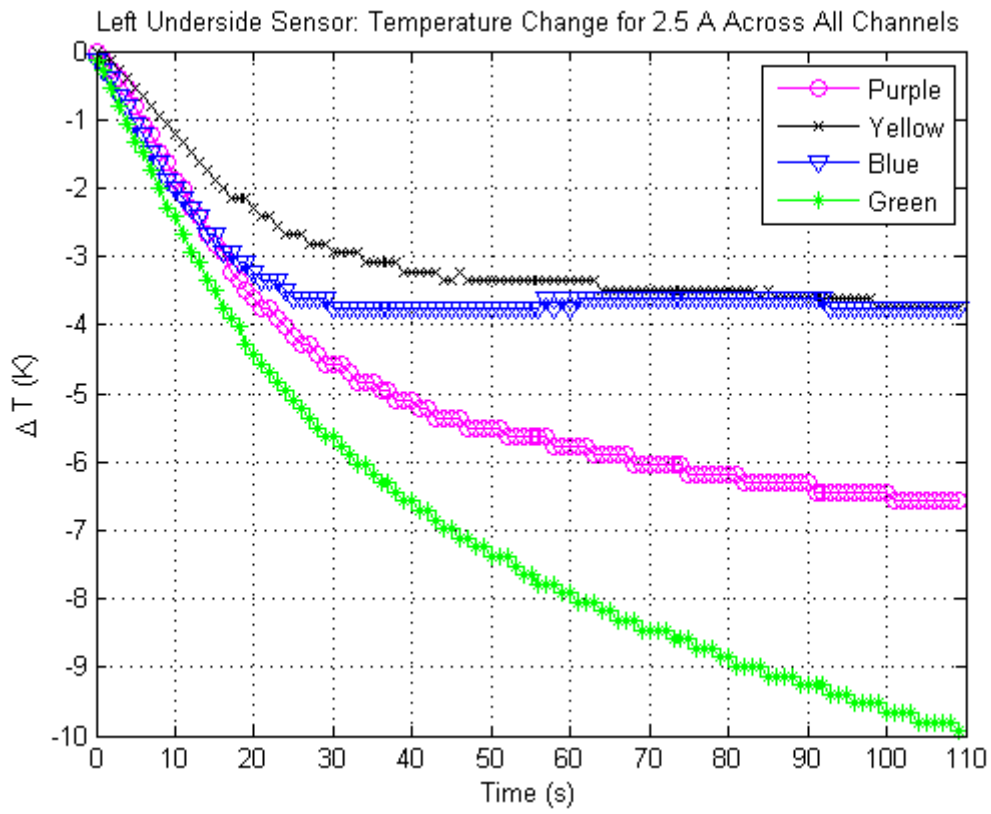

Figure 83: Left underside sensor's measurement of temperature change at different channels for 2.5 A

Analysis of a Single Channel at a Constant Amperage

Reviewing the temperature data from multiple locations on a single channel provides insight on the system as a whole. Figure 84 shows the temperature readings at five different locations on the TE device. According to the data depicted in the graph there is a significant temperature gradient occurring on the left hand side of the device. Also the center underside temperature initially cools down at the same rate as the left side of the device. However after 20 seconds it begins rising in temperature. It was found that all but the purple channel would cool at the center and then increase in temperature, sometimes almost reaching their initial temperature. Reasons for this behavior are not understood. It is strongly believed to be the result of an assembly defect such as shorting of elements due to excess solder as noted above.

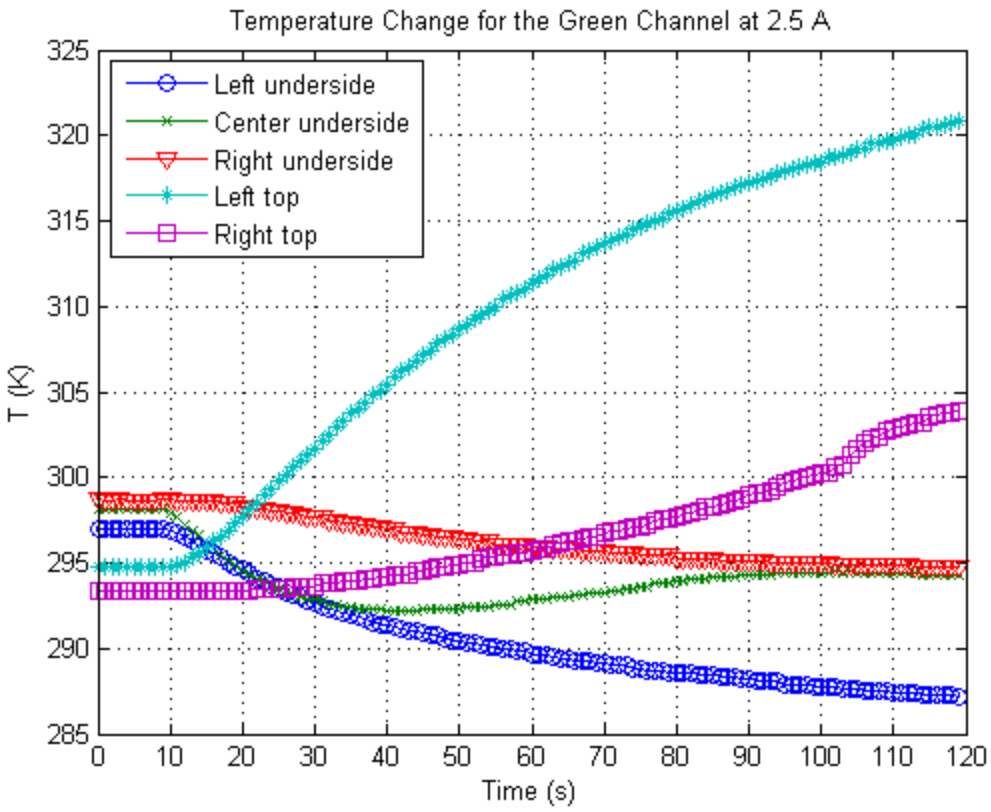

Figure 84: Temperature changes at different locations of the green channel at 2.5 A

Calculated Time Constants

The temperature change time constant for each channel's performance, specific to each supply amperage, was calculated for each sensor's location. This involved calculating the difference between the initial (T_i) and final temperatures (T_f) for the data set of interest. For the unique instance where the center of the device's underside began to warm, T_f was taken as the lowest temperature value prior to the heating phenomenon. The time at which 63% of this temperature difference occurred, according to Equation 40, was located. This time value represents the time constant (τ) for that data set.

$$T(t) = T_f + (T_i - T_f) \cdot e^{-1} \qquad \text{Equation 40}$$

The average of each channel's time constants across all amperage ranges and locations were calculated (Table 14). This shows the trend that as amperage is increased the final temperature values on the underside are approached much faster. Alternatively, the increasing topside time constant value indicates that their terminal temperature values were not reached within the data set.

Table 14: Averaged area and amperage specific time constants

	Area and Amperage Specific Time Constant Values (s)				
	Underside Left	Underside Center	Underside Right	Topside Left	Topside Right
0.5 A	48	44	65	50	64
1.0 A	46	35	63	57	69
1.5 A	44	30	59	59	74
2.0 A	39	28	57	62	79
2.5 A	34	26	51	62	82

Comparison with the 1-D Model

The following subsections compare the experimental results with the initial 1-D model and an updated 1-D model which better reflects the device's final design

Results Comparison with the Initial 1-D Model

The 1-D model in its early state estimates the temperature change rather poorly when compared to the temperature values gathered experimentally from the center of the purple channel's underside. This can be seen graphically in Figure 85, and between numerical comparisons that can be made with Table 15, where a maximum difference in temperature values is 26.2 K.

Table 15: Numerical comparison between predicted temperatures from the 1-D model and the experimental values obtained from the underside center of the purple channel

Amperage	Predicted Temperature Value (K)	Experimentally Measured Value (K)	Difference in Temperature (K)
0.5	286.3	296.6	10.2
1.0	279.9	294.3	14.4

Table 15 (Continued)

1.5	274.3	292.8	18.5
2.0	269.7	292.2	22.5
2.5	265.8	292.0	26.2

Results Comparison with a 1-D Model Reflecting Final Design

The 1-D model comparison in the previous subsection (Results Comparison with the Initial 1-D Model) still presumes a K_h composed of an extra layer of copper and solder. If this were updated to the solder, copper, and polyimide layers that better reflect the hot side's conductance then K_h changes from 8990 to 2338 *W/(m^2 K)*. Table 16 shows the updated numerical differences between estimated and experimental results, and Figure 85 makes this graphical comparison with the inclusion of experimental results. The updated model's maximum difference from the experimental value is half of the previous model's difference (12.9 vs 26.2 K). The peak magnitudes of interest (fluxes and temperatures) for the new model are explained in Table 17. Figure 86 compares the cooling flux profiles of the initial and updated 1-D models. From Figure 85 and Figure 86 it can be seen that the temperature profile of the updated 1-D model follows a similar trend to the experimental results. The predicted temperature change varies by more than a factor of two. This remaining difference is likely due to a combination of thermal shorts resulting from, manufacturing errors and incorrect parameter inputs for the 1-D model.

Table 16: Numerical comparison between estimated temperatures from the updated 1-D model and the experimental values obtained from the underside center of the purple channel

Amperage	**Estimated Temperature Value (K)**	**Experimentally Measured Value (K)**	**Difference in Temperature (K)**
0.5	290.3	296.6	6.25
1.0	286.1	294.3	8.17
1.5	282.9	292.8	9.92
2.0	280.6	292.2	11.6
2.5	279.2	292.0	12.9

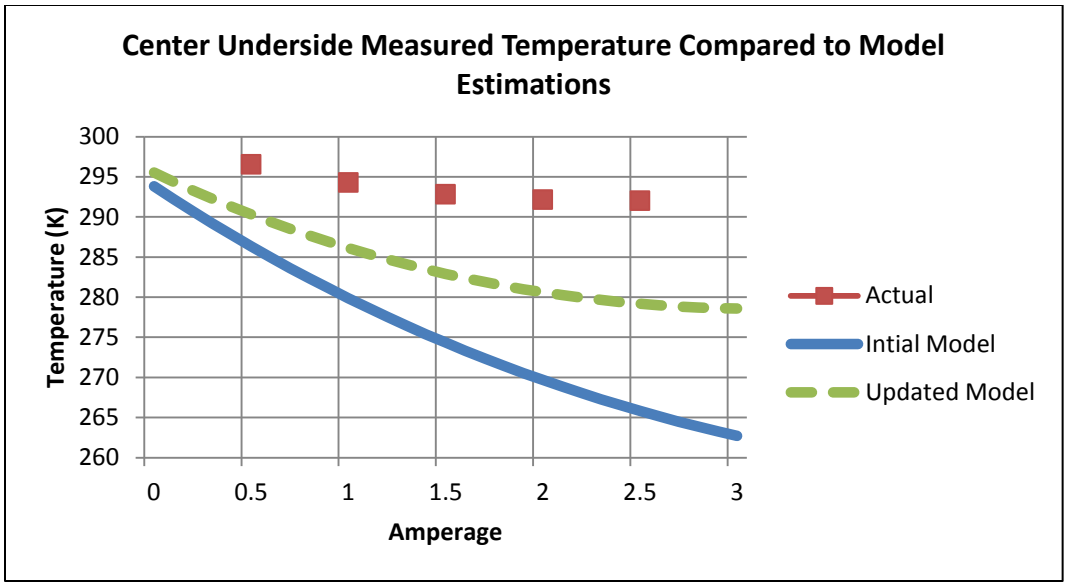

Figure 85: Comparison between actual results, initial theoretical 1-D estimates, and estimates from the updated 1-D model

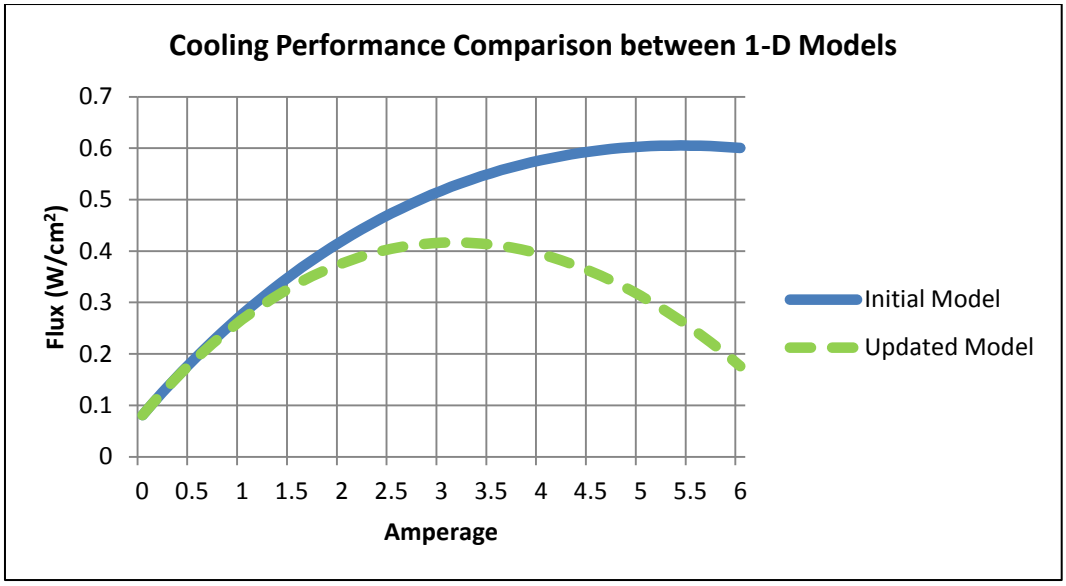

Figure 86: Cooling flux comparison between the initial 1-D model and the updated 1-D model which better reflects the final design's materials and dimensions

Table 17: Updated 1-D model's peak magnitudes

Parameter	Value
Cooling flux, Q_c	0.417 $\frac{W}{cm^2}$
Cold side temperature, T_c	278.5 K
Hot side conductance, K_h	2338 $\frac{W}{m^2 K}$
Cold side conductance, K_c	1320 $\frac{W}{m^2 K}$

Calculated Seebeck Coefficient

Approximating the device's equivalent Seebeck coefficient will provide insight on the magnitude of the device's thermoelectric inefficiency. In order to calculate this value for each channel hot and cold reservoirs were placed underneath and on top of the device, respectively. Their initial surface temperatures were 40 °F and 91 °F (4 and 33 °C). The device was left alone to reach equilibrium between the surfaces and the reservoirs over the span of 20 minutes. The reservoir surface temperatures and channel voltages were measured. By this time the heating and cooling reservoirs had reached 87 °F and 46 °F (31 and 8 °C). It was assumed that the device's surfaces were at the same temperatures as well. These voltages (Table 18) along with the difference in temperatures between the surfaces were used in combination with Equation 41 to calculate an effective module Seebeck coefficient, where n represents the number of thermoelements in a channel (36). In addition to this effective Seebeck coefficient Table 18 also displays estimated material Seebeck coefficients. This was completed using the updated 1-D model with zero current to approximate the temperature across the thermoelectric element itself without including the effects of the petroleum jelly or thermal contact resistance (Table 19). This provides a lower bound on the effective material Seebeck coefficient.

$$\alpha = \frac{V}{n(T_2 - T_1)} \qquad \text{Equation 41}$$

Table 18: Voltages of each channel when the outermost hot and cold side device surfaces are at 31 and 8 °C

Channel	Voltage (V)	Eff Module Seebeck Coeff. (μV/K)	Estimated Material Seebeck Coeff (μV/K)
Purple	0.047	57	137
Yellow	0.049	59	143

Table 18 (Continued)

Blue	0.047	57	137
Green	0.050	60	146

The experimentally calculated module values are approximately 25% of ideal value (240 $\mu V/K$). This shows that there is substantial thermal resistance in the device seeing how these were calculated from temperatures measured at the device's surfaces and not at the top and bottom of the thermoelement. Performance would be improved substantially by increasing the hot and cold side thermal conductances.

Meanwhile, the 1-D model temperature estimates predict the effective Seebeck coefficient to be at least 59% of their optimal value. This serves as a lower bound estimate for the device and suggests that the performance could have been degraded by the assembly process. This could be due to solder contacting the edges of the elements. That would permit atoms from the solder to diffuse into the elements and decrease their Seebeck coefficients. This could have also been caused by shorts between adjacent copper pads due to spreading of the solder paste during solder reflow. Device performance (time constant, max temperature range) will be improved dramatically when these issues are resolved.

Table 19: Updated 1-D model temperature inputs and corresponding zero amperage thermoelement surface temperatures

Model Parameter	**Value (K)**
Model input: T_a	281
Model input: T_s	305
Model output: T_1	289.6
Model output: T_2	299.1

Testing Procedure Errors

There were multiple sources of testing errors to be considered. The first source of error is from the temperature sensors. The differences between calibrated and reference temperatures were used to estimate the errors in the temperature

measurements (Table 20). This was completed by placing the temperature sensors in mutual contact with the same area (in between my index finger and thumb) as a Type K thermocouple. These differences represent an inaccuracy in measuring the device's temperatures and they are on the same scale as the temperature changes that are produced on the underside of the device. This could explain the asymmetries between the underside's left and right temperature readings (sensors 0 and 2), and the topside's left and right temperature readings as well (sensors 4 and 5).

Table 20: Difference between temperature sensor's value and the temperature obtained by the temperature probe used for calibration

Sensor	RTD Temperature (°F)	Type K T/C (°F)	Difference (°F)
0	89.0	95.5	6.5
1	90.7	93.5	2.8
2	88.8	93.4	4.6
4	90.2	95.7	5.5
5	88.9	95.3	6.4

In an effort to understand the time response of the temperature measurement system each sensor was placed in between my thumb and index finger and the resulting temperature readings taken over time were recorded (Figure 87). The sensors take approximately 30 seconds in order to reach a value within adequate range of the measured surface. This empirical result falls between the manufacturers specified response time for measuring water flowing at 0.4 *m/s* and measuring air flowing at 1 *m/s*. [34] This means a significant difference between the actual and measured interface temperature's change over time may be occurring because the sensor's delay is close to that of the device's time constant. The differences between actual and measured temperature, and the system's time response signifies the present system's inability to accurately quantify the device's temperature profile.

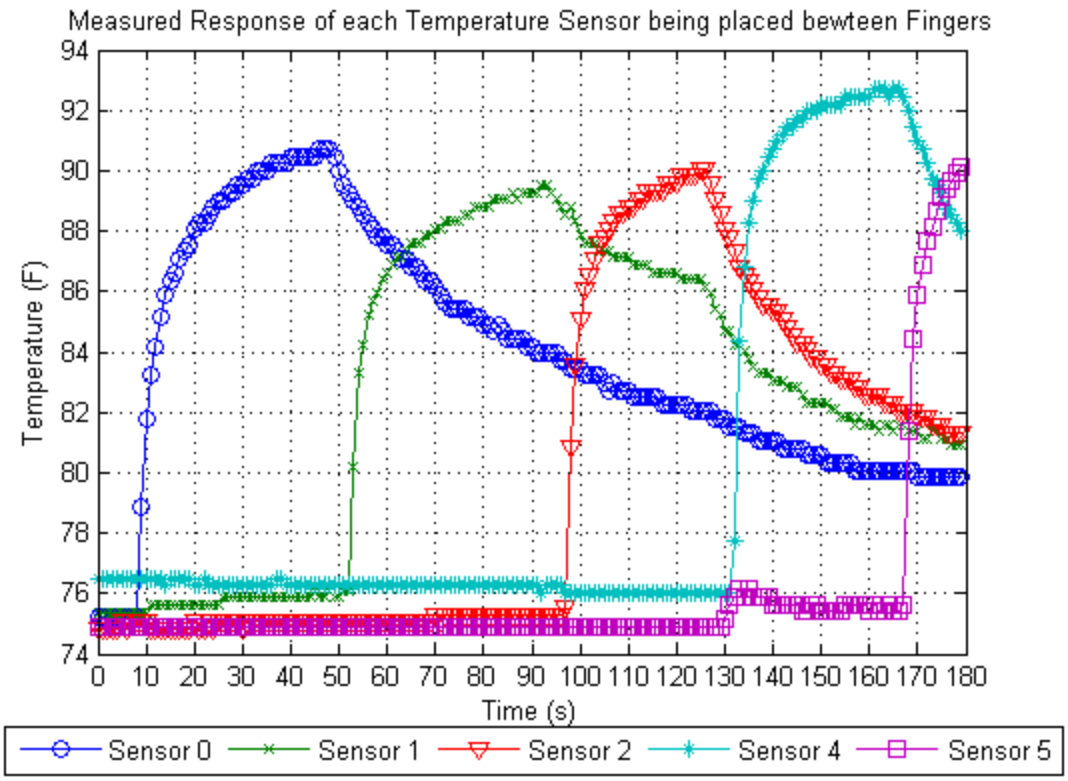

Figure 87: Measured response of each temperature sensor being placed in between my thumb and index fingers.

Another potential source of error is poor contact between the TE device, the RTD, and the cold/hot source. Due to the RTD shape, an angle developed between the bottom of the TE device and the reservoir surface it was intended to be in contact with. The cause of this contact angle were the temperature sensors (Figure 88).

The third source of primary errors was the procedure I administered. By placing my hand on the top fluid reservoir in an attempt to improve thermal contact I may have introduced a lower thermal contact on the bottom side. This would occur because the force exerted by my hand on top of the device could cause a concave deflection on the top surface of the bottom reservoir. This concavity could reduce the mating between the surface and the bottom of the device.

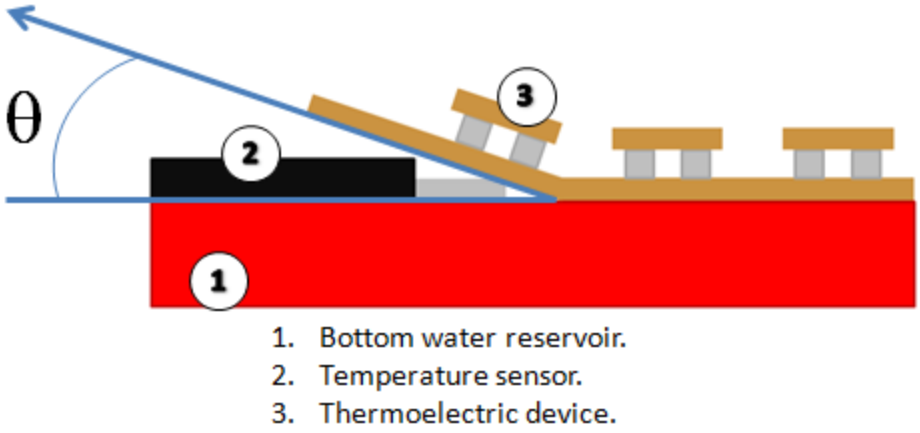

Figure 88: Development of a contact angle between the TE device and the bottom reservoir

Alternative Arrangement for Bottom Temperature Sensors

The bottom center temperature sensor recorded strange temperature behavior when current values 2.0 *A* or greater were supplied (did not occur on the purple wire channel). To see if this problem was due to a faulty temperature sensor the locations of sensors 1 and 2 were switched. With this switch also came a change to the manner in which bottom sensors retained their positioning. A piece of spare flexible tube was taken and cut at 25 mm spacing intervals. The sensor wires were placed in each of these fissures and a thin metal rod was placed through the inside diameter of the tube (Figure 89). This rigidly separated the sensors, allowed for easier repositioning, and circumvented the use of adhesives. The sensor positioned in the middle of the device continued to measure high temperatures as it did before. Therefore, the phenomenon was not due to a faulty sensor.

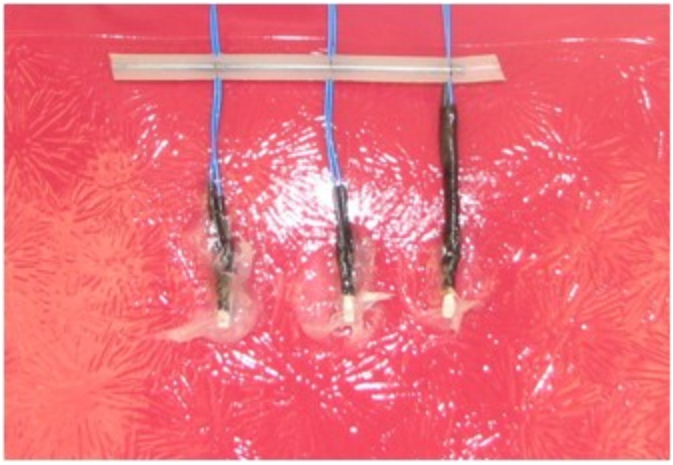

Figure 89: Sensor mounting alternative to tape

Adequacy of Performance

While the device may only create a 2 °C degree interface temperature change in 10 seconds that is still enough for a cold sensation to be recognized (Figure 84). According to *The Fundamentals of Sensory Physiology*, a change of -0.2 °C or more from an adapted temperature of 31 to 27 °C will be recognized as the perception of something becoming colder. [35] While this requirement has been met, testing has yet to prove if the device can create an interface temperature as low as 16 °C yet. Assuming an initial and final interface temperature of 27 and 16 °C, to meet the 8 °C temperature drop in 10 seconds would require an 8 second time response. Currently the fastest cooling responses measured are at the center of the device's underside ($\tau \cong 20$ seconds), but an 8 °C temperature decrease is not achieved and heating shortly begins at that surface after the lowest temperature is reached. Further testing is necessary to fully understand the scope of the device's performance. With improved manufacturing methods, the device performance should improve significantly.

CHAPTER SIX: CONCLUSIONS AND FUTURE WORK

This chapter addresses the performance of the test device relative to the project goals and identifies areas for future work.

Design Conclusions

The seed that gave rise to the results of this research was sown during the design stage. A one dimensional model was utilized to estimate the performance of different device configurations. The surface energy balance from the forearm model allowed for quantifying the adequacy of the proposed design. An understanding of the device's parameters and requirements confined and guided the decision making process. Understanding how the components were going to be attached and keeping the next step in mind allowed for the device's development to be fluid and adaptive.

The device has met the reparability requirement. When the wires were first being soldered to the full scale assembly's power connections the soldering iron accidentally unsoldered a thermoelement. However, localized repair was conducted without damaging the surrounding elements. Occupying a 3 x 4 inch overlay area the overall device is also within a scale that is comparable to its 2 x 3 inch requirement. The overlay area is capable of being trimmed down, however, this size was chosen to help distance body hair and skin from electrically conductive surfaces.

A cost oriented approach toward minimizing alignment was used to reduce sacrificial material. Lastly an assembly stage was made to establish a datum that would facilitate the process' repeatability and ease of handling assembly.

Sources of Design Error

The performance of the one dimensional model was a function of the thermoelectric property data. The lack of material property data (ideally batch specific) from the manufacturer led to assuming the material matched published values for bismuth telluride. The errors in these assumptions can have a compounding effect, especially when the thermal pathway has more than 10 layers (based upon conductivity and contact resistance).

Likewise, the forearm model provided a lower bound estimate for the skin's heat flux since it estimated the outbound heat flux based upon convection, conduction, evaporation and radiation but neglected conduction. Moreover, it used charted data that may not be representative of the population this device might interact with.

Future Work for the Design

A possible solution would be to increase the TE model's complexity to two dimensions. This will require more familiarity with the subject matter, potentially longer time spent in the design process, and more terms and assumptions (e.g. initial and boundary conditions, material, etc.) to be accounted for. These same additions however are what decrease the model's sensitivity when compared to the single dimension alternative.

Manufacturing Conclusions

The overall process was successful in assembling a functional TE device. However, there were significant defects that must be addressed in order to achieve a reliable process. Chief among these is the low effective Seebeck coefficient of the assembled module. This is likely due to excess solder either shorting between elements or coating elements and degrading their performance. This needs to be addressed by

improving the solder application process. Additionally, there was one of the five channels that had an open circuit rendering it entirely nonfunctional.

There are also opportunities to improve the circuit board patterning process. The dimensional variation from the various manufacturing processes was not analyzed rigorously, but attempts were made at quantifying dimensional tolerances. The maximum observed trace width deviation was approximately 0.002 inch (0.05 mm). Moreover, the trace widths were all larger than the intended 2 mm. They were 2.4 mm (0.096 inches) or wider (Figure 90).

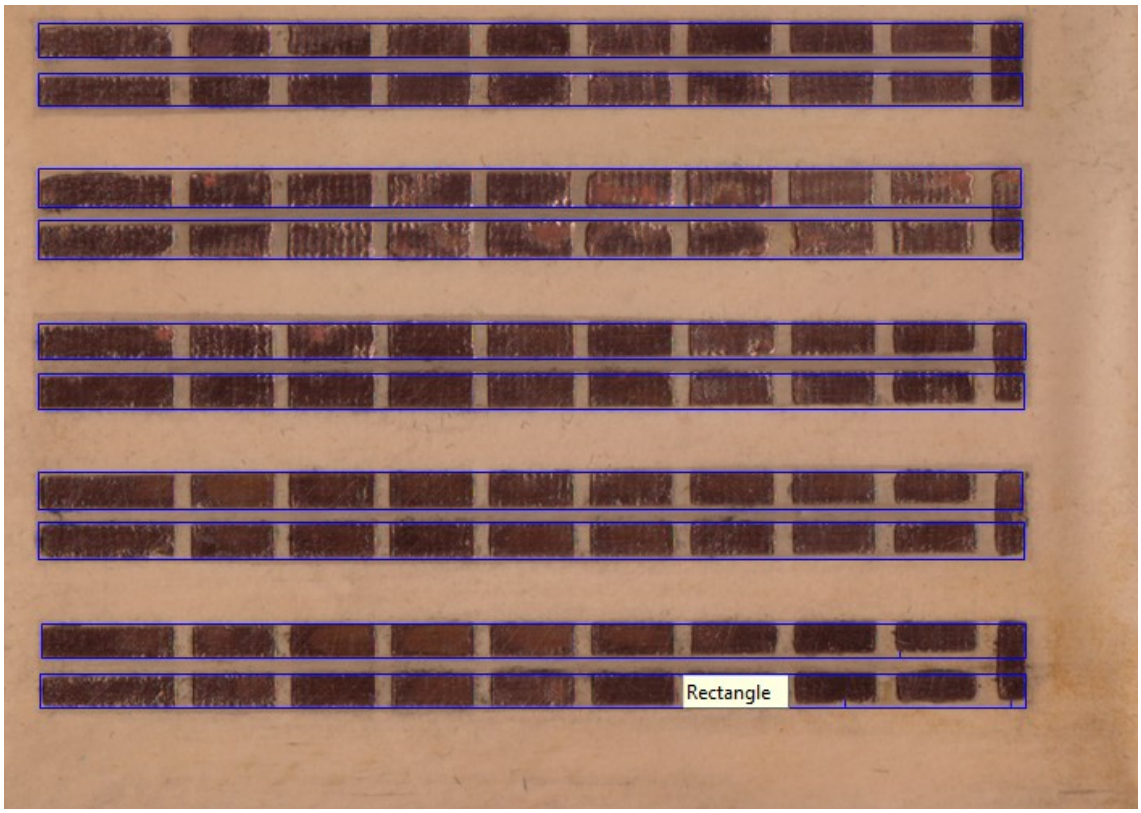

Figure 90: Graphical datum analysis used for determining maximum and minimum differences from a specific trace segment within the channel

Sources of Manufacturing Error

There was also an absence of models for the etching and ironing processes. As a result these were developed by meaningful (an understanding of the contributing

factors towards the process) trial and error attempts. Their effects of these errors were immediately apparent but circumventing their causes took time.

Solder stencil apertures must be adjusted. In an effort to prevent aligning the thermoelement to a space partially or entirely void of solder paste I chose to oversize the aperture dimension. This proved to be just as hazardous because the present heating effect which occurs when currents higher than 1.5 *A* are supplied to the yellow, blue, and green channels is believed to be a result of excessive solder and or flux. The apertures of the full scale solder stencil were not machined as well as the trials scale's were. Even with the work board sanded flat, the mill head leveled, the transparency pulled flush against the work board, and the work board over restrained there were still instances of inconsistent depth cut into the work piece. Figure 91 shows the differences between the full scale assembly's solder stencil and the trial assembly's. The relatively heavy shadows behind the holes of the full scale assembly's solder stencil indicates protrusions on the posterior side of the stencil. These irregularities prevented flush mating between the stencil and the circuit board, diminishing its ability to contain the solder. Furthermore, it is believed that the rough surfaces at the aperture periphery caused unintentional solder retention to the stencil while it was being removed. This would lead to something of a suspended surface wave at the solder pad's surface rather than a flat plateau (Figure 92).

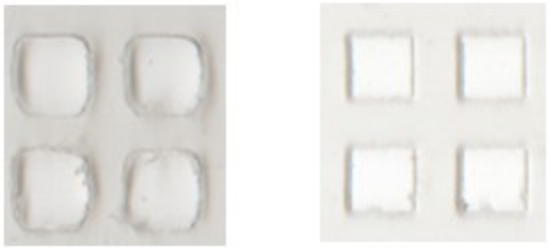

Figure 91: Comparison between the apertures of the full scale assembly's solder stencil (left) and the trial assembly's (right)

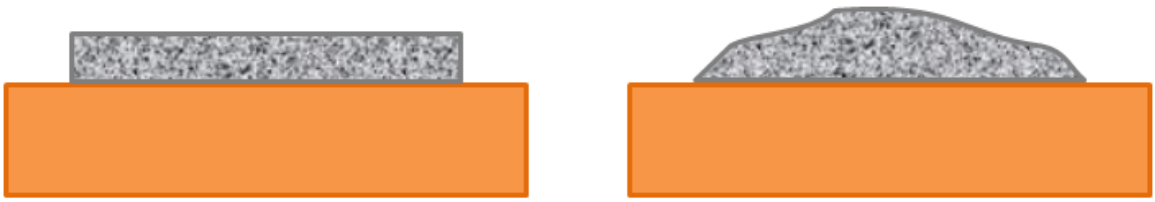

Figure 92: Intended solder pad profile (left) and an example of the hypothesized solder pad profile (right) produced by the full scale assembly's solder stencil

Future Work for the Manufacturing Process

It is strongly recommended that an understanding of scientific formulas that allow for the prediction of outcomes from the ironing and etching process be understood. With respect to the full scale assembly, the etching process takes the most time to complete. An understanding of the reaction rates would allow for work load scheduling during the etching process instead of a guess and check approach which does not provide schedule consistency.

A reduction in aperture size would decrease the likelihood of solder paste related inefficiencies: solder diffusion into the thermoelement, alternate thermal pathways through the thermoelement, and electrical shorting between copper trace segments. A 1.5 mm square aperture size is recommended for future projects with the 1.397 x 1.397 x 1.696 mm thermoelement. This would provide a small tolerance for thermoelement misalignment with the solder pad. Unlike the 1 mm square solder pad which either has the thermoelement positioned correctly on top of it or is misaligned. Along with this should come a minimum standard of machined aperture quality.

Assembly Conclusion

The assembled device allows temperature variance between 4 independent locations. The fifth channel is inoperable only because of one thermoelement's intermittent electrical connection. The device can also be worn and provides enough flexibility to be draped over an adult's finger (approximately 0.5 inch bending diameter).

Sources of Assembly Error

The circuit boards were not taut when they were placed on top of the staging area. This ability to gather small cumulative deflections could have been a cause of unfavorable alignment. Also the lack of an appropriate model for the oven may have led to diminished device performance due to excessively spreading of the solder during the reflow process.

Future Work for the Assembly Process

To improve the precision of solder and thermoelement placement a solder stencil with smaller apertures and corresponding thermoelement alignment templates are recommended for future builds.

Performance Conclusions

Sources of Performance Error

The dominant source of performance error is in the reduced properties of the TE elements. This degradation is believed to be due to some combination of solder diffusion into the TE elements and shorting between copper pads. Both problems are likely related to excessive solder paste deposition. The effect of this degradation was quantified by establishing a range of Seebeck coefficient estimates, $137 \leq \alpha \leq 240 \mu V$ (Calculated Seebeck Coefficient).

A flaw was also observed in the previous method of affixing the bottom temperature sensors; as testing progressed from one channel to the next the device was moved upward in the direction of the temperature sensors. The sensors acted as a pivoting point, introducing a ramping effect that produced an angle of separation between the bottom of the device and the surface of the water bottle. Moreover, the placement of my hand's weight on the top of the device may have contributed to concavities between the temperature sensors and their respective surfaces.

The temperature of the reservoirs should also be better controlled. This would allow for an appropriate comparison between the channels and their respective performance rather than just proving a trend. It would also presumably permit longer testing durations, and higher amperages.

Conclusion

All of the suggested corrections for the sources of error were researched to varying depths. However, the project needed to meet a deadline and this limited further investigation.

Despite the heat that develops in the middle of the device at amperages above 1.5 *A,* the device still provides cooling along the bottom surface until that point is reached. Moreover, the temperature change, albeit small is still within the threshold of Schmidt's criteria for sensible temperature change. For this reason and those explained in Table 21, I believe the research conducted in this project and the resulting design produced meets the requirements to consider this a successful design, manufacturing, and assembly project. With some minor process changes, the next iteration in the process could substantially improve the device performance. If the effective Seebeck coefficient of the device is raised to even 2/3 of theoretical, then the device should exceed the design requirements.

The biggest limit to the device performance is the large entry and exit thermal conductances resulting from the use of a polymer layer. Further improvement could be achieved by increasing the thermal conductances of these layers.

Table 21: Result comparison between the project requirements and those achieved

Requirement	Achieved result
Independently vary temperature at 5 locations.	Independently vary temperature at 4 locations.
Capable of a 2 inch bending diameter.	Capable of an approximate 0.75 inch bending diameter (without temperature sensors attached).

Table 21 (Continued)

Wearer is isolated from hazardous components.	Condition satisfied.
Device dimensions of approximately 2 x 3 inches.	Device dimensions of 3 x 4 inches.
Supplies a heat flux greater than 8.2 mW/cm^2.	Supplies a heat flux less than 417 W/cm^2.
Interface temperature range between 60 and 90 °F.	Maximum interface temperature drop of 18 °F.
Allow temperature sensor attachment.	Space allotted for temperature sensor attachment.
Constructed by standardized manufacturing processes.	Condition satisfied.
Minimal allowable temperature of 56 °F.	Device temperature can be regulated to temperatures above 56 °F.
Not all causes of device failure should be terminal.	Condition satisfied.
Completed by the summer of 2013.	Condition satisfied.

REFERENCES

[1] Craig A. D., 2002, “How do you feel? Interoception: the sense of the physiological condition of the body,” Nat Rev Neurosci, 3(8), pp. 655–666.

[2] Barrett K. E., and Ganong W. F., 2010, "Ganong’s Review of Medical Physiology," McGraw-Hill Medical, New York, NY. pp. 174.

[3] McClure M., 2012, “Stanford researchers’ cooling glove ‘better than steroids’” [Online]. Available: http://news.stanford.edu/news/2012/august/cooling-glove-research-082912.html. [Accessed: 25-Sep-2012].

[4] Hartemann A., Attal N., Bouhassira D., Dumont I., Gin H., Jeanne S., Said G., and Richard J.-L., 2011, “Painful diabetic neuropathy: Diagnosis and management," Diabetes Metab., 37(5), pp. 377–388.

[5] McKnight P. T., 2010, "Finite element analysis of thermoelectric systems with applications in self assembly and haptics," M.S. thesis, Mechanical Engineering, University of South Florida, Tampa, FL.

[6] Bell L. E., 2004, “Flexible Thermoelectric Circuit,” U.S. Patent 6700052 B2.

[7] Huang I.-Y., Lin J.-C., She K.-D., Li M.-C., Chen J.-H., and Kuo J.-S., 2008, “Development of low-cost micro-thermoelectric coolers utilizing MEMS technology," Sensors Actuators Phys., 148(1), pp. 176–185.

[8] Goldsmid H. J., 2010, "Introduction to thermoelectricity," Springer, Heidelberg; New York. pp. 1-4, 43, 81, 145, 150.

[9] Francioso L., De Pascali C., Farella I., Martucci C., Cretì P., Siciliano P., and Perrone A., 2011, “Flexible thermoelectric generator for ambient assisted living wearable biometric sensors,” J. Power Sources, 196(6), pp. 3239–3243.

[10] Rowe D. M.,2006, "Thermoelectrics handbook: macro to nano," CRC/Taylor & Francis, Boca Raton, FL. pp. 1-3, 1-9, 37-5-7, 9-14.

[11] Ioffe, Abram, 1957, "Semiconductor Thermoelements and Thermoelectric Cooling," Infosearch Ltd., London, England, pp. 44, 85.

[12] Incropera F. P., Dewitt D. P., Bergman T. L., and Lavine A. S., 2007, "Introduction to heat transfer," Wiley, Hoboken, NJ. pp. 61, 102, 103, 126, 840, 843, 850, 851.

[13] Miner A., 2007, “The Compatibility of Thin Films and Nanostructures in Thermoelectric Cooling Systems,” J. Heat Transf., 129(7), p. 805.

[14] Fiala D., Lomas K. J., and Stohrer M., “A computer model of human thermoregulation for a wide range of environmental conditions: the passive system,” J. Appl. Physiol. [Online]. Available: http://jap.physiology.org/content/87/5/1957. [Accessed: 20-Jul-2012].

[15] Coombs C. F. 2008, "Printed circuits handbook," McGraw-Hill, New York, New York. pp 40.4-40.29.

[16] DuPont, “DuPont Pyralux FR Copper-Clad Laminates” [Online]. Available: http://www2.dupont.com/Pyralux/en_US/assets/downloads/pdf/FRclad_H-73233.pdf. [Accessed 14-May-2013].

[17] All Flex Flexible Circuits, LLC, “All Flex Design Guide Revised Master Fall 2011.pdf,” Flex Flex. Circuits Heaters [Online]. Available: http://www.allflexinc.com/PDF/All%20Flex%20Design%20Guide%20rev%20Master%20Fall%202011.pdf. [Accessed: 22-Feb-2013]. pp 13, 20.

[18] DuPont, "Summary of properties for Kapton polyimide films," [Online]. Available: http://www2.dupont.com/Kapton/en_US/assets/downloads/pdf/summaryofprop.pdf. [Accessed 14-May-2013].

[19] Callister W. D., 2007, Materials science and engineering: an introduction, John Wiley & Sons, New York, NY. pp. A18, A23, A26, A31-33.

[20] 3M, “3M Scotch-Weld," [Online]. Available: http://multimedia.3m.com/mws/mediawebserver?66666UF6EVsSyXTtnxfcLx46EVtQEVs6EVs6EVs6E666666--. [Accessed 14-May-2013].

[21] Engineering Toolbox [Online], “Amps and Wire Gauge - 12V Circuit,” [Online]. Available: http://www.engineeringtoolbox.com/amps-wire-gauge-d_730.html. [Accessed: 22-Feb-2013].

[22] Loctite, “Product RA10 (Multicore solder cream),” [Online]. Available: http://www.farnell.com/datasheets/314582.pdf. [Accessed 15-May-2013].

[23] “SN62RA10BAS86-25G CARTRIDGE - MULTICORE (SOLDER) - SOLDER PASTE, 62/36/2 SN/PB/AG | Newark,” [Online]. Available: http://www.newark.com/multicore-solder/sn62ra10bas86-25g-cartridge/solder-paste-62-36-2-sn-pb-ag-179/dp/18K6979?in_merch=Popular%20Soldering%20Stations%20And%20Accessories. [Accessed: 15-May-2013].

[24] Covey S. R., 2004, "The 7 habits of highly effective people: restoring the character ethic," Free Press, New York, NY. pp 95.

[25] Boothroyd G., 2005, "Assembly automation and product design," Taylor & Francis, Boca Raton, FL. pp 220.

[26] Swift K. G., 2013, "Manufacturing process selection handbook," Elsevier, Oxford.

[27] “ANSI External Screw Threads Size & Tolerances Chart - Engineers Edge” [Online]. Available: http://www.engineersedge.com/screw_threads_chart.htm. [Accessed: 18-May-2013].

[28] Avery W. F., Baskin P. A., "Soldering aluminum," [Online]. Available: http://www.superiorflux.com/papers/Soldering_Aluminum_Brazing_Soldering.pdf, Cleveland, OH. [Accessed 22-May-2013].

[29] Saughnessy L., “Let’s Etch Some Brass! - YouTube,” [Online]. Available: http://www.youtube.com/watch?v=m69aHYMw_yY. [Accessed: 30-May-2013].

[30] Lawton N., “Brass Etching for Beginners,” Etch. Begineers [Online]. Available: http://www.nigellawton009.com/Etching_for_Beginners_Version_5.htm. [Accessed: 30-May-2013].

[31] Gotang, “Etching brass plates,” Etchign Brass Plates [Online]. Available: http://www.instructables.com/id/Etching-brass-plates/. [Accessed: 30-May-2013].

[32] Virginia V., 2010, "DIY: Acid Etching on Brass & Copper Metal for Jewelry Making - Part II & Part III,” Mystique Artisan Jewelry, Tucson, Arizona. [Online]. Available: http://espritmystique.blogspot.com/2010/02/diy-acid-etching-on-brass-and-copper.html. [Accessed: 30-May-2013].

[33] Otto K. N., and Wood K. L., 2001, "Product design : techniques in reverse engineering and new product development," Prentice Hall, Upper Saddle River, NJ. pp 840.

[34] Omega, “Thin Film Detector,” [Online]. Available: http://www.omega.com/Temperature/pdf/TFD_RTD.pdf. [Accessed 01-June-2013].

[35] Schmidt R. F., 1981, “Somatovisceral Sensibility,” Fundamentals of Sensory Physiology, R. F. Schmidt, Springer Berlin Heidelberg, Berlin, Heidelberg, pp. 81–125.

APPENDICES

Appendix A: 1D Model MATLAB Code

```
%% 1-D, Steady State Thermoelectric model
% Based up Andrew Miner's equations in his paper
% "The Compatibility of Thin Films and Nanostructures in Thermoelectric
%  Cooling Systems", DOI: 10.1115/1.2717941
% Code written by Christopher Martinez
% Last Revised: 06/13/2013


clc
clear all

Ta= 288.71 ; % (60 F) top reservoir temp, K
Ts= 299.61; % (79.62 F) bottom reservoir temp, K
f=0.15 ; % fill factor, is a percentage
S=0.00024; % Seebeck Coefficient, V/K [8]

%Thermoelement and trace dimensions
H_BiTe=1.6764*10^-3; % Bismuth Telluride block height, m
W_BiTe=1.397*10^-3; % Bismuth Telluride block width, m
D_BiTe=1.397*10^-3; % Bismuth Telluride block depth, m
H_Cu=.0084*.0254; % Copper strip height, m
% H_Cu=7.5*10^-5 % initial model value
W_Cu=0.002; % Copper trace width, m
% W_Cu=0.0038 % initial model value
D_Cu=0.006; % Copper trace length, m
% D_Cu=0.01588 % initial model value


% Thermal conductivities
Kcu=401; % Thermal Conductivity of Copper, W/(m*K) [12]
KBiTe=2; % Thermal Conductivity of Bismuth Telluride, W/(m*K) [8]
K_sold=66.6 ; % thermal conductivity of solder, W/(m*K) (assumed tin)
[12]
K_polyimide=0.12 ; % thermal conductivity of polyimide, W/(m*K) [18]
K_pvc=(0.15+0.21)/2 ; % Thermal conductivity of PVC, W/(m K) [19]
K_rub=0.16 ; % Thermal conductivity of hard rubber, W/(m K) [12]
K_adh=0.147 ; % thermal conductivity of assumed adhesive, W/(m*K) [20]
K_parr=0.24 ; % Thermal conductivity of paraffin, W/(m K) [12]



% Material Thickness
T_layer=.001*.0254 ; % polyimide layer thicknesses, m
% T_layer=0.00004 % initial model value
T_sold=.010*.0254 ; % solder layer thickness, m
% T_sold=0.001 % initial model value
T_parr=0.001 ; % estimated thickness of paraffin layer, in meters
T_pvc=0.00067/2; % thickness of two layers of PVC divided by 2, in
meters
T_rub=0.0036/2; % thickness of two layers of rubber divided by 2, in m
```

Appendix A (Continued)

```
% Thermal Conductances
k_polyimide=K_polyimide/T_layer;  % thermal conductance of polyimide,
W/(m^2*K)
k_adh=K_adh/T_layer;  % thermal conductance of adhesive, W/(m^2*K)
K=KBiTe/H_BiTe; % One dimensional block conductance, W/(m^2*K)
k_cu_1=Kcu/H_Cu; %(0.28448*10^-3); % thermal conductance of copper,
                                   %W/(m^2*K)
k_sold=K_sold/T_sold ; % thermal conductance of solder, in W/(m^2 K)
k_parr=K_parr/T_parr ; % conductance of paraffin, in W/(m^2 K)
k_pvc=K_pvc/T_pvc ; % conductance of PVC, in W/(m^2 K)
k_rub=K_rub/T_rub ; % conductance of hard rubber, in W/(m^2 K)
K=KBiTe/H_BiTe; % One dimensional block conductance, W/(m^2*K)


% Thermal Contact Resistances
R_epoxy=(0.2+0.9)/2*10^-4 ; % Thermal contact resistance for epoxy,
                            %(m^2*K)/W (silicon with aluminum) [12]
R_solder=(0.25+.14)/2*10^-4 ; % Thermal contact resistance for solder,
                              %(m^2*K)/W (brass/brass) [12]
R_skin=(2.75*10^-4) ; % Thermal contact resistance with skin,
%(m^2*K)/W (aluminum interface with air) [12]


% Current
I=0:0.1:12 ; % Current , A
Rd=1 % Redundancy, # of blocks per cell
J=I/(Rd*W_BiTe*D_BiTe) ; % Current Density, A/m^2


% Electrical Resistivities and Contact Resistances
RBiTe=1*10^-5; % Resistivity of Bismuth Telluride, ohm*m [10]
Rcu=17.2*10^-9; % Resistivity of Copper, ohm*m [19]
R=RBiTe*H_BiTe; % electrical contact resistance, ohm*m^2
% The resistance affects the value for the amperage that creates a max
Tc
Rr=0; % electrical connection resistances (total), ohm*m^2


% Values of interest
Kc = (k_rub^-1+k_parr^-1+k_polyimide^-1+R_epoxy+k_adh^-1+k_cu_1^-
1+R_solder+k_sold^-1+R_solder)^-1 % cold side thermal conductance, in
W/(m^2 K)
% Initial Model -> Kc=(k_sold^-1+k_polyimide^-1+k_adh^-1+k_cu_1^-
1+.025*10^-3+R_skin+2*R_solder+2*R_epoxy)^-1
% Test Arrangement Model -> Kc = (k_rub^-1+k_parr^-1+k_polyimide^-
1+R_epoxy+k_adh^-1+k_cu_1^-1+R_solder+k_sold^-1+R_solder)^-1

Kh = (R_solder+k_sold^-1+R_solder+k_cu_1^-1+k_adh^-1+k_polyimide^-
1+k_parr^-1+k_pvc^-1)^-1 % hot side thermal conductance, in W/(m^2 K)
% Initial Model -> Kh=(4*R_solder+2*k_sold^-1+k_cu_1^-1+(.001)/Kcu)^-1
% Test Arrangement Model -> Kh = (R_solder+k_sold^-1+R_solder+k_cu_1^-
1+k_adh^-1+k_polyimide^-1+k_parr^-1+k_pvc^-1)^-1
```

Appendix A (Continued)

```
% Equation Solver
syms Tc Th
for i=1:length(J)
b4Tc(i)=(Ta-(Tc+(-J(i).^2.*(R./2+Rr)+J(i).*S.*Tc-(Ts-
Tc).*Kc)./K)).*Kh+J(i).*S*(Tc+(-J(i).^2.*(R./2+Rr)+J(i).*S.*Tc-(Ts-
Tc).*Kc)./K)+(Tc-(Tc+(-J(i).^2.*(R./2+Rr)+J(i).*S.*Tc-(Ts-
Tc).*Kc)./K)).*K+J(i).^2.*(R./2+Rr);
Tcs(i)=solve(b4Tc(i),Tc);
Tcs(i)=eval(Tcs(i)); % Cold side temperature solved (K)
J(i);
end



for i=1:length(J)
    b4Th(i)=(Th-(Th+(-(Ta-Th).*Kh-J(i).*S.*Th-
J(i).^2.*(R./2+Rr))./K)).*K+J(i).^2.*(R./2+Rr)-J(i).*S.*(Th+(-(Ta-
Th).*Kh-J(i).*S.*Th-J(i).^2.*(R./2+Rr))./K)+(Ts-(Th+(-(Ta-Th).*Kh-
J(i).*S.*Th-J(i).^2.*(R./2+Rr))./K)).*Kc;
Ths(i)=solve(b4Th(i),Th);
Ths(i)=eval(Ths(i)); % Hot side temperature solved (K)
end

for i=1:length(J)
% Cold side flux, positive means heat flowing into the device
Qc(i)=f*(J(i).*S.*Tcs(i)-J(i).^2*(R./2+Rr)-K.*(Ths(i)-Tcs(i)));
end

for i=1:length(J)
%Hot side flux, positive means heat flowing out of the device
Qh(i)=f*(S.*Ths(i).*J(i)+0.5.*J(i).^2*(R./2+Rr)-K.*(Ths(i)-Tcs(i)));
end



% Plot of Cooling Flux
figure
plot(I,Qc,'o-')
xlabel('Current (A)')
ylabel('Cooling Flux (W/m^2)')
title('Cooling Flux vs Current')
grid on

I = I';
Tcs = eval(Tcs)';
Ths = eval(Ths)';
Qc = eval(Qc)';
Qh = eval(Qh)';

clab = 'Current Tc Qc Th Qh'; % column label for table
rlab = 0:length(I); % row label for table
rlab = num2str(rlab); % converts numbers to string value for table
results = [I Tcs Qc Ths Qh];
printmat(results,'Results',rlab,clab) % Results table
```

Appendix B: Human Heat Flux Calculations

Table A: Human heat flux calculations using the Fiala et al model

Convection		
Variable	**Value**	**Units**
a_nat	8.3	(W^2)/(K^(2.5))
a_frc	216	(W^2*s)/(m*K^2)
a_mix	-10.8	(W/K)^2
Tsf	302.594	K
Tair	294.261	K
V_air,eff	0.01	m/s
h_c	3.914021	W/(m^2*K)
q_c	32.61553	W/m^2

Evaporation		
Variable	**Value**	**Units**
T_osk	29.444	C
P_osk,sat	4111.934	
1/R_e,sk	0.003	W/(m^2*P)
q_e	12.3358	W/m^2

Radiation		
Variable	**Value**	**Units**
Sigma	5.67E-08	W/(m^2*K^4)
E_sf	0.99	
E_sr	0.93	
Psi_sf.sr	0.8	
Tsf	302.594	K
Tsr,m	294.261	K
h_R	4.440709	W/(m^2*K)
q_R	37.00443	W/m^2

Total Heat Flux	81.95577	W/m^2
	0.008196	W/cm^2

Source

"A computer model of human thermoregulation for a wide range of environmental conditions: the passive system", by Fiala et al. [14]

Appendix C: MATLAB Gcode Generator

```
%% Middle Block template, (2x2)mm blocks spaced 2 mm apart, 10 rows
total.
% Written by Christopher Martinez
% Last revised: 06/13/2013


% The code this program produces is copied and pasted into a notepad
file
% where it is saved with the extension ".ncd". Once the code is copied
into
% a notepad file an additional command must be entered. After the third
% line of code an "M3" command must be manually written in. This code
turns
% on the mill motor and is omitted on purpose for safety reasons. This
way
% the code's outputs can be double checked without the motor spinning.

clc
clear all
format long
fprintf('G90 \n')
fprintf('G0 X0 Y0 Z0 \n')
syms G Z F X Y
z=-.032; % plunge depth
del=(1/1000)*(5280/1609)*(12/1); % box size converted from mm to inches
x=0; % origin x coordinate
y=0; % origin y coordinate
% Where mill bit is located before running this code is where the x and
y
% origins are referenced.
xL=2; % aperture size in millimeters
zL=0.125 % mill bit lift off height in inches

% channel 1, row 1
for i=1:18

    x1=4*del*(i-1); % space each aperture in 4 mm increments (2mm for
%the aperture width and 2 mm for the space between them) away from the
%origin in the x direction.
    y1=0; % beginning y position in inches
    z1=zL; % beginning z position in inches

    % *** The following code traces out a square. For each row
%adjustments are made to incorporate -2 mm of spacing in the y
%direction between rows of the same channel, and -6 mm of spacing in
%the y direction between channels. ***

    y=xL*del; % instruction: move mill bit from beginning y position to
              % this y position
    x=x1+xL*del;% instruction: move mill bit from beginning x position
%to this x position
    yy=0; % instruction: move mill bit from previous y position to
          % this y position
```

Appendix C (Continued)

```
    xx=x1;% instruction: move mill bit from previous x position to
          % this x position

    %Initial bit position
    fprintf('G0 X%g Y%g Z%g\n',x1,y1,z1)

    % Plunge bit "F5.0" is the plunge rate in inches per minute
    fprintf('G1 Z%g F5.0 \n',z)


    fprintf('Y%g F5.0 \n',y)
    fprintf('X%g \n',x)
    fprintf('Y%g \n',yy)
    fprintf('X%g \n',xx)
    fprintf('Z%g \n',zL)

end

% channel 1, row 2
for i=1:18
    x1=4*del*(i-1);
    y1=-4*del; % beginning y position for this row in inches (-2 mm
%spacing between apertures, and -2 mm spacing to allow for 2 mm mill
%bit travel)
    z1=zL;

    y=y1+xL*del;
    x=x1+xL*del;
    yy=y1;
    xx=x1;

    fprintf('G0 X%g Y%g Z%g\n',x1,y1,z1)
    fprintf('G1 Z%g F5.0 \n',z)

    fprintf('Y%g F5.0 \n',y)
    fprintf('X%g \n',x)
    fprintf('Y%g \n',yy)
    fprintf('X%g \n',xx)
    fprintf('Z%g \n',zL)

end

% channel 2, row 1

for i=1:18

    x1=4*del*(i-1);
    y1=-12*del; % beginning y position for this row in inches (-4 mm
                % spacing to reach the bottom of the first channel, -6
%mm spacing to reach the top of the next channel, - 2 mm spacing to
%allow for 2 mm vertical mill bit travel)
    z1=zL;
```

Appendix C (Continued)

```
    y=y1+xL*del;
    x=x1+xL*del;
    yy=y1;
    xx=x1;

    fprintf('G0 X%g Y%g Z%g\n',x1,y1,z1)
    fprintf('G1 Z%g F5.0 \n',z)

    fprintf('Y%g F5.0 \n',y)
    fprintf('X%g \n',x)
    fprintf('Y%g \n',yy)
    fprintf('X%g \n',xx)
    fprintf('Z%g \n',zL)

end

% channel 2, row 2

for i=1:18

    x1=4*del*(i-1);
    y1=-16*del;
    z1=zL;

    y=y1+xL*del;
    x=x1+xL*del;
    yy=y1;
    xx=x1;

    fprintf('G0 X%g Y%g Z%g\n',x1,y1,z1)
    fprintf('G1 Z%g F5.0 \n',z)

    fprintf('Y%g F5.0 \n',y)
    fprintf('X%g \n',x)
    fprintf('Y%g \n',yy)
    fprintf('X%g \n',xx)
    fprintf('Z%g \n',zL)

end

% channel 3, row 1

for i=1:18

    x1=4*del*(i-1);
    y1=-24*del;
    z1=zL;

    y=y1+xL*del;
    x=x1+xL*del;
```

Appendix C (Continued)

```
    yy=y1;
    xx=x1;

    fprintf('G0 X%g Y%g Z%g\n',x1,y1,z1)
    fprintf('G1 Z%g F5.0 \n',z)

    fprintf('Y%g F5.0 \n',y)
    fprintf('X%g \n',x)
    fprintf('Y%g \n',yy)
    fprintf('X%g \n',xx)
    fprintf('Z%g \n',zL)

end

% channel 3, row 2

for i=1:18

    x1=4*del*(i-1);
    y1=-28*del;
    z1=zL;

    y=y1+xL*del;
    x=x1+xL*del;
    yy=y1;
    xx=x1;

    fprintf('G0 X%g Y%g Z%g\n',x1,y1,z1)
    fprintf('G1 Z%g F5.0 \n',z)

    fprintf('Y%g F5.0 \n',y)
    fprintf('X%g \n',x)
    fprintf('Y%g \n',yy)
    fprintf('X%g \n',xx)
    fprintf('Z%g \n',zL)

end

% channel 4, row 1

for i=1:18

    x1=4*del*(i-1);
    y1=-36*del;
    z1=zL;

    y=y1+xL*del;
    x=x1+xL*del;
    yy=y1;
    xx=x1;
```

Appendix C (Continued)

```
    fprintf('G0 X%g Y%g Z%g\n',x1,y1,z1)
    fprintf('G1 Z%g F5.0 \n',z)

    fprintf('Y%g F5.0 \n',y)
    fprintf('X%g \n',x)
    fprintf('Y%g \n',yy)
    fprintf('X%g \n',xx)
    fprintf('Z%g \n',zL)

end

% channel 4, row 2

for i=1:18

    x1=4*del*(i-1);
    y1=-40*del;
    z1=zL;

    y=y1+xL*del;
    x=x1+xL*del;
    yy=y1;
    xx=x1;

    fprintf('G0 X%g Y%g Z%g\n',x1,y1,z1)
    fprintf('G1 Z%g F5.0 \n',z)

    fprintf('Y%g F5.0 \n',y)
    fprintf('X%g \n',x)
    fprintf('Y%g \n',yy)
    fprintf('X%g \n',xx)
    fprintf('Z%g \n',zL)

end

% channel 5, row 1

for i=1:18

    x1=4*del*(i-1);
    y1=-48*del;
    z1=zL;

    y=y1+xL*del;
    x=x1+xL*del;
    yy=y1;
    xx=x1;

    fprintf('G0 X%g Y%g Z%g\n',x1,y1,z1)
    fprintf('G1 Z%g F5.0 \n',z)
```

Appendix C (Continued)

```
    fprintf('Y%g F5.0 \n',y)
    fprintf('X%g \n',x)
    fprintf('Y%g \n',yy)
    fprintf('X%g \n',xx)
    fprintf('Z%g \n',zL)

end

% channel 5, row 2

for i=1:18

    x1=4*del*(i-1);
    y1=-52*del;
    z1=zL;

    y=y1+xL*del;
    x=x1+xL*del;
    yy=y1;
    xx=x1;

    fprintf('G0 X%g Y%g Z%g\n',x1,y1,z1)
    fprintf('G1 Z%g F5.0 \n',z)

    fprintf('Y%g F5.0 \n',y)
    fprintf('X%g \n',x)
    fprintf('Y%g \n',yy)
    fprintf('X%g \n',xx)
    fprintf('Z%g \n',zL)

end

% left mounting hole

x1=-27.73*del;
y1=-27.68*del;
z1=zL;

y=y1+0.25;
x=x1+0.25;
yy=y1;
xx=x1;

fprintf('G0 X%g Y%g Z%g\n',x1,y1,z1)
fprintf('G1 Z%g F5.0 \n',z)

fprintf('Y%g F5.0 \n',y)
fprintf('X%g \n',x)
fprintf('Y%g \n',yy)
fprintf('X%g \n',xx)
fprintf('Z%g \n',zL)
```

Appendix C (Continued)

```
% right mounting hole

x1=127.85*del;
y1=-27.68*del;
z1=zL;

y=y1+0.25;
x=x1+0.5;
yy=y1;
xx=x1;

fprintf('G0 X%g Y%g Z%g\n',x1,y1,z1)
fprintf('G1 Z%g F5.0 \n',z)

fprintf('Y%g F5.0 \n',y)
fprintf('X%g \n',x)
fprintf('Y%g \n',yy)
fprintf('X%g \n',xx)
fprintf('Z%g \n',zL)

% motor stop, program close
fprintf('G0 Z1 \n')
fprintf('M5 \n')
fprintf('M30 \n')
```

Appendix D: Stencil and Middle Template Gcode

```
G90
G0 X0 Y0 Z0
G0 X0 Y0 Z0.125
M3
G1 Z-0.032 F5.0
Y0.078757 F5.0
X0.078757
Y0
X0
Z0.125
G0 X0.157514 Y0 Z0.125
G1 Z-0.032 F5.0
Y0.078757 F5.0
X0.236271
Y0
X0.157514
Z0.125
G0 X0.315028 Y0 Z0.125
G1 Z-0.032 F5.0
Y0.078757 F5.0
X0.393785
Y0
X0.315028
Z0.125
G0 X0.472542 Y0 Z0.125
G1 Z-0.032 F5.0
Y0.078757 F5.0
X0.551299
Y0
X0.472542
Z0.125
G0 X0.630056 Y0 Z0.125
G1 Z-0.032 F5.0
Y0.078757 F5.0
X0.708813
Y0
X0.630056
Z0.125
G0 X0.78757 Y0 Z0.125
G1 Z-0.032 F5.0
Y0.078757 F5.0
X0.866327
Y0
X0.78757
Z0.125
G0 X0.945084 Y0 Z0.125
G1 Z-0.032 F5.0
Y0.078757 F5.0
X1.02384
```

Appendix D (Continued)

```
Y0
X0.945084
Z0.125
G0 X1.1026 Y0 Z0.125
G1 Z-0.032 F5.0
Y0.078757 F5.0
X1.18135
Y0
X1.1026
Z0.125
G0 X1.26011 Y0 Z0.125
G1 Z-0.032 F5.0
Y0.078757 F5.0
X1.33887
Y0
X1.26011
Z0.125
G0 X1.41763 Y0 Z0.125
G1 Z-0.032 F5.0
Y0.078757 F5.0
X1.49638
Y0
X1.41763
Z0.125
G0 X1.57514 Y0 Z0.125
G1 Z-0.032 F5.0
Y0.078757 F5.0
X1.6539
Y0
X1.57514
Z0.125
G0 X1.73265 Y0 Z0.125
G1 Z-0.032 F5.0
Y0.078757 F5.0
X1.81141
Y0
X1.73265
Z0.125
G0 X1.89017 Y0 Z0.125
G1 Z-0.032 F5.0
Y0.078757 F5.0
X1.96892
Y0
X1.89017
Z0.125
G0 X2.04768 Y0 Z0.125
G1 Z-0.032 F5.0
Y0.078757 F5.0
X2.12644
```

Appendix D (Continued)

```
Y0
X2.04768
Z0.125
G0 X2.2052 Y0 Z0.125
G1 Z-0.032 F5.0
Y0.078757 F5.0
X2.28395
Y0
X2.2052
Z0.125
G0 X2.36271 Y0 Z0.125
G1 Z-0.032 F5.0
Y0.078757 F5.0
X2.44147
Y0
X2.36271
Z0.125
G0 X2.52022 Y0 Z0.125
G1 Z-0.032 F5.0
Y0.078757 F5.0
X2.59898
Y0
X2.52022
Z0.125
G0 X2.67774 Y0 Z0.125
G1 Z-0.032 F5.0
Y0.078757 F5.0
X2.75649
Y0
X2.67774
Z0.125
G0 X0 Y-0.157514 Z0.125
G1 Z-0.032 F5.0
Y-0.078757 F5.0
X0.078757
Y-0.157514
X0
Z0.125
G0 X0.157514 Y-0.157514 Z0.125
G1 Z-0.032 F5.0
Y-0.078757 F5.0
X0.236271
Y-0.157514
X0.157514
Z0.125
G0 X0.315028 Y-0.157514 Z0.125
G1 Z-0.032 F5.0
Y-0.078757 F5.0
X0.393785
```

Appendix D (Continued)

Y-0.157514
X0.315028
Z0.125
G0 X0.472542 Y-0.157514 Z0.125
G1 Z-0.032 F5.0
Y-0.078757 F5.0
X0.551299
Y-0.157514
X0.472542
Z0.125
G0 X0.630056 Y-0.157514 Z0.125
G1 Z-0.032 F5.0
Y-0.078757 F5.0
X0.708813
Y-0.157514
X0.630056
Z0.125
G0 X0.78757 Y-0.157514 Z0.125
G1 Z-0.032 F5.0
Y-0.078757 F5.0
X0.866327
Y-0.157514
X0.78757
Z0.125
G0 X0.945084 Y-0.157514 Z0.125
G1 Z-0.032 F5.0
Y-0.078757 F5.0
X1.02384
Y-0.157514
X0.945084
Z0.125
G0 X1.1026 Y-0.157514 Z0.125
G1 Z-0.032 F5.0
Y-0.078757 F5.0
X1.18135
Y-0.157514
X1.1026
Z0.125
G0 X1.26011 Y-0.157514 Z0.125
G1 Z-0.032 F5.0
Y-0.078757 F5.0
X1.33887
Y-0.157514
X1.26011
Z0.125
G0 X1.41763 Y-0.157514 Z0.125
G1 Z-0.032 F5.0
Y-0.078757 F5.0
X1.49638

Appendix D (Continued)

Y-0.157514
X1.41763
Z0.125
G0 X1.57514 Y-0.157514 Z0.125
G1 Z-0.032 F5.0
Y-0.078757 F5.0
X1.6539
Y-0.157514
X1.57514
Z0.125
G0 X1.73265 Y-0.157514 Z0.125
G1 Z-0.032 F5.0
Y-0.078757 F5.0
X1.81141
Y-0.157514
X1.73265
Z0.125
G0 X1.89017 Y-0.157514 Z0.125
G1 Z-0.032 F5.0
Y-0.078757 F5.0
X1.96892
Y-0.157514
X1.89017
Z0.125
G0 X2.04768 Y-0.157514 Z0.125
G1 Z-0.032 F5.0
Y-0.078757 F5.0
X2.12644
Y-0.157514
X2.04768
Z0.125
G0 X2.2052 Y-0.157514 Z0.125
G1 Z-0.032 F5.0
Y-0.078757 F5.0
X2.28395
Y-0.157514
X2.2052
Z0.125
G0 X2.36271 Y-0.157514 Z0.125
G1 Z-0.032 F5.0
Y-0.078757 F5.0
X2.44147
Y-0.157514
X2.36271
Z0.125
G0 X2.52022 Y-0.157514 Z0.125
G1 Z-0.032 F5.0
Y-0.078757 F5.0
X2.59898

Appendix D (Continued)

```
Y-0.157514
X2.52022
Z0.125
G0 X2.67774 Y-0.157514 Z0.125
G1 Z-0.032 F5.0
Y-0.078757 F5.0
X2.75649
Y-0.157514
X2.67774
Z0.125
G0 X0 Y-0.472542 Z0.125
G1 Z-0.032 F5.0
Y-0.393785 F5.0
X0.078757
Y-0.472542
X0
Z0.125
G0 X0.157514 Y-0.472542 Z0.125
G1 Z-0.032 F5.0
Y-0.393785 F5.0
X0.236271
Y-0.472542
X0.157514
Z0.125
G0 X0.315028 Y-0.472542 Z0.125
G1 Z-0.032 F5.0
Y-0.393785 F5.0
X0.393785
Y-0.472542
X0.315028
Z0.125
G0 X0.472542 Y-0.472542 Z0.125
G1 Z-0.032 F5.0
Y-0.393785 F5.0
X0.551299
Y-0.472542
X0.472542
Z0.125
G0 X0.630056 Y-0.472542 Z0.125
G1 Z-0.032 F5.0
Y-0.393785 F5.0
X0.708813
Y-0.472542
X0.630056
Z0.125
G0 X0.78757 Y-0.472542 Z0.125
G1 Z-0.032 F5.0
Y-0.393785 F5.0
X0.866327
```

Appendix D (Continued)

Y-0.472542
X0.78757
Z0.125
G0 X0.945084 Y-0.472542 Z0.125
G1 Z-0.032 F5.0
Y-0.393785 F5.0
X1.02384
Y-0.472542
X0.945084
Z0.125
G0 X1.1026 Y-0.472542 Z0.125
G1 Z-0.032 F5.0
Y-0.393785 F5.0
X1.18135
Y-0.472542
X1.1026
Z0.125
G0 X1.26011 Y-0.472542 Z0.125
G1 Z-0.032 F5.0
Y-0.393785 F5.0
X1.33887
Y-0.472542
X1.26011
Z0.125
G0 X1.41763 Y-0.472542 Z0.125
G1 Z-0.032 F5.0
Y-0.393785 F5.0
X1.49638
Y-0.472542
X1.41763
Z0.125
G0 X1.57514 Y-0.472542 Z0.125
G1 Z-0.032 F5.0
Y-0.393785 F5.0
X1.6539
Y-0.472542
X1.57514
Z0.125
G0 X1.73265 Y-0.472542 Z0.125
G1 Z-0.032 F5.0
Y-0.393785 F5.0
X1.81141
Y-0.472542
X1.73265
Z0.125
G0 X1.89017 Y-0.472542 Z0.125
G1 Z-0.032 F5.0
Y-0.393785 F5.0
X1.96892

Appendix D (Continued)

Y-0.472542
X1.89017
Z0.125
G0 X2.04768 Y-0.472542 Z0.125
G1 Z-0.032 F5.0
Y-0.393785 F5.0
X2.12644
Y-0.472542
X2.04768
Z0.125
G0 X2.2052 Y-0.472542 Z0.125
G1 Z-0.032 F5.0
Y-0.393785 F5.0
X2.28395
Y-0.472542
X2.2052
Z0.125
G0 X2.36271 Y-0.472542 Z0.125
G1 Z-0.032 F5.0
Y-0.393785 F5.0
X2.44147
Y-0.472542
X2.36271
Z0.125
G0 X2.52022 Y-0.472542 Z0.125
G1 Z-0.032 F5.0
Y-0.393785 F5.0
X2.59898
Y-0.472542
X2.52022
Z0.125
G0 X2.67774 Y-0.472542 Z0.125
G1 Z-0.032 F5.0
Y-0.393785 F5.0
X2.75649
Y-0.472542
X2.67774
Z0.125
G0 X0 Y-0.630056 Z0.125
G1 Z-0.032 F5.0
Y-0.551299 F5.0
X0.078757
Y-0.630056
X0
Z0.125
G0 X0.157514 Y-0.630056 Z0.125
G1 Z-0.032 F5.0
Y-0.551299 F5.0
X0.236271

Appendix D (Continued)

```
Y-0.630056
X0.157514
Z0.125
G0 X0.315028 Y-0.630056 Z0.125
G1 Z-0.032 F5.0
Y-0.551299 F5.0
X0.393785
Y-0.630056
X0.315028
Z0.125
G0 X0.472542 Y-0.630056 Z0.125
G1 Z-0.032 F5.0
Y-0.551299 F5.0
X0.551299
Y-0.630056
X0.472542
Z0.125
G0 X0.630056 Y-0.630056 Z0.125
G1 Z-0.032 F5.0
Y-0.551299 F5.0
X0.708813
Y-0.630056
X0.630056
Z0.125
G0 X0.78757 Y-0.630056 Z0.125
G1 Z-0.032 F5.0
Y-0.551299 F5.0
X0.866327
Y-0.630056
X0.78757
Z0.125
G0 X0.945084 Y-0.630056 Z0.125
G1 Z-0.032 F5.0
Y-0.551299 F5.0
X1.02384
Y-0.630056
X0.945084
Z0.125
G0 X1.1026 Y-0.630056 Z0.125
G1 Z-0.032 F5.0
Y-0.551299 F5.0
X1.18135
Y-0.630056
X1.1026
Z0.125
G0 X1.26011 Y-0.630056 Z0.125
G1 Z-0.032 F5.0
Y-0.551299 F5.0
X1.33887
```

Appendix D (Continued)

```
Y-0.630056
X1.26011
Z0.125
G0 X1.41763 Y-0.630056 Z0.125
G1 Z-0.032 F5.0
Y-0.551299 F5.0
X1.49638
Y-0.630056
X1.41763
Z0.125
G0 X1.57514 Y-0.630056 Z0.125
G1 Z-0.032 F5.0
Y-0.551299 F5.0
X1.6539
Y-0.630056
X1.57514
Z0.125
G0 X1.73265 Y-0.630056 Z0.125
G1 Z-0.032 F5.0
Y-0.551299 F5.0
X1.81141
Y-0.630056
X1.73265
Z0.125
G0 X1.89017 Y-0.630056 Z0.125
G1 Z-0.032 F5.0
Y-0.551299 F5.0
X1.96892
Y-0.630056
X1.89017
Z0.125
G0 X2.04768 Y-0.630056 Z0.125
G1 Z-0.032 F5.0
Y-0.551299 F5.0
X2.12644
Y-0.630056
X2.04768
Z0.125
G0 X2.2052 Y-0.630056 Z0.125
G1 Z-0.032 F5.0
Y-0.551299 F5.0
X2.28395
Y-0.630056
X2.2052
Z0.125
G0 X2.36271 Y-0.630056 Z0.125
G1 Z-0.032 F5.0
Y-0.551299 F5.0
X2.44147
```

Appendix D (Continued)

Y-0.630056
X2.36271
Z0.125
G0 X2.52022 Y-0.630056 Z0.125
G1 Z-0.032 F5.0
Y-0.551299 F5.0
X2.59898
Y-0.630056
X2.52022
Z0.125
G0 X2.67774 Y-0.630056 Z0.125
G1 Z-0.032 F5.0
Y-0.551299 F5.0
X2.75649
Y-0.630056
X2.67774
Z0.125
G0 X0 Y-0.945084 Z0.125
G1 Z-0.032 F5.0
Y-0.866327 F5.0
X0.078757
Y-0.945084
X0
Z0.125
G0 X0.157514 Y-0.945084 Z0.125
G1 Z-0.032 F5.0
Y-0.866327 F5.0
X0.236271
Y-0.945084
X0.157514
Z0.125
G0 X0.315028 Y-0.945084 Z0.125
G1 Z-0.032 F5.0
Y-0.866327 F5.0
X0.393785
Y-0.945084
X0.315028
Z0.125
G0 X0.472542 Y-0.945084 Z0.125
G1 Z-0.032 F5.0
Y-0.866327 F5.0
X0.551299
Y-0.945084
X0.472542
Z0.125
G0 X0.630056 Y-0.945084 Z0.125
G1 Z-0.032 F5.0
Y-0.866327 F5.0
X0.708813

Appendix D (Continued)

Y-0.945084
X0.630056
Z0.125
G0 X0.78757 Y-0.945084 Z0.125
G1 Z-0.032 F5.0
Y-0.866327 F5.0
X0.866327
Y-0.945084
X0.78757
Z0.125
G0 X0.945084 Y-0.945084 Z0.125
G1 Z-0.032 F5.0
Y-0.866327 F5.0
X1.02384
Y-0.945084
X0.945084
Z0.125
G0 X1.1026 Y-0.945084 Z0.125
G1 Z-0.032 F5.0
Y-0.866327 F5.0
X1.18135
Y-0.945084
X1.1026
Z0.125
G0 X1.26011 Y-0.945084 Z0.125
G1 Z-0.032 F5.0
Y-0.866327 F5.0
X1.33887
Y-0.945084
X1.26011
Z0.125
G0 X1.41763 Y-0.945084 Z0.125
G1 Z-0.032 F5.0
Y-0.866327 F5.0
X1.49638
Y-0.945084
X1.41763
Z0.125
G0 X1.57514 Y-0.945084 Z0.125
G1 Z-0.032 F5.0
Y-0.866327 F5.0
X1.6539
Y-0.945084
X1.57514
Z0.125
G0 X1.73265 Y-0.945084 Z0.125
G1 Z-0.032 F5.0
Y-0.866327 F5.0
X1.81141

Appendix D (Continued)

Y-0.945084
X1.73265
Z0.125
G0 X1.89017 Y-0.945084 Z0.125
G1 Z-0.032 F5.0
Y-0.866327 F5.0
X1.96892
Y-0.945084
X1.89017
Z0.125
G0 X2.04768 Y-0.945084 Z0.125
G1 Z-0.032 F5.0
Y-0.866327 F5.0
X2.12644
Y-0.945084
X2.04768
Z0.125
G0 X2.2052 Y-0.945084 Z0.125
G1 Z-0.032 F5.0
Y-0.866327 F5.0
X2.28395
Y-0.945084
X2.2052
Z0.125
G0 X2.36271 Y-0.945084 Z0.125
G1 Z-0.032 F5.0
Y-0.866327 F5.0
X2.44147
Y-0.945084
X2.36271
Z0.125
G0 X2.52022 Y-0.945084 Z0.125
G1 Z-0.032 F5.0
Y-0.866327 F5.0
X2.59898
Y-0.945084
X2.52022
Z0.125
G0 X2.67774 Y-0.945084 Z0.125
G1 Z-0.032 F5.0
Y-0.866327 F5.0
X2.75649
Y-0.945084
X2.67774
Z0.125
G0 X0 Y-1.1026 Z0.125
G1 Z-0.032 F5.0
Y-1.02384 F5.0
X0.078757

Appendix D (Continued)

```
Y-1.1026
X0
Z0.125
G0 X0.157514 Y-1.1026 Z0.125
G1 Z-0.032 F5.0
Y-1.02384 F5.0
X0.236271
Y-1.1026
X0.157514
Z0.125
G0 X0.315028 Y-1.1026 Z0.125
G1 Z-0.032 F5.0
Y-1.02384 F5.0
X0.393785
Y-1.1026
X0.315028
Z0.125
G0 X0.472542 Y-1.1026 Z0.125
G1 Z-0.032 F5.0
Y-1.02384 F5.0
X0.551299
Y-1.1026
X0.472542
Z0.125
G0 X0.630056 Y-1.1026 Z0.125
G1 Z-0.032 F5.0
Y-1.02384 F5.0
X0.708813
Y-1.1026
X0.630056
Z0.125
G0 X0.78757 Y-1.1026 Z0.125
G1 Z-0.032 F5.0
Y-1.02384 F5.0
X0.866327
Y-1.1026
X0.78757
Z0.125
G0 X0.945084 Y-1.1026 Z0.125
G1 Z-0.032 F5.0
Y-1.02384 F5.0
X1.02384
Y-1.1026
X0.945084
Z0.125
G0 X1.1026 Y-1.1026 Z0.125
G1 Z-0.032 F5.0
Y-1.02384 F5.0
X1.18135
```

Appendix D (Continued)

```
Y-1.1026
X1.1026
Z0.125
G0 X1.26011 Y-1.1026 Z0.125
G1 Z-0.032 F5.0
Y-1.02384 F5.0
X1.33887
Y-1.1026
X1.26011
Z0.125
G0 X1.41763 Y-1.1026 Z0.125
G1 Z-0.032 F5.0
Y-1.02384 F5.0
X1.49638
Y-1.1026
X1.41763
Z0.125
G0 X1.57514 Y-1.1026 Z0.125
G1 Z-0.032 F5.0
Y-1.02384 F5.0
X1.6539
Y-1.1026
X1.57514
Z0.125
G0 X1.73265 Y-1.1026 Z0.125
G1 Z-0.032 F5.0
Y-1.02384 F5.0
X1.81141
Y-1.1026
X1.73265
Z0.125
G0 X1.89017 Y-1.1026 Z0.125
G1 Z-0.032 F5.0
Y-1.02384 F5.0
X1.96892
Y-1.1026
X1.89017
Z0.125
G0 X2.04768 Y-1.1026 Z0.125
G1 Z-0.032 F5.0
Y-1.02384 F5.0
X2.12644
Y-1.1026
X2.04768
Z0.125
G0 X2.2052 Y-1.1026 Z0.125
G1 Z-0.032 F5.0
Y-1.02384 F5.0
X2.28395
```

Appendix D (Continued)

```
Y-1.1026
X2.2052
Z0.125
G0 X2.36271 Y-1.1026 Z0.125
G1 Z-0.032 F5.0
Y-1.02384 F5.0
X2.44147
Y-1.1026
X2.36271
Z0.125
G0 X2.52022 Y-1.1026 Z0.125
G1 Z-0.032 F5.0
Y-1.02384 F5.0
X2.59898
Y-1.1026
X2.52022
Z0.125
G0 X2.67774 Y-1.1026 Z0.125
G1 Z-0.032 F5.0
Y-1.02384 F5.0
X2.75649
Y-1.1026
X2.67774
Z0.125
G0 X0 Y-1.41763 Z0.125
G1 Z-0.032 F5.0
Y-1.33887 F5.0
X0.078757
Y-1.41763
X0
Z0.125
G0 X0.157514 Y-1.41763 Z0.125
G1 Z-0.032 F5.0
Y-1.33887 F5.0
X0.236271
Y-1.41763
X0.157514
Z0.125
G0 X0.315028 Y-1.41763 Z0.125
G1 Z-0.032 F5.0
Y-1.33887 F5.0
X0.393785
Y-1.41763
X0.315028
Z0.125
G0 X0.472542 Y-1.41763 Z0.125
G1 Z-0.032 F5.0
Y-1.33887 F5.0
X0.551299
```

Appendix D (Continued)

```
Y-1.41763
X0.472542
Z0.125
G0 X0.630056 Y-1.41763 Z0.125
G1 Z-0.032 F5.0
Y-1.33887 F5.0
X0.708813
Y-1.41763
X0.630056
Z0.125
G0 X0.78757 Y-1.41763 Z0.125
G1 Z-0.032 F5.0
Y-1.33887 F5.0
X0.866327
Y-1.41763
X0.78757
Z0.125
G0 X0.945084 Y-1.41763 Z0.125
G1 Z-0.032 F5.0
Y-1.33887 F5.0
X1.02384
Y-1.41763
X0.945084
Z0.125
G0 X1.1026 Y-1.41763 Z0.125
G1 Z-0.032 F5.0
Y-1.33887 F5.0
X1.18135
Y-1.41763
X1.1026
Z0.125
G0 X1.26011 Y-1.41763 Z0.125
G1 Z-0.032 F5.0
Y-1.33887 F5.0
X1.33887
Y-1.41763
X1.26011
Z0.125
G0 X1.41763 Y-1.41763 Z0.125
G1 Z-0.032 F5.0
Y-1.33887 F5.0
X1.49638
Y-1.41763
X1.41763
Z0.125
G0 X1.57514 Y-1.41763 Z0.125
G1 Z-0.032 F5.0
Y-1.33887 F5.0
X1.6539
```

Appendix D (Continued)

```
Y-1.41763
X1.57514
Z0.125
G0 X1.73265 Y-1.41763 Z0.125
G1 Z-0.032 F5.0
Y-1.33887 F5.0
X1.81141
Y-1.41763
X1.73265
Z0.125
G0 X1.89017 Y-1.41763 Z0.125
G1 Z-0.032 F5.0
Y-1.33887 F5.0
X1.96892
Y-1.41763
X1.89017
Z0.125
G0 X2.04768 Y-1.41763 Z0.125
G1 Z-0.032 F5.0
Y-1.33887 F5.0
X2.12644
Y-1.41763
X2.04768
Z0.125
G0 X2.2052 Y-1.41763 Z0.125
G1 Z-0.032 F5.0
Y-1.33887 F5.0
X2.28395
Y-1.41763
X2.2052
Z0.125
G0 X2.36271 Y-1.41763 Z0.125
G1 Z-0.032 F5.0
Y-1.33887 F5.0
X2.44147
Y-1.41763
X2.36271
Z0.125
G0 X2.52022 Y-1.41763 Z0.125
G1 Z-0.032 F5.0
Y-1.33887 F5.0
X2.59898
Y-1.41763
X2.52022
Z0.125
G0 X2.67774 Y-1.41763 Z0.125
G1 Z-0.032 F5.0
Y-1.33887 F5.0
X2.75649
```

Appendix D (Continued)

```
Y-1.41763
X2.67774
Z0.125
G0 X0 Y-1.57514 Z0.125
G1 Z-0.032 F5.0
Y-1.49638 F5.0
X0.078757
Y-1.57514
X0
Z0.125
G0 X0.157514 Y-1.57514 Z0.125
G1 Z-0.032 F5.0
Y-1.49638 F5.0
X0.236271
Y-1.57514
X0.157514
Z0.125
G0 X0.315028 Y-1.57514 Z0.125
G1 Z-0.032 F5.0
Y-1.49638 F5.0
X0.393785
Y-1.57514
X0.315028
Z0.125
G0 X0.472542 Y-1.57514 Z0.125
G1 Z-0.032 F5.0
Y-1.49638 F5.0
X0.551299
Y-1.57514
X0.472542
Z0.125
G0 X0.630056 Y-1.57514 Z0.125
G1 Z-0.032 F5.0
Y-1.49638 F5.0
X0.708813
Y-1.57514
X0.630056
Z0.125
G0 X0.78757 Y-1.57514 Z0.125
G1 Z-0.032 F5.0
Y-1.49638 F5.0
X0.866327
Y-1.57514
X0.78757
Z0.125
G0 X0.945084 Y-1.57514 Z0.125
G1 Z-0.032 F5.0
Y-1.49638 F5.0
X1.02384
```

Appendix D (Continued)

```
Y-1.57514
X0.945084
Z0.125
G0 X1.1026 Y-1.57514 Z0.125
G1 Z-0.032 F5.0
Y-1.49638 F5.0
X1.18135
Y-1.57514
X1.1026
Z0.125
G0 X1.26011 Y-1.57514 Z0.125
G1 Z-0.032 F5.0
Y-1.49638 F5.0
X1.33887
Y-1.57514
X1.26011
Z0.125
G0 X1.41763 Y-1.57514 Z0.125
G1 Z-0.032 F5.0
Y-1.49638 F5.0
X1.49638
Y-1.57514
X1.41763
Z0.125
G0 X1.57514 Y-1.57514 Z0.125
G1 Z-0.032 F5.0
Y-1.49638 F5.0
X1.6539
Y-1.57514
X1.57514
Z0.125
G0 X1.73265 Y-1.57514 Z0.125
G1 Z-0.032 F5.0
Y-1.49638 F5.0
X1.81141
Y-1.57514
X1.73265
Z0.125
G0 X1.89017 Y-1.57514 Z0.125
G1 Z-0.032 F5.0
Y-1.49638 F5.0
X1.96892
Y-1.57514
X1.89017
Z0.125
G0 X2.04768 Y-1.57514 Z0.125
G1 Z-0.032 F5.0
Y-1.49638 F5.0
X2.12644
```

Appendix D (Continued)

```
Y-1.57514
X2.04768
Z0.125
G0 X2.2052 Y-1.57514 Z0.125
G1 Z-0.032 F5.0
Y-1.49638 F5.0
X2.28395
Y-1.57514
X2.2052
Z0.125
G0 X2.36271 Y-1.57514 Z0.125
G1 Z-0.032 F5.0
Y-1.49638 F5.0
X2.44147
Y-1.57514
X2.36271
Z0.125
G0 X2.52022 Y-1.57514 Z0.125
G1 Z-0.032 F5.0
Y-1.49638 F5.0
X2.59898
Y-1.57514
X2.52022
Z0.125
G0 X2.67774 Y-1.57514 Z0.125
G1 Z-0.032 F5.0
Y-1.49638 F5.0
X2.75649
Y-1.57514
X2.67774
Z0.125
G0 X0 Y-1.89017 Z0.125
G1 Z-0.032 F5.0
Y-1.81141 F5.0
X0.078757
Y-1.89017
X0
Z0.125
G0 X0.157514 Y-1.89017 Z0.125
G1 Z-0.032 F5.0
Y-1.81141 F5.0
X0.236271
Y-1.89017
X0.157514
Z0.125
G0 X0.315028 Y-1.89017 Z0.125
G1 Z-0.032 F5.0
Y-1.81141 F5.0
X0.393785
```

Appendix D (Continued)

```
Y-1.89017
X0.315028
Z0.125
G0 X0.472542 Y-1.89017 Z0.125
G1 Z-0.032 F5.0
Y-1.81141 F5.0
X0.551299
Y-1.89017
X0.472542
Z0.125
G0 X0.630056 Y-1.89017 Z0.125
G1 Z-0.032 F5.0
Y-1.81141 F5.0
X0.708813
Y-1.89017
X0.630056
Z0.125
G0 X0.78757 Y-1.89017 Z0.125
G1 Z-0.032 F5.0
Y-1.81141 F5.0
X0.866327
Y-1.89017
X0.78757
Z0.125
G0 X0.945084 Y-1.89017 Z0.125
G1 Z-0.032 F5.0
Y-1.81141 F5.0
X1.02384
Y-1.89017
X0.945084
Z0.125
G0 X1.1026 Y-1.89017 Z0.125
G1 Z-0.032 F5.0
Y-1.81141 F5.0
X1.18135
Y-1.89017
X1.1026
Z0.125
G0 X1.26011 Y-1.89017 Z0.125
G1 Z-0.032 F5.0
Y-1.81141 F5.0
X1.33887
Y-1.89017
X1.26011
Z0.125
G0 X1.41763 Y-1.89017 Z0.125
G1 Z-0.032 F5.0
Y-1.81141 F5.0
X1.49638
```

Appendix D (Continued)

```
Y-1.89017
X1.41763
Z0.125
G0 X1.57514 Y-1.89017 Z0.125
G1 Z-0.032 F5.0
Y-1.81141 F5.0
X1.6539
Y-1.89017
X1.57514
Z0.125
G0 X1.73265 Y-1.89017 Z0.125
G1 Z-0.032 F5.0
Y-1.81141 F5.0
X1.81141
Y-1.89017
X1.73265
Z0.125
G0 X1.89017 Y-1.89017 Z0.125
G1 Z-0.032 F5.0
Y-1.81141 F5.0
X1.96892
Y-1.89017
X1.89017
Z0.125
G0 X2.04768 Y-1.89017 Z0.125
G1 Z-0.032 F5.0
Y-1.81141 F5.0
X2.12644
Y-1.89017
X2.04768
Z0.125
G0 X2.2052 Y-1.89017 Z0.125
G1 Z-0.032 F5.0
Y-1.81141 F5.0
X2.28395
Y-1.89017
X2.2052
Z0.125
G0 X2.36271 Y-1.89017 Z0.125
G1 Z-0.032 F5.0
Y-1.81141 F5.0
X2.44147
Y-1.89017
X2.36271
Z0.125
G0 X2.52022 Y-1.89017 Z0.125
G1 Z-0.032 F5.0
Y-1.81141 F5.0
X2.59898
```

Appendix D (Continued)

```
Y-1.89017
X2.52022
Z0.125
G0 X2.67774 Y-1.89017 Z0.125
G1 Z-0.032 F5.0
Y-1.81141 F5.0
X2.75649
Y-1.89017
X2.67774
Z0.125
G0 X0 Y-2.04768 Z0.125
G1 Z-0.032 F5.0
Y-1.96892 F5.0
X0.078757
Y-2.04768
X0
Z0.125
G0 X0.157514 Y-2.04768 Z0.125
G1 Z-0.032 F5.0
Y-1.96892 F5.0
X0.236271
Y-2.04768
X0.157514
Z0.125
G0 X0.315028 Y-2.04768 Z0.125
G1 Z-0.032 F5.0
Y-1.96892 F5.0
X0.393785
Y-2.04768
X0.315028
Z0.125
G0 X0.472542 Y-2.04768 Z0.125
G1 Z-0.032 F5.0
Y-1.96892 F5.0
X0.551299
Y-2.04768
X0.472542
Z0.125
G0 X0.630056 Y-2.04768 Z0.125
G1 Z-0.032 F5.0
Y-1.96892 F5.0
X0.708813
Y-2.04768
X0.630056
Z0.125
G0 X0.78757 Y-2.04768 Z0.125
G1 Z-0.032 F5.0
Y-1.96892 F5.0
X0.866327
```

Appendix D (Continued)

Y-2.04768
X0.78757
Z0.125
G0 X0.945084 Y-2.04768 Z0.125
G1 Z-0.032 F5.0
Y-1.96892 F5.0
X1.02384
Y-2.04768
X0.945084
Z0.125
G0 X1.1026 Y-2.04768 Z0.125
G1 Z-0.032 F5.0
Y-1.96892 F5.0
X1.18135
Y-2.04768
X1.1026
Z0.125
G0 X1.26011 Y-2.04768 Z0.125
G1 Z-0.032 F5.0
Y-1.96892 F5.0
X1.33887
Y-2.04768
X1.26011
Z0.125
G0 X1.41763 Y-2.04768 Z0.125
G1 Z-0.032 F5.0
Y-1.96892 F5.0
X1.49638
Y-2.04768
X1.41763
Z0.125
G0 X1.57514 Y-2.04768 Z0.125
G1 Z-0.032 F5.0
Y-1.96892 F5.0
X1.6539
Y-2.04768
X1.57514
Z0.125
G0 X1.73265 Y-2.04768 Z0.125
G1 Z-0.032 F5.0
Y-1.96892 F5.0
X1.81141
Y-2.04768
X1.73265
Z0.125
G0 X1.89017 Y-2.04768 Z0.125
G1 Z-0.032 F5.0
Y-1.96892 F5.0
X1.96892

Appendix D (Continued)

```
Y-2.04768
X1.89017
Z0.125
G0 X2.04768 Y-2.04768 Z0.125
G1 Z-0.032 F5.0
Y-1.96892 F5.0
X2.12644
Y-2.04768
X2.04768
Z0.125
G0 X2.2052 Y-2.04768 Z0.125
G1 Z-0.032 F5.0
Y-1.96892 F5.0
X2.28395
Y-2.04768
X2.2052
Z0.125
G0 X2.36271 Y-2.04768 Z0.125
G1 Z-0.032 F5.0
Y-1.96892 F5.0
X2.44147
Y-2.04768
X2.36271
Z0.125
G0 X2.52022 Y-2.04768 Z0.125
G1 Z-0.032 F5.0
Y-1.96892 F5.0
X2.59898
Y-2.04768
X2.52022
Z0.125
G0 X2.67774 Y-2.04768 Z0.125
G1 Z-0.032 F5.0
Y-1.96892 F5.0
X2.75649
Y-2.04768
X2.67774
Z0.125
G0 X-1.09197 Y-1.09 Z0.125
G1 Z-0.032 F5.0
Y-0.839997 F5.0
X-0.841966
Y-1.09
X-1.09197
Z0.125
G0 X5.03454 Y-1.09 Z0.125
G1 Z-0.032 F5.0
Y-0.839997 F5.0
X5.53454
```

Appendix D (Continued)

```
Y-1.09
X5.03454
Z0.125
G0 Z1
M5
M30
```

Appendix E: System Wiring Diagram

Figure A, Figure B, and Figure C serve to illustrate the electrical current pathways which provide power to each of the device's channels, measure temperature change, and temperature sensor signal conditioning.

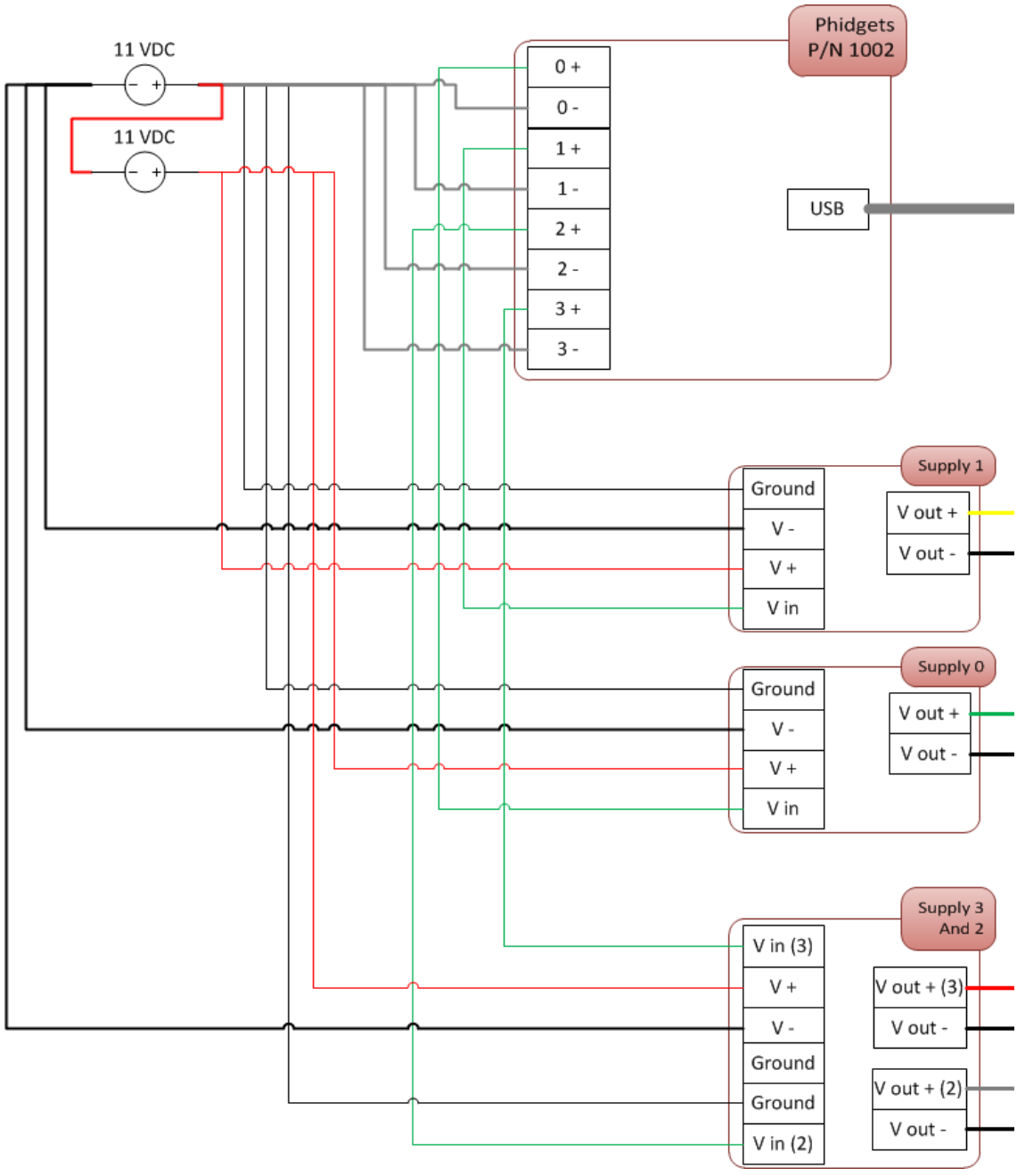

Figure A: Wiring diagram describing how power is supplied to the different channels (Supply for channels 0, 1, 2, and 3), and how the information is relayed to the Phidget P/N 1002 board

Appendix E (Continued)

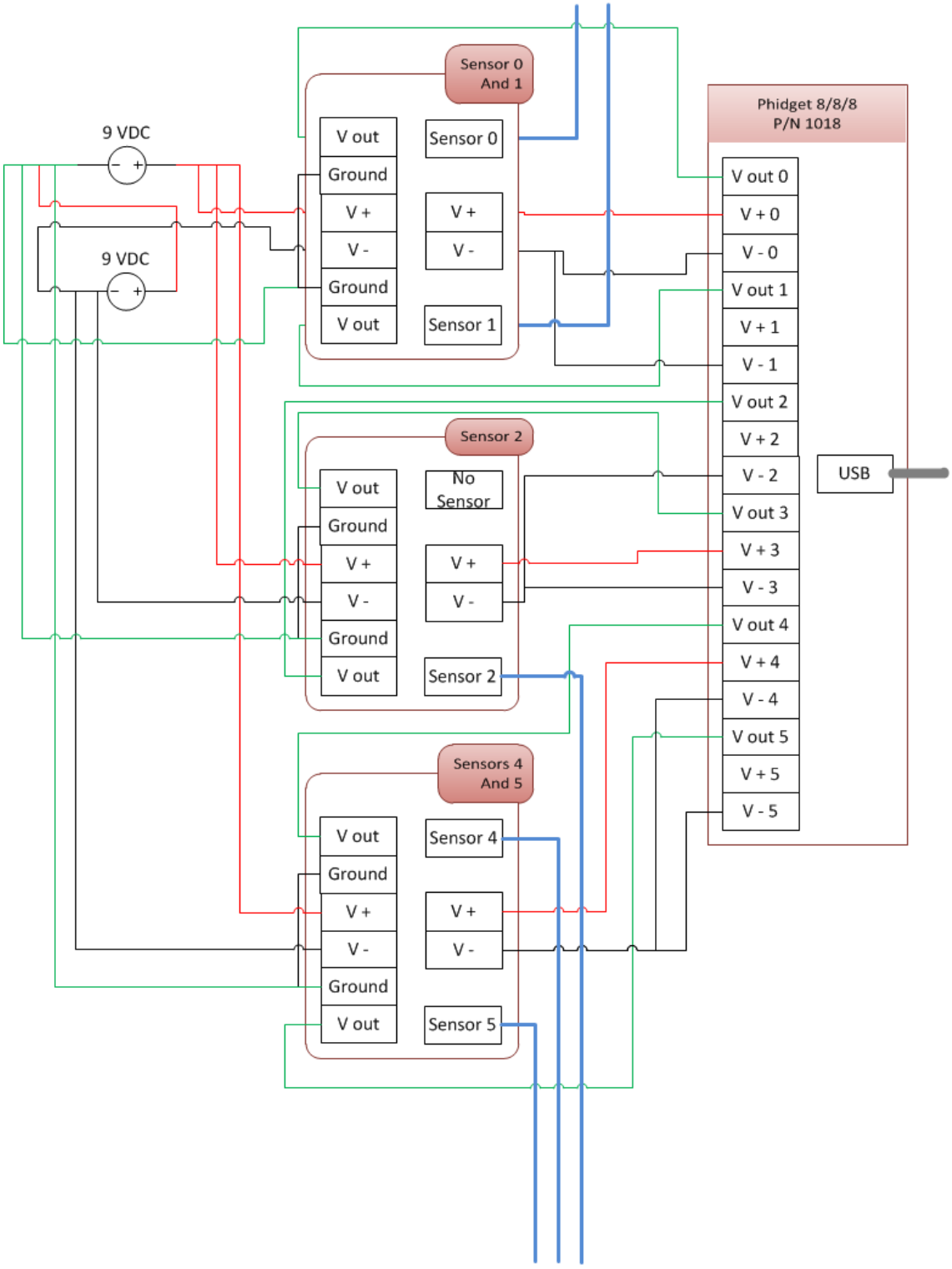

Figure B: Wiring diagram describing how power is supplied to the different temperature sensor boards (sensors 0, 1, 2, 4, and 5), and how the information is relayed to the Phidget 8/8/8 board

Appendix E (Continued)

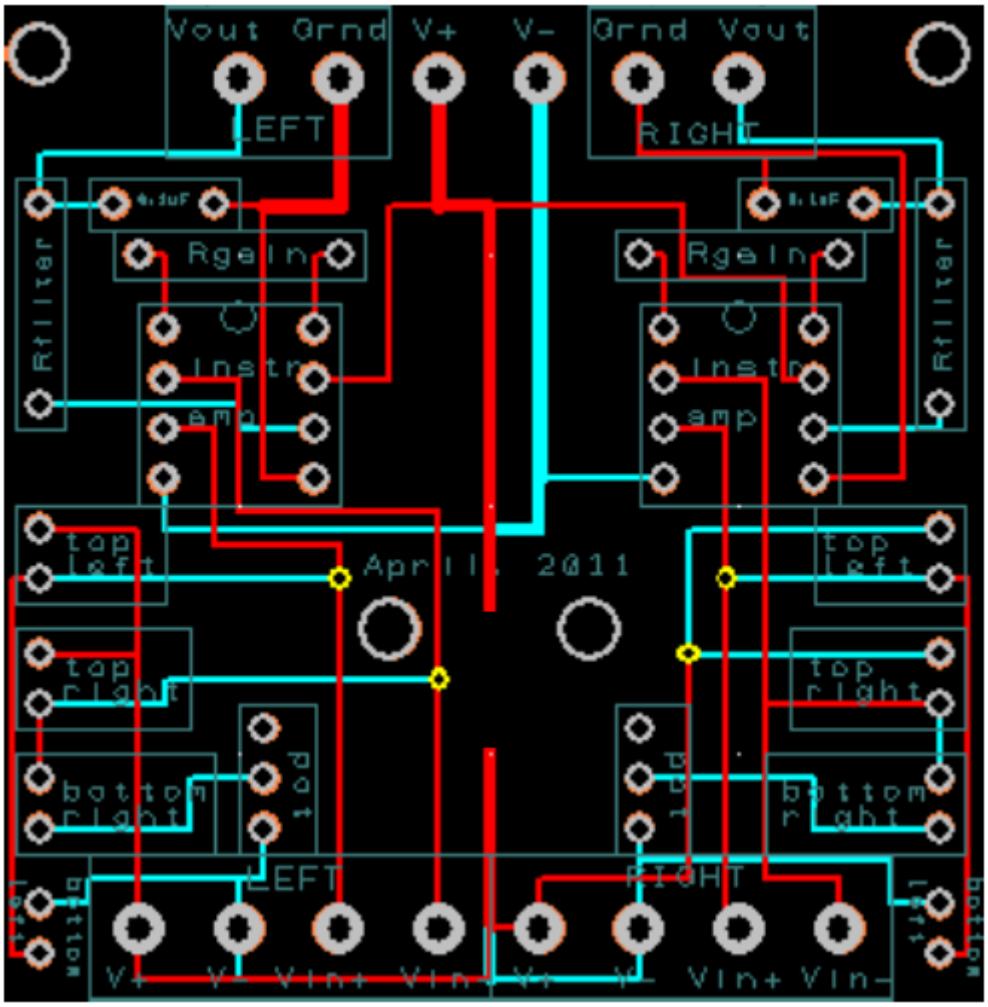

Figure C: Trace diagram for the temperature sensor circuit boards

Appendix F: Control System MATLAB Code

```
clc
clear all

if ~libisloaded('phidget21')
    loadlibrary phidget21 phidget21Matlab.h
end

%%
n=0; % initial iteration count
v(1)=0; % initial voltage level for sensor 0
v(2)=0; % initial voltage level for sensor 1
v(3)=0; % initial voltage level for sensor 2
v(6)=0; % initial voltage level for sensor 5
p=1; %pause length
er=.12; %error percentage reapplied to correct loop
jj=180; %iterations
desiredT = 66.0000; %desired tempsc=5; % sensor count
sc=5; % sensor count
ss=sc+1; % sensor count plus one, used for iternation number

%%
ptr=libpointer('int32Ptr',0);
Tptr = libpointer('int32Ptr',0); % temperature pointer

volptr=libpointer('doublePtr',0); % voltage pointer


if calllib('phidget21', 'CPhidgetAnalog_create', ptr)==0; %verifying
successful creation of pointer
    fprintf('good analog create\n')
    handle=get(ptr,'Value');
else
    fprintf('bad analog create\n')
    calllib('phidget21', 'CPhidgetAnalog_create', ptr)
end

handle=get(ptr,'Value'); %creates handle that retrieves pointer value
if calllib('phidget21', 'CPhidget_open', handle, -1)==0; %verify
successful handle operation
    calllib('phidget21', 'CPhidget_open', handle, -1);
    fprintf('good volt open\n')
else
    fprintf('bad volt open\n')
    calllib('phidget21', 'CPhidget_open', handle, -1)
    end

if calllib('phidget21','CPhidget_waitForAttachment',handle,2500)==0 %
2.5 second wait for Matlab to recognize the device via handle
attachment
   % n % debugging redundancy, check to see if attachment was
successful
   % Temperature Control
calllib('phidget21', 'CPhidgetInterfaceKit_create', Tptr);
```

Appendix F (Continued)

```
% Was previously used to verify a good attachment
if calllib('phidget21', 'CPhidgetAnalog_getOutputCount', handle,
ptr)==0
    fprintf('good output count\n')
    disp(get(ptr,'Value'));
else
    fprintf('bad output count\n')
    calllib('phidget21', 'CPhidgetAnalog_getOutputCount', handle, 0)
end

handleT = get(Tptr, 'Value'); %creates temp sensor handle that
retrieves pointer value


    if calllib('phidget21', 'CPhidget_open', handleT, -1)==0;
        calllib('phidget21', 'CPhidget_open', handleT, -1);
        fprintf('good temp open\n')
    else
        fprintf('bad temp open\n')
        calllib('phidget21', 'CPhidget_open', handleT, -1)
    end

if calllib('phidget21', 'CPhidget_waitForAttachment', handleT, 2500) ==
0
fprintf('good temp sensor wait\n')
    else
    calllib('phidget21', 'CPhidgetInterfaceKit_getSensorValue',
handleT, 0, Tptr)
    disp('Error in temp pointer, get sensor value')

end
    while n<jj

    fprintf('good volt wait\n')
    calllib('phidget21', 'CPhidgetAnalog_getVoltageMin', handle, 0,
volptr);
    minVoltage=get(volptr,'Value');
    calllib('phidget21', 'CPhidgetAnalog_getVoltageMax', handle, 0,
volptr);
    maxVoltage=get(volptr,'Value');

    %Temp Sensor Readings

    if calllib('phidget21', 'CPhidgetInterfaceKit_getSensorValue',
handleT, 0, Tptr) == 0

                x = get(Tptr, 'Value');
                x= cast (x, 'double');
                fprintf('Good temp sensor interface\n')
            else
                fprintf('bad temp sensor interface\n')
```

Appendix F (Continued)

```
                calllib('phidget21',
'CPhidgetInterfaceKit_getSensorValue', handleT, 0, Tptr)
    end

    if calllib('phidget21', 'CPhidgetInterfaceKit_getSensorValue',
handleT, 1, Tptr) == 0

                x(2) = get(Tptr, 'Value');
                x(2)= cast (x(2), 'double');
                fprintf('Good temp sensor interface\n')
            else
                fprintf('bad temp sensor interface\n')
                calllib('phidget21',
'CPhidgetInterfaceKit_getSensorValue', handleT, 1, Tptr)
    end

    if calllib('phidget21', 'CPhidgetInterfaceKit_getSensorValue',
handleT, 2, Tptr) == 0

                x(3) = get(Tptr, 'Value');
                x(3)= cast (x(3), 'double');
                fprintf('Good temp sensor interface\n')
            else
                fprintf('bad temp sensor interface\n')
                calllib('phidget21',
'CPhidgetInterfaceKit_getSensorValue', handleT, 2, Tptr)
    end

    if calllib('phidget21', 'CPhidgetInterfaceKit_getSensorValue',
handleT, 4, Tptr) == 0

                x(5) = get(Tptr, 'Value');
                x(5)= cast (x(5), 'double');
                fprintf('Good temp sensor interface\n')
            else
                fprintf('bad temp sensor interface\n')
                calllib('phidget21',
'CPhidgetInterfaceKit_getSensorValue', handleT, 4, Tptr)
     end

     if calllib('phidget21', 'CPhidgetInterfaceKit_getSensorValue',
handleT, 5, Tptr) == 0

                x(6) = get(Tptr, 'Value');
                x(6)= cast (x(6), 'double');
                fprintf('Good temp sensor interface\n')
            else
                fprintf('bad temp sensor interface\n')
                calllib('phidget21',
'CPhidgetInterfaceKit_getSensorValue', handleT, 5, Tptr)
     end
```

Appendix F (Continued)

```
%% Temperature Values and Finding Error
format long
    pause(p) % delay "" number of seconds until next iteration
    actualT(1)= 0.2419*x(1)+31.2475; %sensor 0
    actualT(2)= 0.2412*x(2)+29.2405; %sensor 1
    actualT(3)= 0.2569*x(3)+45.4281; %sensor 2
    actualT(5)= 0.2479*x(5)+32.1083; %sensor 4, ambient air temp
    actualT(6)= 0.2532*x(6)+45; %sensor 5
    error(1)= actualT(1) - desiredT;
    error(2)= actualT(2) - desiredT;
    error(3)= actualT(3) - desiredT;
    error(6)= actualT(6) - desiredT;

    %% Inputing Voltage Signal for Each Channel to Reach Desired Temp

    v(1)=-6; %v(1)+er*error(1) ; % voltage to sensor 0
    v(2)=-6; %v(2)+er*error(2) ; % voltage to sensor 1
    v(3)=-6; %v(3)+er*error(3) ; % voltage to sensor 2
    v(6)=-6; %v(6)+er*error(6) ; % voltage to sensor 5

    %%
    amp(1)=v(1)/1.5;
    amp(2)=v(2)/1.5;
    amp(3)=v(3)/1.5;
    amp(6)=v(6)/1.5;

  calllib('phidget21', 'CPhidgetAnalog_setVoltage',handle, 0, v(1));
  calllib('phidget21', 'CPhidgetAnalog_setVoltage',handle, 1, v(2));
  calllib('phidget21', 'CPhidgetAnalog_setVoltage',handle, 2, v(3));
  calllib('phidget21', 'CPhidgetAnalog_setVoltage',handle, 3, v(6));
  calllib('phidget21', 'CPhidgetAnalog_setEnabled',handle, 0, 1);
  calllib('phidget21', 'CPhidgetAnalog_setEnabled',handle, 1, 1);
  calllib('phidget21', 'CPhidgetAnalog_setEnabled',handle, 2, 1);
  calllib('phidget21', 'CPhidgetAnalog_setEnabled',handle, 3, 1);


   %% Saftey Measure
if abs(v(1)) >= 6.1;
    v;
    fprintf('Last measured voltage was %g.\n ',v)
    v(1)=0;
    calllib('phidget21', 'CPhidgetAnalog_setVoltage',handle, 0, v(1));
    disp('Trying to signal high voltage')
    break
end
if abs(v(2)) >= 6.1;
    v;
    fprintf('Last measured voltage was %g.\n ',v)
    v(2)=0;
    calllib('phidget21', 'CPhidgetAnalog_setVoltage',handle, 0, v(2));
    disp('Trying to signal high voltage')
    break
```

Appendix F (Continued)

```
end
if abs(v(3)) >= 6.1;
    v;
    fprintf('Last measured voltage was %g.\n ',v)
    v(3)=0;
    calllib('phidget21', 'CPhidgetAnalog_setVoltage',handle, 0, v(3));
    disp('Trying to signal high voltage')
    break
end
if abs(v(6)) >= 6.1;
    v;
    fprintf('Last measured voltage was %g.\n ',v)
    v(6)=0;
    calllib('phidget21', 'CPhidgetAnalog_setVoltage',handle, 0, v(6));
    disp('Trying to signal high voltage')
    break
end


%%
    n=n+1;
    lt=p*n; %lapsed time


   time=datestr(now,0);
    fprintf('\n\nDesired Temp, %g F\n',desiredT)
    fprintf('Ambient Air Temp, %g F\n',actualT(5))
    fprintf('Actual Temp, %g F, %g F, %g F, %g F
\n',actualT(1),actualT(2),actualT(3),actualT(6))
    fprintf('Error, %g F, %g F, %g F, %g
F\n',error(1),error(2),error(3),error(6))
    fprintf('Voltage Signal, %g V, %g V, %g V, %g
V\n',v(1),v(2),v(3),v(6))
    fprintf('Signal Amperage, %g A, %g A, %g A, %g
A\n',amp(1),amp(2),amp(3),amp(6))
    fprintf('Iteration Count, %g\n',n)
  A(:,n)=[p er desiredT actualT(1) actualT(2) actualT(3) actualT(6)
error(1) error(2) error(3) error(6) v(1) v(2) v(3) v(6) amp(1) amp(2)
amp(3) amp(6) lt n];
  B(n,:)=[time];
    end

    if n==jj;
            v(1)=0;
            v(2)=0;
            v(3)=0;
            v(6)=0;
        calllib('phidget21', 'CPhidgetAnalog_setVoltage',handle, 0,
v(1));
        calllib('phidget21', 'CPhidgetAnalog_setVoltage',handle, 1,
v(2));
        calllib('phidget21', 'CPhidgetAnalog_setVoltage',handle, 2,
v(3));
```

Appendix F (Continued)

```
        calllib('phidget21', 'CPhidgetAnalog_setVoltage',handle, 3,
v(6));
    end


else
    fprintf('bad volt wait\n')
    calllib('phidget21','CPhidget_waitForAttachment',handle,2500)
end


actualT
calllib('phidget21', 'CPhidget_close', handle);
calllib('phidget21', 'CPhidget_delete', handle);
calllib('phidget21', 'CPhidget_close', handleT);
calllib('phidget21', 'CPhidget_delete', handleT);

% rand
xlswrite('C:\Documents and
Settings\camarti9\Desktop\testresult.xls',A,1)
xlswrite('C:\Documents and
Settings\camarti9\Desktop\testresult.xls',B,2)
%% Error/Problem Log
%Its running without the enable code Sept 23rd
%Oct 7th, now runs with enable

%Tried to enable other channels with the following code, no repsonse
from
%other channels.
%   calllib('phidget21', 'CPhidgetAnalog_setEnabled',handle, 0, 1);
%   calllib('phidget21', 'CPhidgetAnalog_setEnabled',handle, 1, 2);
%   calllib('phidget21', 'CPhidgetAnalog_setEnabled',handle, 2, 3);
%   calllib('phidget21', 'CPhidgetAnalog_setEnabled',handle, 5, 4);


%   calllib('phidget21', 'CPhidgetAnalog_setVoltage',handle, 0, v(1));
%   calllib('phidget21', 'CPhidgetAnalog_setVoltage',handle, 1, v(2));
%   calllib('phidget21', 'CPhidgetAnalog_setVoltage',handle, 2, v(3));
%   calllib('phidget21', 'CPhidgetAnalog_setVoltage',handle, 3, v(6));
%   calllib('phidget21', 'CPhidgetAnalog_setEnabled',handle, 0, 1);
%   calllib('phidget21', 'CPhidgetAnalog_setEnabled',handle, 1, 1);
%   calllib('phidget21', 'CPhidgetAnalog_setEnabled',handle, 2, 1);
%   calllib('phidget21', 'CPhidgetAnalog_setEnabled',handle, 5, 1);

%   calllib('phidget21', 'CPhidgetAnalog_setVoltage',handle, 0, v(1));
%   calllib('phidget21', 'CPhidgetAnalog_setVoltage',handle, 1, v(2));
%   calllib('phidget21', 'CPhidgetAnalog_setVoltage',handle, 2, v(3));
%   calllib('phidget21', 'CPhidgetAnalog_setVoltage',handle, 3, v(6));
%   calllib('phidget21', 'CPhidgetAnalog_setEnabled',handle, 0, 1);
%   calllib('phidget21', 'CPhidgetAnalog_setEnabled',handle, 1, 1);
%   calllib('phidget21', 'CPhidgetAnalog_setEnabled',handle, 2, 1);
%   calllib('phidget21', 'CPhidgetAnalog_setEnabled',handle, 3, 1);
```

Appendix F (Continued)

```
%   calllib('phidget21', 'CPhidgetAnalog_setVoltage',handle, 0, v(1));
%   calllib('phidget21', 'CPhidgetAnalog_setVoltage',handle, 1, v(2));
%   calllib('phidget21', 'CPhidgetAnalog_setVoltage',handle, 2, v(3));
%   calllib('phidget21', 'CPhidgetAnalog_setVoltage',handle, 3, v(6));
%   calllib('phidget21', 'CPhidgetAnalog_setEnabled',handle, 0, 1);

%Verified output count still good
%Yellow and black wired heat sink is becoming very hot

%Oct 11 Notes
% Original Temp Equations
%     actualT(1)= 0.2419*x(1)+31.2475; %sensor 0
%     actualT(2)= 0.2412*x(2)+29.2405; %sensor 1
%     actualT(3)= 0.2569*x(3)+45.4281; %sensor 2
%     actualT(5)= 0.2479*x(5)+32.1083; %sensor 4, ambient air temp
%     actualT(6)= 0.2532*x(6)+45; %sensor 5
```

Appendix G: MATLAB Temperature Sensor Measurement Code

```
clc
clear all
loadlibrary phidget21 phidget21Matlab.h; % make sure the library is in
your current directory

rand % placed to make sure the code ran a new iteration
n=0;
sc=5; % sensor count
ss=sc+1; % sensor count plus one, used for iternation number
format long
while n<120
    %Create space for interface kit
    ptr = libpointer('int32Ptr',0);
    calllib('phidget21', 'CPhidgetInterfaceKit_create', ptr);

    handle = get(ptr, 'Value');

    calllib('phidget21', 'CPhidget_open', handle, -1);

    if calllib('phidget21', 'CPhidget_waitForAttachment', handle, 2500)
== 0


    dataptr = libpointer('int32Ptr',0);
            %get the value, make sure it's valids
            for i=1:ss
                b=i-1;
                 if calllib('phidget21',
'CPhidgetInterfaceKit_getSensorValue', handle, b, dataptr) == 0
                    x(i) = get(dataptr, 'Value');
                    x = cast (x, 'double'); % converts matrix data
type to double

                 end
            end

            else
                disp('Could not open InterfaceKit') % if the
calllib('phidget21', 'CPhidget_waitForAttachment', handle, 2500) ==
something other than 0 than the number is a diagnostic code
                x=0;
   end


    %Closes phidget connection when finished
    calllib('phidget21', 'CPhidget_close', handle);
    calllib('phidget21', 'CPhidget_delete', handle);

    %Calculates actual temperature (F) from sensor using conversion
    actualT(1)= 0.24156*x(1)+31.769; %sensor 0
    actualT(2)= 0.23974*x(2)+29.588; %sensor 1
    actualT(3)= 0.25024*x(3)+47.043; %sensor 2
```

Appendix G (Continued)

```
    actualT(5)= 0.24498*x(5)+32.907; %sensor 4
    actualT(6)= 0.25*x(6)+45.9; %sensor 5


    n = n+1; %increase iteration count
    A(n,:)=[actualT(1) actualT(2) actualT(3) actualT(5) actualT(6)]; %
temperature array
    fprintf('%5.0f %10.6f %10.6f %10.6f %10.6f %10.6f \n', n,
actualT(1), actualT(2), actualT(3), actualT(5), actualT(6)) % display
temperature array

end
% xlswrite('C:\** INSERT FILE LOCATION HERE**.xls',A) % saves data to a
spreadsheet
```

Appendix H: Measured Temperature Profiles of the Final Assembly

H.1 Purple Channel

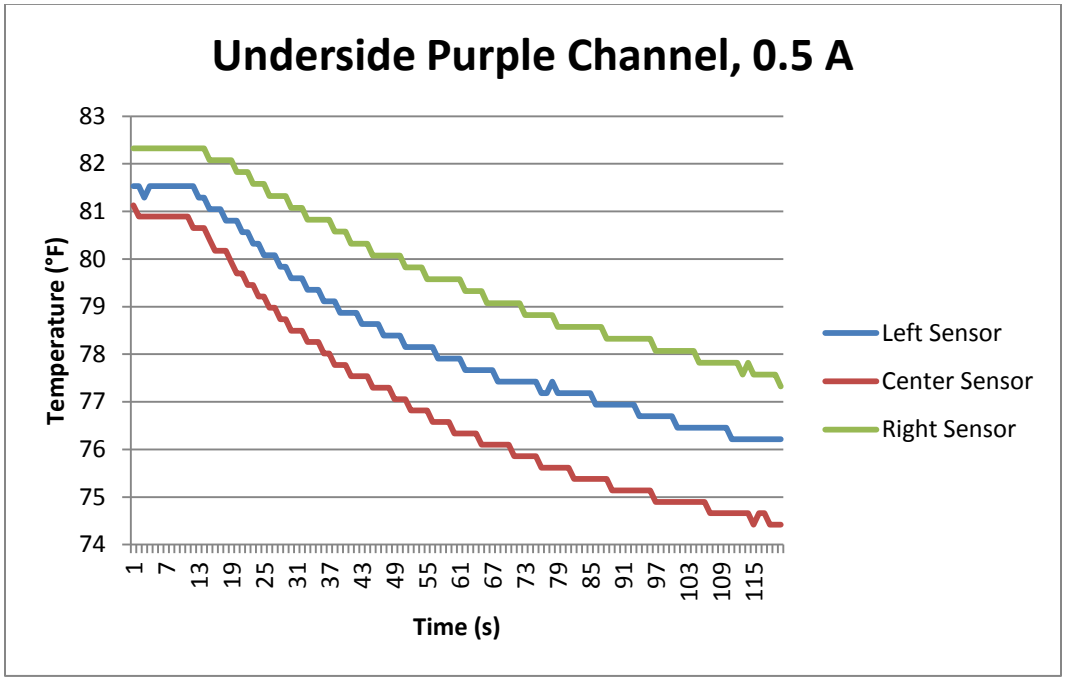

Figure D: Underside purple channel temperature profile at 0.5 amps

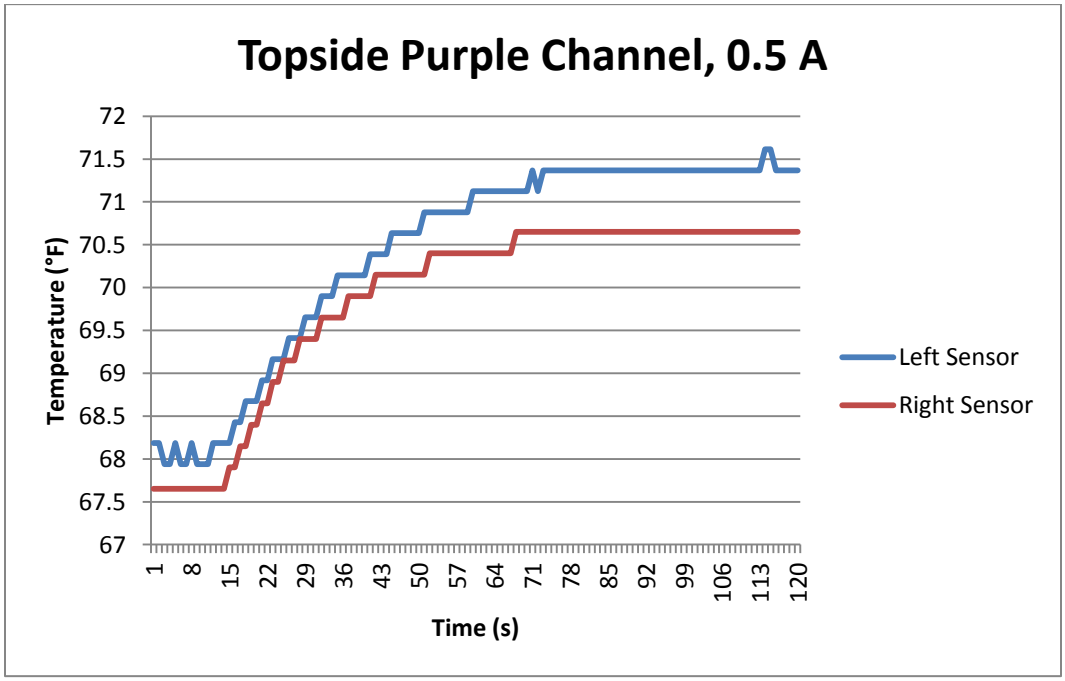

Figure E: Topside purple channel temperature profile at 0.5 amps

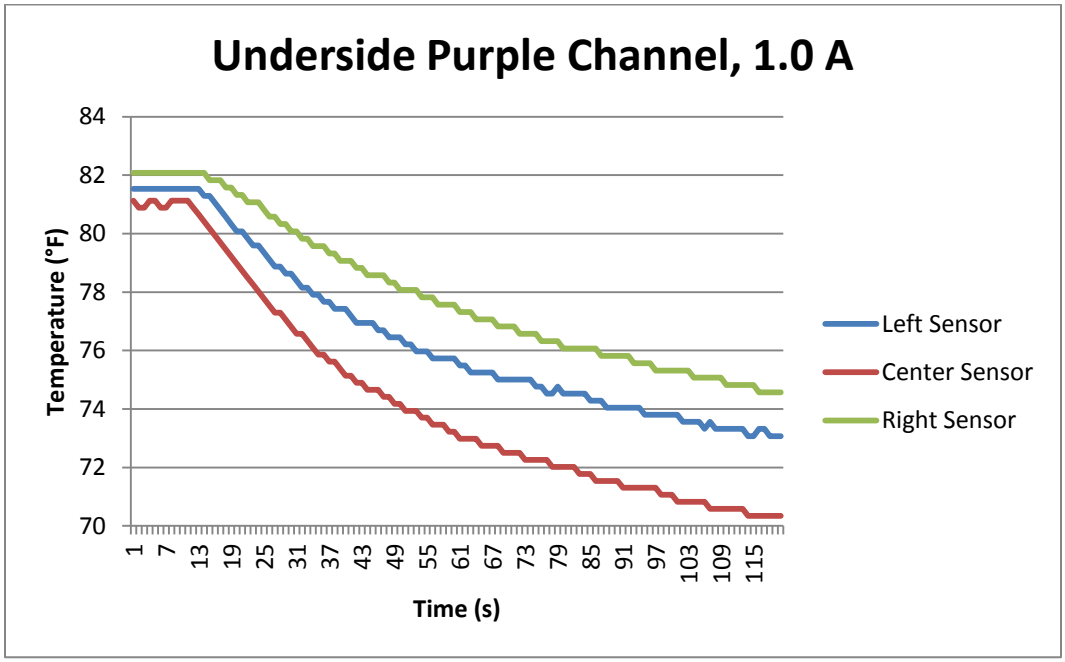

Figure F: Underside purple channel temperature profile at 1.0 amps

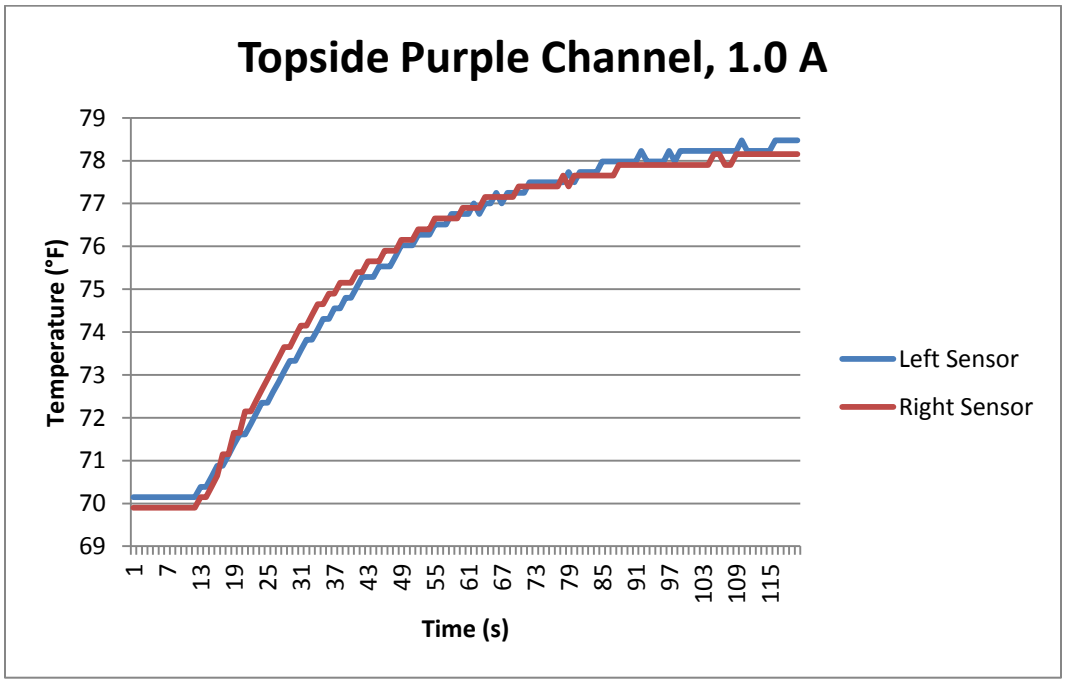

Figure G: Topside purple channel temperature profile at 1.0 amps

Appendix H (Continued)

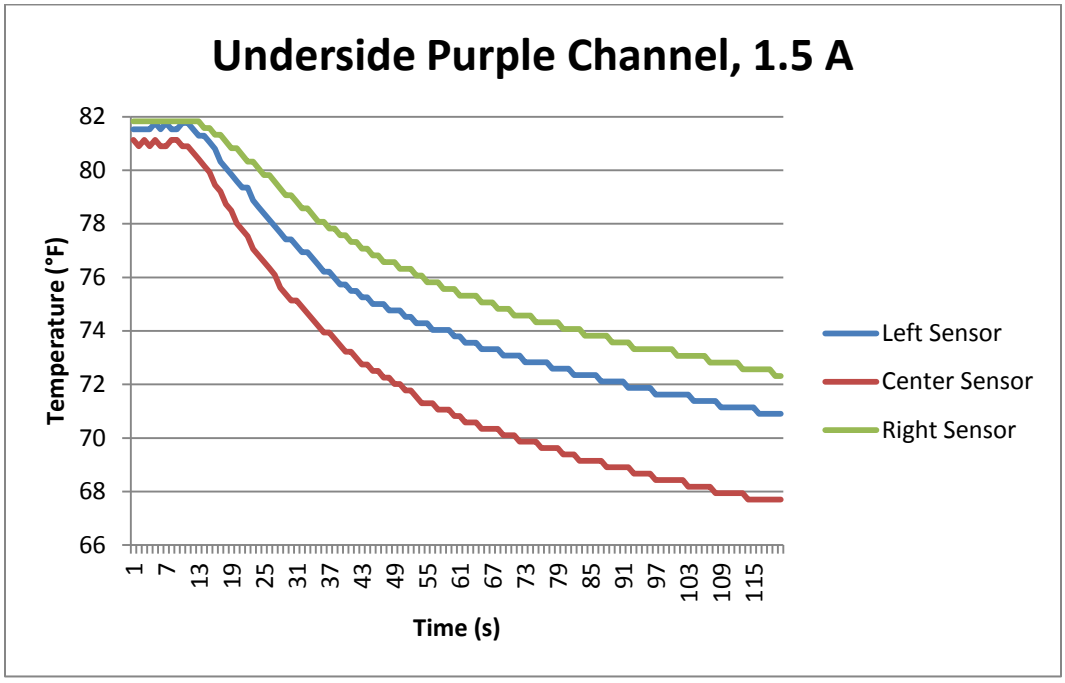

Figure H: Underside purple channel temperature profile at 1.5 amps

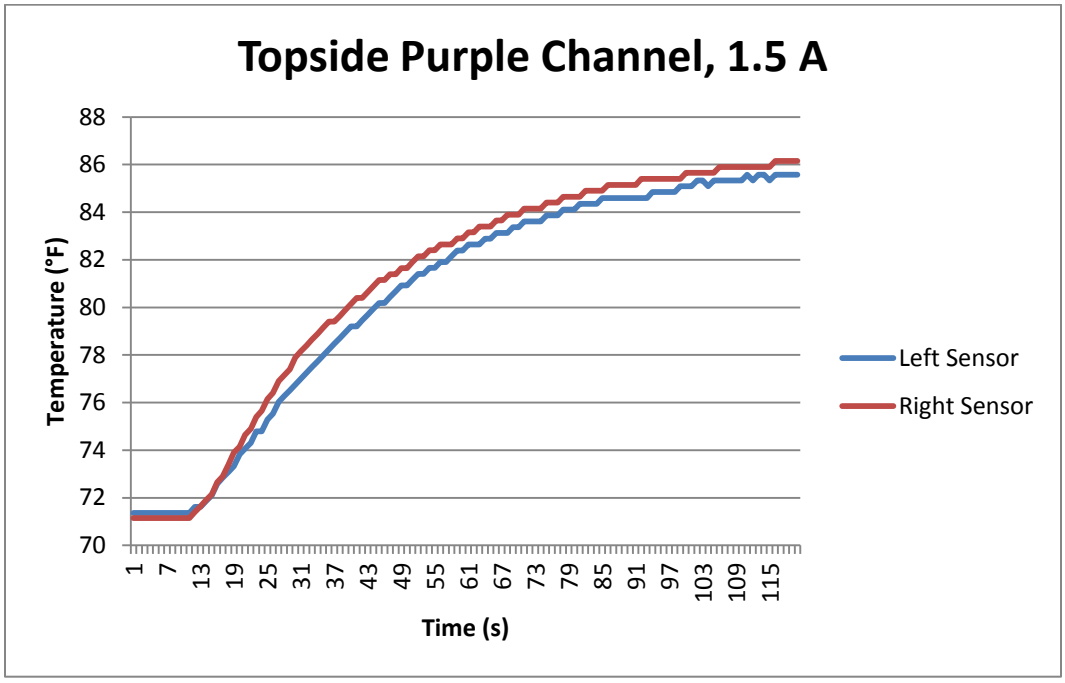

Figure I: Topside purple channel temperature profile at 1.5 amps

Appendix H (Continued)

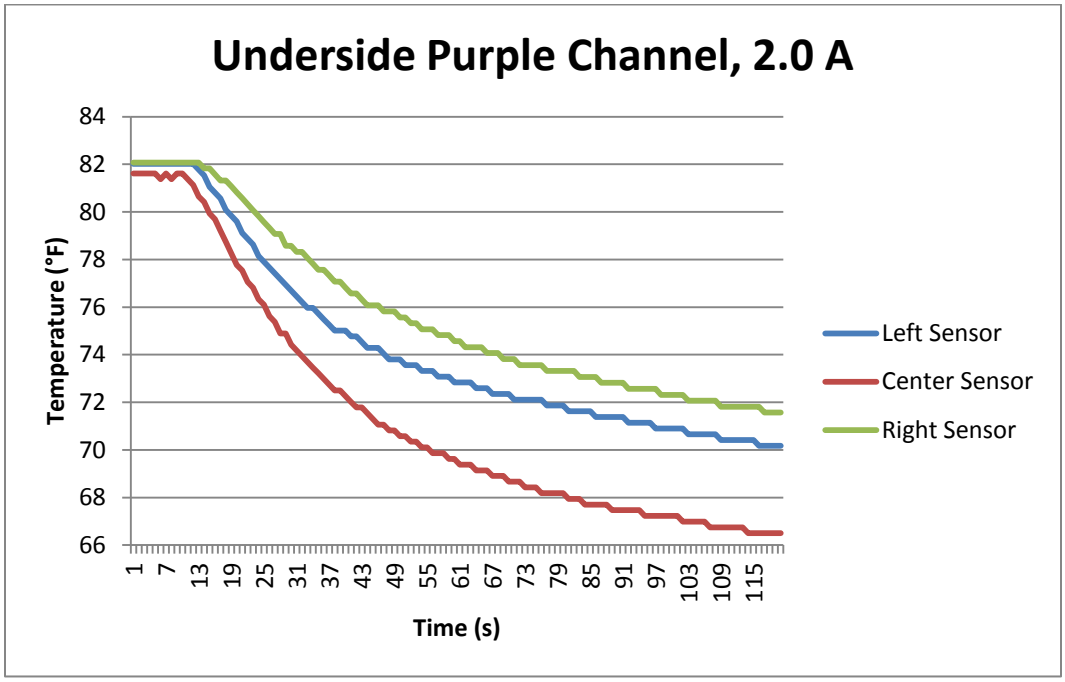

Figure J: Underside purple channel temperature profile at 2.0 amps

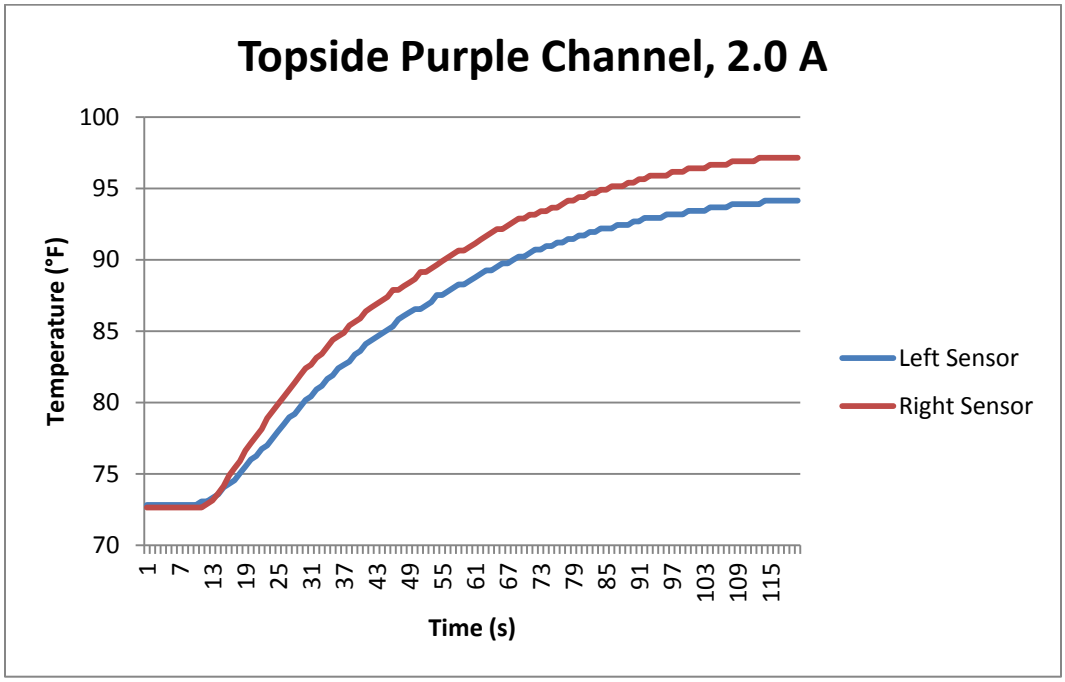

Figure K: Topside purple channel temperature profile at 2.0 amps

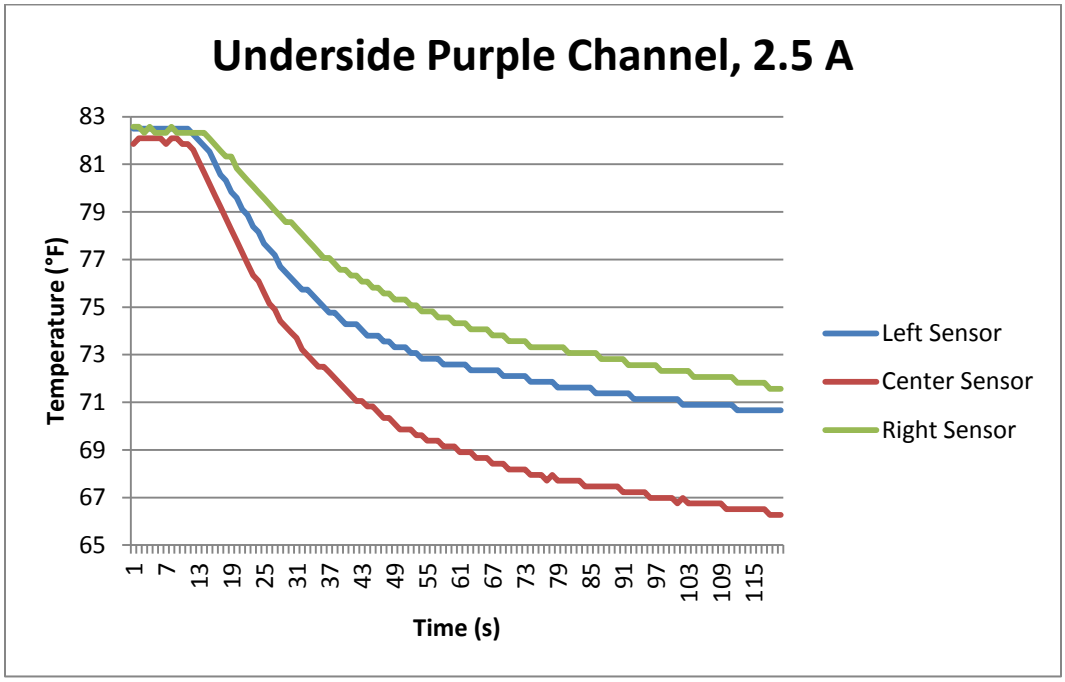

Figure L: Underside purple channel temperature profile at 2.5 amps

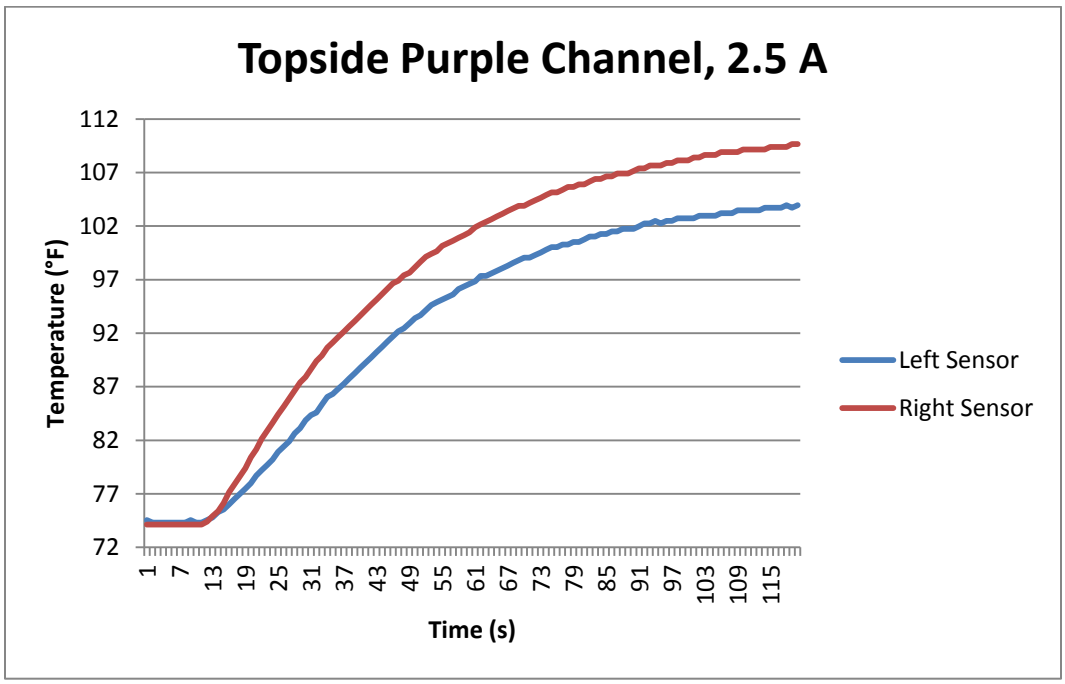

Figure M: Topside purple channel temperature profile at 2.5 amps

Appendix H (Continued)

H.2 Yellow Channel

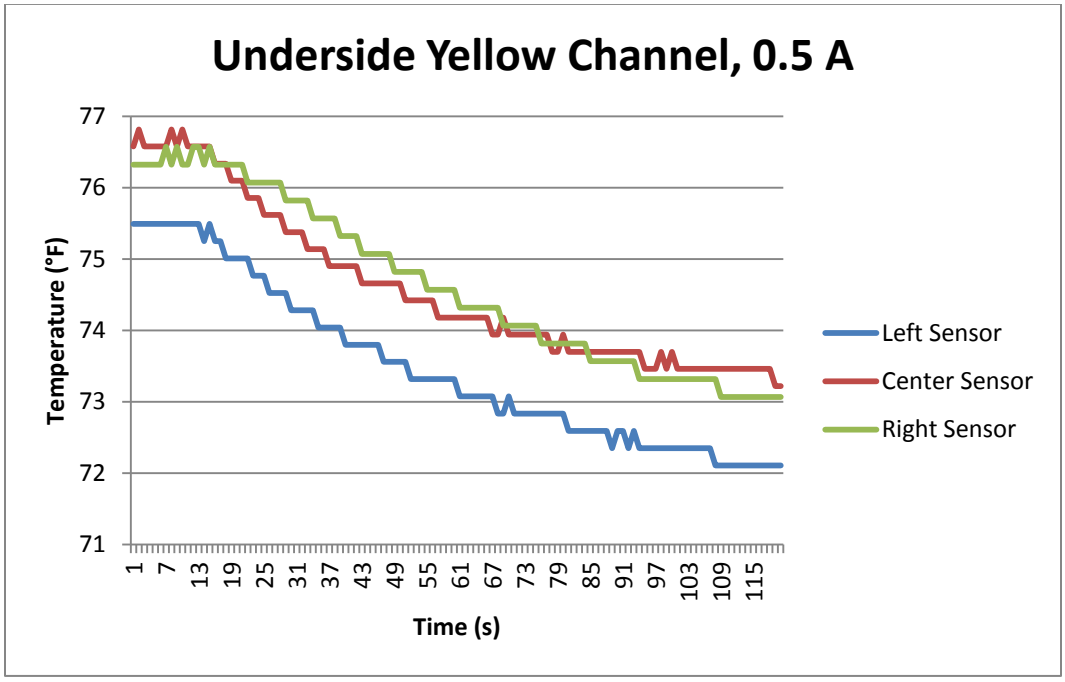

Figure N: Underside yellow channel temperature profile at 0.5 amps

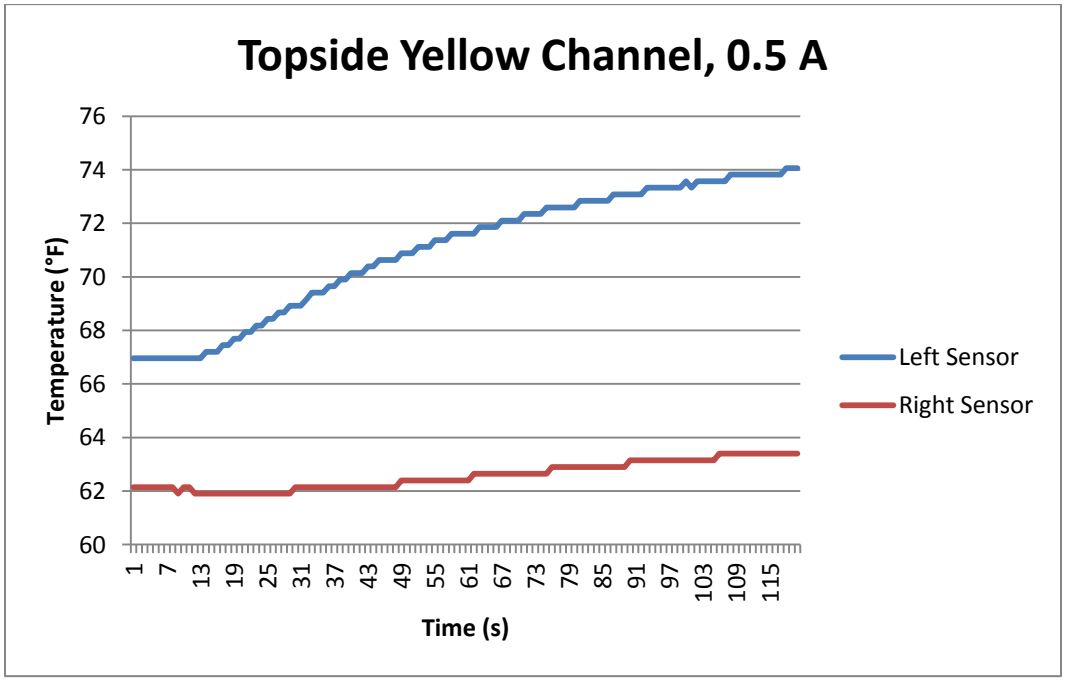

Figure O: Topside yellow channel temperature profile at 0.5 amps

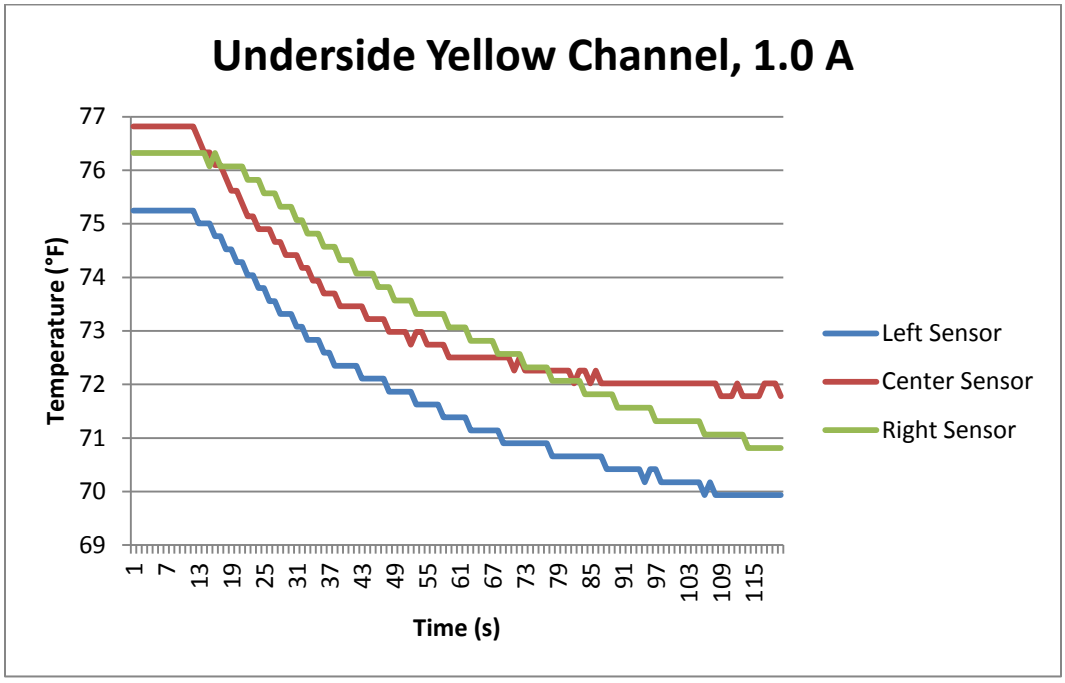

Figure P: Underside yellow channel temperature profile at 1.0 amps

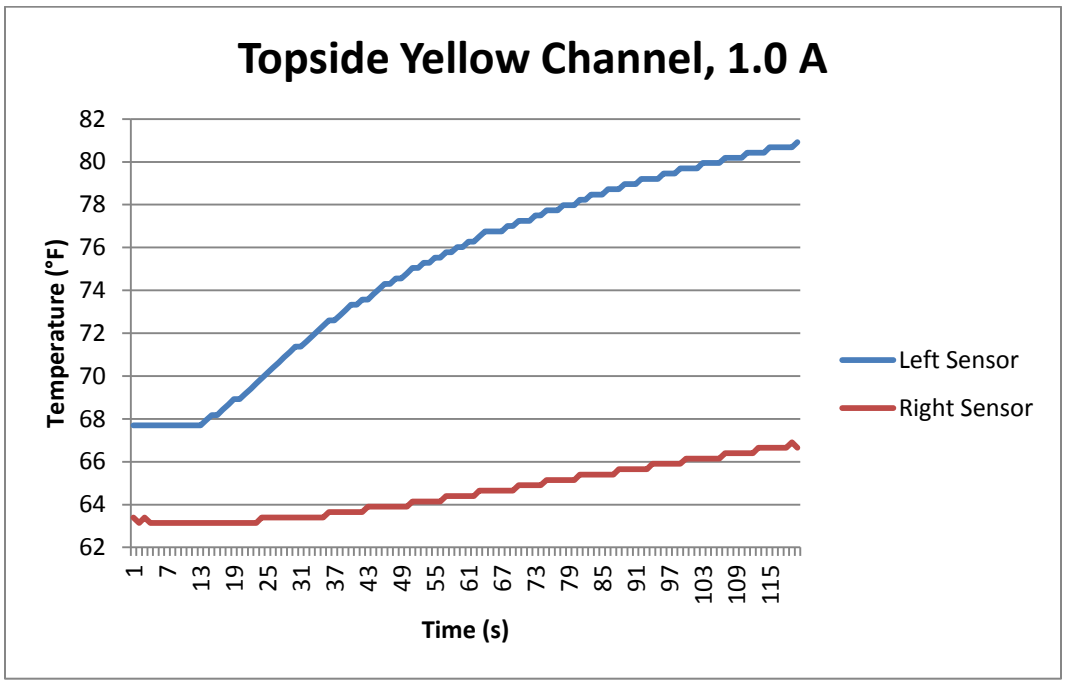

Figure Q: Topside yellow channel temperature profile at 1.0 amps

Appendix H (Continued)

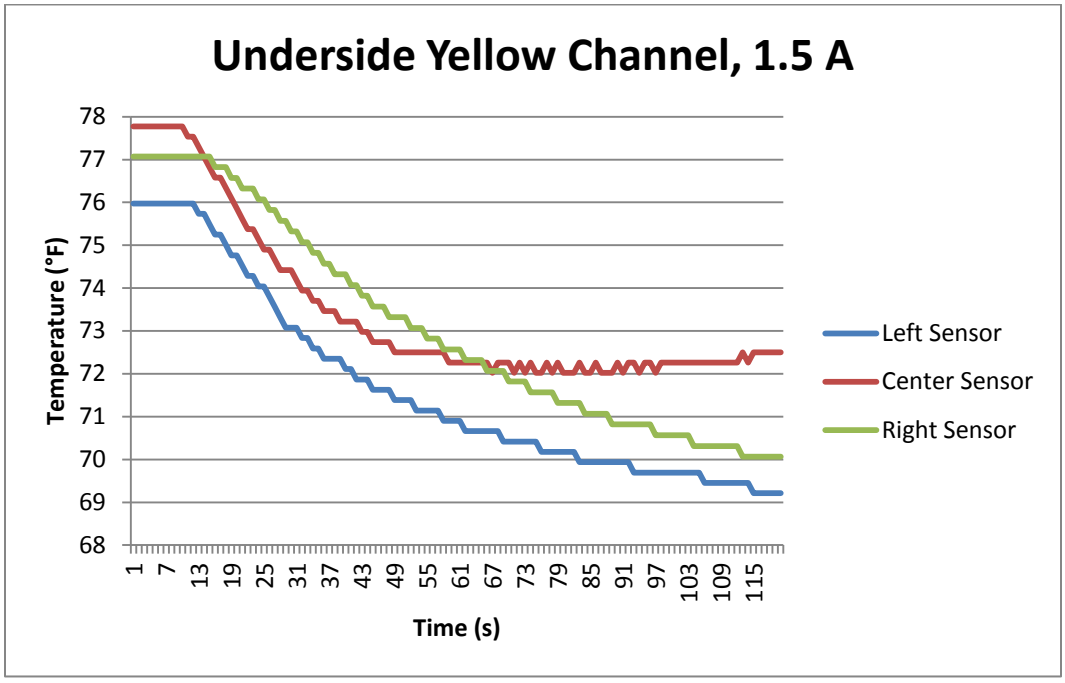

Figure R: Underside yellow channel temperature profile at 1.5 amps

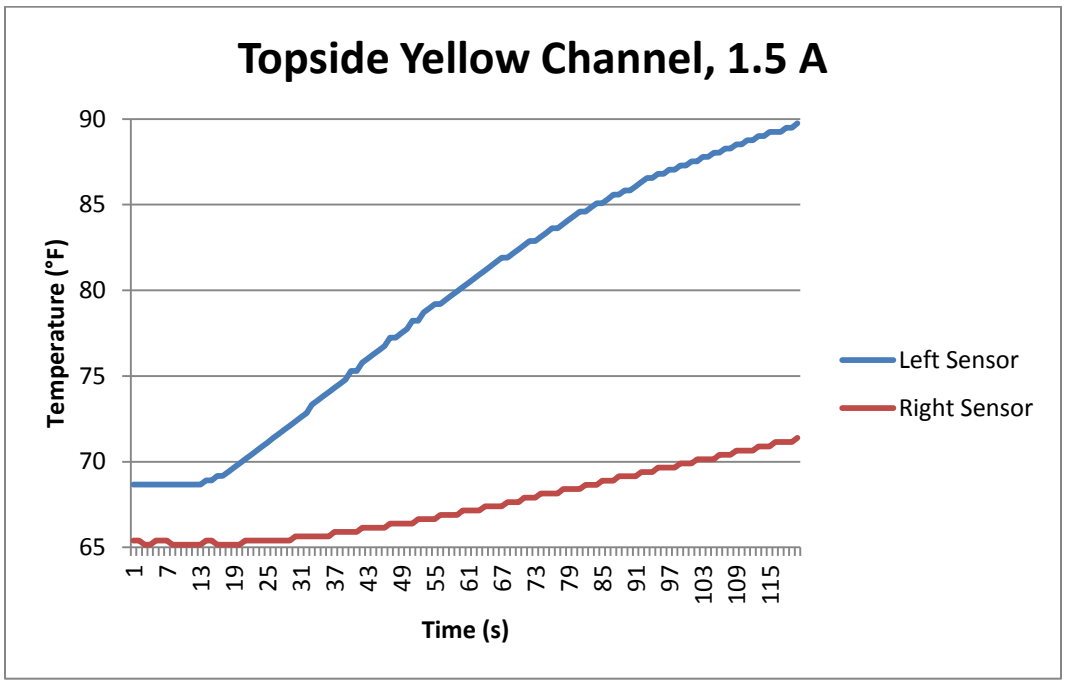

Figure S: Topside yellow channel temperature profile at 1.5 amps

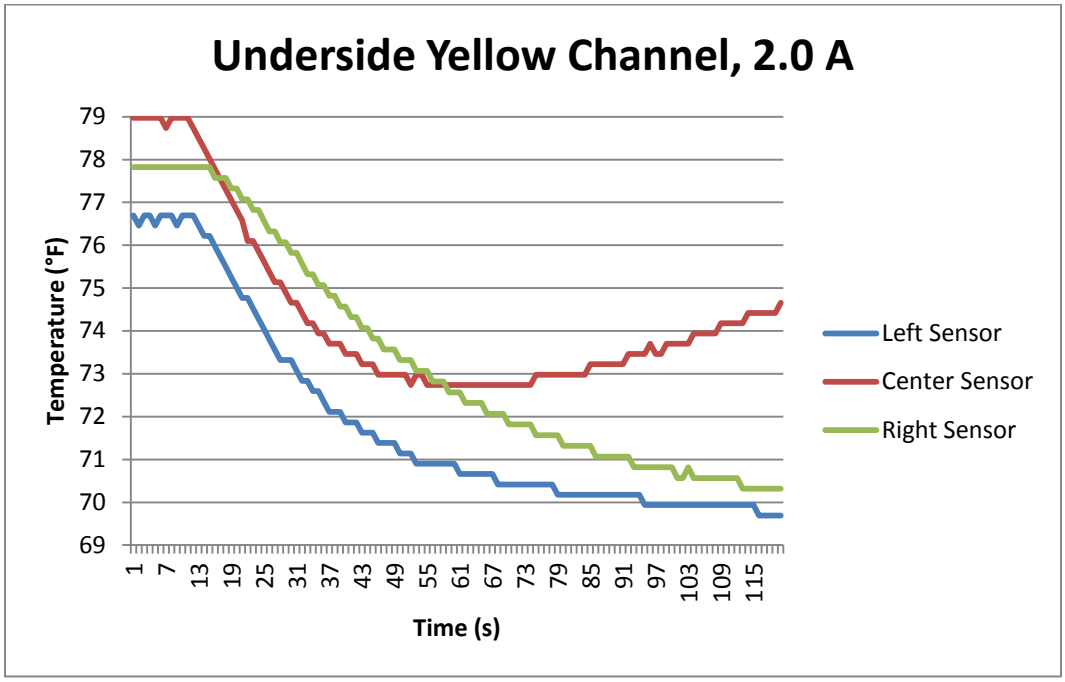

Figure T: Underside yellow channel temperature profile at 2.0 amps

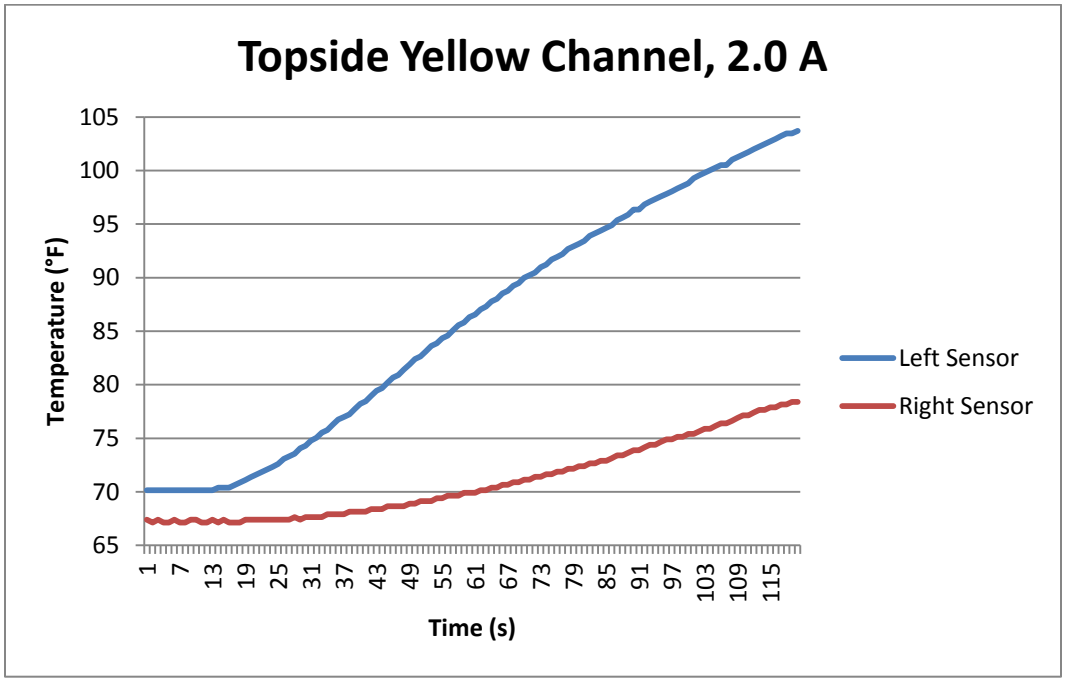

Figure U: Topside yellow channel temperature profile at 2.0 amps

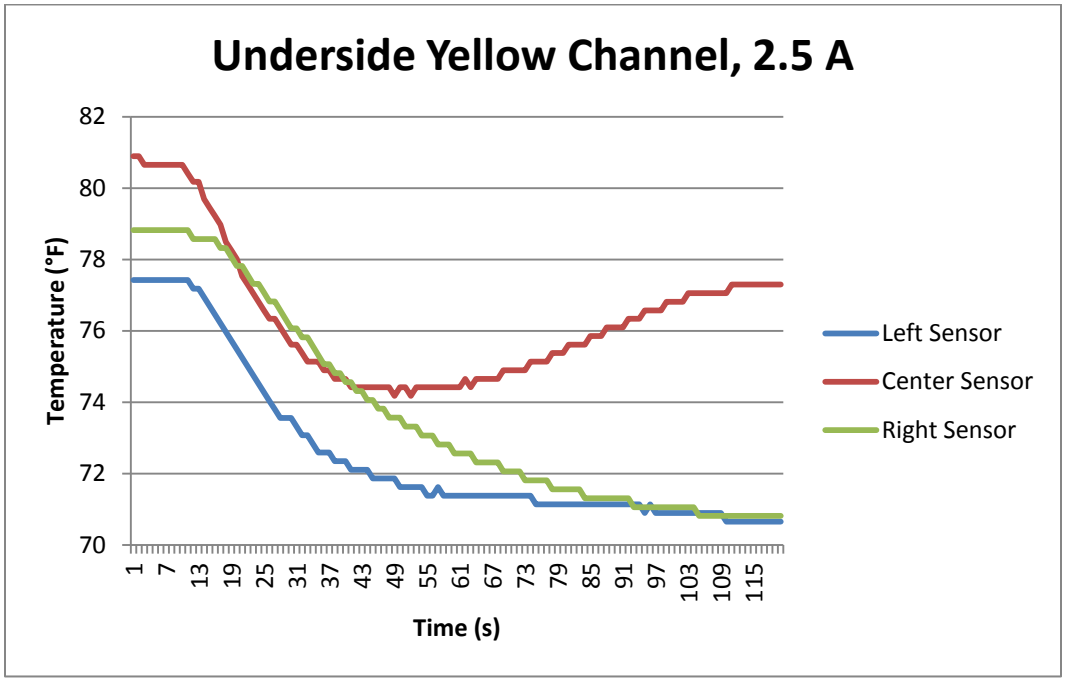

Figure V: Underside yellow channel temperature profile at 2.5 amps

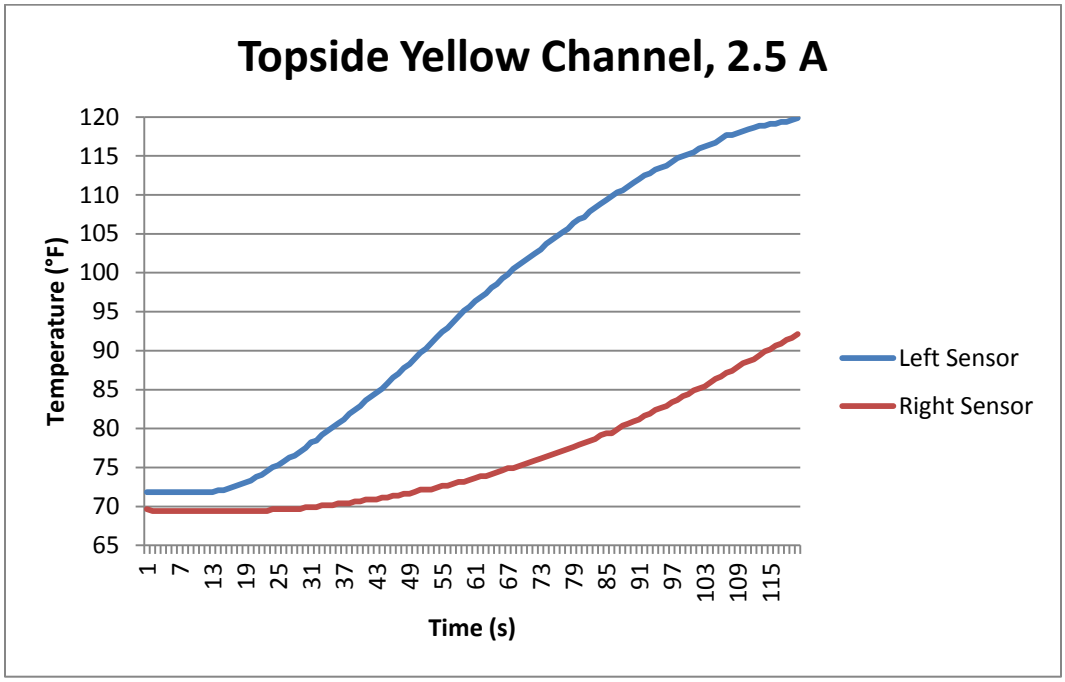

Figure W: Topside yellow channel temperature profile at 2.5 amps

Appendix H (Continued)

H.3 Blue Channel

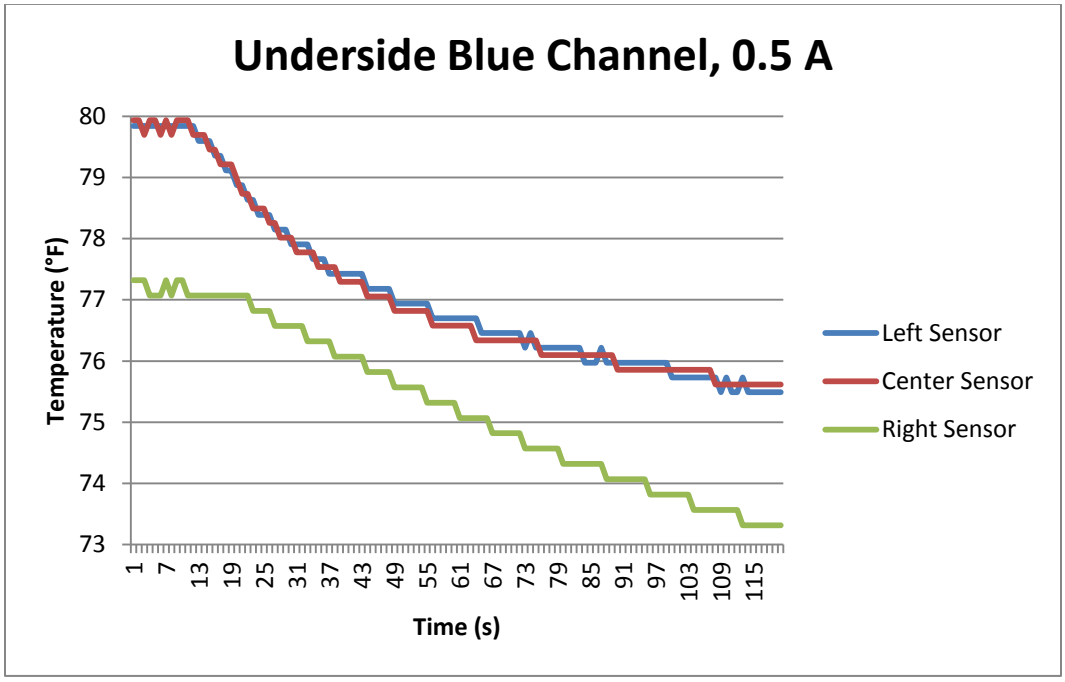

Figure X: Underside blue channel temperature profile at 0.5 amps

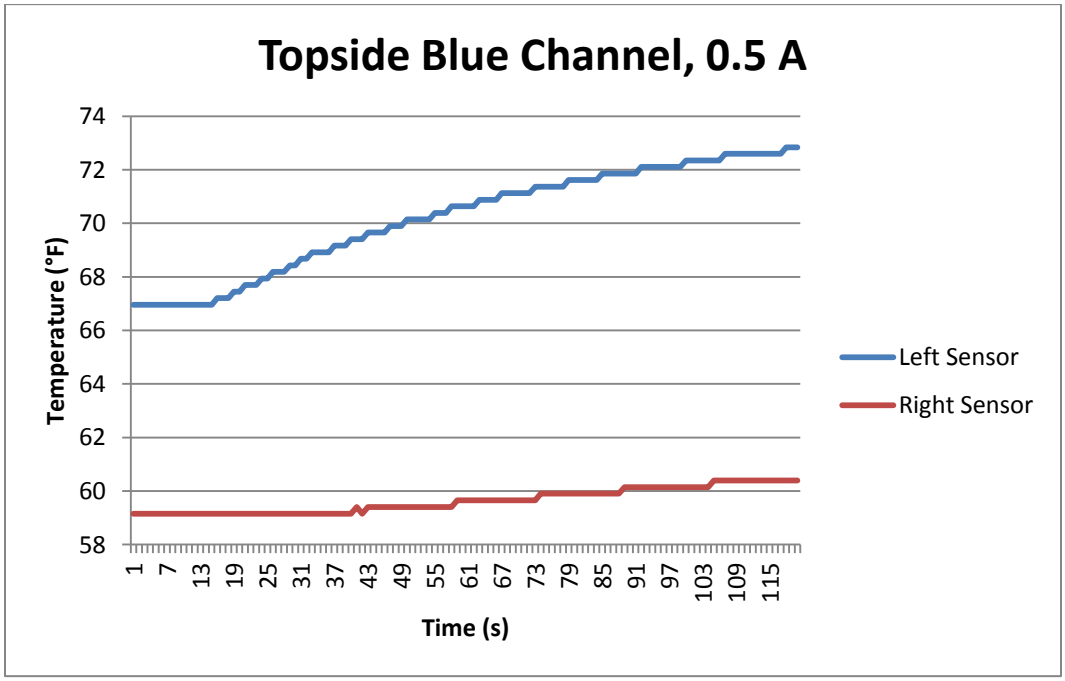

Figure Y: Topside blue channel temperature profile at 0.5 amps

Appendix H (Continued)

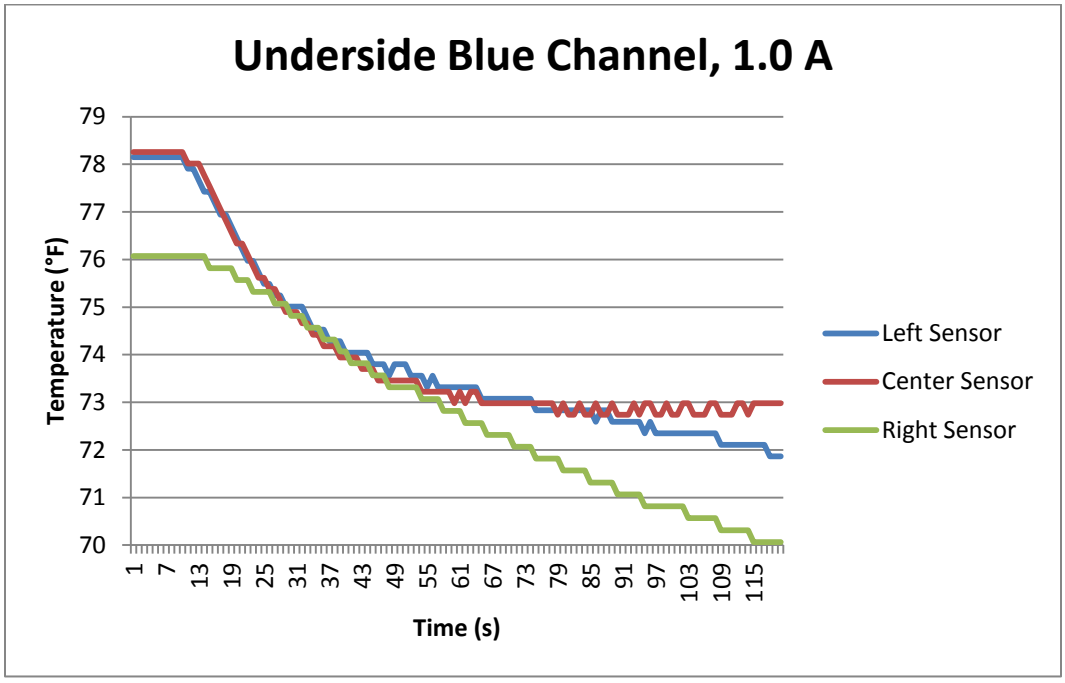

Figure Z: Underside blue channel temperature profile at 1.0 amps

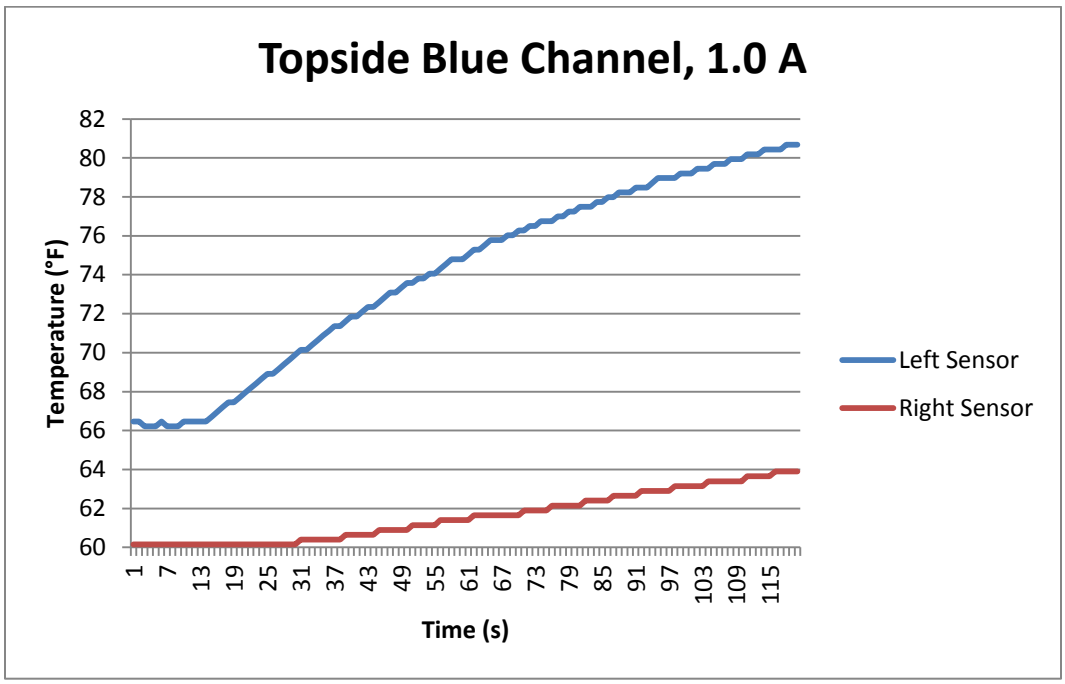

Figure AA: Topside blue channel temperature profile at 1.0 amps

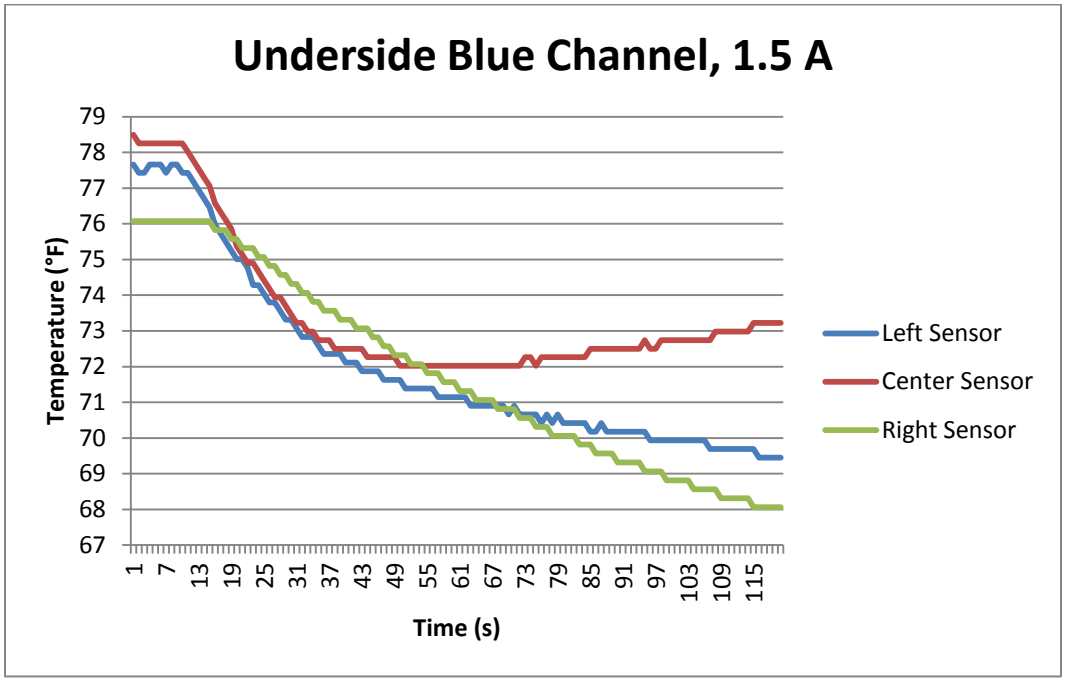

Figure BB: Underside blue channel temperature profile at 1.5 amps

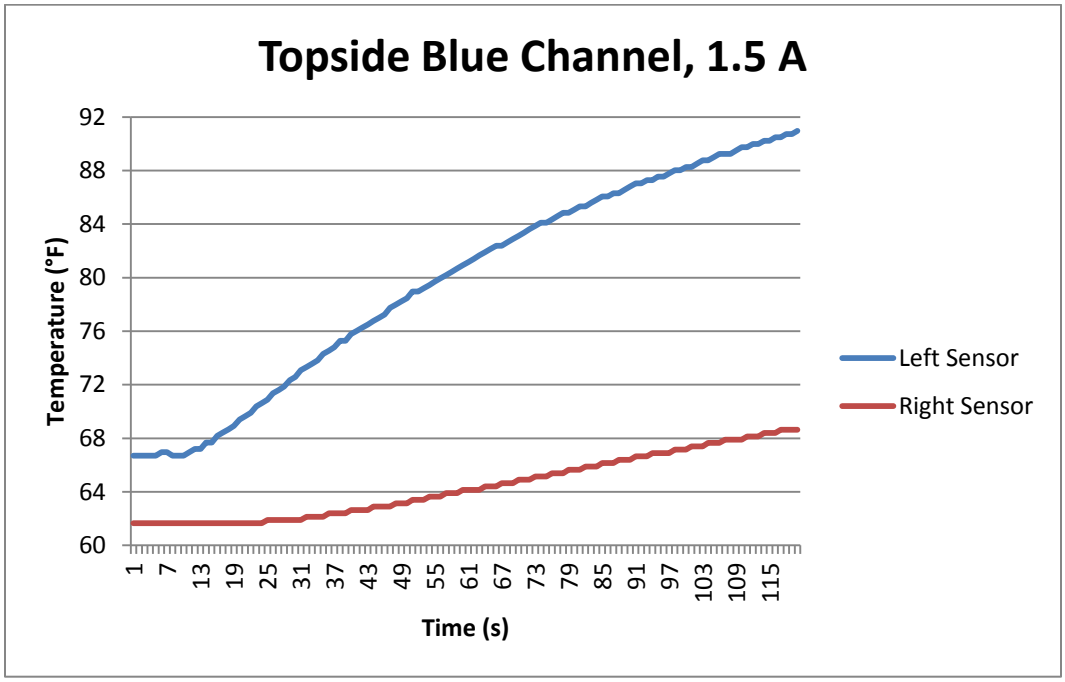

Figure CC: Topside blue channel temperature profile at 1.5 amps

Appendix H (Continued)

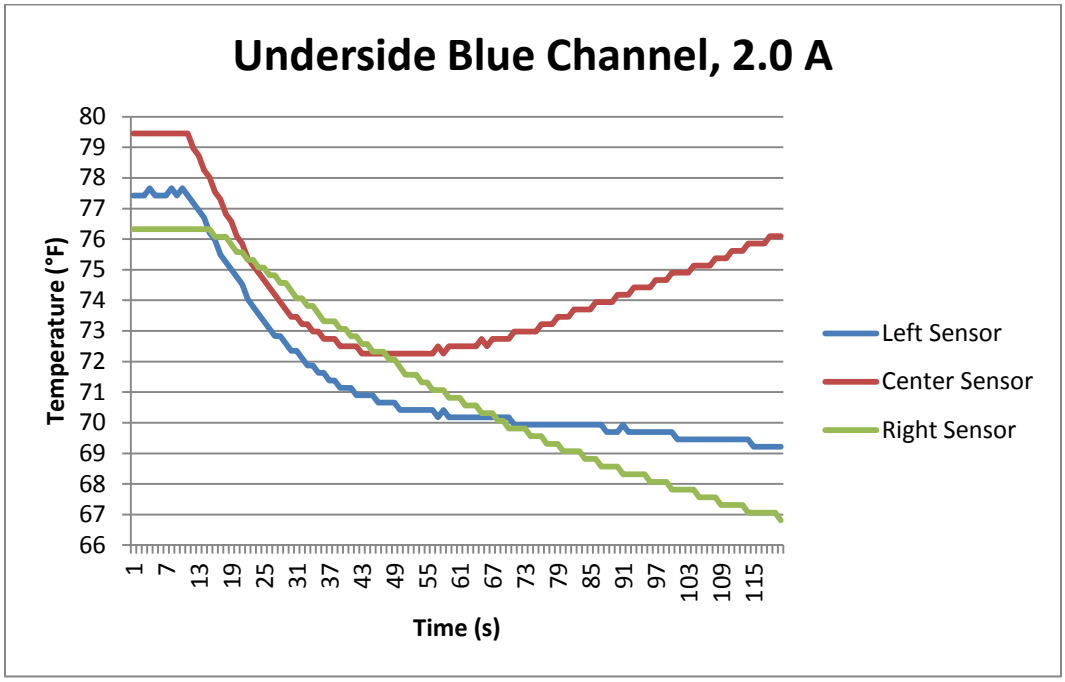

Figure DD: Underside blue channel temperature profile at 2.0 amps

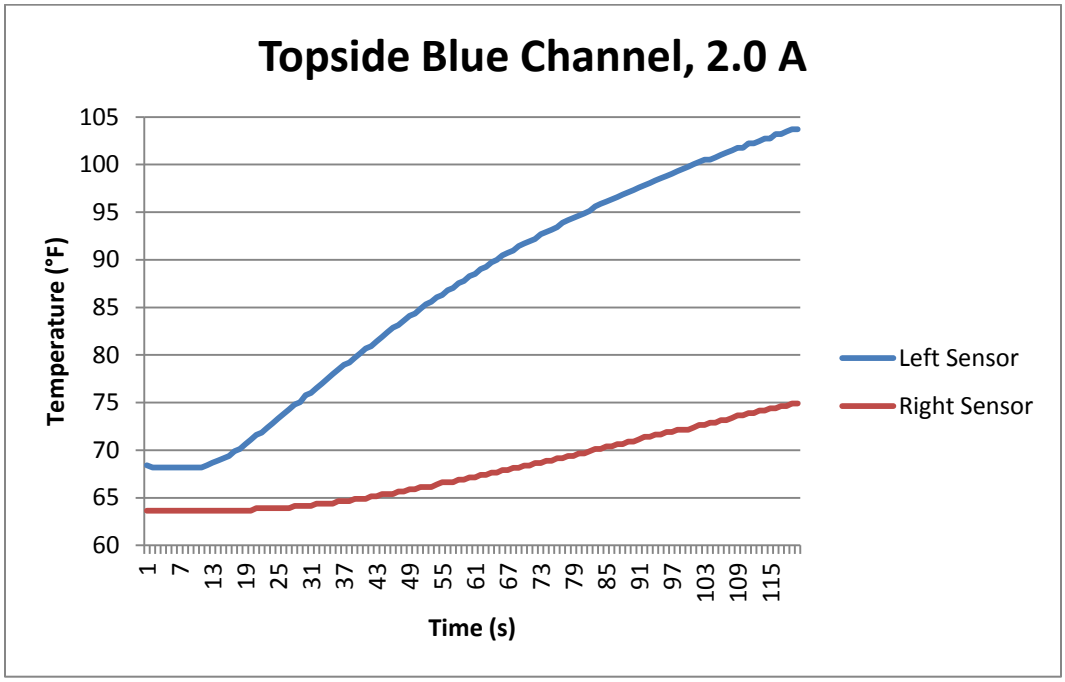

Figure EE: Topside blue channel temperature profile at 2.0 amps

Appendix H (Continued)

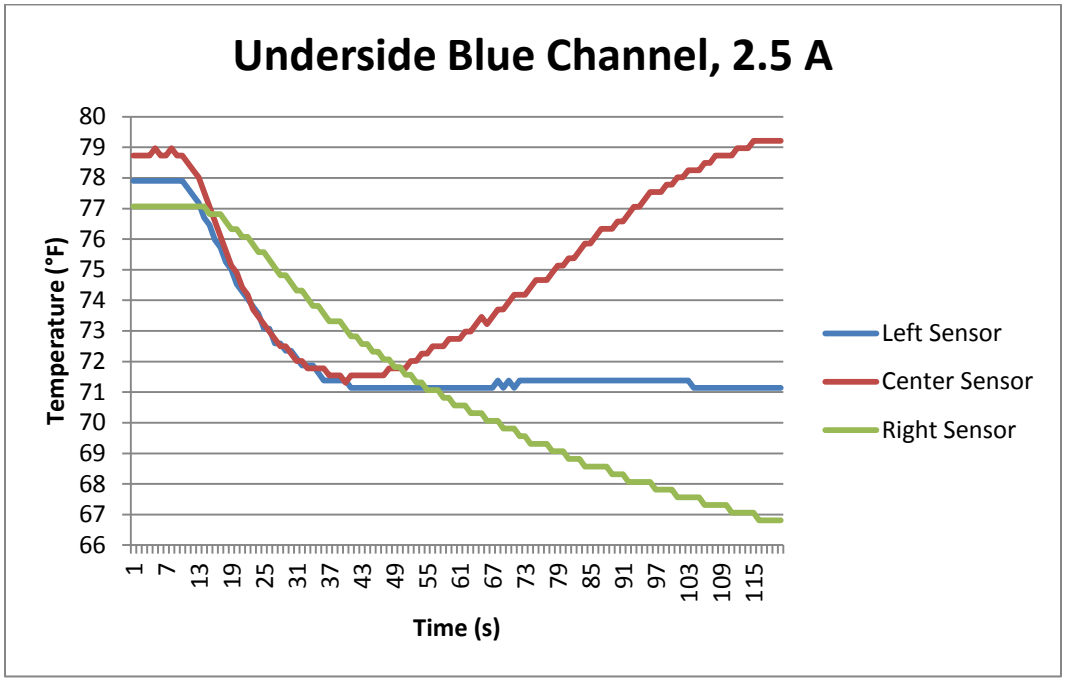

Figure FF: Underside blue channel temperature profile at 2.5 amps

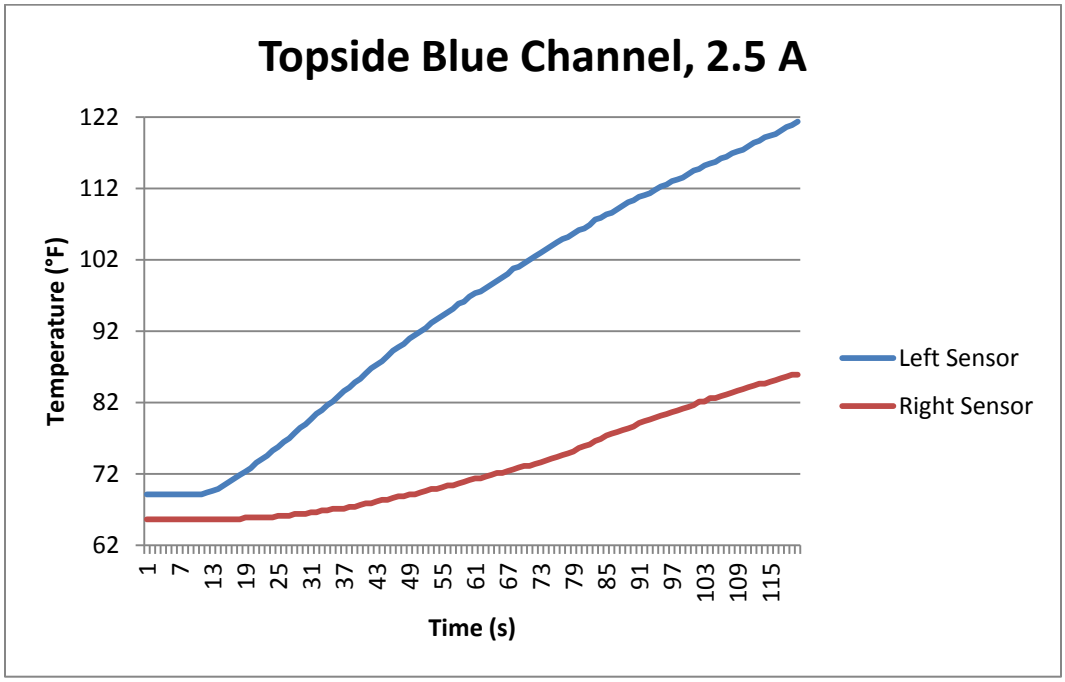

Figure GG: Topside blue channel temperature profile at 2.5 amps

Appendix H (Continued)

H.4 Green Channel

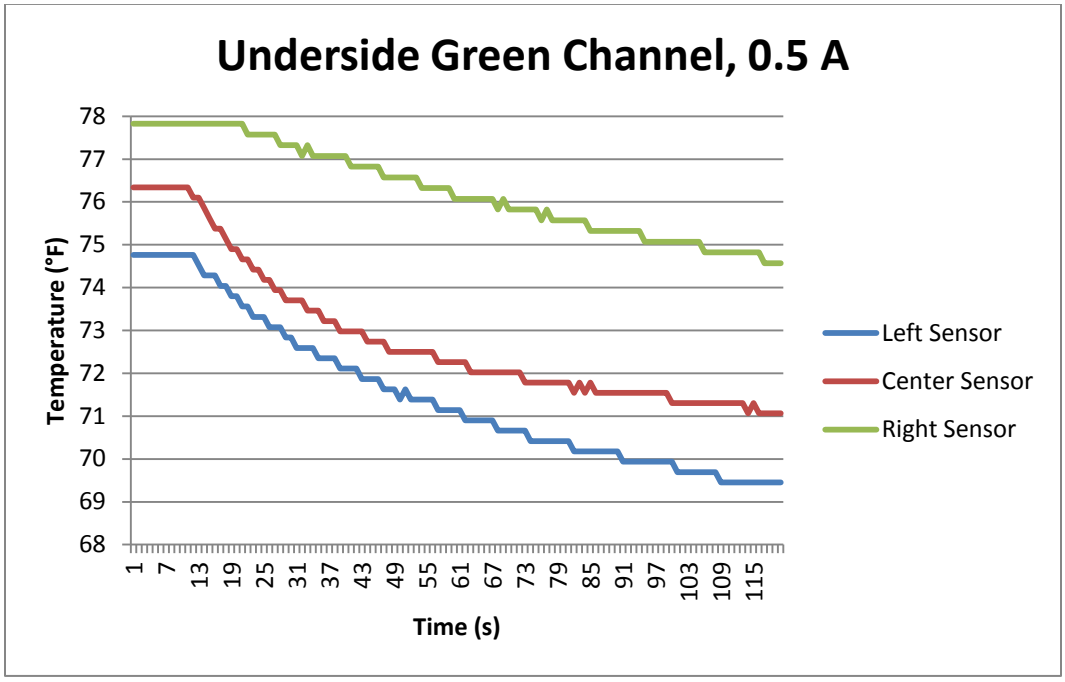

Figure HH: Underside green channel temperature profile at 0.5 amps

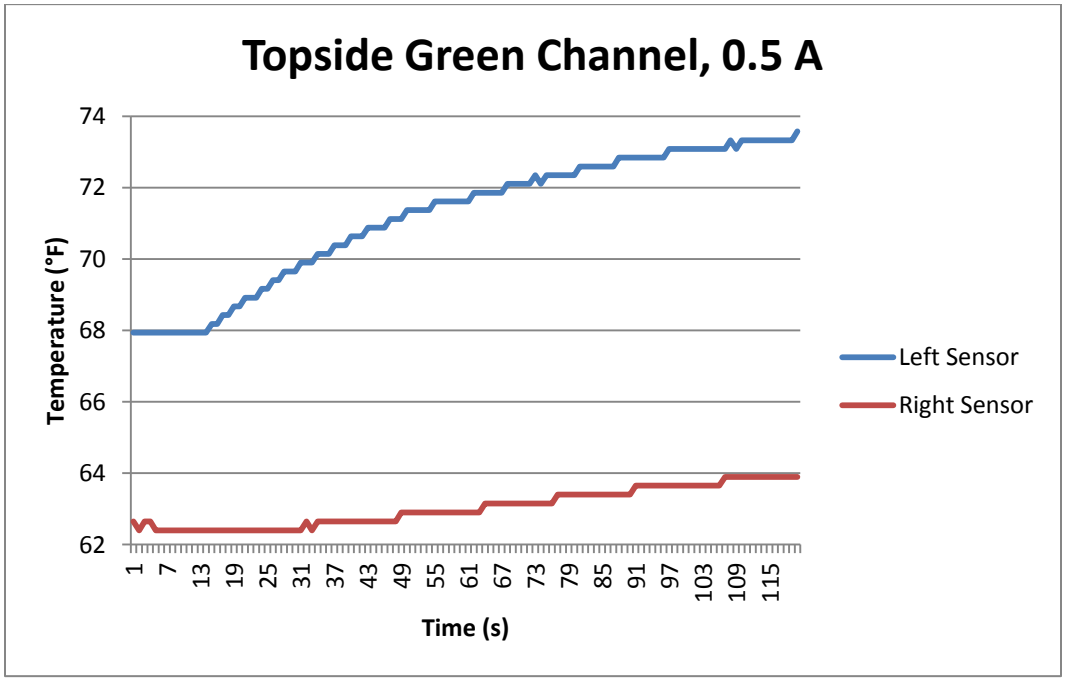

Figure II: Topside green channel temperature profile at 0.5 amps

Appendix H (Continued)

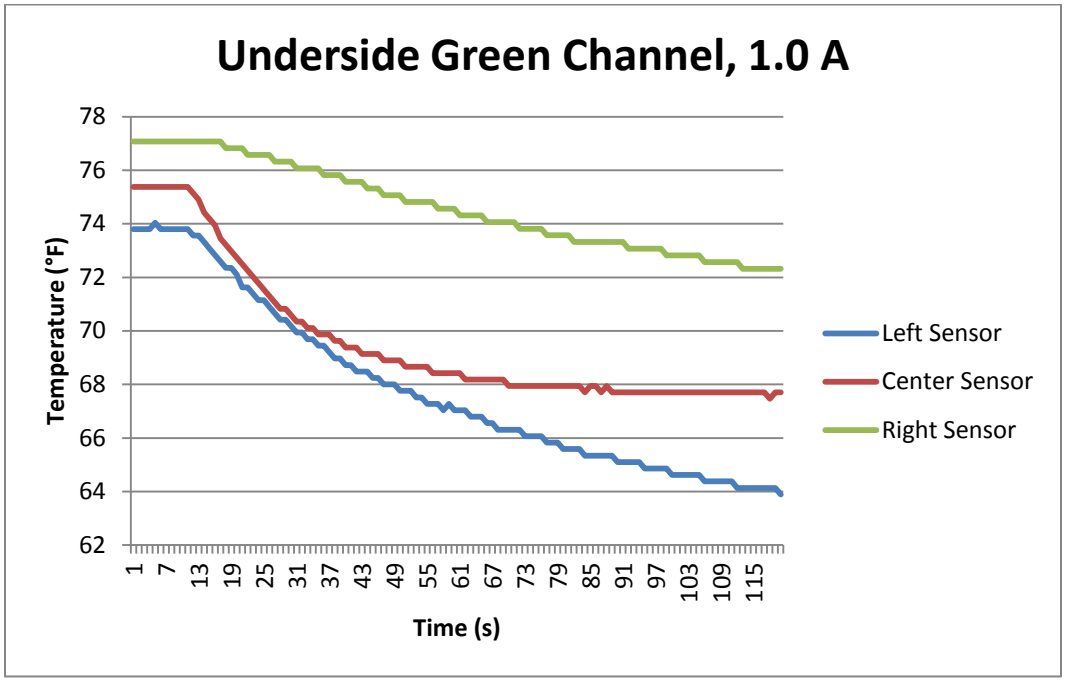

Figure JJ: Underside green channel temperature profile at 1.0 amps

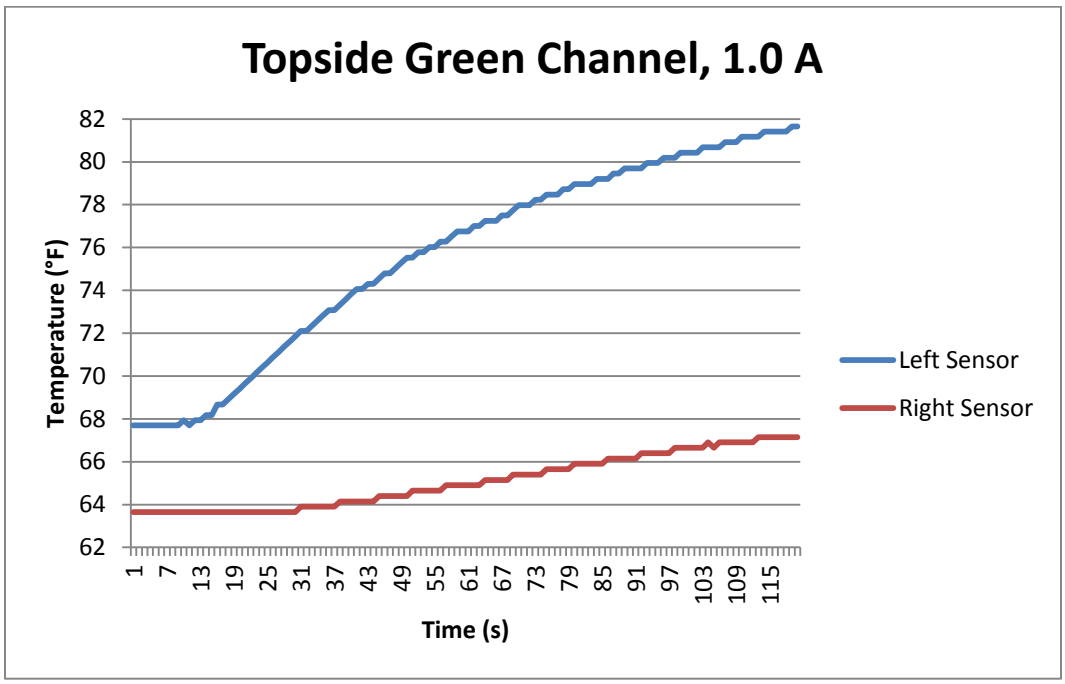

Figure KK: Topside green channel temperature profile at 1.0 amps

Appendix H (Continued)

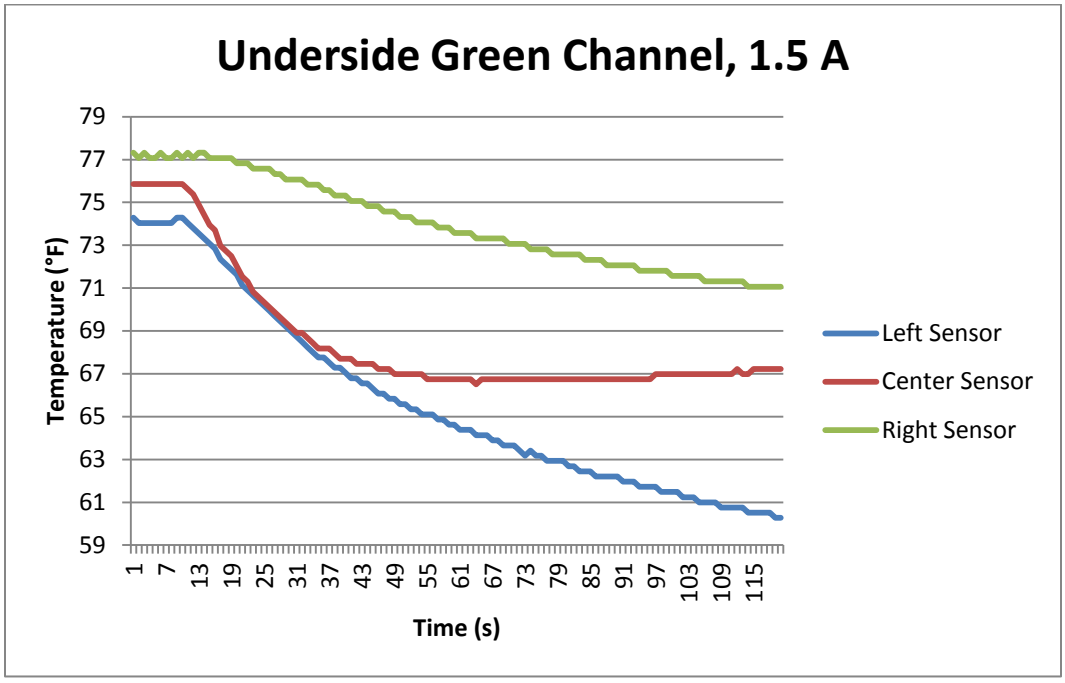

Figure LL: Underside green channel temperature profile at 1.5 amps

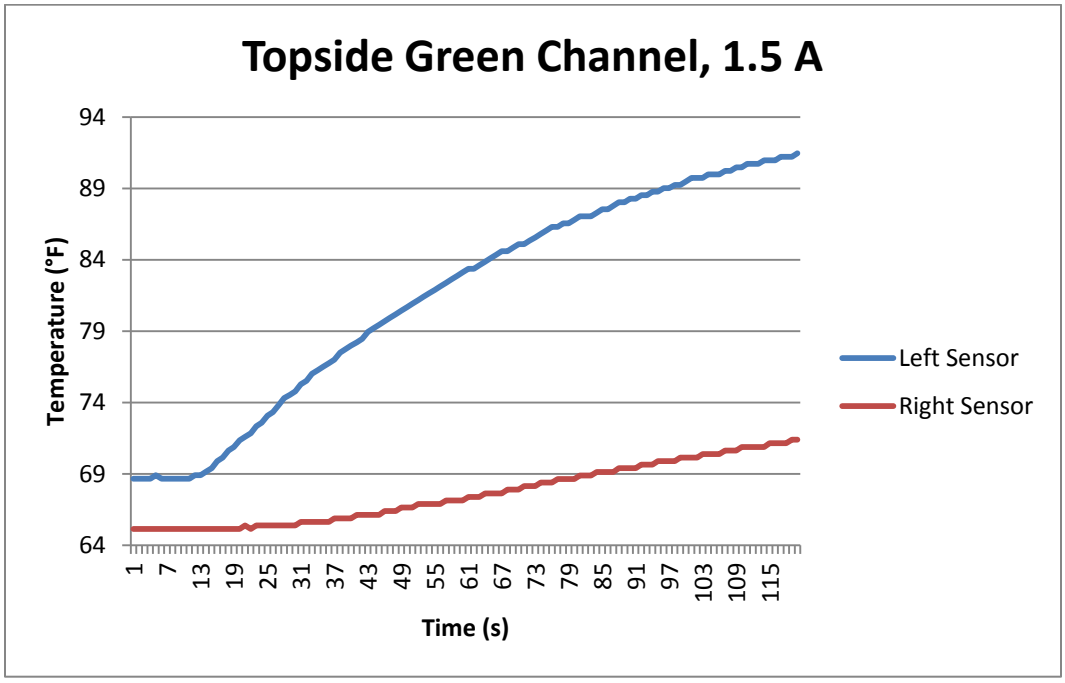

Figure MM: Topside green channel temperature profile at 1.5 amps

Appendix H (Continued)

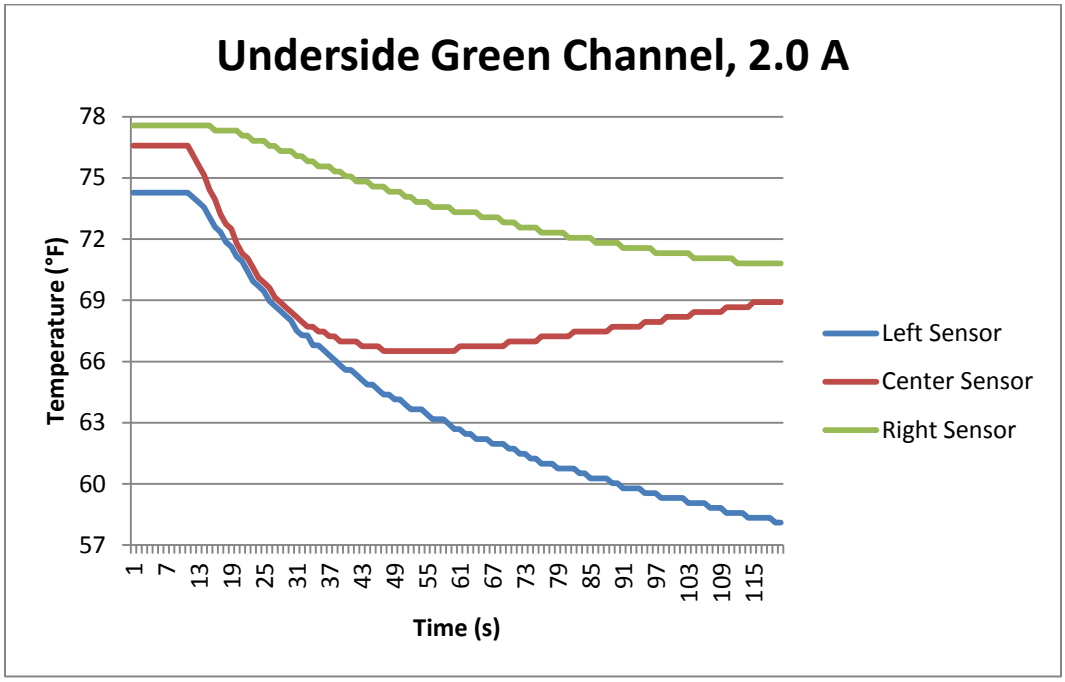

Figure NN: Underside green channel temperature profile at 2.0 amps

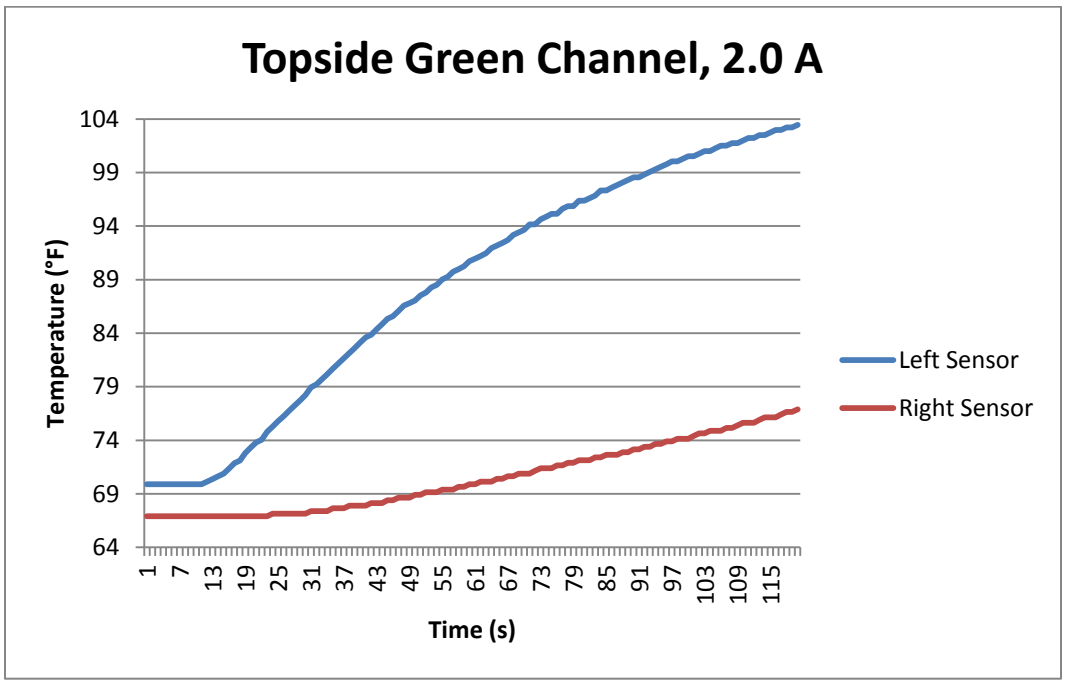

Figure OO: Topside green channel temperature profile at 2.0 amps

Appendix H (Continued)

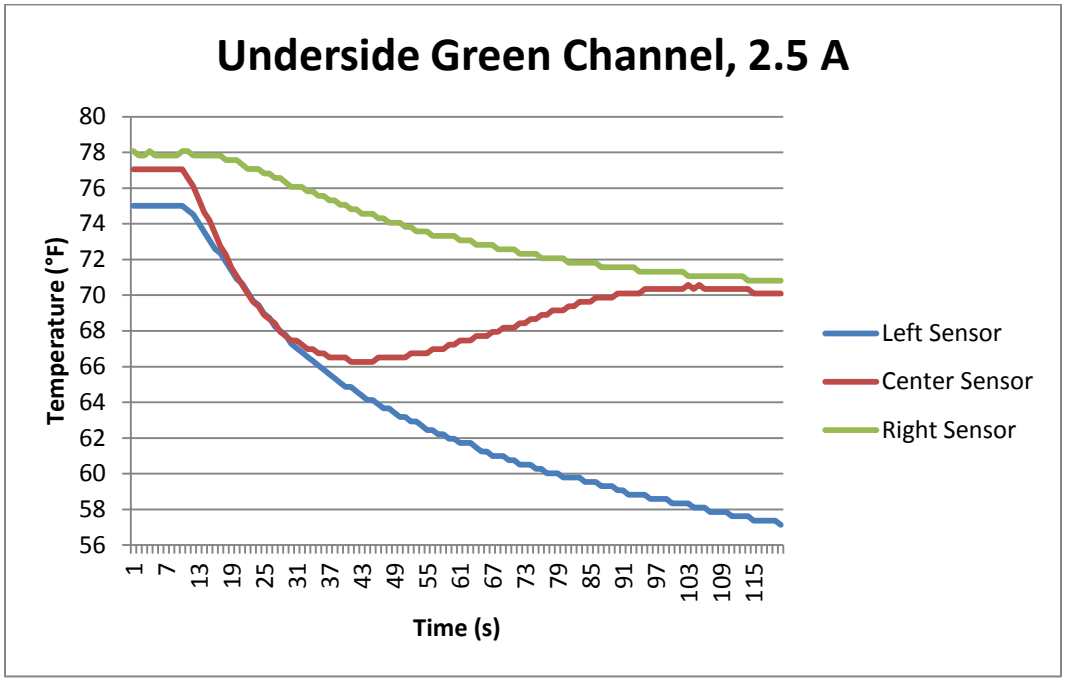

Figure PP: Underside green channel temperature profile at 2.5 amps

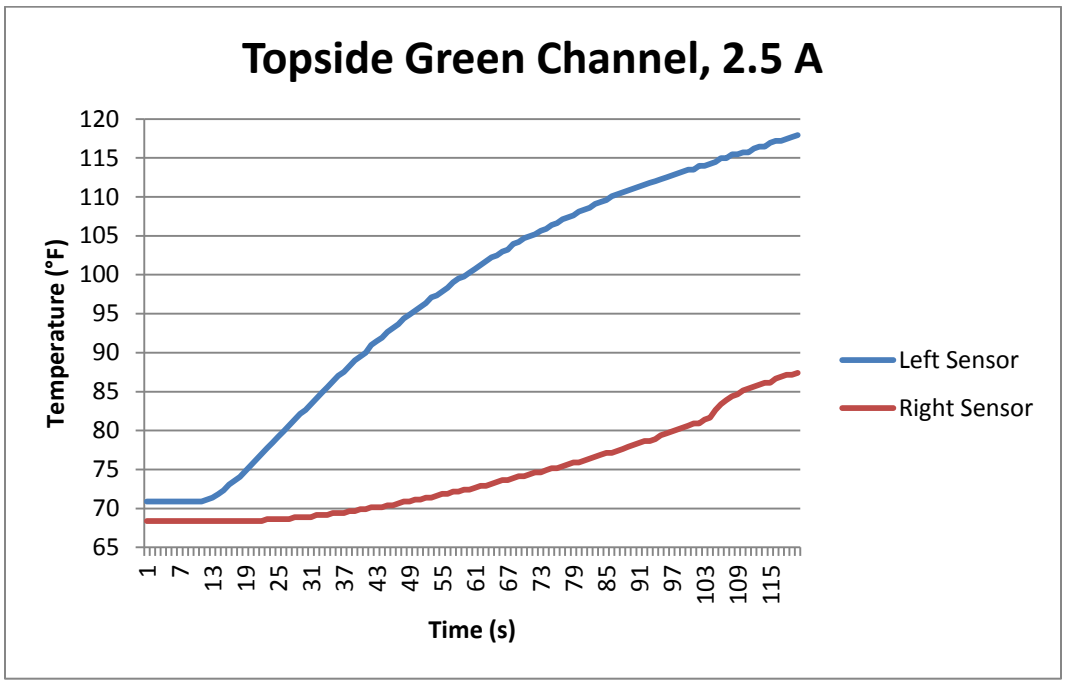

Figure QQ: Topside green channel temperature profile at 2.5 amps